IMPROVING HYDROLOGIC PREDICTION FOR LARGE URBAN AREAS THROUGH STOCHASTIC ANALYSIS OF SCALE-DEPENDENT RUNOFF RESPONSE, ADVANCED SENSING AND HIGH-RESOLUTION MODELING

by

AMIR NOROUZI

Presented to the Faculty of the Graduate School of
The University of Texas at Arlington in Partial Fulfillment
of the Requirements
for the Degree of

DOCTOR OF PHILOSOPHY
THE UNIVERSITY OF TEXAS AT ARLINGTON

MAY 2016

Acknowledgements

I would like to express my deepest gratitude to my advisor Dr. Dong-Jun Seo, not only for his scholarly advice but also for his patience and kindness. I would also like to thank my dissertation committee members, Drs. Xinbao Yu, Nick Fang and Michael Shultz.

I would like to thank Dr. Sunghee Kim and Ms. Hamideh Habibi at the University of Texas at Arlington; Drs. Haksu Lee, Zhengtao Cui, Yu Zhang, and Mr. Brian Cosgrove at the National Weather Service; Drs. Jason Kean and J. Dungan Smith at the US Geological Survey; Dr. Brian Nelson at the National Centers for Environmental Information; Dr. Emad Habib at the University of Louisiana at Lafayette; Dr. Ranjan Muttiah, Ms. Laura Pham, and Mr. Timothy B. Royer at the City of Fort Worth, TX; Mr. Donald E. Colton of DEC Data Systems, Mr. Romin A. Khavari, Ms. Stephanie Griffin and Mr. Barry D. Fulfer at the City of Grand Prairie, TX; Ms. Mandy Clark at the City of Arlington, TX; and Mr. Don Lawrence at the City of Dallas, TX, for providing data and assistance throughout my research.

For supporting me through all my years as a student, I would like to thank my parents, Alireza and Efat, and my brothers, Ehsan and Emad.

April 25, 2016

Abstract

IMPROVING HYDROLOGIC PREDICTION FOR LARGE URBAN AREAS THROUGH STOCHASTIC ANALYSIS OF SCALE-DEPENDENT RUNOFF RESPONSE, ADVANCED SENSING AND HIGH-RESOLUTION MODELING

Amir Norouzi, PhD

The University of Texas at Arlington, 2016

Supervising Professor: Dong-Jun Seo

Due to urbanization and climate change, large urban areas such as the Dallas-Fort Worth Metroplex (DFW) area is vulnerable not only to river flooding but also flash flooding. Due to the nonstationarities involved, projecting how the changes in land cover and climate may modify flood frequency in large urban areas is a challenge. Part I of this work develops a simple spatial stochastic model for rainfall-to-areal runoff in urban areas, evaluates climatological mean and variance of mean areal runoff (MAR) over a range of catchment scales, translates them into runoff frequency as a proxy for flood frequency, and assesses its sensitivity to precipitation, imperviousness and soil, and their changes. The results show that the variability of MAR in urban areas depends significantly on the catchment scale and magnitude of precipitation, and that precipitation, soil, and land cover all exert influences of varying relative importance in shaping the frequency of MAR, and hence flood frequency, for different sizes of urban areas. The findings indicate that, due to large sensitivity of frequency of MAR to multiple hydrometeorological and physiographic factors, estimation of flood frequency for urban catchments is inherently more uncertain, and the approach developed in this work may be useful in developing bounds for flood frequencies in urban areas under nonstationary conditions arising from climate change and urbanization.

High-resolution hydrologic and hydraulic models are necessary to provide location- and time-specific warnings in densely populated areas. Due to the errors in precipitation input, and model parameters, structures and states, however, increasing the nominal resolution of the models may not improve the accuracy of the model output. Part II of this work tests the current limits of high-resolution hydrologic modeling for real-time forecasting by assessing the sensitivity of streamflow and soil moisture simulations in urban catchments to the spatial resolution of the rainfall input and the a priori model parameters. The hydrologic model used is the National Weather Service (NWS) Hydrology Laboratory's Research Distributed Hydrologic Model (HLRDHM) applied at spatial resolutions of 250 m to 2 km for precipitation and 250 m to 4 km for the a priori model parameters. The precipitation input used are the Collaborative Adaptive Sensing of the Atmosphere (CASA) and the Multisensor Precipitation Estimator (MPE) products available at 500 m and 1 min, and 4 km and 1 hr spatiotemporal resolutions, respectively. The streamflow simulation results were evaluated for two urban catchments of 3.4 to 14.4 km^2 in Arlington and Grand Prairie, TX. The streamflow observations used in the evaluation were obtained from water level measurements via the rating curves derived from 1-D steady-state non-uniform hydraulic model. The soil moisture simulation results were evaluated for three locations in Arlington where observations are available at depths of 0.05, 0.10, 0.25, 0.50 and 1.00 m. The soil moisture observations were obtained from three Time Domain Transmissometry (TDT) and Time Domain Reflectometry (TDR) sensors newly deployed for this work. The results show that the use of high-resolution QPE improves streamflow simulation significantly, but that, once the resolution of QPE is increased to the scale of the catchment, no clear relationships are found between the simulation accuracy and the resolution of the QPE or hydrologic modeling, presumably because the errors in QPE and models mask the relationships. The soil moisture results suggest that there are disparate infiltration processes at work within a small area in Arlington, and that, while the near-surface simulation of soil moisture is generally skillful, the Sacramento soil moisture accounting model – heat transfer version (SAC-HT) in HLRDHM has difficulty in simulating the vertical dynamics of soil moisture. The findings point to real-time updating of model states to reduce uncertainties in initial soil moisture conditions, and the need for a dense observing network to improve understanding and to assess the impact at the catchment scale.

Continuing urbanization will continue to alter the hydrologic response of urban catchments in the DFW area and elsewhere. To assess the impact of recent land cover changes in the study area and to predict what may occur in the future, streamflow and soil moisture were simulated using HLRDHM at 250 m and 5 min resolution with the National Land Cover Data of 2001, 2006 and 2011 for five urban catchments in Arlington and Grand Prairie, TX. The analysis indicates that imperviousness increased by about 15 percent in the DFW area between 2001 and 2011. The findings indicate that, in terms of peak flow, time-to-peak and runoff volume, small events are more sensitive to changes in impervious cover than large events, increase in peak flow is more pronounced for catchments with larger increase in impervious cover, increase in peak flow is also impacted by changes in antecedent soil moisture due to increased impervious cover, runoff volume is not significantly impacted by changes in impervious cover, and changes in time-to-peak relative to the response time of the catchment is impacted by the location of the land cover changes relative to the outlet and the time-to-peak itself. In particular, the Johnson Creek Catchment in Arlington (~40 km^2), which has a time-to-peak of only 40 min, shows larger sensitivity in time-to-peak to land cover changes due presumably to the proximity of the area of increased land cover to the catchment outlet. For further evaluation, however, dense observation networks for streamflow and soil moisture, such as the Arlington Urban Hydrology Testbed currently under development, are necessary in addition to the CASA network of X-band polarimetric radars for high-resolution quantitative precipitation information (QPI).

Table of Contents

List of Illustrations

List of Tables

Chapter 1 Introduction

Increasing urbanization due to population growth and increasing frequency and amount of heavy-to-extreme precipitation expected from climate change put urban areas in a vulnerable position. Compared to rural catchments, urban catchments are usually smaller and have larger impervious areas (Bruni et al., 2015) and, consequently, the response times are shorter (Javier et al., 2007; ten Veldhuis et al., 2014; Bruni et al., 2015; and, Rafieeinasab et al., 2015a). To observe and predict fast-occurring flash flooding in small areas, it is necessary to sense and model at high spatiotemporal resolutions. For high-resolution observation and modeling of large urban areas, the use of weather radar and distributed hydrologic modeling is a natural progression. Quantitative precipitation estimates (QPEs) from radar, however, are subject to various sources of error. Also, high-resolution distributed modeling is subject to nonlinear growth of error due to errors in QPE and in model initial conditions (IC), parameters and structures. For example, to reduce parametric uncertainty, expensive calibration efforts are often necessary (Moradkhani and Sorooshian, 2008, Shi et al., 2014). For distributed models, calibration is a particularly daunting challenge due to large dimensionality. To avoid or minimize calibration, much effort has recently been made to derive skillful "a priori" parameters from the physiographic properties, such as soil, land cover and land use, of the area being modeled (Koren et al., 2000; Koren et al., 2003; Anderson et al., 2006; and Zhang et al., 2011). Recent advances in in-situ and remote sensing have increased researchers' and engineers' knowledge of soil (Robinson et al., 2008; Vereecken et al., 2014), land cover and land use (Homer et al., 2012; Homer et al., 2015). Using high-resolution physiographic data, one may derive a priori model parameters at a high resolution and hence allow high-resolution hydrologic modeling for flash flood forecasting in large urban areas.

Currently, in support of CASAWX (http://www.nctcog.org/ep/Special_Projects/CASAWX/) UTA runs the National Weather Service (NWS) Hydrology Laboratory Research Distributed Hydrologic Model (HLRDHM, Koren et al. 2004) in real time and generate hydrologic products for the Dallas-Fort Worth (DFW) Metroplex area, the 4th most populous metropolitan areas in the US (Habibi et al., 2016). HLRDHM uses rainfall data at 500 - 1 min resolution from the network of Collaborative Adaptive Sensing of Atmosphere (CASA) radars. The DFW operation of HLRDHM uses the Sacramento model (SAC, Burnash 1995) for soil moisture accounting and the kinematic wave model (Chow et al. 1988) for hillslope and channel routing. The SAC parameters are available for the conterminous US (CONUS) from NWS at a 4 km resolution (NWS 2009). In the initial DFW operation of HLRDHM, the 4 km-resolution a priori SAC parameters were used. The only exception was the percent impervious area, or PCTIM, which was derived at a 500 m resolution from the GIS layers representing impervious cover (Rafieeinasab et al., 2015a; Habibi et al., 2016). The ill effects of using coarse-resolution a priori parameters may be seen in the runoff accumulation map shown in Figure 1-1; note the blocky patterns stemming from coarse-resolution soil moisture simulation.

While there are large areas of high imperviousness throughout the DFW area, collectively the pervious areas are much larger than the impervious areas. As such, soil moisture is an important factor in runoff generation as well as in the urban water cycle. Soil moisture, however, is rarely observed in reality and there hence exists a large need for soil moisture sensing in urban areas not only to evaluate the performance of high-resolution hydrologic model but also to understand the runoff generation process in built environments.

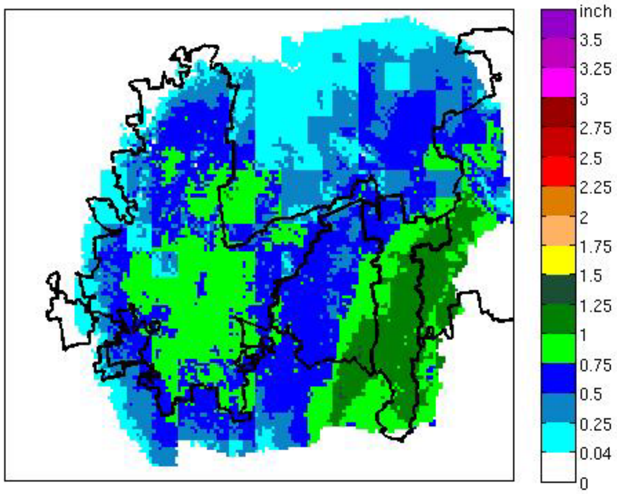

Figure 1-1 3-hr runoff accumulation in the cities of Fort Worth, Arlington and Grand Prairie for a rainfall event on 5/17/2015

The main objectives of this work are:

1. **Advance the knowledge and understanding of the sources of variability in areal runoff in large urban areas and their dependence on catchment scale.** With urbanization and climate change, many areas in the US and abroad face increasing threats of flash flooding. Due to nonstationarities arising from changes in land cover and climate, however, it is not readily possible to project how such changes may modify flood frequency. In this work, we formulate a simple spatial stochastic model for rainfall-to-areal runoff in urban areas, evaluate climatological mean and variance of mean areal runoff (MAR) over a range of catchment scale, translate them into runoff frequency, which is used as a proxy for flood frequency, and assess its sensitivity to precipitation, imperviousness and soil,

and their changes as a function of catchment scale and magnitude of precipitation.

2. **Advance the knowledge and understanding of the runoff generation processes in urban areas.** Soil moisture is rarely observed in the study area. The infiltration and hence the runoff generation processes are not well understood. While most hydrologic models assume some combination of infiltration and saturation excess mechanisms for runoff generation, they have not been verified in the study area based on in-situ sensing.

3. **Advance the knowledge and understanding of the performance of high-resolution hydrologic modeling in a large urban area and its sensitivity to the spatial resolution of the model parameters and rainfall input.** While the need for high-resolution modeling in urban areas is clear, it is not very clear whether increasing (nominal) resolution increases accuracy given the current level of advances in hydrologic-hydraulic modeling and QPE. This work targets objective assessment of the sensitivity of the quality of model simulation of streamflow and soil moisture to the resolutions of model parameters and rainfall input.

4. **Advance the knowledge and understanding of the impact of land cover changes on hydrologic response of catchments.** While there has been significant increase in imperviousness in the study area in recent years, the impact of land cover changes on streamflow response has not been quantitatively assessed in flood-prone catchments of Arlington and Grand Prairie in DFW.

This research seeks to address the following questions:

1. What factors determine flood risks in urban areas of different sizes?
2. How do infiltration processes vary in different parts of the urban areas in DFW?
3. What are the limits of high-resolution hydrologic modeling in large urban areas?
4. How do land cover changes impact the hydrologic response of urban catchments?

To address the 1st question, stochastic analysis of scale-dependent runoff response in urban areas of varying sizes was used. To address the 2nd question, in-situ soil moisture sensors were deployed and observations were made. To address the 3rd question, high-resolution model parameters were derived and used in high-resolution hydrologic modeling for large urban areas. For the 4th question, a simulation study was carried out to assess the impact of land cover changes on streamflow response.

New contributions of this research are as follows:

1. Advanced understanding of the factors shaping flood frequency in urban areas of varying size,
2. Development of a new approach for urban flood frequency analysis under urbanization and climate change,
3. Advanced understanding of runoff generation processes in urban catchments based on soil moisture observations,
4. Advanced understanding of the sensitivity of high-resolution streamflow and soil moisture simulations to spatial resolution of model parameters and rainfall input,
5. Assessment of the impact of land cover changes on streamflow for urban catchments in Arlington and Grand Prairie.

Figure 1-2 depicts the organization and flow of this dissertation.

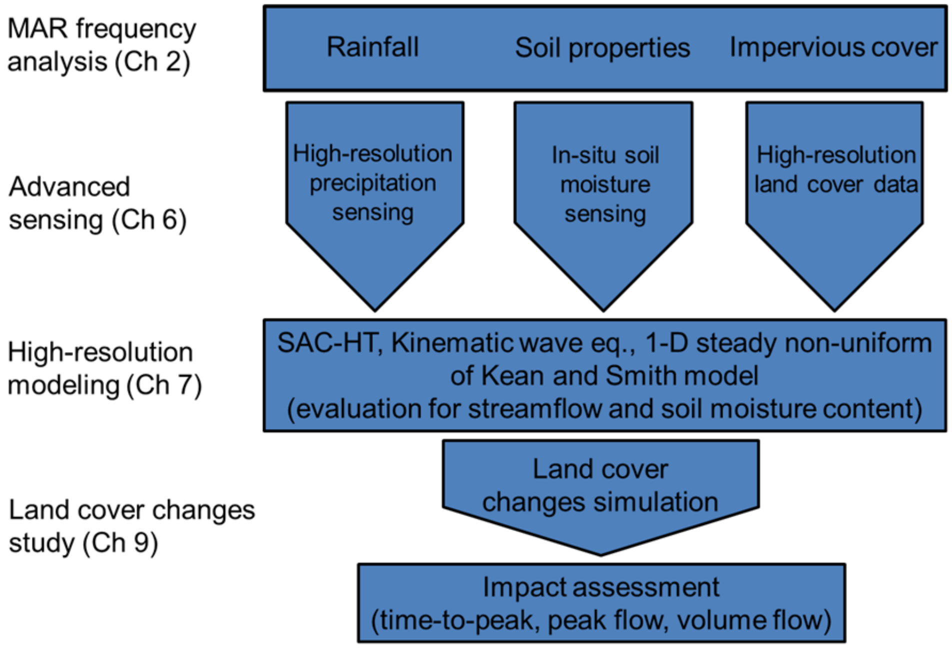

Figure 1-2 Schematic of the structure of the dissertation

This dissertation is organized as follows. Chapter 2 describes the scale-dependent sensitivity of frequency of mean areal runoff in urban areas. Chapter 3 describes the background for high-resolution streamflow and soil moisture simulations and the impact of land cover changes on hydrologic response of urban catchments. Chapter 4 describes the methodology for the derivation of a priori model parameters at higher resolutions, the sensitivity analysis of streamflow and soil moisture simulations to the spatial resolution of the model parameters and the rainfall input, and assessment of the impact of land cover changes on the streamflow simulation in urban areas. Chapter 5 describes the study area and data used. Chapter 6 describes advanced sensing. Chapter 7 and chapter 8 describe high-resolution hydrologic modeling and evaluation of results, respectively. Chapter 9 describes the impact of land cover changes on streamflow response in urban areas. Chapter 10 provides the conclusions and future research commendations.

Chapter 2 Scale-dependent sensitivity of frequency of mean areal runoff in urban areas

2.1 Introduction

Due to nonstationarities arising from urbanization and climate change, assessing flood risks in large urban areas is a large challenge. In such areas, flood frequency analysis, as traditionally practiced (Chow et al., 1988; Stedinger et al., 1993), is unlikely to properly represent the future risk as a consequence of the aforementioned nonstationarities. One way to address the above situation is to design and carry out stochastic simulation experiments in which plausible realizations of precipitation and other fields are generated and input into hydrologic and, as necessary, hydraulic models, and obtain derived distributions of the variables of interest numerically (Mejía and Moglen, 2010; Zhang and Shuster, 2015). Such an approach, however, is computationally too expensive to be practical due to large degrees of freedom associated with hydroclimatic-hydrometeorological-hydrologic-hydraulic systems. In this work, an analytical framework to assess how intermittency of precipitation, inner variability of precipitation, imperviousness of land cover, and variability of soil may jointly shape the statistical characteristics of climatological areal runoff as a function of catchment size, and how their changes may alter scale-dependent variability of areal runoff, and hence flash flooding risks associated with climate change and urbanization is proposed. Specifically, we seek to advance understanding of scale-dependent relationships between the variability of mean areal runoff (MAR) and the above four sources of variability in which MAR would serve as a proxy for peak flow. The specific questions to be addressed include: 1) What are the relative contributions of the four sources of variability to variability of MAR? 2) How does the characteristic spatial scale of each of the four sources of variability impact the scale-dependent variability of MAR? 3) How do imperviousness, its spatial variability, and its variations in different parts of a large urban area (from mostly pervious to mostly impervious) modify the variability of MAR?, and 4) How does spatial variability in soil in pervious areas modify the above relationships?

The range of spatial scales considered in this work corresponds to the areal extent of most cities in the US (see Figure 2-1), i.e., below 40×40 km^2. The study area in this work is the Dallas-Fort Worth Metroplex (DFW) which is part of the so-called flash flood alley that stretches from Central to North Texas (Zahran et al., 2008). The Cities of Dallas, Fort Worth, Arlington and Grand Prairie which stretch the middle of DFW have areas of 999.3 (31.6×31.6), 904.4 (30.1×30.1), 258.2 (16.7×16.7), 210.0 (14.5×14.5) km^2, respectively, and they are hence representative of the US cities in terms of areal extent. Collectively, the 4 cities have an area of about 2,371.9 (48.7×48.7) km^2 which approximately form the upper limit of the US cities (Figure 2-1).

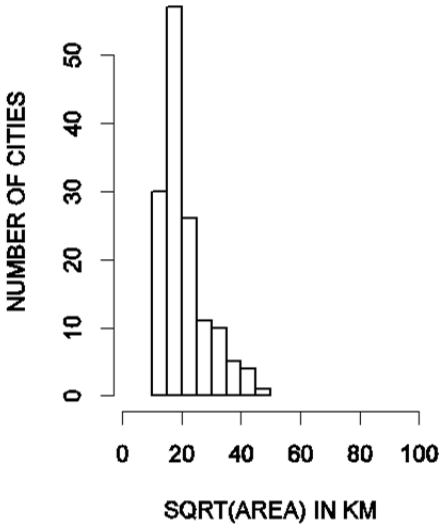

Figure 2-1 Areal extent of most cities in the US

2.2 Approach

A very simple spatial stochastic model for areal runoff is formulated, which accounts for inner variability and intermittency of precipitation, imperviousness of urban land cover and soil conditions in pervious areas, evaluate the first two statistical moments of areal runoff, and derive the areal runoff frequency curves as a proxy for flood frequency curves under assumed distributional models for point precipitation and areal runoff. To that end, the time-integrated surface runoff is expressed over some fixed duration at some location *u* in the area of interest *A* as follows:

$$R_{sfc}(u) = P(u)I_{\text{int}}(u)I_{imp}(u) + R_{per}(u)I_{\text{int}}(u)\{1 - I_{imp}(u)\} \tag{2-1}$$

In the above, $R_{sfc}(u)$ denotes the surface runoff at location *u* (mm), P(u) denotes the precipitation at *u* (mm), and $I_{int}(u)$ and $I_{imp}(u)$ denote the indicator variables for intermittency of precipitation given it is precipitating somewhere in *A* and imperviousness of land cover at location *u*, respectively, and $R_{per}(u)$ denotes the runoff at the impervious location *u*. The first and second terms in Eq.(2-1) hence represent runoff at impervious and pervious location u, respectively. The indicator variables, $I_{int}(u)$ and $I_{imp}(u)$, in Eq.(2-1) are defined as:

$$i_{\text{int}}(u) = \begin{cases} 1 & if \quad u \in A_p \in A, \quad A_p \neq \{\} \\ 0 & otherwise \end{cases} \tag{2-2}$$

$$i_{imp}(u) = \begin{cases} 1 & if \quad u \in A_{imp} \in A \\ 0 & otherwise \end{cases} \tag{2-3}$$

where $i_{int}(u)$ and $i_{imp}(u)$ denote the experimental values of 0 or 1 that the indicator random variables, $I_{int}(u)$ and $I_{imp}(u)$, may take on, respectively, A_p denotes the non-null precipitation area within the area of interest, *A*, and A_{imp} denotes the impervious area within *A*.

To model surface runoff at some pervious location *u*, $R_{per}(u)$, the Curve Number (CN) Method (USDA, 1986) is used. The CN method is attractive for simplicity while capturing the essential nonlinear relationships between rainfall and runoff. Also, its widespread use allows relatively straightforward practical interpretation of the results in this work. In the developments to follow, it is assumed that the initial abstraction, $I_a(u)$, and the water holding capacity, *S(u)*, are spatially uniform for computational tractability. Later, this assumption is relaxed. With the CN method, surface runoff at some pervious location u is given by:

$$R_{per}(u) = \begin{cases} 0 & if \quad P(u) < I_a(u) \\ R(u) = \dfrac{\{P(u) - I_a(u)\}^2}{P(u) - I_a(u) + S(u)} & if \quad P(u) \geq I_a(u) \end{cases} \tag{2-4}$$

where $R_{per}(u)$ denotes the runoff at some pervious location u (mm), $P(u)$ denotes the precipitation at u (mm), $I_a(u)$ denotes that initial abstraction at *u* (mm) given by $I_a(u)=\alpha S(u)$, $0<\alpha<1$, and $S(u)$ denotes the potential maximum retention at u after runoff begins (mm), and *R(u)* denotes the positive runoff at pervious location u (mm). With Eq.(2-4), Eq. (2-1) may be rewritten as:

$$R_{sfc}(u) = P(u)I_{\text{int}}(u)I_{imp}(u) + R(u)I_{\{\circ\}}(u)\{1 - I_{imp}(u)\} \tag{2-5}$$

where the indicator random variable, $I_{\{\circ\}}(u)$, is defined as:

$$i_{\{\circ\}}(u) = \begin{cases} 0 \quad if \quad P(u) < I_a(u) \\ 1 \quad if \quad P(u) \geq I_a(u) \end{cases} \tag{2-6}$$

Using the above model for surface runoff, mean and variance of mean MAR is evaluated. Similar analyses of scale-dependent variability of mean areal precipitation (MAP) and MAR, but without impervious cover, were described in Seo and Smith (1996a, 1996b) using the coefficient of variation (CV) as a representative measure of variability of MAR over a range of catchment size. In this work, it is assumed that point precipitation follows lognormal, Weibull and gamma distributions. Given mean and variance of MAR resulting from the distribution model for precipitation, it is assumed that MAR shares the same distribution and assess the impact of different sources of variability in Eq.(2-1) on exceedance probability of MAR.

2.3 Evaluation of moments of MAR

In this section, it is described how the mean and variance of MAR of Eq.(2-1) is evaluated.

2.3.1 Evaluation of mean of MAR

Climatological mean of MAR over A in which it is precipitating somewhere is given by:

$$
\begin{aligned}
&E[\frac{1}{A}\int_A R_{sfc}(u)du \,|\, \int_A I_{\text{int}}(u)du > 0] \\
&= \frac{1}{A}\int_A E[P(u)I_{\text{int}}(u)I_{imp}(u) + \{R(u)I_{\{\circ\}}(u)\{1 - I_{imp}(u)\} \,|\, \int_A I_{\text{int}}(u)du > 0]du
\end{aligned}
\qquad (2\text{-}7)
$$

where the conditioning event, $\{\int_A I_{\text{int}}(u)du > 0\}$, states that it is precipitating somewhere within *A*. Assuming homogeneity within *A* and independence between precipitation and imperviousness, Eq.(2-7) may be rewritten as:

$$\begin{aligned}
&E[\frac{1}{A}\int_A R_{sfc}(u)du \mid \int_A I_{\mathrm{int}}(u)du > 0] \\
&= \frac{1}{A}\int_A E[P(u)I_{\mathrm{int}}(u) \mid \int_A I_{\mathrm{int}}(u)du > 0]E[I_{imp}(u)] \\
&+ E[R(u)I_{\{\circ\}} \mid \int_A I_{\mathrm{int}}(u)du > 0]E[1 - I_{imp}(u)]du \\
&= \frac{1}{A}\int_A E[P(u) \mid P(u) > 0, \int_A I_{\mathrm{int}}(u)du > 0]\Pr[P(u) > 0 \mid \int_A I_{\mathrm{int}}(u)du > 0]E[I_{imp}(u)] \\
&+ E[R(u) \mid P(u) > I_a, \int_A I_{\mathrm{int}}(u)du > 0]\Pr[P(u) > I_a \mid \int_A I_{\mathrm{int}}(u)du > 0]E[1 - I_{imp}(u)]du \\
&= \frac{1}{A}\int_A E[P(u) \mid P(u) > 0]\Pr[P(u) > 0 \mid \int_A I_{\mathrm{int}}(u)du > 0]E[I_{imp}(u)] \\
&+ E[R(u) \mid P(u) > I_a(u)]\Pr[P(u) > I_a(u) \mid \int_A I_{\mathrm{int}}(u)du > 0]E[1 - I_{imp}(u)]du \\
&= \frac{1}{A}\int_A m_{CP}(u)m_{CI_{\mathrm{int}}}(u)m_{Iimp} + m_{CR}(u)m_{CI\{\circ\}}(u)(1 - m_{Iimp})du \\
&= m_{Iimp}\frac{1}{A}\int_A m_{CP}(u)m_{CI_{\mathrm{int}}}(u)du + (1 - m_{Iimp})\frac{1}{A}\int_A m_{CR}(u)m_{CI\{\circ\}}(u)du
\end{aligned} \qquad (2\text{-}8)$$

In the above, $m_{CP}(u)$ denotes the mean of positive point precipitation at location *u*, $m_{CI_{\mathrm{int}}}(u)$ denotes the probability of precipitation (PoP) at location u given that it is precipitating somewhere in *A*, m_{Iimp} denotes the fractional impervious area within *A*, $m_{CR}(u)$ denotes the mean positive runoff at location *u* given that it is precipitating somewhere in *A*, and $m_{CI\{\circ\}}(u)$ denotes the PoP exceeding $I_a(u)$ given that it is precipitating somewhere in *A*. If precipitation climatology is homogeneous, $m_{CR}(u)$ and $m_{CI\{\circ\}}(u)$ are location-invariant which reduces Eq.(2-8) to:

$$E[\frac{1}{A}\int_A R_{sfc}(u)du \mid \int_A I_{\mathrm{int}}(u)du > 0] = m_{Iimp}m_{CP}m_{CI_{\mathrm{int}}} + (1 - m_{Iimp})m_{CR}m_{CI\{\circ\}} \qquad (2\text{-}9)$$

where m_{CP}, $m_{CI_{\mathrm{int}}}$, m_{CR} and $m_{CI\{\circ\}}$ denote the constant conditional (on occurrence of precipitation) mean precipitation, PoP (or, equivalently, fractional coverage), mean positive runoff and PoP exceeding the threshold, $I_a(u)$, respectively. In this work, it is assumed that the probability distribution of point precipitation, *P(u)* for *P(u)*>0, follows lognormal, Weibull or gamma. Then, the mean positive runoff, m_{CR}, in Eq.(2-9) under known *S(u)* and $I_a(u)$ is given by:

$$m_{CR}(u) = E[R(u) \mid P(u) > I_a(u)] = L_R^{-1} \int_{I_a(u)}^{\infty} \frac{\{P_u - I_a(u)\}^2}{P_u - I_a(u) + S(u)} \bullet f_{P(u)}(p_u) dp_u \qquad (2\text{-}10)$$

In the above, $f_{P(u)}(p_u)$ denotes the marginal probability density function (PDF) of *P(u)* and the normalizing probability, L_R, is given by:

$$L_R = \int_{I_a(u)}^{\infty} f_{P(u)}(p_u) dp_u \qquad (2\text{-}11)$$

In Eq.(2-9), the PoP at some point within *A* given that it is precipitating somewhere therein, $m_{CI_{\text{int}}}$, is given by:

$$m_{CI_{\text{int}}}(u) = \Pr[P(u) > 0 \mid \int_A I_{\text{int}}(u) du > 0] = \frac{\Pr[P(u) > 0]}{1 - \Pr[\int_A I_{\text{int}}(u) du = 0]} \qquad (2\text{-}12)$$

In the above, $\Pr[\int_A I_{\text{int}}(u) du = 0]$ may be estimated numerically via, e.g., indicator kriging given the PoP at point scale and indicator correlation structure (Solow, 1986; Seo et al., 2000). Similarly, the conditional PoP exceeding $I_a(u)$ at some point within *A*, $m_{CI\{\circ\}}(u)$, is given by:

$$m_{CI\{\circ\}}(u) = \Pr[P(u) > I_a \mid \int_A I_{\text{int}}(u) du > 0] = \frac{\Pr[P(u) > I_a(u)]}{1 - \Pr[\int_A I_{\text{int}}(u) du = 0]} \qquad (2\text{-}13)$$

2.3.2 Evaluation of second moment of MAR

To evaluate the second moment of areal runoff:

$$
\begin{aligned}
&E[\{\frac{1}{A}\int_A R_{sfc}(u)du\}^2 \mid \int_A I_{\text{int}}(u)du > 0] \\
&= \frac{1}{A^2}\int_A \int_A E[\{P(u)I_{\text{int}}(u)I_{imp}(u) + R(u)I_{\{\circ\}}(u)(1 - I_{imp}(u))\} \\
&\{P(v)I_{\text{int}}(v)I_{imp}(v) + R(v)I_{\{\circ\}}(v)(1 - I_{imp}(v))\} \mid \int_A I_{\text{int}}(u)du > 0]dudv \\
&= \frac{1}{A^2}\int_A \int_A E[P(u)P(v) \mid i_{I\text{int}}(u) = 1, i_{I\text{int}}(v) = 1, \int_A I_{\text{int}}(u)du > 0] \\
&E[I_{I\text{int}}(u)I_{I\text{int}}(v) \mid \int_A I_{\text{int}}(u)du > 0]E[I_{imp}(u)I_{imp}(v)] \qquad \text{(2-14)} \\
&+ 2E[P(u)R(v) \mid i_{I\text{int}}(u) = 1, i_{I\{\circ\}}(v) = 1, \int_A I_{\text{int}}(u)du > 0] \\
&E[I_{I\text{int}}(u)I_{I\{\circ\}}(v) \mid \int_A I_{\text{int}}(u)du > 0]E[I_{imp}(u)I_{per}(v)] \\
&+ E[R(u)R(v) \mid i_{\{\circ\}}(u) = 1, i_{\{\circ\}}(v) = 1, \int_A I_{\text{int}}(u)du > 0] \\
&E[I_{I\{\circ\}}(u)I_{I\{\circ\}}(v) \mid \int_A I_{\text{int}}(u)du > 0]E[I_{per}(u)I_{per}(v)]dudv
\end{aligned}
$$

In the above, the indicator variable, $I_{per}(u)$, is the same as $1\text{-}I_{imp}(u)$ and is defined as:

$$
i_{per}(u) = \begin{cases} 1 & if \quad u \in A_{per} \in A \\ 0 & otherwise \end{cases} \qquad \text{(2-15)}
$$

where A_{per} denotes the pervious area in A and is equal to A_{imp}^C where the superscript C denotes complement. Eq.(2-14) decomposes the uncentered variance of mean areal runoff into contributions from runoff over the impervious area, runoff over the pervious area and the cross term, and allows assessment of the impact on variability of MAR of intermittency of precipitation, precipitation amount and its variability within the precipitation area, imperviousness and its spatial variability, initial abstraction, $I_a(u)$, and water holding capacity of the soil, $S(u)$, and its variability, where $I_a(u)$ and $S(u)$ are assumed for now to be spatially uniform. Descriptions of how the terms in the integrand of Eq. (2-14) may be specified are as follows.

Under the assumption that precipitation and imperviousness are second-order homogeneity in A, the uncentered covariance terms in Eq.(2-14) may be modelled as follows (see also Seo and Smith, 1996a, 1996b; Seo, 1998; Zhang et al., 2015). The uncentered spatial covariance of positive precipitation may be modeled as:

$$E[P(u)P(v) \mid i_{I\,\mathrm{int}}(u)=1, i_{I\,\mathrm{int}}(v)=1, \int_A I_{\mathrm{int}}(u)du > 0] = \sigma_{CP}^2 \rho_{CP}(|u-v|) + m_{CP}^2 \tag{2-16}$$

where σ_{CP}^2, $\rho_{CP}(|u-v|)$ and m_{CP} denote the variance, spatial correlation function and mean of positive precipitation, respectively. The uncentered indicator covariance for precipitation intermittency may be modeled as (Seo and Smith, 1991):

$$E[I_{\mathrm{int}}(u)I_{\mathrm{int}}(v) \mid \int_A I_{\mathrm{int}}(u)du > 0] = m_{CI\,\mathrm{int}}\{(1-m_{CI\,\mathrm{int}})\rho_{CI\,\mathrm{int}}(|u-v|) + m_{CI\,\mathrm{int}}\} \tag{2-17}$$

where $m_{CI\,\mathrm{int}}$ and $\rho_{CI\,\mathrm{int}}(|u-v|)$ denote the PoP at point scale and spatial indicator correlation function of occurrence of precipitation, respectively. The statistics in Eqs.(2-16) and (2-17) may be estimated empirically using radar-based precipitation data unconditionally or conditionally on significant precipitation events (see the Precipitation Modeling Section). The uncentered indicator covariance for imperviousness may be modeled analogously as:

$$E[I_{imp}(u)I_{imp}(v)] = m_{Iimp}\{(1-m_{Iimp})\rho_{Iimp}(|u-v|) + m_{Iimp}\} \tag{2-18}$$

where m_{Iimp} and $\rho_{Iimp}(|u-v|)$ denote fractional imperviousness and spatial indicator correlation function of occurrence of imperviousness, respectively.

The cross term, $E[P(u)R(v) \mid i_{I\,\mathrm{int}}(u)=1, i_{I\{\circ\}}(v)=1, \int_A I_{\mathrm{int}}(u)du > 0]$, in Eq.(2-14) may be evaluated numerically from:

$$
\begin{aligned}
&E[P(u)R(v) \mid i_{I\,\mathrm{int}}(u)=1, i_{I\{\circ\}}(v)=1, \int_A I_{\mathrm{int}}(u)du>0] \\
&= L_{PR}^{-1}\int_{-\infty}^{\infty}\int_{I_a(v)}^{\infty} P_u \frac{\{P_v - I_a(v)\}^2}{P_v - I_a(v)+S(v)} \bullet f_{P(u),P(v)}(P_u, P_v)dp_v p_u
\end{aligned}
\tag{2-19}
$$

In the above, $f_{P(u),P(v)}(P_u, P_v)$ denotes the bivariate PDF of P(u) and P(v), and the normalizing probability, L_{PR}, is given by:

$$
L_{PR} = \int_{I_a(v)}^{\infty} f_{P(v)}(P_v)dp_v \tag{2-20}
$$

Similarly, $E[R(u)R(v) \mid i_{\{\circ\}}(u)=1, i_{\{\circ\}}(v)=1, \int_A I_{\mathrm{int}}(u)du>0]$ in Eq.(2-14) may be evaluated numerically by:

$$
\begin{aligned}
&E[R(u)R(v) \mid i_{I\{\circ\}}(u)=1, i_{I\{\circ\}}(v)=1, \int_A I_{\mathrm{int}}(u)du>0] \\
&= L_{RR}^{-1}\int_{I_a(u)}^{\infty}\int_{I_a(v)}^{\infty} \frac{\{P_u - I_a(u)\}^2}{P_u - I_a(u)+S(u)} \frac{\{P_v - I_a(v)\}^2}{P_v - I_a(v)+S(v)} \bullet f_{P(u),P(v)}(P_u, P_v)dp_v p_u
\end{aligned}
\tag{2-21}
$$

In the above, the normalizing probability, L_{RR}, is given by:

$$
L_{RR} = \int_{I_a(u)}^{\infty}\int_{I_a(v)}^{\infty} f_{P(u),P(v)}(P_u, P_v)dp_v p_u \tag{2-22}
$$

In Eq.(7-14),

$E[I_{I\,\mathrm{int}}(u)I_{I\{\circ\}}(v) \mid \int_A I_{\mathrm{int}}(u)du>0] = \Pr[P(u)>0, P(v)>I_a \mid \int_A I_{\mathrm{int}}(u)du>0]$ may be estimated via:

$$
\begin{aligned}
&E[I_{I\,\mathrm{int}}(u)I_{I\{\circ\}}(v) \mid \int_A I_{\mathrm{int}}(u)du>0] \\
&= \Pr[P(u)>0, P(v)>I_a(v) \mid \int_A I_{\mathrm{int}}(u)du>0] \\
&= \Pr[P(u)>0, P(v)>I_a(v) \mid P(u)>0, P(v)>0, \int_A I_{\mathrm{int}}(u)du>0] \bullet \\
&\Pr[P(u)>0, P(v)>0 \mid \int_A I_{\mathrm{int}}(u)du>0] \\
&= \Pr[P(u)>0, P(v)>I_a(v) \mid P(u)>0, P(v)>0]\Pr[P(u)>0, P(v)>0 \mid \int_A I_{\mathrm{int}}(u)du>0] \\
&\approx \Pr[P(v)>I_a(v) \mid P(v)>0] m_{CI\,\mathrm{int}}\{(1-m_{CI\,\mathrm{int}})\rho_{CI\,\mathrm{int}}(|u-v|)+m_{CI\,\mathrm{int}}\}
\end{aligned}
\tag{2-23}
$$

In Eq.(7-14), $E[I_{imp}(u)I_{per}(v)]$ may be specified using $E[I_{imp}(u)I_{imp}(v)]$ via:

$$E[I_{imp}(u)I_{per}(v)] = E[I_{imp}(u)\{1 - I_{imp}(v)\}] = m_{Iimp}(1 - m_{Iimp})\{1 - \rho_{Iimp}(|u - v|)\} \quad \text{(2-24)}$$

In Eq.(2-14), $E[I_{I\{\circ\}}(u)I_{I\{\circ\}}(v) \mid \int_A I_{\text{int}}(u)du > 0]$ may be evaluated using the bivariate probability model for positive P(u) and P(v):

$$\begin{aligned}
&E[I_{I\{\circ\}}(u)I_{I\{\circ\}}(v) \mid \int_A I_{\text{int}}(u)du > 0] \\
&= \Pr[P(u) > I_a(u), P(v) > I_a(v) \mid P(u) > 0, P(v) > 0, \int_A I_{\text{int}}(u)du > 0] \bullet \\
&\Pr[P(u) > 0, P(v) > 0 \mid \int_A I_{\text{int}}(u)du > 0] \\
&= \Pr[P(u) > I_a(u), P(v) > I_a(v) \mid P(u) > 0, P(v) > 0] \Pr[P(u) > 0, P(v) > 0 \mid \int_A I_{\text{int}}(u)du > 0]
\end{aligned} \quad \text{(2-25)}$$

In the above, $\Pr[P(u) > I_a(u), P(v) > I_a(v) \mid P(u) > 0, P(v) > 0]$ may be evaluated numerically (see Eq.(2-22)). In Eq.(2-14), $E[I_{per}(u)I_{per}(v)]$ may be specified by $E[I_{imp}(u)I_{imp}(v)]$ assuming that imperviousness is homogeneous in A:

$$\begin{aligned}
&E[I_{per}(u)I_{per}(v)] = E[\{1 - I_{imp}(u)\}\{1 - I_{imp}(v)\}] \\
&= (1 - m_{Iimp})[1 - m_{Iimp}\{1 - \rho_{Iimp}(|u - v|)\}]
\end{aligned} \quad \text{(2-26)}$$

As noted above, lognormal, Weibull and gamma probability distributions were used for point precipitation. Multiple models exist for bivariate Weibull and gamma distributions whose marginal distributions collapse to their respective univariate distributions. In this work, the Nagao and Kadoya Model 1 (Nagao and Kadoya, 1970; Iliopoulos et al., 2005) was used for bivariate gamma distribution which is based on the 5-parameter model of (Izawa, 1953). For bivariate Weibull distribution, the mixture-type model of Lu and Bhattacharyya (1990) and Johnson (1999) were used. For details on the lognormal, Weibull and gamma distributions used, the reader is referred to Appendices E, F and G, respectively. For numerical integration, the multidimensional integration library, CUBA (Hahn, 2007) was used, which offers a choice of four independent routines for multidimensional numerical integration: Vegas, Suave, Divonne, and Cuhre. Based on comparative evaluation of accuracy and computational cost, Vegas was selected for all numerical integration performed in this work.

2.4 Spatial variability of soil

In the development above, it was assumed that *S(u)* (and hence $I_a(u)$) are spatially uniform. Here *S(u)* is allowed to vary randomly in space with prescribed second-order statistics with $I_a(u)=\alpha S(u)$ where 0<α<1. Under second-order homogeneity, the conditional mean of MAR is obtained (see Eq.(2-9)):

$$
\begin{aligned}
&E[\frac{1}{A}\int_A R_{sfc}(u)du \mid \int_A I_{\mathrm{int}}(u)du > 0] \\
&= m_{CP}m_{CI\,\mathrm{int}}m_{Iimp} + (1-m_{Iimp})\int_0^\infty m_{CR}(S(u))m_{CI\{\circ\}}(S(u))\, f_{S(u)}(S(u))dS(u)
\end{aligned}
\tag{2-27}
$$

where $f_{S(u)}(S(u))$ denotes the PDF of *S(u)*, and $m_{CR}(S(u))$ and $m_{CI\{\circ\}}(S(u))$ denote that they are functions of the water holding capacity of soil. Similarly, using Eq.(2-14), the uncentered second-order moment of MAR is obtained:

$$
\begin{aligned}
&E[(\frac{1}{A}\int_A R_{sfc}(u)du)^2 \mid \int_A I_{\mathrm{int}}(u)du > 0] \\
&= \frac{1}{A^2}\int_A \int_A \int_0^\infty \int_0^\infty E[\{P(u)I_{\mathrm{int}}(u)I_{imp}(u) + R(u,S(u))I_{\{\circ\}}(u,S(u))(1-I_{imp}(u))\} \\
&\{P(v)I_{\mathrm{int}}(v)I_{imp}(v) + R(v,S(v))I_{\{\circ\}}(v,S(v))(1-I_{imp}(v))\} \mid \int_A I_{\mathrm{int}}(u)du > 0] \\
&f_{S(u),S(v)}(S_u, S_v)dS(u)dS(v)dudv
\end{aligned}
\tag{2-28}
$$

where $f_{S(u),S(v)}(S(u),S(v))$ denotes the bivariate PDF of *S(u)* and *S(v)*, and $R(u,S(u))$ and $I_{\{\circ\}}(u,S(u))$ signify that they are functions of *u* and *S(u)*. Unfortunately, the explicit numerical evaluation of Eq.(2-28) is computationally extremely expensive. Instead, S_u may be used, with a realization of the spatial random field of *S(u)* with known second-order statistics, to evaluate the resulting quadruple integral. The above steps need to be repeated multiple times using different realizations, and calculating the ensemble mean as an approximation of Eq.(2-28). In this work, it is assumed that *S(u)* is distributed lognormally with known mean, variance and spatial correlation structure. To generate lognormal random fields, the Turning Bands Method (TBM, Mantoglou and Wilson, 1982) was used to first generate normally-distributed random fields with known mean, variance and exponential spatial correlation, which were then exponential-transformed. Note that, if there is no variability in *S(u)*, Eqs.(2-27) and (2-28) are reduced to Eqs.(2-9) and (2-14), respectively. From the above developments, one may evaluate CV of MAR as a function of the catchment area and assess the impact of precipitation intermittency and its spatial variability, precipitation amount and its variability and spatial variability with the precipitation area, imperviousness and its spatial variability, initial abstraction, and the water holding capacity of the soil and its spatial variability.

2.5 Study area and data used

The study area is the 160×160 km^2, or 40×40 HRAP, domain that encompasses DFW in North Central Texas. The radar-based QPE used in this study is the historical MPE (Seo et al., 2000) products obtained from the West Gulf River Forecast Center (WGRFC). They are on the Hydrologic Rainfall Analysis Project (HRAP) grid (Greene and Hudlow, 1982) which is about 4 km a side in mid-latitudes. The MPE data used are from 1998 through 2014 (17 yrs). The focus of this work is on urban flash flooding. The National Weather Service (NWS) defines flash flood as a flood caused by heavy or excessive rainfall in a short period of time, generally less than 6 hours. In DFW, even relatively large urban catchments have time-to-peaks well under 6 hours (Rafieeinasab et al., 2015). As such, this work consider the accumulation periods of 3 and 6 hours in this work. These accumulation periods were of particular relevance to extreme flooding that occurred in the area in May and June of 2015 due to record-breaking rainfall. While the maximum daily rainfall during this period had a return period of less than 100 years, the maximum 3- and 6-hr rainfall had return periods exceeding 200 and 300 years, respectively.

To assess the impact of the controlling factors and their variations to runoff frequency with respect to flash flood-causing heavy-to-extreme precipitation events, three subsets of precipitation events were considered in this study: 1) all 3- or 6-hourly MPE fields that report precipitation somewhere within the 40×40 HRAP domain, 2) all 3- or 6-hourly MPE fields that report maximum precipitation of 50.8 mm or larger somewhere within the domain, and 3) all 3- or 6-hourly MPE fields that report annual maximum precipitation within the domain; the above are referred to as Subsets 1, 2 and 3, respectively. The 2nd choice above is based on the comments by the city emergency and stormwater managers that, in general, storm events that produce 50.8 mm or more precipitation are responsible for flash flooding in this area. Table 2-1 shows the summary statistics associated with the precipitation events in the 3 subsets above. The subset of annual maximum precipitation is of particular interest as it is generally associated with high-impact flooding events. In this period, the annual maximum precipitation ranges from 63.9 to 238 mm for 3-hr precipitation and from 66.8 to 285.5 mm for 6-hr precipitation. Large variability exists in the annual maximum-bearing precipitation fields. For 3-hr precipitation over the 40×40 HRAP area, mlint ranges from 0.15 to 1, mpc ranges from 5.3 to 20.4 mm, and cvcp ranges from 0.70 to 2.50. For 6-hr precipitation over the same area, mlint ranges from 0.16 to 1, mpc ranges from 6.3 to 30.6 mm, and cvcp ranges from 0.57 to 2.64.

Table 2-1 Summary statistics of 3- and 6-hr point precipitation

Subset	Conditioning event	Summary statistics		
		mlint	mpc (mm)	cvcp
1	Max. 6-hr precip. > 0	0.31 [0.21,0.40]	5.50 [4.13,6.86]	1.70 [1.59,1.95]
2	Max. 6-hr precip. > 50.8 (mm)	0.71 [0.55,0.88]	14.24 [10.16,18.50]	1.12 [0.91,1.55]
3	Max. 6-hr precip.=annual max.	0.78 [0.49,1.00]	20.6 [12.5,29.8]	1.30 [0.75,1.57]
N/A	Max. 3-hr precip. > 0	0.27 [0.17,0.36]	3.90 [2.82,5.00]	1.77 [1.63,2.00]
N/A	Max. 3-hr precip. > 50.8 (mm)	0.63 [0.49,0.86]	11.40 [8.15,14.20]	1.18 [0.89,1.48]
N/A	Max. 3-hr precip.=annual max.	0.69 [0.61,0.99]	13.36 [5.53,19.08]	1.55 [0.96,2.28]

The impervious cover used in this work is estimated from the GIS layers obtained from the Cities of Arlington, Dallas, Fort Worth and Grand Prairie that contribute to imperviousness. All available contributing layers, such as building footprints, roads and parking lots, were combined and the percent impervious cover, defined as the percentage of the impervious area within a grid box, was calculated for each pixel ranging from 1/16 HRAP (~250 m) to 1/2 HRAP (~2 km). For further details, the reader is referred to Rafieeinasab et al., (2015a). Figure 7-4-a shows the resulting imperviousness map at 1/16 HRAP resolution. Note the very large spatial variability across the 4-cities area which is also captured in the histogram of imperviousness fraction at 1 km resolution (see Figure 2-2).

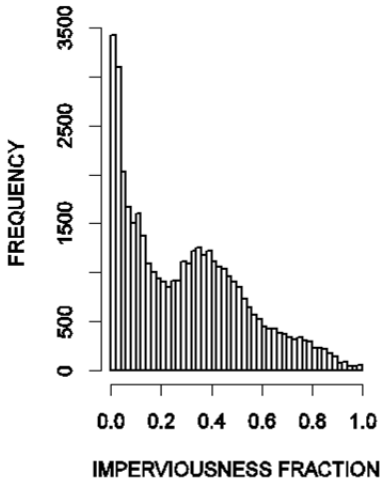

Figure 2-2 Histogram of imperviousness fraction at 1 km resolution

Because the GIS layers used in this work do not account for all sources of imperviousness, Figure 7-4a may be an underestimate. To check for possible biasedness, Figure 7-4a was also compared with the impervious maps derived from the National Land Cover Database (NLCD, *Homer et al.,* 2012) of 2001, 2006 and 2011 (Figure 7-4b, c and d). The results over the 4-cities area indicate that the two estimates are consistent, and that there is about 15% increase in imperviousness in the 4-cities area between 2001 and 2011. Figure 2-3 shows the uncentered spatial correlograms of imperviousness fraction along 8 different directions over the 4-cities area. They indicated a correlation length of ranging from 0.1 to 2 km for imperviousness fraction.

The water holding capacity of soil used in the CN Method (USDA, 1986) was obtained from the observed CN statistics for Dallas and Fort Worth (McLendon, 2002). For Dallas, the average CN is 79.5 with a standard deviation of 7.2. Fort Worth, the average CN is 70.3 with a standard deviation of 3.4. Assuming that both CN and S are lognormally distributed, S+10=1000/CN was used to obtain the mean and standard deviation of S of 2.68 and 1.15 (in), respectively, for Dallas and 4.26 and 0.69 (in), respectively, for Fort Worth. McLendon (2002) reports that the above observed CNs are significantly smaller than the CNs of 84.5 and 85.6 for Dallas and Fort Worth, respectively, estimated under the antecedent moisture condition (AMC) II from Landsat data (McLendon, 2002). Assuming that both CN and S are lognormally distributed, mean and standard deviation of S via S+10=1000/CN may be estimated. For the observed CN, the resulting mean and standard deviation of S are 47.0 and 10.41 (m), respectively, for Dallas, and 43.2 and 11.17 (m) for Fort Worth, respectively. To consider dry and wet antecedent conditions, CN I (wet) and CN III (dry) were estimated. Note that, because impervious areas were accounted for explicitly in the formulation, it is not necessary to consider CNs for urban areas separately. For the average CN II for Dallas and Fort Worth, mean and standard deviation of S are 1.77 and 0.43, respectively. For the corresponding CN III (dry) for Dallas and Fort Worth, the mean and standard deviation of S are 0.78 and 0.36, respectively. For the corresponding CN I (wet), the mean and standard deviation are 4.2 and 0.62, respectively.

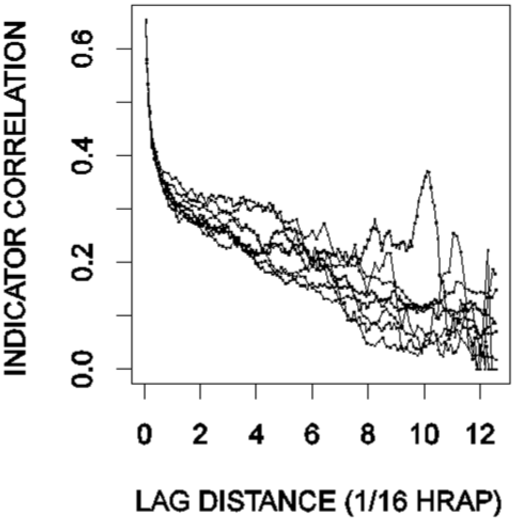

Figure 2-3 Indicator spatial correlograms of imperviousness along 8 different directions over the 4-cities area

2.6 Precipitation modeling

Evaluation of Eqs. (2-8) and (2-14) requires modeling probability distribution of precipitation. In this work, rather than pursuing a single model that may work best for all subsets of the precipitation events summarized in Table 2-1, multiple distributions were considered that may provide reasonable models for different subsets, and assess variations among the different models. To model marginal distribution of 3- and 6-hr precipitation at an HRAP grid box within the study area, two-parameter distributions only for parsimony were considered. The results indicate that the gamma distribution is generally the best for Subset 1 (see Table 2-1) but, for Subsets 2 and 3, the Weibull distribution is generally better, and that, for cases with most extreme precipitation amounts, the lognormal distribution is more appropriate. Figure 2-4 shows an example of a Weibull fit for a case in Subset 3 for which the Maximum Likelihood and Bayesian Estimation of Univariate Probability Distributions were used, FAmle (Aucoin, 2015).

While there exists large sampling uncertainty due to small sample size, the fit is reasonable. For bivariate gamma and Weibull distributions, multiple models are available. For bivariate gamma distribution, the Nagao and Kadoya Model 1 (NKM1, Nagao and Kadoya, 1970; Iliopoulos et al., 2005) were used which is based on the 5-parameter model of Izawa, 1953. For details, the reader is referred to Appendix E. For bivariate Weibull distribution, the mixture-type model of Lu and Bhattacharyya (1990) and Johnson (1999) were used. For details, the reader is referred to Appendix D. For details on modeling of bivariate lognormal distribution, the reader is referred to Appendix C.

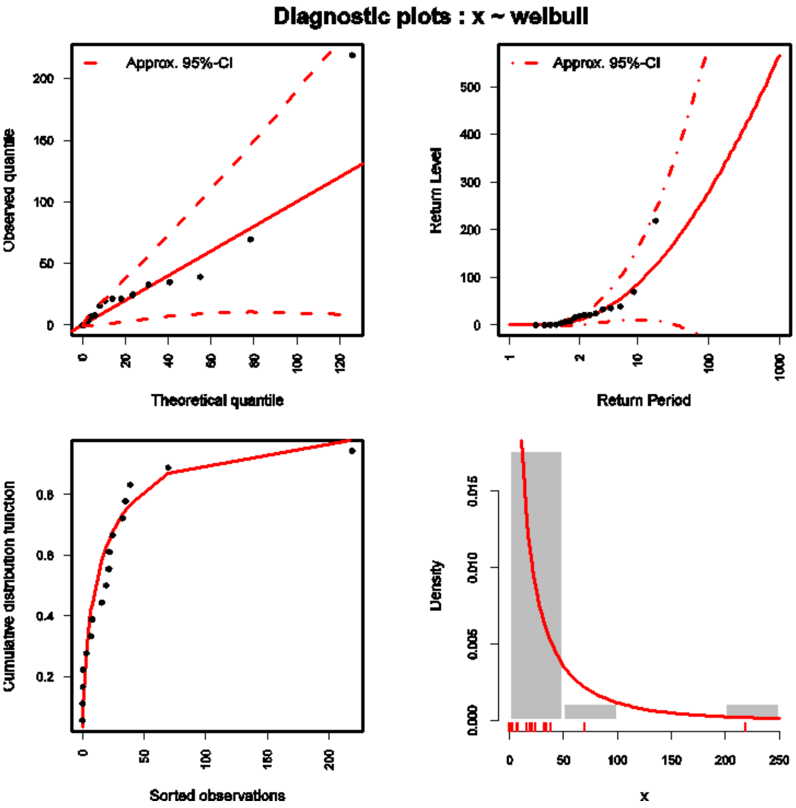

Figure 2-4 Weibull fit for a case in Subset 3

Spatial variability of 3- and 6-hr precipitation is modeled using correlation models for intermittency and inner variability (Seo and Smith, 1996a) for the subsets of events in Table 2-1. In the table, the bracketed numbers represent the minimum and maximum values for the variable in question among the 12 monthly estimates. To model spatial variability, the three widely used semi-variogram models, namely, exponential, Gaussian and spherical (Journel and Huijbregts, 1978) were used shown below in Eqs.(2-29), (2-30) and (7-31), respectively:

$$\rho(h) = c - (c - c_0)\exp(-h/r), \quad h > 0 \tag{2-29}$$

$$\rho(h) = c - (c - c_0)\exp\{-(h/r)^2\}, \quad h > 0 \tag{2-30}$$

$$\rho(h) = c_0 + (c - c_0)\{1.5(h/r) - 0.5(h/r)^3\}, \quad h > 0 \qquad (2\text{-}31)$$

where c, c_0, h and r denote the sill, nugget effect, lag distance and range, respectively. The modeling results for each month indicate that the exponential model provides the best fit for the indicator correlation function, $\rho_{CI\mathrm{int}}(|u-v|)$, for all months and for all subsets. The exponential model also provides a good fit for the conditional correlation function, $\rho_{CP}(|u-v|)$, for most cases but, for a number of cases, the Gaussian or the spherical model is better. Table 2-5 shows examples of the correlation modeling results for 6-hr precipitation fields that are associated with annual maxima. Note that, for these examples, the indicator and conditional correlation functions are best fitted by the spherical and Gaussian models, respectively.

Table 2-2 summarizes the results in which the scale parameters were multiplied in the Gaussian and spherical models by $\sqrt{\pi}/2$ and 3/8, respectively, to convert them to the equivalent settings of the scale parameter (i.e., range) in the exponential model. As in Table 2-1, the bracketed numbers in Table 2-2 represent the minimum and maximum values among the 12 monthly estimates of the variable in question. Table 2-1 and Table 2-2 show that the statistics of 3-hr precipitation largely overlap with those of 6-hr precipitation. For example, the statistics for 3-hr precipitation containing annual maximum are comparable to those of 6-hourly precipitation. As such, analysis were only carried out based on 6-hr precipitation.

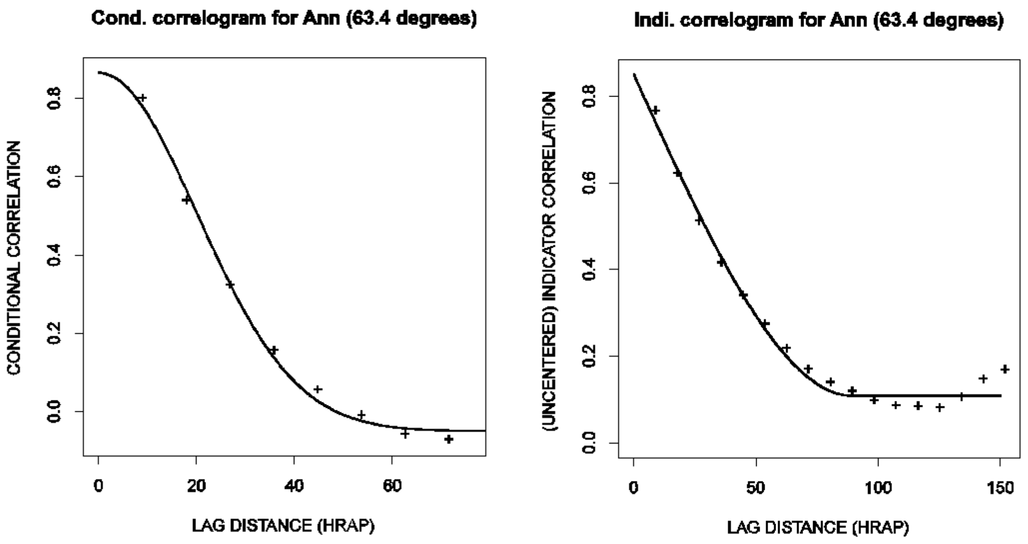
Cond. correlogram for Ann (63.4 degrees)

Indi. correlogram for Ann (63.4 degrees)

Figure 2-5 Spatial (left) and indicator (right) correlograms for 6-hr precipitation fields associated with annual maxima, and fitted gaussian and spherical models, respectively

Table 2-2 Parameters for exponential model for spatial correlation for precipitation intermittency and inner variability

Subset	Intermittency		Inner variability	
	Nugget effect	scaleIint (km)	Nugget effect	scalepc (km)
1	0.10 [0.08,0.15]	73.5 [53.2,94.0]	0.00 [0.00,0.01]	70.5 [28.3,114.8]
2	0.11 [0.07,0.17]	68.4 [27.2,122.3]	0.00 [0.00,0.07]	50.2 [32.9,67.7]
3	0.12 [0.03,0.19]	51.6 [16.5,128.8]	0.05 [0.01,0.07]	30.8 [19.0,75.4]

2.7 Sensitivity analysis

The scale-dependent sensitivity of climatological mean areal runoff to the following factors were assessed under the assumption of constant water holding capacity of soil and initial abstraction: water holding capacity of soil (denoted as “SS”), initially abstracted fraction of SS (denoted as “alpha”), PoP or climatological mean fractional coverage (denoted as “mIint”), spatial correlation scale of intermittency (denoted as “scaleIint”), climatological mean of precipitation conditional on occurrence of precipitation (denoted as “mcp”), climatological CV of precipitation conditional on occurrence of precipitation (denoted as “cvpc”), spatial correlation scale of inner variability (denoted as “scalepc”), mean fractional impervious cover (denoted as “mIimp”) and spatial correlation scale of fractional impervious cover (denoted as “scaleIimp”). Table 2-3 summarizes the settings for soil and imperviousness variables.

Table 2-3 Settings for soil and imperviousness variables

Levels	SS (in)	alpha	mIimp	scaleIimp (km)
1	0.8	0.05	0.1	0.125
2	1.3	0.10	0.2	0.25
3	1.8	0.15	0.3	0.5
4	3.0	0.20	0.4	1
5	4.2	0.25	0.5	2

Table 2-4 through Table 2-6 summarize the settings of the precipitation-related variables and their ranges considered for the three subsets of precipitation events.

Table 2-4 Settings for precipitation variables for Subset 1

Level	mIint	scaleIint (km)	mpc (mm)	cvpc	scalepc (km)
1	0.20	54	4.1	1.60	28.0
2	0.25	64	4.8	1.65	63.5
3	0.30	74	5.5	1.70	71.0
4	0.35	84	6.2	1.85	93.0
5	0.40	94	6.9	2.00	115.0

The settings are chosen to be representative of the conditions that an urban area of varying sizes in different parts of DFW may experience during the course of a year. The settings for SS are based on McLendon (2002) and The middle setting of 45.7 (mm) corresponds approximately to the mean value of the AMC II estimates for Dallas and Fort

Worth, the maximum of 101.60 (mm) corresponds approximately the AMC II estimate for drier Fort Worth (see the Spatial Variability of Soil Section). The settings for alpha bracket the default of 0.20 with minimum and maximum of 0.05 and 0.25. In an urban environment, one may expect reduced initial abstraction due to reduced interception. As such, it is possible that the above range may be higher than the actual range of initial abstraction.

Table 2-5 Settings for precipitation variables for Subset 2

Level	mlint	scalelint (km)	mpc	cvpc	scalepc (km)
1	0.56	30	10.0	0.75	30
2	0.64	50	12.0	1.03	40
3	0.72	70	14.0	1.30	50
4	0.80	95	16.0	1.45	60
5	0.88	120	18.0	1.60	70

Table 2-6 Settings for precipitation variables for Subset 3

Level	mlint	scalelint (km)	mpc	cvpc	scalepc (km)
1	0.50	16.	13.0	0.80	20
2	0.65	34.	17.0	1.05	25
3	0.80	52.	21.0	1.30	30
4	0.90	91.	25.0	1.45	55
5	1	130.	29.0	1.60	80

The settings for the precipitation-related parameters are based on the summary statistics shown in Table 2-1 and Table 2-2. Note that, as the maximum precipitation amount increases from Subset 1 to Subset 3, PoP, or mlint, increases. It is a reflection of the fact that, when it is precipitating heavily, it is more likely to rain at any given location within the analysis domain than when it is precipitating less. The tables also indicate that, as the maximum precipitation amount increases, the correlation scales of both intermittency and inner variability tend to decrease (Seo, 1996). The settings for mean impervious fraction, mIimp, are based on Figure 7-4a, which has a mean of about 0.3. The minimum and maximum settings for mIimp, are chosen based on mean impervious fraction over different 10×10 km^2 areas within the 4-cities area, which ranges from 0.1 to 0.5.

2.8 Results

The scale-dependent variability, as measured by CV, of climatological MAR for each of the 9 variables examined: SS, alpha, scaleIint, scalepc, scaleIimp, mpc, cvpc, mIint, and mIimp is presented. To assess the sensitivity of climatological variability of MAR to variations in each of the 9 variables, five curves of CV vs. catchment scale were plotted based on the five settings shown in Table 2-4, Table 2-5 and Table 2-6 for Subsets 1, 2 and 3, respectively. In these plots, the variable in question is varied over the 5 different settings while all other variables are held fixed at the middle settings (i.e., Level 3 in Tables 4 through 6). Accordingly, each plot shows the sensitivity of scale-dependent variability of climatological MAR to changes in each of the 9 variables. Given the same subset of precipitation events (see Table 2-1), the pattern of dependence on catchment scale and its sensitivity to changes in the 9 variables are generally similar among the 3 distributional models considered, i.e., lognormal, Weibull and gamma. As such, only the representative results are shown.

Figure 2-6 shows the CV vs. the catchment scale for the 9 variables for Subset 1, i.e., the analysis is conditioned on the event that it is precipitating somewhere within the 6-hr precipitation field over the 40×40 HRAP domain regardless of the amount (see Figure 7-4a). The distribution model used in Figure 2-6 is bivariate gamma (see Appendix E). Small oscillations seen in Figure 2-6 are due to sampling errors associated with Monte Carlo integration. Figure 2-6 shows that the scale dependence of climatological

CV of MAR varies from variable to variable, and that, for most cases, the variability peaks at catchment scales of 20×20 to 50×50 km^2 for Subset 1. It is readily seen that variations in mIimp, scalepc and cvpc produce the largest changes in variability of climatological MAR, followed by SS, mIint and scaleIint. Increasing mIimp significantly reduces variability of climatological MAR but increases the catchment size at which the variability peaks (Figure 2-6c). Increasing mIint, on the other hand, decreases both the variability and the catchment size of peak variability (Figure 2-6d). Figure 2-6f shows that increasing scaleIimp increases the variability at very small catchment scales, and that, the larger scaleIimp is, the larger, albeit marginally, the range of catchment scales being impacted. Note that the above pattern of slightly increased CV near the origin due to scaleIimp is seen in all cases in Figure 2-6 increasing scaleIint reduces the variability and slightly increases the catchment scale of peak variability (Figure 2-6g). The above observations suggest that, in addition to mean imperviousness, the spatial variability of imperviousness plays a role in shaping the scale-dependent variability of climatological MAR for small urban areas. Figure 2-6h indicates that scalepc has a large influence on both the magnitude of variability and the catchment scale of peak variability, and that increasing scalepc increases both.

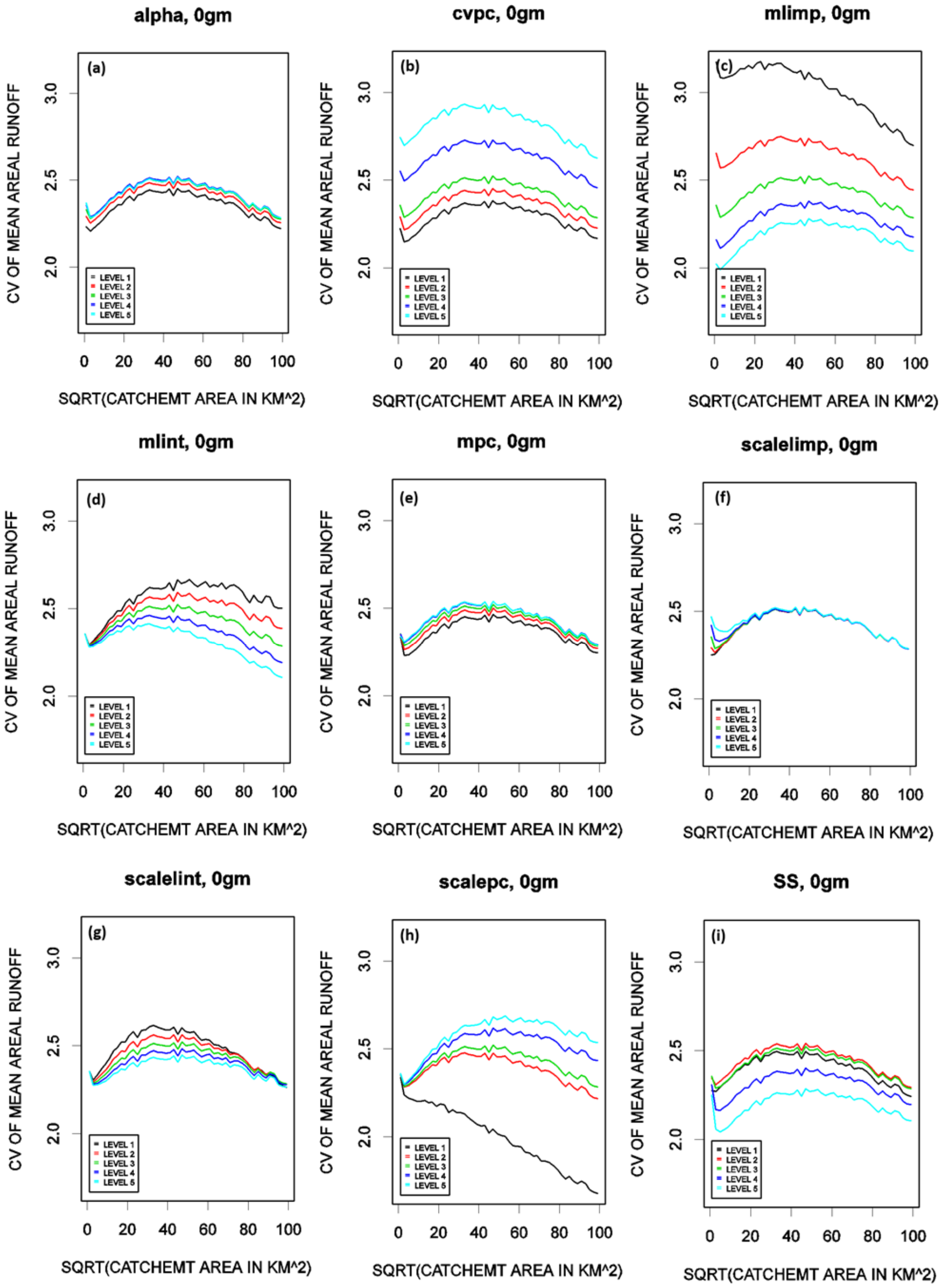
alpha, 0gm

cvpc, 0gm

mlimp, 0gm

mlint, 0gm

mpc, 0gm

scalelimp, 0gm

scalelint, 0gm

scalepc, 0gm

SS, 0gm

Figure 2-6 CV vs. the catchment scale for the 9 variables for Subset 1

Figure 2-7 is the same as Figure 2-6 but for Subset 3, i.e., the analysis is conditioned on those 6-hr precipitation fields that contain annual maximum precipitation within the analysis domain. The distribution model used for precipitation is bivariate Weibull (see Appendix D). The results for Subset 2 are similar and are not shown. For both Subsets 2 and 3, the CV generally decreases monotonically as the catchment scale increases. Between Subsets 2 and 3, the rate of decrease in CV is somewhat faster for Subset 3. The distinctly different pattern of scale dependence for Subsets 2 and 3 vs. Subset 1 stems from the fact that the former are associated with much larger PoP (see Table 2-1); because it is already precipitating over most of the analysis domain, there is little room for intermittency of precipitation to exert influence whereas, for the same reason, inner variability, i.e., the variability of precipitation within the precipitating area, can exert large influence. Figure 2-7 indicates that variations in cvpc, mlimp and scalepc exert the largest influences on the magnitude of variability of MAR, followed by mlint, and that the sensitivity is generally larger over smaller catchment scales for all variables. It is worth noting in Figure 2-7i that the largest variability due to variations in SS occurs not at the maximum setting of SS but at an intermediate level at all catchment scales, suggesting a nonlinear response of scale-dependent variability of climatological MAR to variations in soil water holding capacity. For Subset 2, i.e., the analysis is conditioned on 6-hr precipitation fields in each of which the maximum amount exceeds 50.8 mm, the above nonlinear response is more pronounced as SS plays a larger role due to reduced precipitation amounts in comparison with Subset 3.

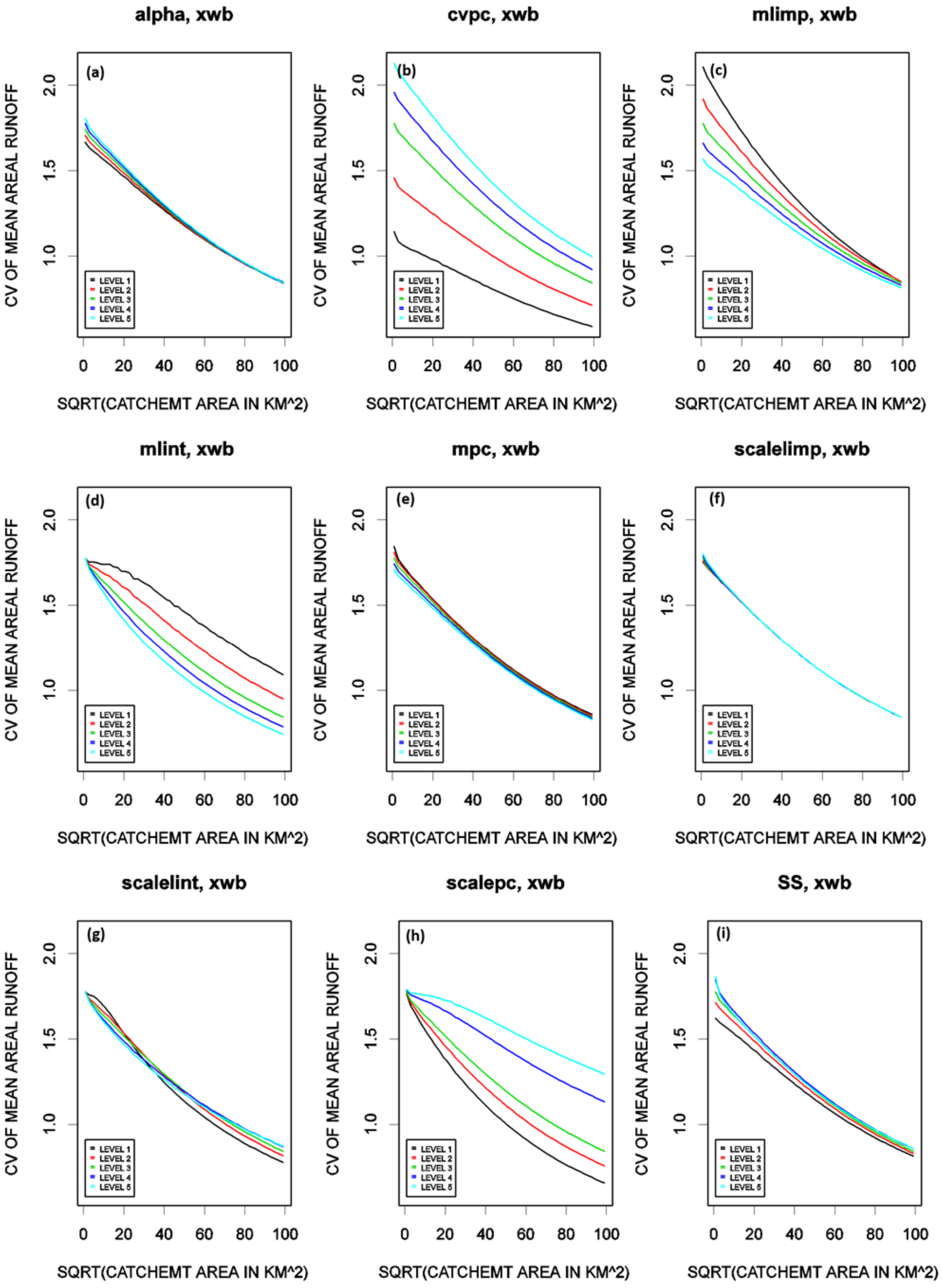

Figure 2-7 CV vs. the catchment scale for the 9 variables for Subset 3

The results above assume constant SS. To assess the impact of spatially-varying SS, Eq.(7-28) was numerically evaluated by generating a random field of SS with known second-order statistics, evaluating mean and variance of MAR, i.e., Eqs. (7-8) and (7-14), respectively, under spatially-varying SS (and hence alpha), and repeating the above steps multiple times to obtain ensemble mean and variance. Due to computational cost, the above runs were made only for a limited range of correlation scales for SS. The mean and standard deviation of SS used were 45.70 and 11.17 (mm), respectively, which correspond to the average statistics for Dallas and Fort Worth (McLendon, 2002) (see the Study Area and Data Used Section). Figure 2-8 shows the result for CV for correlation scale of 4 km for SS based on an 8-member ensemble. Note that the spatially-varying SS significantly increases CV across all ranges of catchment scale and slightly flattens the CV-vs.-catchment scale relationship compared to the spatially uniform SS. Additional research is needed to reduce the computational cost and hence to examine the impact of spatially varying SS more systematically.

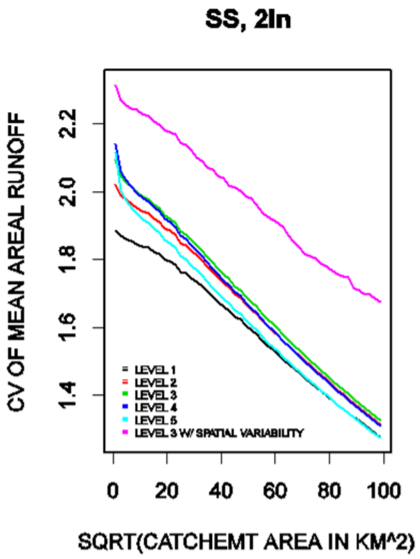

Figure 2-8 CV of mean areal runoff vs. catchment scale for SS. Also shown are those for spatially-varying SS with correlation scales of 4 and 32 km

With the above analyses alone, it is difficult to assess how the combination of scale dependence of variability of climatological MAR and its sensitivity to variations in the 9 variables may modify flood frequency curves. To allow such assessment, here it is examined how the scale dependence and sensitivity may shape MAR frequency. Without observations or a combination of observations and simulations of runoff and peak flow, it is not possible to directly relate MAR frequency with flood frequency. One may expect, however, frequency and scale dependence of MAR to shape those of peak flow, given that peak flow is generally a monotonically increasing function of runoff volume (see, e.g., Bradley and Potter, 1992), and that CV of runoff volume is the same as that of MAR. Toward that end, it is assumed that MAR has the same marginal distribution as precipitation, i.e., gamma, Weibull and lognormal, and produce exceedance probability plots of MAR at various catchment scales. The above distributional assumption amounts to assuming that areal runoff volume shares the same probability distribution as point precipitation. To test this assumption, additional research is needed. Only a limited set of results exists in the literature on distributions of sums of gamma, Weibull and lognormal random variables (see Nadarajah, 2008 and references therein). Moschopoulos (1985) derived the PDF of a sum of independent gamma random variables. Alouini et al., (2001) extended the above result for correlated gamma random variables. Many researchers approximated sums of independent lognormal random variables with lognormal (Nadarajah, 2008). Pratesi et al., 2006, e.g., approximated a linearly weighted sum of correlated lognormal random variables with lognormal. For sums of Weibull random variables, no results or approximations currently exist.

Figure 2-9 shows the exceedance probability plots of MAR at catchment scale of 20×20 km^2 for Subset 2 (i.e., the analysis is conditioned on 6-hr precipitation fields with a maximum of 50.8 mm or larger) based on Weibull distribution.

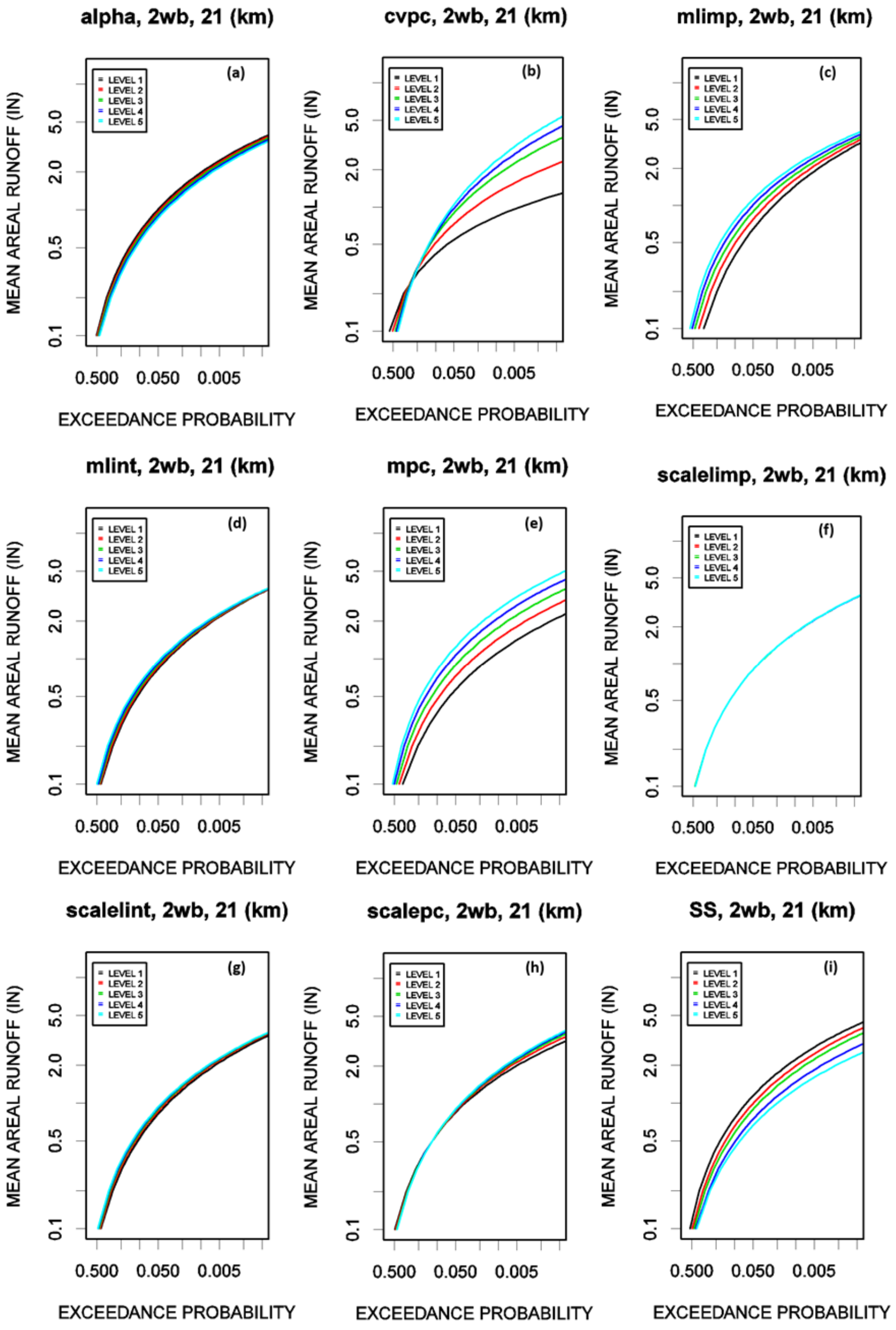

Figure 2-9 Exceedance probability plots of MAR at catchment scale of 20×20 km^2 for Subset 2 based on Weibull distribution

The results based on gamma and lognormal distributions are qualitatively similar but have smaller and larger MAR at the same level exceedance probability at the right-tail end and larger and smaller MAR over the mid-ranges relative to those based on Weibull distribution (see Figure 2-10).

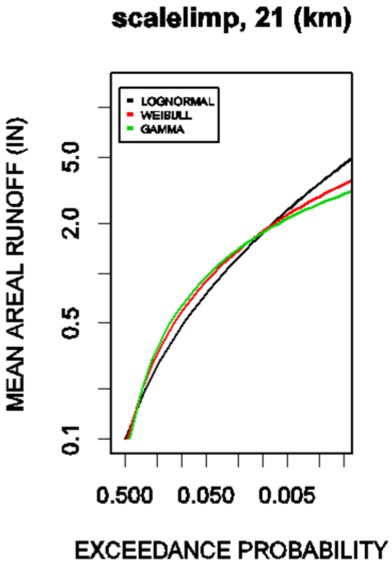

Figure 2-10 Exceedance probability plots of MAR at catchment scale of 20×20 km^2 for Subset 2 based on Weibull, lognormal and gamma distributions

Figure 2-9 indicates that the variations in exceedance probability of MAR vary from variable to variable, and that, for Subset 2, variations in cvpc and mpc result in largest variations in exceedance probability, followed by SS and mlimp. Note also that the variations in mpc and SS produce similar variations in exceedance probability but in opposite directions. Figure 2-9 points out the challenges associated with determining flood frequencies in urban areas where variations in precipitation, soil and impervious cover lead to very significant variations of varying characteristics in exceedance probabilities of MAR.

While Figure 2-9 allows assessment of changes in MAR frequency due to variations in the 9 variables considered, it is difficult to identify and characterize their dependence on the catchment scale. To summarize the MAR frequency as a function of catchment scale and magnitude of precipitation events, the influence factor, F_I, was defined and calculated as the area encompassed by the lower- and upper-bounding exceedance probability curves in Figure 2-9 in which the difference in probability is weighted according to the magnitude of MAR:

$$F_I = \int_0^{\infty} x\{F^R(x) - F^L(x)\}dx \qquad \text{(2-32)}$$

where x denotes MAR, $F^R(x)$ and $F^L(x)$ denote the right- and left-bounding CDFs, respectively. The weighted averaging based on the magnitude of MAR in Eq.(2-32) is motivated by the importance of extreme events. The interpretation of Eq.(2-32) is that, the larger the influence factor, F_I, is, the more sensitive the MAR frequency is to the variations in the variable. Figure 2-11a through Figure 2-11c show the resulting plots for Subsets 1, 2 and 3 based on gamma, Weibull and lognormal distributions, respectively. The above choices for different distributions for different subsets are based on the observation (see the Precipitation Modeling Section) that gamma, Weibull and lognormal distributions are most appropriate for Subsets 1, 2 and 3, respectively. Because MAR and hence F_I depend on the catchment scale, in Figure 2-11 the relative magnitude of F_I, rather than the absolute magnitude, for each Subset is of most interest. In the figure, the colors, brown, green and blue denote the large, medium and small influences. The figure indicates that, for precipitation events of all magnitudes (i.e., Subset 1), the variations in mpc, mImp and SS exert the largest influence on exceedance probability, followed by cvpc. The figure also indicates that the influences are very scale-dependent; variations in mpc, mIimp and SS result in large variations in MAR frequency over catchment areas up to 40×40 km^2 but result in much smaller variations in MAR frequency for larger areas. Note that the above upper range of scale of increased F_I corresponds approximately to the areal extent of the 4 Cities in DFW (48.7×48.7 km^2).

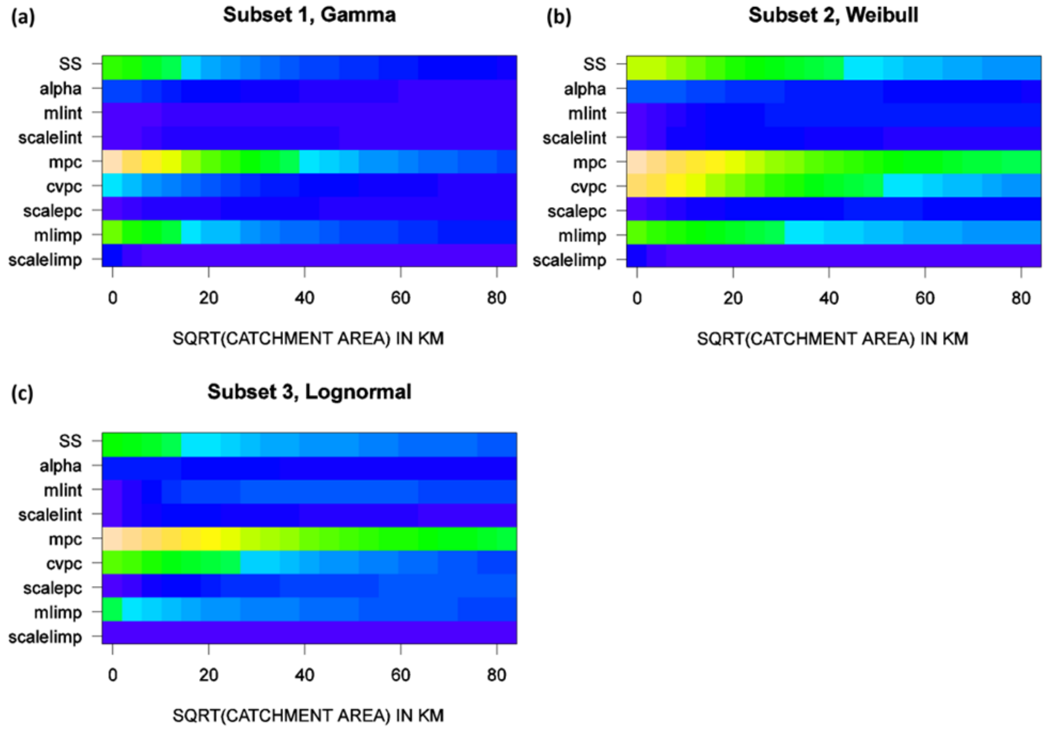

Figure 2-11 Influence factor for the 9 variables vs. catchment scale for Subset 1 based on a) gamma distribution, b) Weibull distribution and c) lognormal distribution

For precipitation events in which maximum point rainfall exceeds 50.8 mm (i.e., Subset 2), mpc, cvpc, SS and mlimp are the most influential, of which mpc and cvpc extend their influence beyond the catchment scale of 40×40 km^2. For precipitation events associated with annual maximum precipitation (i.e., Subset 3), mpc is by far the most influential, followed by cvpc, SS and, to a lesser degree, mlimp. As was the case for Subset 2, mpc exerts dominant influence well beyond the catchment scale of 40×40 km^2

for Subset 3. The above summary results indicate that, over the range of spatial scales of most cities in the US, precipitation, impervious cover and soil all exert significant influences in shaping the MAR frequency. The findings above suggest that, in addition to accurate high-resolution quantitative precipitation information (QPI), accurate high-resolution modeling of soil properties, soil moisture dynamics and land cover conditions are also necessary to capture the large and scale-dependent variability in areal runoff in urban areas, in particular, for small catchments. The findings above also suggest that, given the large sensitivity of MAR frequency to multiple factors, accurate estimation of flood frequency for urban catchments is inherently more difficult and subject to large uncertainties. As such, particular care is necessary in projecting changes in flood frequency in urban areas due to, e.g., urbanization and climate change. The approaches developed in this work may be useful in enveloping flood frequencies in urban areas under such nonstationary conditions (e.g., Villarini et al., 2009).

2.9 Conclusions and future recommendations

With urbanization and climate change, many areas in the US and elsewhere face increasing threats from flash flooding. Due to nonstationarities arising from changes in land cover and climate, however, it is not readily possible to project how such changes may modify flood frequency. In this work, a very simple spatial stochastic model for rainfall-to-areal runoff in urban areas is formulated, evaluating climatological mean and variance of mean areal runoff (MAR) over a range of spatial scales, translating them into MAR frequency, and assessing its sensitivity to precipitation, imperviousness and soil, and their changes. The precipitation durations considered are 3 and 6 hours which are most relevant to flash flooding. The probability distributions used for point precipitation include lognormal, Weibull and gamma. The rainfall-runoff model used is the Curve Number (CN) Method.

It was found that, given the same magnitude of precipitation events, the pattern of dependence of MAR on catchment scale and its sensitivity to changes in the 9 variables considered, i.e., intermittency of precipitation (scaleIint), precipitation amount (mpc) and its variability (cvpc) and spatial variability (mIint, scalepc), impervious cover (mIimp) and its spatial variability (scaleIimp), water holding capacity of soil (SS) and its spatial variability, and initial abstraction (alpha), are generally similar among the 3 distributional models considered, i.e., lognormal, Weibull and gamma. For precipitation events of all magnitudes, it was found that the scale dependence of climatological CV of MAR varies from variable to variable, that, for most cases, the variability peaks at catchment scales of 20x20 to 50x50 km^2, and that variations in mIimp, scalepc and cvpc produce the largest changes in variability of climatological MAR, followed by SS, mIint and scaleIint. For very heavy to extreme precipitation events, it was found that 1) the CV generally decreases monotonically as the catchment scale increases; 2), between very heavy and extreme events, the rate of decrease in CV is somewhat faster for the latter; 3) the distinctly different pattern of scale dependence between very heavy-to-extreme events and all events stems from the fact that the former are associated with much larger probability of precipitation (PoP), that variations in cvpc, mIimp and scalepc exert the largest influences on the magnitude of variability of MAR, followed by mIint, and that the sensitivity is generally larger over smaller catchment scales for all variables. It was found that the spatially-varying SS significantly increases CV across all ranges of catchment scale and slightly flattens the CV-vs.-catchment scale relationship compared to the spatially uniform SS. Further research is necessary, however, to reduce computational cost and hence to assess the impact of spatially variability in SS more systematically.

The above findings indicate that, over the range of spatial scales of most cities in the US, precipitation, impervious cover and soil all exert significant influences in shaping the MAR frequency, that, in addition to accurate high-resolution quantitative precipitation information (QPI), accurate high-resolution modeling of soil properties, soil moisture dynamics and land cover conditions are necessary to capture the large and scale-dependent variability in areal runoff in urban areas, in particular, for small catchments.

Although total impervious area (TIA) was used to represent imperviousness of urban area in this study, directly connected impervious areas (DCIA) could be a more realistic indicator for flooding in the future study (e.g, Lee and Heaney, 2003; Seo et al., 2013). The findings also suggest that, given large sensitivity of MAR frequency to multiple hydroclimatological, hydrometeorological, physiographic and hydrologic factors, accurate estimation of flood frequency for urban catchments is inherently more difficult and subject to large uncertainties, and that particular care is hence needed in projecting changes in flood frequency in urban areas due to, e.g., urbanization and climate change. The approaches developed in this work may be useful in enveloping flood frequencies in urban areas under such nonstationary conditions.

The results indicate that to be able to predict streamflow accurately in large urban areas, soil properties, soil moisture dynamics, impervious cover, and precipitation need to be observed and modeled accurately.

Chapter 3 Literature review

This section includes a review of literature relevant to the stated objectives. Topics covered include a summary of high-resolution streamflow and soil moisture simulations and the impact of land cover changes on hydrologic response of urban catchments.

3.1 High-resolution hydrologic modeling

High-resolution hydrologic models have been widely used for streamflow simulation for different purposes. The River Forecast Centers of NWS implemented the NWS Hydrologic Laboratory's Distributed Hydrologic Model to forecast streamflow in basin outlets (Koren et al., 2003; Jones et al., 2009). High-resolution hydrologic modeling has also been used for streamflow simulation and flash flood forecasting in urban areas (Javier et al., 2007; Fares et al., 2014; ten Veldhuis et al., 2014; Bruni et al., 2015; Ochoa-Rodriguez et al., 2015; and Rafieeinasab et al., 2015a).

High-resolution rainfall data is needed for streamflow simulation in urban areas. Many researchers have assessed the sensitivity of high-resolution hydrologic models to the spatial and temporal resolution of rainfall data in urban areas. Gires et al. (2011) used a semi-distributed model for streamflow simulation of a 900 ha urban area located in Cranbrook, UK and recommended using high temporal and spatial rainfall resolution (at least 1 km × 1 km × 5 min). Gires et al. (2014) carried out a similar study with a fully-distributed model in Paris, and obtained similar results; however, the fully distributed model showed more sensitivity to the spatial and temporal resolution of the input rainfall than the semi-hydrologic model. Based on a research carried out in Mediterranean urban areas, the spatiotemporal resolution of rainfall for urban catchments of the order of 1000 ha is about 3 km and 5 min. For urban catchments of the order of 100 ha, it becomes a resolution of about 2 km and 3 min and (Berne et al., 2004).

Bruni et al. (2015) used a semi-distributed hydrologic model with high-resolution rainfall data and analyzed the relationship between spatial and temporal resolution of rainfall input, and storm and catchment sizes. The results showed that the modeling outputs are highly sensitive to high-resolution rainfall variability, and that this will increase once the rainfall inputs are aggregated to coarse resolution.

Ochoa-Rodriguez et al. (2015) investigated the impact of rainfall input resolution on the outputs of detailed hydrodynamic models of seven urban catchments in Northwest Europe. The native spatiotemporal resolution of the nine selected storm events for analysis was 100 m and 1 min. Then, 15 different combinations of coarser spatial and temporal resolutions, up to 3000 m and 10 min, were generated. These estimates were then applied to the operational semi-distributed hydrodynamic models of the urban catchments, all of which were of similar size (between 3 and 8 km^2) but had different morphological, hydrological, and hydraulic characteristics. Three main features were observed in the results: (1) the impact of rainfall input resolution decreases rapidly as the catchment drainage area increases; (2) in general, variations in temporal resolution of rainfall inputs affect hydrodynamic modelling results more strongly than variations in spatial resolution; and (3) there is a strong interaction between the spatial and temporal resolutions of rainfall input estimates.

Rafieeinasab et al. (2015a) assessed the sensitivity of streamflow simulation in urban catchments to the spatiotemporal resolution of precipitation input and hydrologic modeling in order to identify the resolution at which the simulation errors may be minimal, given the quality of the precipitation input, the hydrologic models used, and the response time of the catchment. The hydrologic modeling system used was the National Weather

Service (NWS) Hydrology Laboratory's Research Distributed Hydrologic Model (HLRDHM) applied at spatiotemporal resolutions ranging from 250 m to 2 km and from 1 min to 1 hr, applied to the cities of Fort Worth, Arlington and Grand Prairie in DFW. The high-resolution precipitation input was from the DFW Demonstration Network of the Collaborative Adaptive Sensing of the Atmosphere (CASA) radars. For comparison, the NWS Multisensor Precipitation Estimator (MPE) product, which is available at a 4-km 1-h resolution, was also used. The streamflow simulation results were evaluated for five urban catchments ranging in size from 3.4 to 54.6 km^2 and from about 45 min to 3 hrs in time-to-peak in the cities of Fort Worth, Arlington and Grand Prairie. The results indicated that a spatiotemporal resolution of 500 m and 15 min or more is a good choice for streamflow prediction.

Soil moisture is one of the most important state variables (in space and time) of the water cycle, controlling a wide range of hydrological processes (Western et al., 2004; Pandey and Pandey, 2010; Romano 20014; and Vereecken et al., 2014). Soil moisture plays an important role in determining the partitioning of the precipitation in runoff, infiltration, and groundwater recharge (Seiler and Gat, 2004). Therefore, observation of soil moisture in space and time is crucial in water resources management. In-situ soil moisture measurement using Time Domain Reflectometry (TDR) has been reported in many studies as one of the most accurate methods (Romano, 2014). However, while TDR sensors can measure the soil moisture content in limited locations, they cannot represent the spatial variability of soil moisture for an area.

Using a distributed hydrological model is a viable alternative for the estimation of soil moisture in space and time, and has been used successfully by many researchers to simulate and evaluate soil moisture. Smith et al. (1994) used Soil Hydrologic Model (SHM) for the soil moisture simulation. The results captured the general trend of the field measurement values. Crawford et al. (2000) compared soil moisture observations of 38 Oklahoma Mesonet sites (Brock et al., 1995) with simulations obtained with the Soil Hydrology Model (SHM). Blyth (2002) enforced the 5 km × 5 km gridded network of observed meteorological data across the UK to two soil moisture prediction models, i.e., MORECS (Met Office Rainfall and Evaporation Calculation Scheme) and MOSES (Met Office Surface Exchange Scheme) and compared the simulated and observed soil moistures. Frankenberger et al. (1999) used the Soil Moisture Routing model, a daily water balance model, and simulated soil moisture. The comparison between simulated and observed soil moisture showed a similar trend, with errors on the order of the standard error of measurements. Mehta et al. (2004) simulated soil moisture content in two rural watersheds by using the Soil Moisture Routing model and reported good agreement between simulated and observed soil moisture. Zhang et al. (2006) integrated the Moderate Resolution Imaging Spectrometer (MODIS) vegetation data into a simple model for the spatially distributed simulation of soil water content and evapotranspiration, and used TDR soil moisture observation for the validation. Sheikh et al. (2009) simulated soil moisture content in the CATSOP experimental catchment with a spatially distributed daily basis hydrological model, called Bridge Event And Continuous Hydrological (BEACH). Brimelow et al. (2010) validated soil moisture simulations from the Canadian prairie agrometeorological (PAMII) model and assessed the sensitivity of the model to uncertainties in soil hydraulic parameters.

Koren et al. (2006) evaluated the performance of the Sacramento Soil Moisture Accounting model with a new heat transfer component (SAC-HT), using runoff and soil moisture from 75 basins, with watershed areas varying from 20 km^2 to 15,000 km^2. The results showed that the modified Sacramento model, driven by a priori parameters, performed reasonably well and allowed explicit estimation of soil moisture at desired layers.

Koren et al. (2008) used the Sacramento Soil Moisture Accounting model with a new heat transfer component (SAC-HT) to simulate soil moisture content of more than 20 watersheds of sizes ranging from 200 to 4000 km^2 in the Oklahoma Mesonet, and calibrated the model using the spatially-averaged soil moisture content of these watersheds.

Tavakoli and Smedt (2012) tested the ability of the Water and Energy Transfer in Soil, Plant and Atmosphere (WetSpa) model to simulate soil moisture. Comparing the simulated soil moisture with the observations, it was shown that the performance of the model to simulate soil moisture is promising.

3.2 Impact of urbanization on streamflow simulation

Increasing population and migration towards urban areas lead to land cover changes and an increase of impervious areas. Increasing impervious surfaces in urban areas has considerable impacts on the hydrological response of the urban catchments. Dams et al. (2013) grouped the impact of the expansion of impervious areas due to urbanization on the hydrological response of urban catchments into three categories: (i) increased surface runoff, (ii) increased flow velocities due to decreased surface roughness, and (iii) increased peak flow magnitudes and flood probability. Researchers developed different approaches to assess the impact of land cover changes in urban areas on hydrological responses.

Rose and Peters (2001) analyzed the streamflow characteristics of highly urbanized, less-urbanized, and non-urbanized watersheds from 1958 to 1996. They found that annual runoff coefficients for the urban streams were not significantly greater than for the less-urbanized watersheds. However, for the 25 largest stormflows, the peak flows for urbanized watershed were 30% to 100% greater than peak flows for the other streams. The storm recession period for the urban stream was 1–2 days less than that for the other streams. Burns et al. (2005) used the hydrograph analysis technique to study the effects of impervious areas on runoff generation in three small headwater catchments that represented a range of suburban developments (high-density residential, medium-density residential and undeveloped). Using data from 27 storms, they showed that peak magnitudes increased and recession time decreased with increasing development, but lags in peak arrival and peak discharge/mean discharge were greatest in the medium-density residential catchment, which contains a wetland in which storm runoff is retained before entering the stream. Using five land cover scenarios, Chu et al. (2013) studied the potential effects of varying degrees of urban expansion on the frequency of discharge, velocity, and water depth using the physically-based watershed model, MIKE-SHE, and the 1D-hydrodynamic river model, MIKE-11. Results indicated that the frequency of low flow events decreased as urban expansion increased, while the frequency of average and high-flow events increased as urbanization increased. Ali et al. (2011) combined an empirical land use change model and an event scale with a rainfall-runoff model to quantify the impacts of potential land use change on the storm-runoff generation. The results indicated that future land use is projected to increase the total runoff between 51.6 and 100.0%, as well as the peak discharge between 45.4 and 83.3%, and that the magnitude of the peak discharge increment relates to the expansion rate of a built-up area.

Such studies suggest incorporating land cover changes data of urban areas in distributed hydrological modeling. However, including land cover changes data in distributed hydrologic models remains complicated due to the variability of land covers in urban areas in space and time. Recent studies showed that using remote sensing data is more appropriate and more cost effective for providing spatially-consistent values for land cover changes in urban areas.

Chormanski et al. (2008) examined different methods for estimating the impact of impervious surface cover on the prediction of peak discharges, as determined by a fully distributed rainfall-runoff model (WetSpa). The study showed that detailed information on the spatial distribution of impervious surfaces, as obtained from remotely-sensed data, produces substantially different estimates of peak discharges than traditional approaches based on expert judgment of average imperviousness for different types of urban land use.

Du et al. (2012) combined a distributed hydrologic model and a dynamic land use model to examine the effects of urbanization on annual runoff and flood events. The Hydrologic Engineering Center’s Hydrologic Modeling System (HEC-HMS) was used to calculate runoff generation and the integrated Markov Chain and Cellular. Landsat Thematic Mapper (TM) images from 1988, 1994 and 2006, Enhanced Thematic Mapper Plus (ETM+) images from 2001 and 2003, and a China–Brazil Earth Resources Satellite (CBERS) image from 2009 were used to obtain historical land use maps. The simulation results of the HEC-HMS model for the various urbanization scenarios indicate that annual runoff, daily peak flow, and flood volume have increased to different degrees due to urban expansion during the study period (1988–2009) and that they will continue to increase as urban areas increase in the future.

Verbeiren et al. (2013) used Landsat and SPOT imagery to generate a time series of five medium-resolution urban masks and corresponding sub-pixel impervious surfaces to assess urban dynamics in urban catchments and the related impact on hydrology, using physically based rainfall-runoff model WetSpa. The results revealed:

(i) the importance of detailed information on the impervious surface proportion for hydrological simulations in urbanized catchments, (ii) the steady urban growth in the Tolka Basin between 1988 and 2006 which had a considerable impact on peak discharges, and (iii) the hydrological response is quicker as a result of urbanization.

Miller et al. (2014) investigated changes in storm runoff resulting from the transformation of previously rural landscapes into peri-urban areas. Two adjacent catchments (~5 km^2) were monitored during 2011 and 2012, providing continuous records of rainfall, runoff, and actual evaporation. One catchment was highly urbanized, and the other was a recently developed peri-urban area containing two distinct areas of drainage: one with mixed natural and storm drainage pathways and the other entirely of storm drainage. Historical levels of urbanization and impervious cover were mapped from the 1960s to the 2010s, based on digitized historical topographic maps, and were combined with a hydrological model to enable backcasting of the present day storm runoff response to that of the catchments in their earlier states. Comparisons with changes in storm runoff response in the more urban areas suggest that the relative increase in peak flows and reduction in flood duration and response time of a catchment are greatest at low levels of urbanization and that the introduction of storm water conveyance systems significantly increases the flashiness of storm runoff above that attributed to the impervious area alone.

Gumindoga et al. (2014) used Landsat Thematic Mapper (TM) images for the years 1986, 1994 and 2008 and generated the land cover maps for two medium-sized catchments in Zimbabwe. The generated land cover maps were used for the assessment of hydrological impacts of land cover changes in these two catchments. The rainfall-runoff model used was TOPMODEL. The results of land cover classification showed that the urbanization increased by more than 600% in one catchment and more than 200% in another one from 1980 to 2010. The TOPMODEL simulation results indicated that streamflow increased 84.8% and 73.6%, respectively in these two catchments.

Based on the literature review, the following gaps have been identified:

1. **Runoff generation processes in urban areas are not fully understood.** Whereas the runoff generation processes in the natural environment are generally well understood, those in the built environment are not. The runoff generation process in natural environments is typically divided into saturation excess and infiltration excess. Using soil moisture observations obtained from soil moisture sensors at different locations in large urban areas can resolve the runoff generation process in those areas.

2. **While the need for high-resolution modeling in urban areas is clear, it is not clear whether increasing (nominal) resolution increases accuracy, given the current level of advances in hydrologic-hydraulic modeling and quantitative precipitation estimation (QPE).** In the DFW area, most of the catchments are smaller than 1 HRAP cell, and the time-to-peak is less than 1 hour. Therefore, being able to observe and predict flash flooding at higher resolution is important to providing location-specific warnings. High-resolution distributed modeling is subject to nonlinear growth of error due to errors in QPE and in model parameters, structures, and initial conditions. As such, there is a practical limit to the resolution of modeling, given the quality of the QPE products available.

3. **Impact of land cover changes on streamflow response has not been investigated in flooding-prone catchments of urban areas based on high-**

resolution hydrologic modeling. Population growth in urban areas increased the imperviousness in urban areas. It is expected that the trend of population growth and migration towards urban areas leads to an increase of impervious areas. Increasing impervious covers impacts hydrologic response of the catchments and may reduce the time-to-peak and increase the runoff volume and peak flow of the catchments. The impact of land cover changes and increasing impervious covers in urban areas has not been investigated using high-resolution land cover data and high-resolution model parameters, and high-resolution radar-based rainfall products.

Chapter 4 Methodology

This chapter describes the methodology for derivation of a priori model parameters at higher resolutions. The sensitivity analysis of streamflow and soil moisture simulations to the spatial resolution of the model parameters and the rainfall input, and assessment of the impact of land cover changes on the streamflow simulation in urban areas are also discussed.

4.1 Derivation of a priori model parameters at higher resolutions

The NWS distributed hydrologic modeling system, Hydrology Laboratory Research Distributed Hydrologic Model (HLRDHM), was used for streamflow and soil moisture simulations. HLRDHM uses the Sacramento soil moisture accounting model (SAC-SMA, Burnash et al., 1973) for soil moisture accounting (i.e., rainfall-runoff), and kinematic-wave routing (Koren et al., 2004) for channel and hillslope routing. HLRDHM is a grid-based model with a default spatial resolution of 4 km × 4 km, which corresponds to the Hydrologic Rainfall Analysis Project grid (HRAP, Greene and Hudlow 1982). Currently, 11 a priori model parameters, based on soil and land cover data, are available for CONUS at 1 HRAP resolution (Anderson et al., 2006; Zhang et al., 2011). The 11 a priori SAC-SMA parameters at higher resolutions of 1/2, 1/4, 1/8 and 1/16 HRAP were derived in the study area, and then used in the streamflow and soil moisture simulations. To derive the high-resolution soil and land cover-based a priori SAC-SMA parameters, the automated model of OHD/NWS (Office of Hydrologic Development), developed for the derivation of the a priori SAC parameters at 1 HRAP resolution (Zhang et al., 2011) was modified and used. The soil data and the land cover data used were from the Soil Survey Geographic (SSURGO) database and the National Land Cover Database (NLCD), respectively. Three sets of a priori SAC-SMA parameters at higher resolutions were derived by using NLCD 2001, 2006, and 2011. In addition to 11 a priori SAC parameters, the percent of impervious area (PCTIM), which is another gridded a priori SAC-SMA parameter, was derived at resolutions of 1, 1/2, 1/4, 1/8 and 1/16 HRAP in the study area and used in high-resolution hydrologic modeling. PCTIM was derived from NLCD 2001, 2006 and 2011 and GIS layers of impervious areas available in the study area.

4.2 Sensitivity analysis of streamflow and soil moisture simulations to spatial resolution of a priori model parameters and rainfall input

After derivation of the a priori SAC-SMA parameters at 1/2, 1/4, 1/8, and 1/16 HRAP resolutions, the sensitivity analyses of the spatial resolution of the model parameters and the spatial resolution of two radar-based rainfall data were carried out. The two radar-based rainfall data were the Multisensor Precipitation Estimator (MPE) and Collaborative Adaptive Sensing of Atmosphere (CASA), with the temporal and spatial resolution of 1 h and 4 km and 1 min and 500 m, respectively.

The model was run with 40 different combinations of rainfall input and a priori SAC-SMA parameters. The combinations of a priori SAC parameters and rainfall input for streamflow and soil moisture simulations are as follows:

- Simulate streamflow at the outlets of urban catchments in the DFW area using CASA and MPE data of 2015 at 1/2, 1/4, 1/8, and 1/16 HRAP resolution and a priori SAC-SMA parameters at 1, 1/2, 1/4, 1/8, and 1/16 HRAP resolutions.
- Simulate soil moisture content at the location of three soil moisture sensors within the DFW area at 5 different depths (i.e. 0.05, 0.10, 0.25, 0.50, and 1.00 m), using CASA and MPE data of 2015 at 1/2, 1/4, 1/8, and 1/16

HRAP resolution and a priori model parameters at 1, 1/2, 1/4, 1/8, and 1/16 HRAP resolutions.

Table 4-1 shows the combination of the rainfall data (MPE and CASA) and a priori SAC-SMA parameters at different resolutions for soil moisture and streamflow simulations.

Table 4-1 Combination of the rainfall data (MPE and CASA) and a priori SAC-SMA parameters at different resolutions for soil moisture and streamflow simulations

No.	Resolution of SAC-SMA parameters (HRAP)	Resolution of Rainfall data (HRAP)	No.	Resolution of SAC-SMA parameters (HRAP)	Resolution of Rainfall data (HRAP)
1	1	1/2	11	1	1/8
2	1/2		12	1/2	
3	1/4		13	1/4	
4	1/8		14	1/8	
5	1/16		15	1/16	
6	1	1/4	16	1	1/16
7	1/2		17	1/2	
8	1/4		18	1/4	
9	1/8		19	1/8	
10	1/16		20	1/16	

The temporal resolution was fixed at 5 min, which corresponded to the highest temporal soil moisture observations at all depths (i.e. 0.05, 0.10, 0.25, 0.50, and 1.00 m) in three different locations within the study area. SAC-SMA has five state variables which were initialized with intermediate parameters. These parameters are: 1) Upper Zone Tension Water Content (UZTWC), 2) Upper Zone Free Water Content (UZFWC), 3) Lower Zone Tension Water Content (LZTWC), 4) Lower Zone Free Supplemental

Content (LZFSC) and 5) Lower Zone Free Primary Content (LZFPC). The duration of the simulation was one year (from 1/1/2015 to 12/31/2015).

4.3 Impact of land cover changes on the streamflow simulation

HLRDHM was used at 1/16 HRAP resolution to simulate streamflow at the outlets of five urban catchments in Arlington and Grand Prairie, TX, for 2015. The a priori SAC-SMA parameters derived from the SSURGO database and NLCD 2001, 2006 and 2011 were used. The model states were initialized with intermediate initial condition, and the temporal resolution was fixed at 5 minutes.

Chapter 5 Study area and data used

In this section, the study area and the data used are described. The data consisted of water level data, grain size distribution of river beds, land use and land cover data, soil data, and elevation data.

5.1 Study area

The study area encompassed the cities of Fort Worth, Arlington, Grand Prairie, and Dallas in the Dallas-Fort Worth (DFW) Metroplex in North Texas, approximately 400 km north of the Gulf of Mexico (Figure 5-1). The entire study area and its population (as of 2012) were 1,378 km^2 and 2,591,313, respectively. The topography can be described as rolling hills, ranging between 150 to 245 m (NWS 2015).

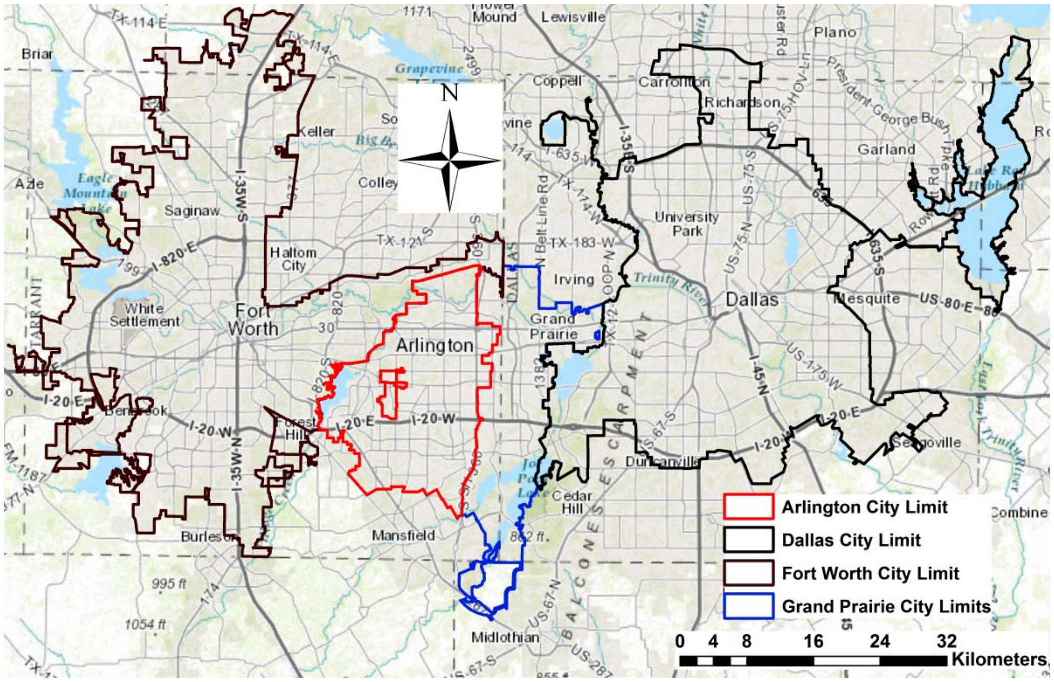

Figure 5-1 Model domain encompassing the Cities of Fort Worth, Arlington, Grand Prairie and Dallas in North Texas

5.2 Water level

Water level observations were made available from the cities of Fort Worth, Arlington and Grand Prairie through the High Water Warning System (HWWS) every 15 minutes. The raw water level observations have been recently available from http://70.128.162.107:81/datawise/webview/dataAPI/index.php. The water level sensors used in the HWWS are the pressure transducer type. The water level sensors in Arlington and Grand Prairie monitor the variations of the water levels in creeks; however, the water level sensors of Fort Worth monitor the variations of water levels in the lakes and streets once the streets are inundated during rainfall events. The 15-min water level observations made possible by the Grand Prairie sensors have been successfully used in validating streamflow simulations (Rafieeinasab et al., 2015a) following conversion to streamflow via rating curves derived from 1-D steady state non-uniform hydraulic modeling (Kean and Smith 2005, 2010; Norouzi et al., 2015).

UTA will deploy additional sonar-type water level sensors at multiple locations within the study area to observe and collect water level data in the creeks. For this purpose, 20 locations in Fort Worth, 2 locations close to downtown Dallas, and 7 locations in Arlington have been proposed. Figure 5-2 shows the prospective locations for the water level sensors deployment. The observed water level data from the sonar-type water level sensors, along with the water level observations from the pressure transducer types, will be used to monitor the variations of water levels in the creeks, particularly during rainfall events, and to validate the streamflow simulations.

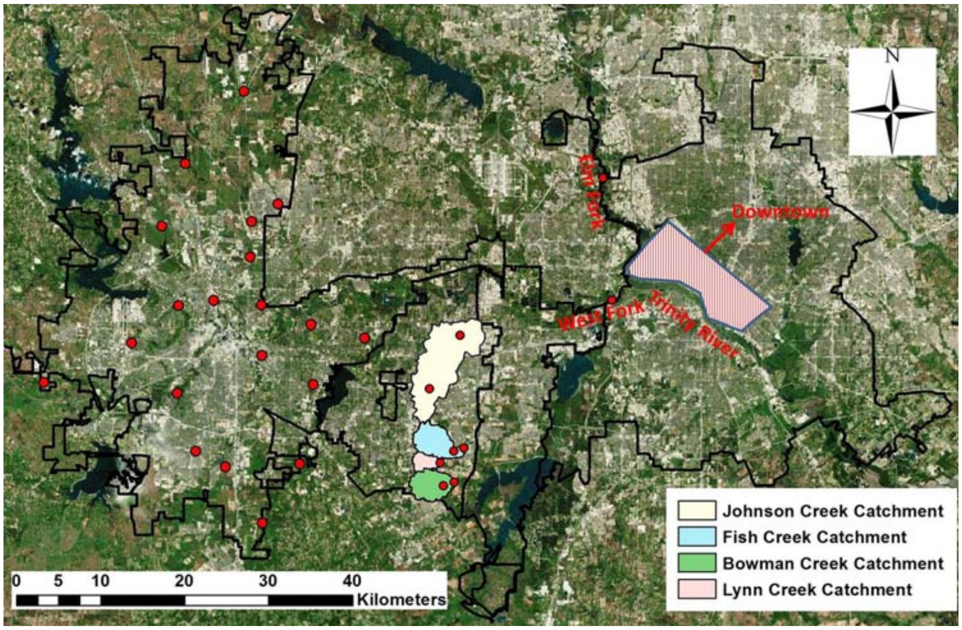

Figure 5-2 Prospective locations for water level sensor deployment (red dots) throughout the study area

5.3 Grain size distribution of river beds

The grain size distribution of channel beds, obtained from the cities of Grand Prairie and Fort Worth, will be used to determine D_{84} and the relative roughness of the beds (Table 5-1).

Table 5-1 D_{84} at different locations within the study area

D_{84} (mm)	Location
15.0	Arbor Creek, Grand Prairie, TX
15.0	Cotton Wood Creek, Grand Prairie, TX
20.0	Warrior Creek, Grand Prairie, TX
30.0	Fish Creek, Grand Prairie, TX
50.0	Royal Creek (downstream), Fort Worth, TX
60.0	Royal Creek (upstream), Fort Worth, TX

5.4 Land cover

The National Land Cover Database 2011, 2006, and 2001 (NLCD 2011, NLCD 2006 and NLCD 2001) were used in this research. NLCD 2001, 2006, and 2011 were produced by the Multi-Resolution Land Characteristics (MRLC) consortium to provide a land cover database with a spatial resolution of 30 m across the United States (Homer et al., 2015) in 20 land cover classifications (Table 5-2). Figure 5-3 shows the NLCD 2011, with 15 distinct classifications over the study area.

Table 5-2 National Land Cover Data 2011 (NLCD 2011) Classes

No.	**Class**	**Code**	**Classification description**
1	Water	11	Open Water
		12	Perennial Ice/Snow
2	Developed	21	Open Space
		22	Low Intensity
		23	Medium Intensity
		24	High Intensity
3	Barren	31	Barren Land(Rock/Sand/Clay)
4	Forest	41	Deciduous Forest
		42	Evergreen Forest
		43	Mixed Forest
5	Shrubland	51	Dwarf Scrub
		52	Shrub/Scrub
6	Herbaceous	71	Grassland/Herbaceous
		72	Sedge/Herbaceous
		73	Lichens
		74	Moss
7	Planted/Cultivated	81	Pasture/Hay
		82	Cultivated Crops
8	Wetlands	90	Woody Wetlands
		95	Emergent Herbaceous Wetlands

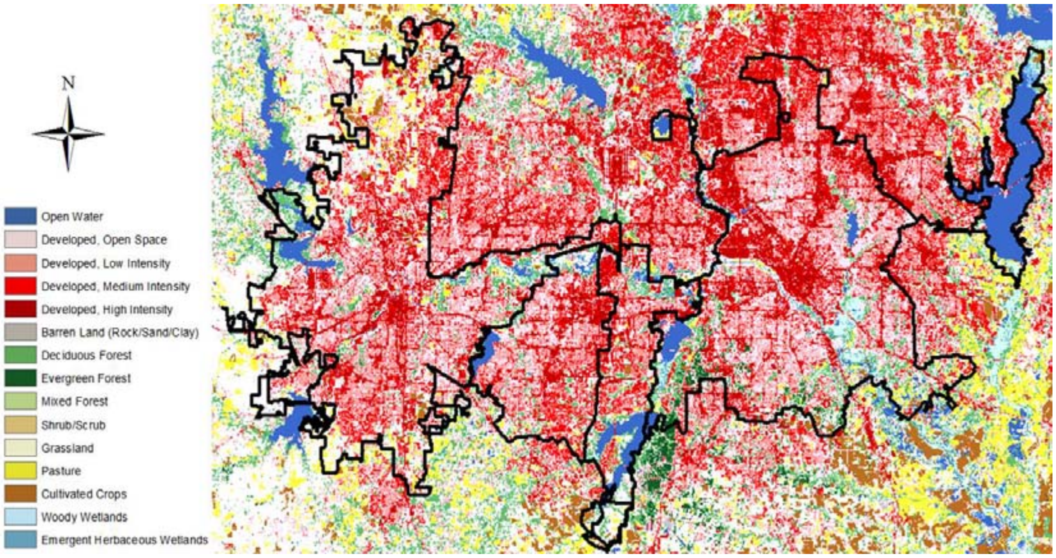

Figure 5-3 National Land Cover Data 2011 (NLCD 2011) with 15 distinctive classes over the study area

5.5 Impervious cover

To derive the percent of impervious area maps, four sources of datasets (i.e. GIS layers of impervious areas, NLCD 2001, NLCD 2006 and NLCD 2011) were used. The GIS layers of impervious areas were obtained from the cities of Fort Worth, Arlington, Grand Prairie and Dallas, and the percent of impervious area maps were derived from them, as shown in Table 5-3 (Rafieeinasab et al., 2015a).

Table 5-3 GIS layers from the cities of Fort Worth, Arlington, Grand Prairie and Dallas used for the estimation of impervious area

Map Layer	Fort Worth	Arlington	Grand Prairie	Dallas
Building footprint	√	√	√	√
Impervious cover of commercial	√	-	√	√
Pavements	√	√	-	√
Centerline of sidewalk	√	-	-	√
Centerline of streets	-	-	√	√

5.6 Soil

The Soil Survey Geographic (SSURGO) database was used to obtain the soil texture information for the study area. The SSURGO database was collected by the National Cooperative Soil Survey for the United States, based on field observations and laboratory tests (Natural Resources Conservation Service Soils, 2015). The soil polygons defined in the SSURGO data range in size from about 10 to 20 km^2 (Zhang et al., 2011).

5.7 Elevation

The 0.7 m-resolution LiDAR data obtained from the Texas Natural Resources Information System (TNRIS 2015) was used to derive the Digital Elevation Model (DEM) and to delineate the river cross sections at different locations around the study area.

Chapter 6 Advanced sensing

In this chapter, three real-time radar-based QPE products available in the study area, rain gauge data and soil moisture data will be described. Rain gauge data will be used to evaluate the available QPEs, QPEs will be used in high-resolution hydrologic modeling and soil moisture data will be used for investigation of runoff generation processes in the study area and for evaluation of high-resolution hydrologic modeling.

6.1 Precipitation

6.1.1 Radar

In the DFW area, there are currently three real-time radar-based QPE products available: the MPE (Seo et al., 2010, Kitzmiller et al., 2011), Q2 (Next Generation QPE, Zhang et al., 2011) and CASA (Chandrasekar and Cifelli 2012). To date, a network of five CASA X-band radars, referred to as the DFW Demonstration Network, has been deployed in the area. The five CASA X-band radars are located in Addison, Arlington, Cleburne, Denton, and Midlothian. Figure 6-1 shows the coverage of XUTA and the city limits of Fort Worth, Arlington, Grand Prairie, and Dallas. The nearest WSR-88D, KFWS, is located in Burleson, TX, shown as the red triangle in the figure.

All three QPE products were considered in this research, as well as the multi-QPE fusion products (Rafieeinasab et al., 2015a), which provide the highest-resolution rainfall estimates and are more accurate than the ingredient QPEs at their native resolutions. Table 6-1 shows the spatiotemporal resolution of the radar-based QPE products.

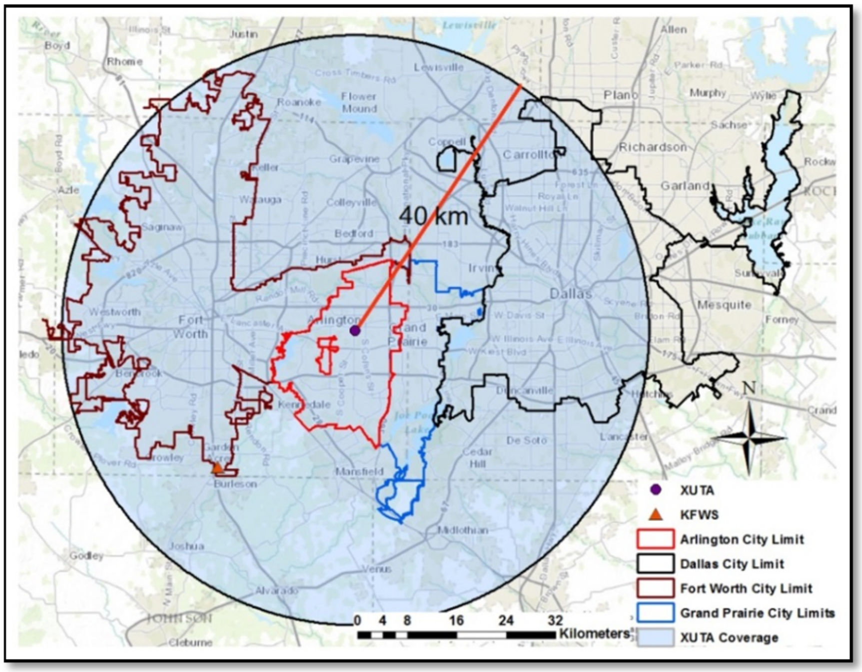

Figure 6-1 Coverage area of XUTA

Table 6-1 Spatiotemporal resolution of the available QPE products in the study area

QPE product	Temporal resolution	Spatial resolution
MPE	60 min	4 km × 4 km
Q2	5 min	1 km × 1 km
CASA	1 min	500 m × 500 m
Multi-QPE fusion	15 min	1 km × 1 km

6.1.2 Rain gauges

Rainfall observations are available from the cities of Fort Worth, Arlington and Grand Prairie. The above cities have been operating High Water Warning Systems (HWWS) at 19, 5, and 21 locations throughout the cities since 2007, 2013, and 2009, respectively (Figure 6-2a). Thirty-nine additional ones have been recently installed. Rainfall observations are available every 15 minutes through the tipping bucket rain gauges used in HWWS.

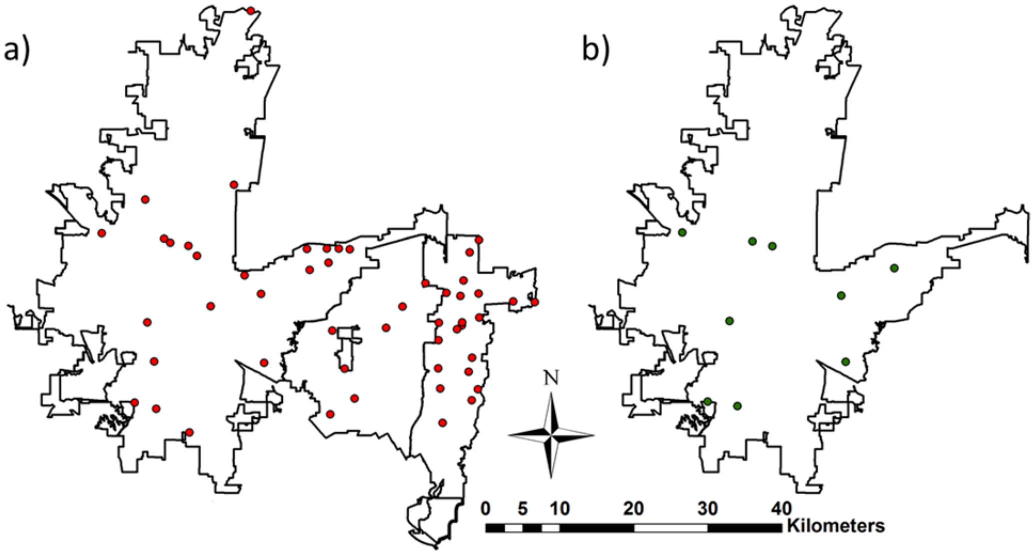

Figure 6-2 Location of High Water Warning Systems (HWWS) throughout the cities of Fort Worth, Arlington and Grand Prairie (left) and the location of UTA tipping bucket rain gauges throughout the city of Fort Worth (right)

The University of Texas at Arlington (UTA) deployed nine tipping bucket rain gauges throughout the city of Fort Worth. UTA rain gauges were deployed as close as possible to the HWWSs, so that the distance between the UTA rain gauges and the HWWS varied from 110 m to 1150 m (Figure 6-2b). The resolution of the tipping bucket rain gauges is 1 mm/tip, and the resolution of the HWWS rain gauges is 0.254 mm/tip.

6.1.3 Evaluation of available QPEs in the DFW area

For evaluation of the available radar-based QPEs in the DFW area, 15-minute rainfall observations from 20 rain gauges in Grand Prairie were used. To check the quality of rain gauge data, the scatter, quantile-quantile plot, and double-mass plots of rainfall observations between each rain gauge and its closest neighbor were examined. The results indicated the rain gauge data from the City of Grand Prairie is viable.

QPEs were validated after conducting quality control for the rainfall observations. The common period among all three QPEs was only 7 months in 2013. The results of the validation showed that: 1) Q2 has the least bias in mean, most biased in variability, and is more skillful for larger amounts, 2) MPE is the most skillful for smaller amounts and has significantly reduced skill for larger amounts, and 3) CASA is the most skillful overall, particularly for larger amounts. Figure 6-3 shows the scatterplots between available QPEs in the DFW area and 15-min rain gauge observations.

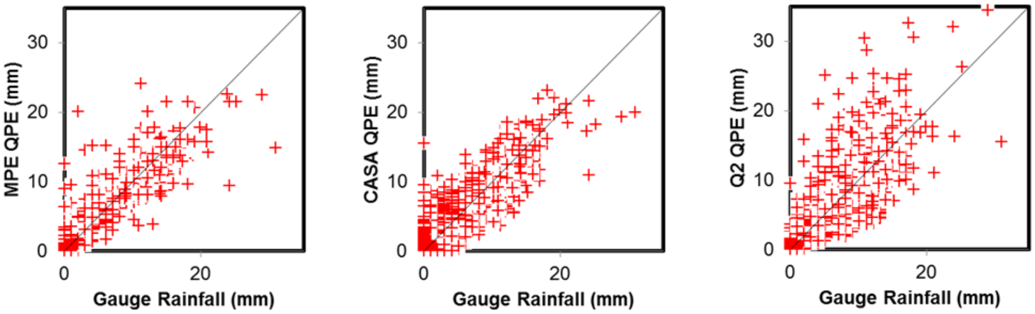

Figure 6-3 Scatterplots between available QPEs in the DFW area and 15-min rain gauge observations

6.2 Soil moisture

Since soil moisture is highly variable in space and time (Vereecken et al., 2014), it is necessary to observe it at a high temporal frequency and in a large number of locations to evaluate model simulations. Several methods exist for in-situ measurement of soil moisture. They may be grouped into direct and indirect methods (Romano, 2014). The direct methods measure the soil moisture at the point of interest. The indirect methods measure those properties of soil such as electrical constant, conductivity, or neutron-scattering effects that are highly correlated with soil water content (Romano, 2014).

The most widely used direct method is the gravimetric method (Blonquist Jr. et al., 2006; Romano, 2014). Gravimetric soil water content measurement is a destructive method that requires 24 hr of oven drying. It appears that the soil moisture content in the field changes within the 24 hr of oven drying. Continuous observation of the soil moisture content, using the gravimetric soil water content measurement at multiple locations and at different depths in specified time intervals, is not feasible. For the evaluation of high-resolution hydrologic modeling, continuous soil moisture observations at multiple locations and at different depths within the study area are needed.

Using the Time Domain Reflectometery (TDR) and Time Domain Transmissomtery (TDT) sensors is recognized as one of the best methods for in-situ soil moisture measurement (Blonquist Jr. et al., 2006; Robinson et al., 2008). A TDR sensor measures the dielectric constant and electrical conductivity of soil by propagating electromagnetic signals along the probes placed at different depths of the soil column (Yu et al., 2004; Blonquist Jr. et al., 2006; and Romano, 2014). The two soil properties of dielectric constant and electrical conductivity are then related to soil water content. The main advantages of TDTs and TDRs are: 1) superior accuracy to within 1 or 2% of volumetric water content, 2) minimal calibration requirements, and 3) lack of radiation hazards associated with neutron probe or gamma-attenuation techniques, 4) high temporal resolution, and 5) measurements that are simple to obtain (Jones et al. 2002).

To observe the soil moisture content in the study area, three locations were selected in the Johnson Creek Catchment (Figure 6-4) for deployment of two TDTs and one TDR soil moisture sensor. The distance between the two locations was approximately 1.3 km. To observe the variations of the soil moisture by depth, five soil moisture sensors (SMS) were deployed at each of the selected locations in August 2015, at depths of 0.05, 0.10, 0.25, 0.50, and 1.00 m from the soil surface. The SMSs were placed near a creek or a channel to enable understanding of the runoff generation process in a large urban area (Figure 6-4).

SMS1 (CELB) is located at (32.7281, -97.1245) near a man-made channel (Figure 6-4). The topography of this location is flat, and based on NLCD 2011 (Figure 5-3), the land cover of this location is categorized as developed, open space, which is an area with a mixture of some constructed materials, but mostly vegetation in the form of lawn grasses (see Table 5-2). Based on lab test analysis, the soil type at this location is sand clay-silty sand (SC-SM).

SMS2 (Bridge), is located at (32.7272, -97.1127) by the Timber Brook Creek (Figure 6-4). The slope of the land at this location is steep toward the Timber Brook Creek. Based on NLCD 2011 (Figure 5-3), the land cover of this location is categorized as developed, low intensity, which is an area with a mixture of constructed materials and vegetation. Based on lab test analysis, the soil type at this location is sand clay (SC).

SMS3 (Cemetery) is located at (32.7272, -97.1127) by the Johnson Creek (Figure 6-4). The slope of the land at this location is flat, similar to the CELB. Based on NLCD 2011 (Figure 5-3) the land cover of this location is categorized as developed, open space. Based on lab test analysis, the soil type at this location is sand clay (SC).

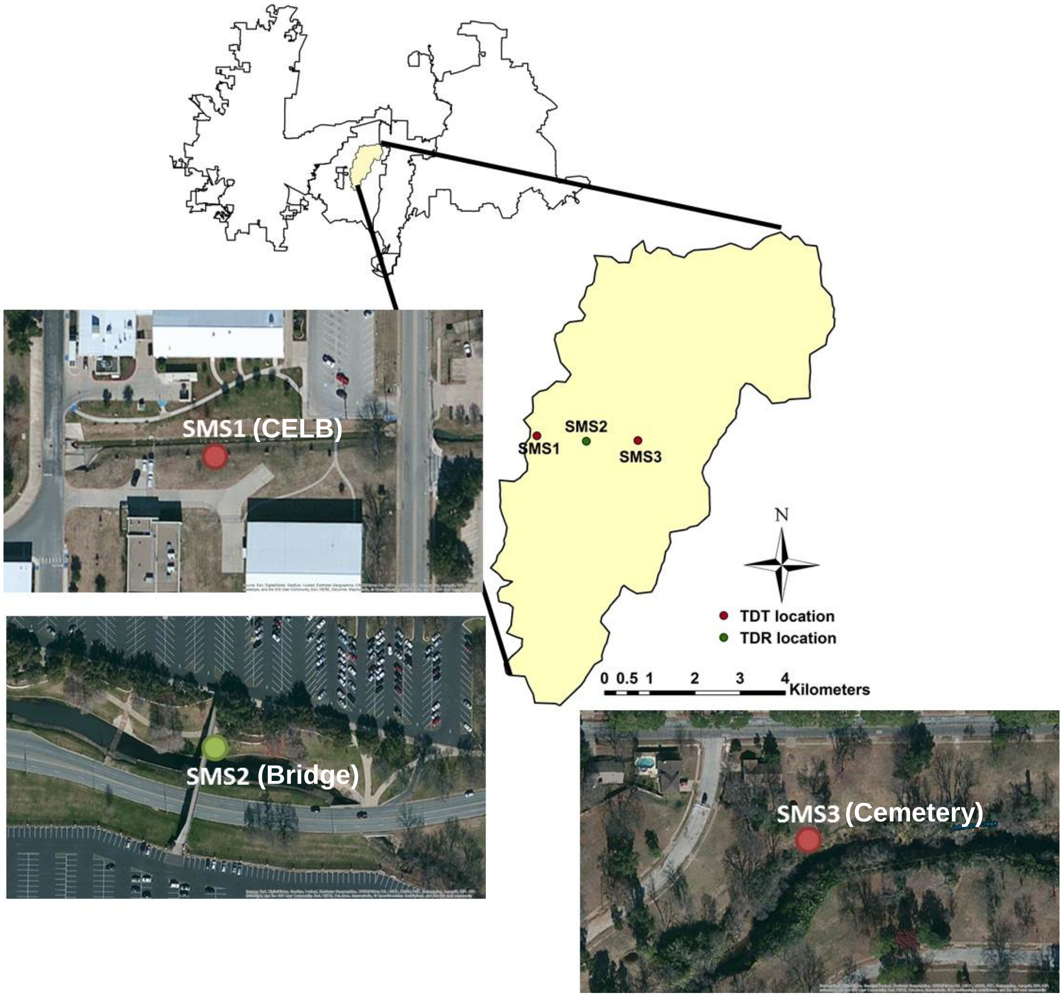

Figure 6-4 Locations of the three deployed soil moisture sensors (SMS) within the Johnson Creek Catchment

6.2.1 *Evaluation of soil moisture sensors' performance*

The performance of the soil moisture sensors at three locations (CELB, Bridge and Cemetery) at the first three depths was verified. To do this, the soil moisture content obtained from the sensors was compared with that obtained from the lab test (Table 6-2). The relative difference between the gravimetric and in-situ soil moisture content at the three locations was smaller than 7%.

Table 6-2 In-situ and lab test soil moisture content measurements at the locations of the soil moisture sensors within the study area at 0.05, 0.10, and 0.25 m

Depth (m)	Soil moisture content at CELB		Soil moisture content at Bridge		Soil moisture content at Cemetery	
	lab	In-situ	lab	In-situ	lab	In-situ
0.05	35.56	35.54	16.83	15.76	23.93	22.31
0.1	35.46	35.14	13.42	12.68	25.74	23.99
0.25	33.35	34.75	16.84	15.79	28.73	26.95

6.3 Model simulation of soil moisture

The model used for the soil moisture simulation was the Sacramento soil moisture accounting model (SAC, Burnash et al., 1973) with heat transfer, or the SAC-HT. SAC-HT is an extension of the SAC model. The Sacramento soil moisture accounting model (SAC-SMA), uses conceptual water storage at a soil column and converts the conceptual water storage to a soil moisture state via a physically-based heat-moisture transfer model.

6.3.1 Comparisons of soil parameters: SAC-HT vs. lab test vs. field tests

Before using SAC-HT for soil moisture simulation at the location of soil moisture sensors, three parameters of SAC-HT were evaluated (i.e., porosity, saturated hydraulic conductivity, and permanent wilting point). For evaluation of porosity and permanent wilting point, the lab test was performed at three locations. For evaluation of saturated hydraulic conductivity, the results of the lab test and infiltration test were used and compared to the saturated hydraulic conductivity used by SAC-HT. Table 6-3 shows the infiltration test results and the lab test results for the saturated hydraulic conductivity at three locations. The table shows that the lab test result for saturated hydraulic conductivity at the CELB location was approximately 10 times smaller than that of the SAC-HT; however, the saturated hydraulic conductivity from the lab test was very close to the SAC-HT.

Table 6-3 Saturated hydraulic conductivity (m/s) obtained from infiltration test, lab test, and soil texture map at the location of soil moisture sensors

Location	Infiltration test	Lab test	SAC-HT
CELB	7.60×10^{-5}	3.47×10^{-6}	3.46×10^{-5}
Bridge	4.95×10^{-6}	2.25×10^{-6}	1.27×10^{-6}
Cemetery	1.09×10^{-6}	1.20×10^{-6}	1.27×10^{-6}

Table 6-4 summarizes the lab test results for the permanent wilting point and porosity and those used by SAC-HT. The lab test result for the permanent wilting point was significantly different than the permanent wilting point used by the SAC-HT at the CELB location. The main reason for this significant difference is based on field observations. The soil at the CELB is backfill soil and was imported to the CELB site from other locations.

Table 6-4 Porosity and permanent wilting point at the location of soil moisture sensors obtained from the lab test and soil texture map

Location	Porosity		Permanent Wilting Point	
	Lab test	SAC-HT	Lab test	SAC-HT
CELB	0.493	0.42	0.238	0.09
Bridge	0.42	0.46	0.270	0.28
Cemetery	0.502	0.46	0.225	0.28

6.3.2 Observed and simulated soil moisture at the Bridge location

Figure 6-5 shows the time series of observed and simulated soil moisture content at the Bridge location at five depths from Aug 24, 2015 to Dec 31, 2015. For the soil moisture simulation, MPE data at 1/8HRAP was used. The resolution of the a priori model parameters was 1/8HRAP. The comparison between simulated and observed soil moisture showed that the result was under-simulation in the lower zone and over-simulation in the upper zone. The soil moisture observations indicated high ground water level at this location.

To understand the runoff generation process based on the observed soil moisture, the observed and simulated soil moisture profile associated with the 10/22/2015 to 10/25/2015 rainfall event was analyzed (Figure 6-6). The total MPE rainfall for this event was 195 mm. Analysis of the observed and simulated soil moisture indicated that while the model response was similar to infiltration excess, the observed response was similar to saturation excess. The observed soil moisture profile also showed that TDR measurements are not stable at depths greater than 25 cm.

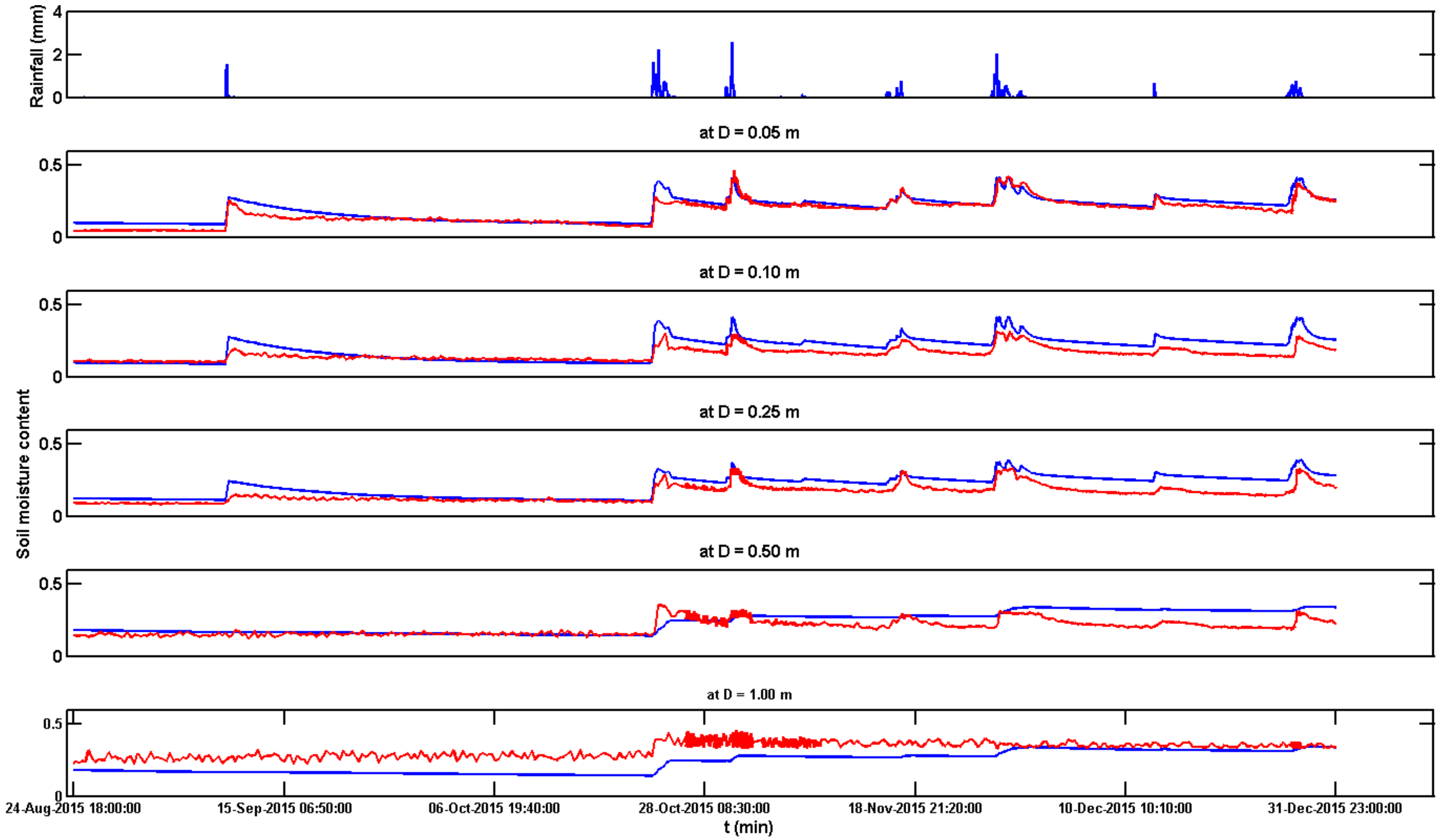

Figure 6-5 Time series of simulated and observed soil moisture content at the Bridge location using MPE data at 1/8 HRAP resolution and a priori SAC parameters at 1/8 HRAP resolution Simulated soil moisture is depicted in blue and observed soil moisture in red.

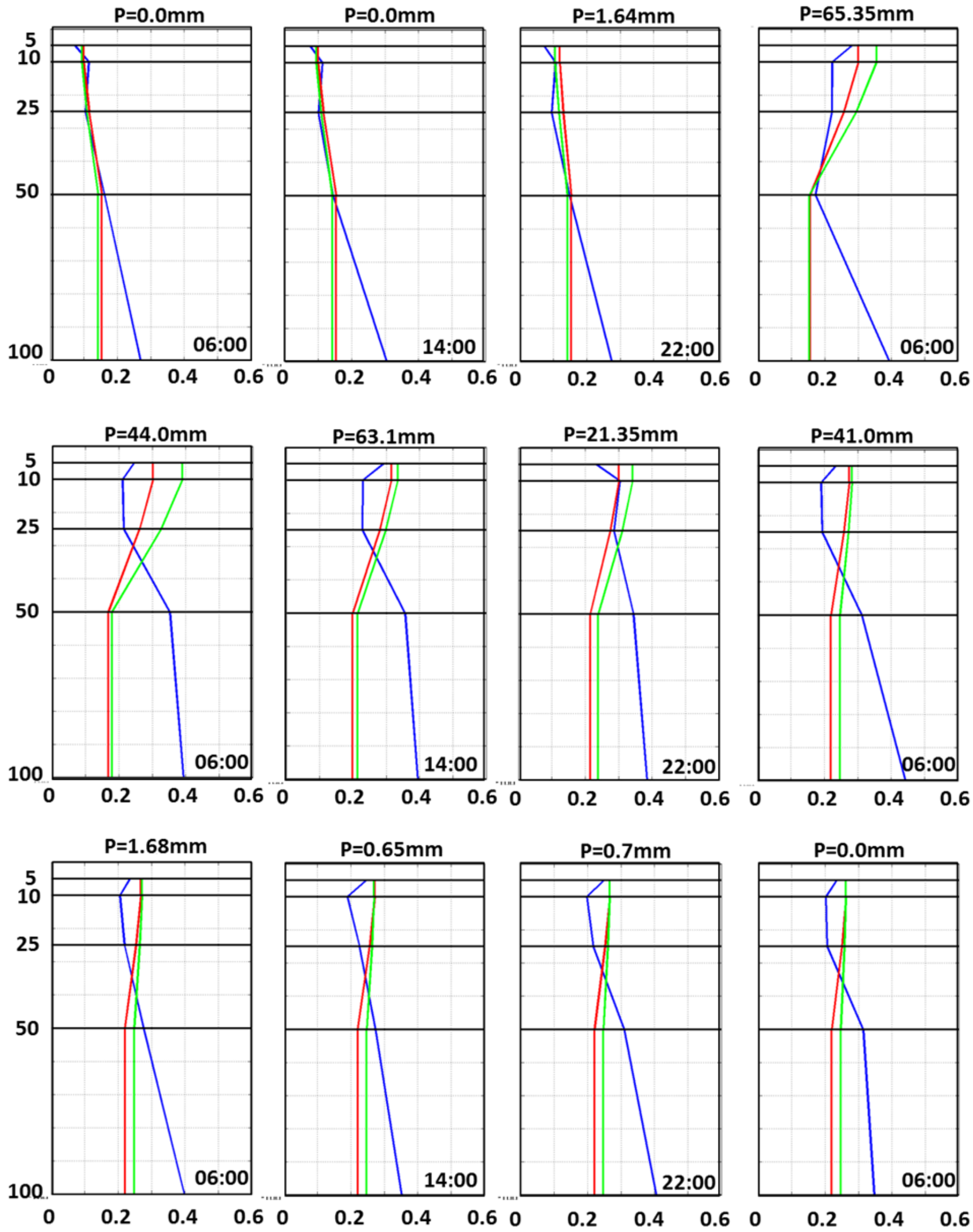

Figure 6-6 Simulated and observed soil moisture profile at the Bridge location for 10/22/2015 to 10/25/2015 rainfall event (observed (blue), MPE-forced rainfall (green) and CASA-forced rainfall (red))

6.3.3 Observed and simulated soil moisture at CELB location

Figure 6-7 shows the time series of observed and simulated soil moisture content at CELB location at five depths from Aug 19, 2015 to Dec 31, 2015. This figure shows the simulated soil moisture based on MPE data and a priori model parameters at 1/8 HRAP resolution. The comparison between simulated and observed soil moisture shows that the result is under-simulation at all depths. Also, the model soil moisture was significantly biased. The soil moisture observations indicate that after the rainfall event of Oct 22, 2015, the soil was consistently close to saturated condition, and with a small rainfall, the soil reached fully saturated condition.

The analysis of the simulated and observed soil moisture profile associated with the rainfall events of Oct. 22, 2015 to Oct. 25, 2015 (Figure 6-8) indicates that while the model soil's moisture response to initial rainfall was similar to infiltration excess, the observed soil moisture quickly reached near saturation at all depths and remained nearly saturated. At this location, infiltration was dominated by suction pressure. While there is a departure between model simulation and observation, model soil moisture in the lower zone approaches the observed after a few days. This departure would under-simulate runoff at this location.

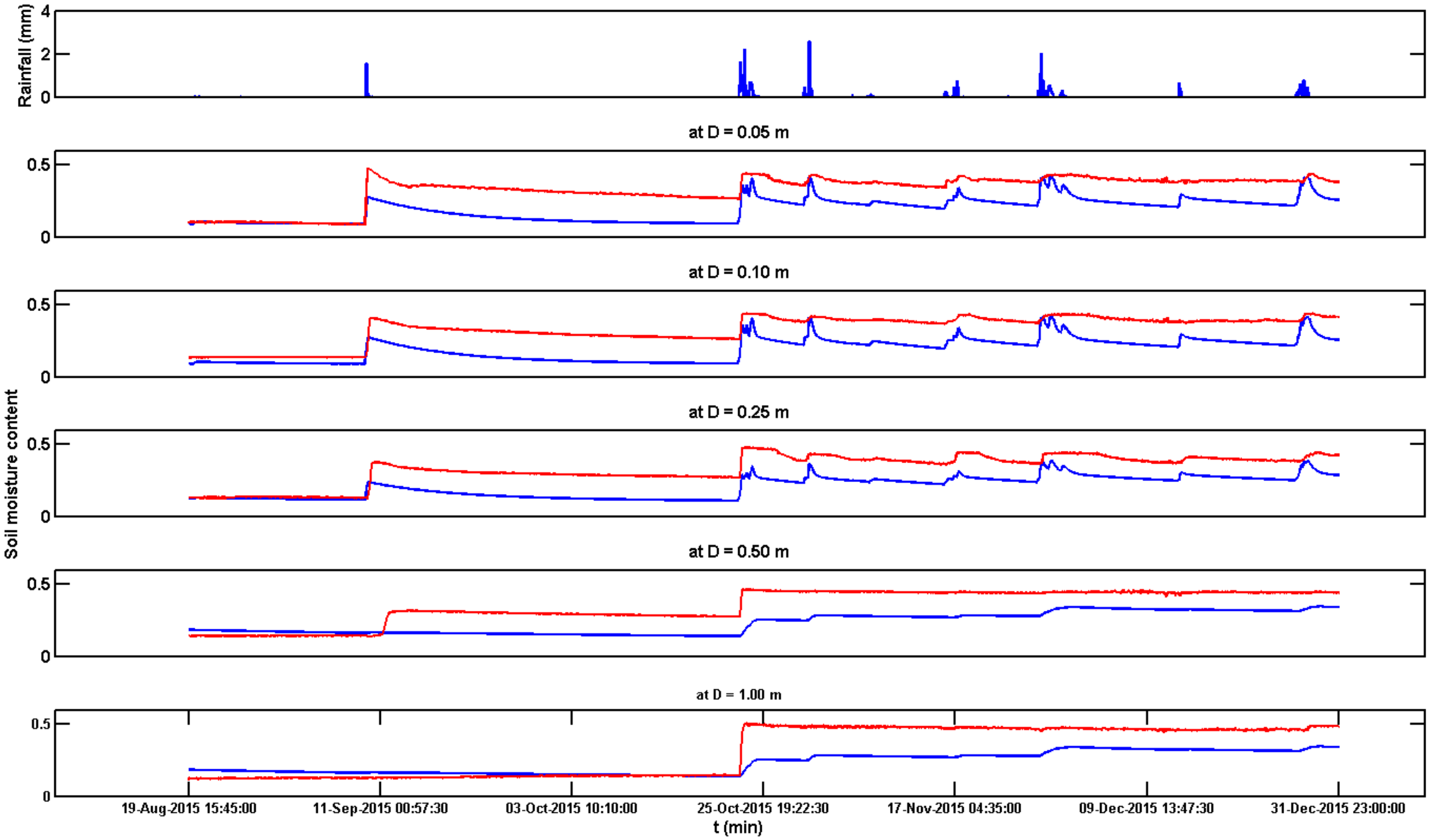

Figure 6-7 Time series of simulated and observed soil moisture content at CELB location using MPE data at 1/8 HRAP resolution and a priori SAC parameters at 1/8 HRAP resolution. Simulated soil moisture is depicted in blue and observed soil moisture in red.

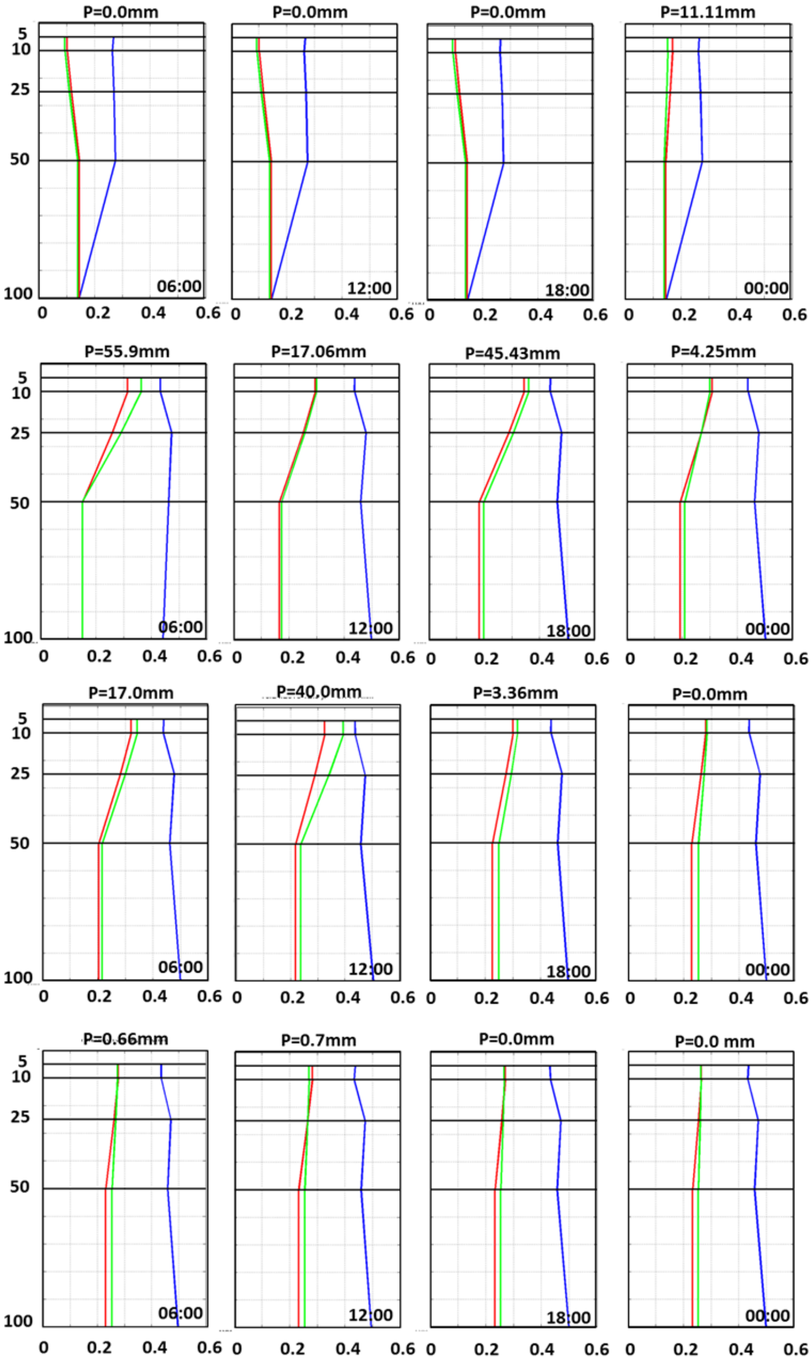

Figure 6-8 Simulated and observed soil moisture profile at CELB location for 10/22/2015 to 10/25/2015 rainfall event (observed (blue), MPE-forced rainfall (green) and CASA-forced rainfall (red))

6.3.4 Observed and simulated soil moisture at Cemetery location

Similar to the Bridge and CELB locations, MPE data and a priori model parameters at 1/8 HRAP resolution were used for the soil moisture simulation at the Cemetery location. Figure 6-9 shows the time series of simulated and observed soil moisture at five depths at the Cemetery location from Aug. 19, 2015 to Dec. 31, 2015. The comparison between simulated and observed soil moisture shows over-simulation at all depths, and the model soil moisture had a large bias. The model soil moisture had a lag in the lower depths. The lag can be seen clearly in the Oct. 22, 2015 rainfall event. The rate of decrease in the observed soil moisture was faster than in the simulated soil moisture in the upper layers; however, this rate was approximately the same in the lower layers.

The analysis of the simulated and observed soil moisture profile associated with the rainfall events of Oct. 22, 2015 to Oct. 25, 2015 (Figure 6-10) indicates that while observed soil moisture shows a clear wetting front following infiltration excess, model soil moisture quickly increases to near saturation at all depths. The model soil moisture profile approached the observed only after the leading edge reached a depth of 100 cm after nearly 2 days, which would result in model over-simulation of runoff.

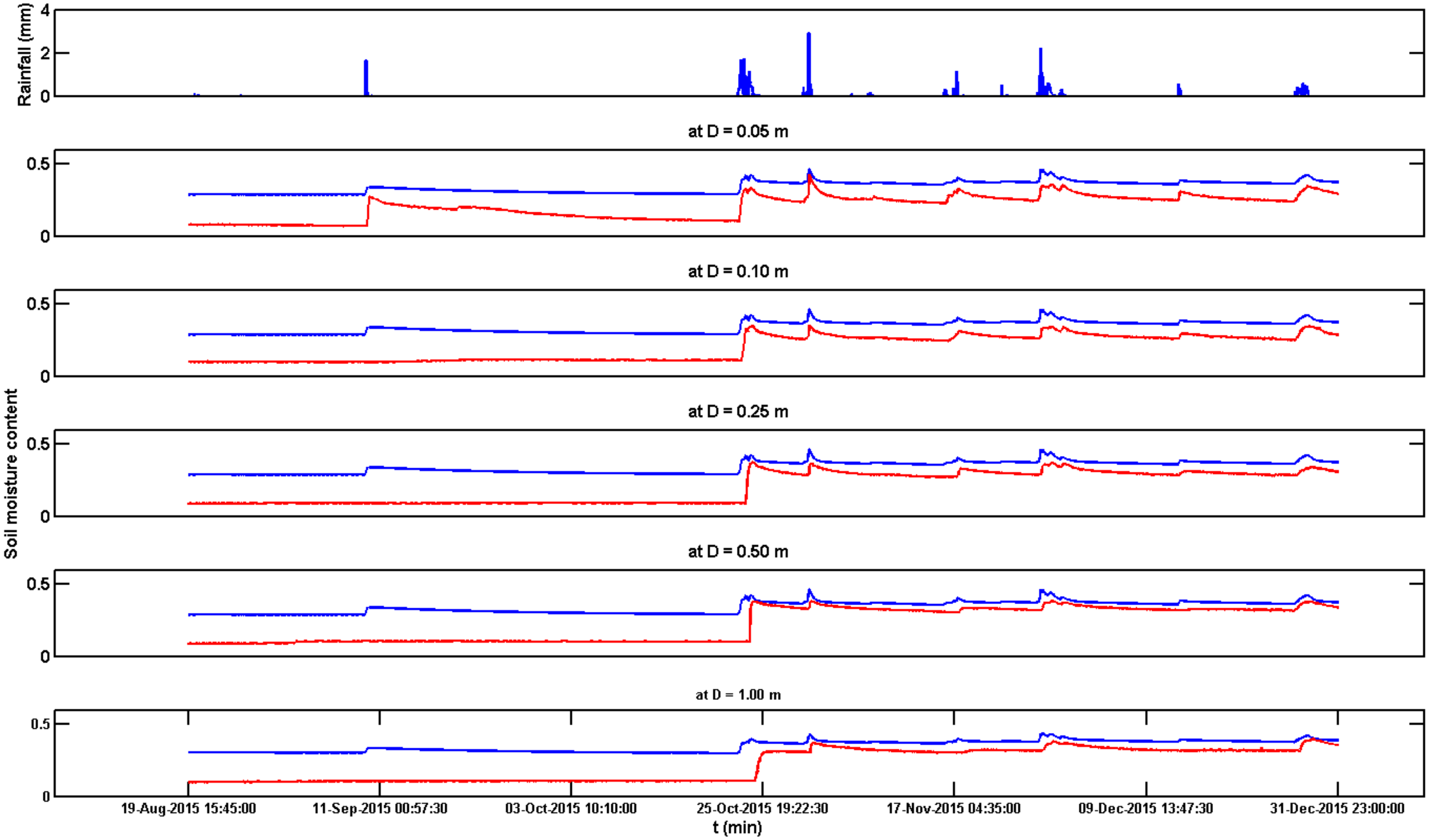

Figure 6-9 Time series of simulated and observed soil moisture content at the Cemetery location using MPE data at 1/8 HRAP resolution and a priori SAC parameters at 1/8 HRAP resolution. Simulated soil moisture depicted in blue and observed soil moisture in red.

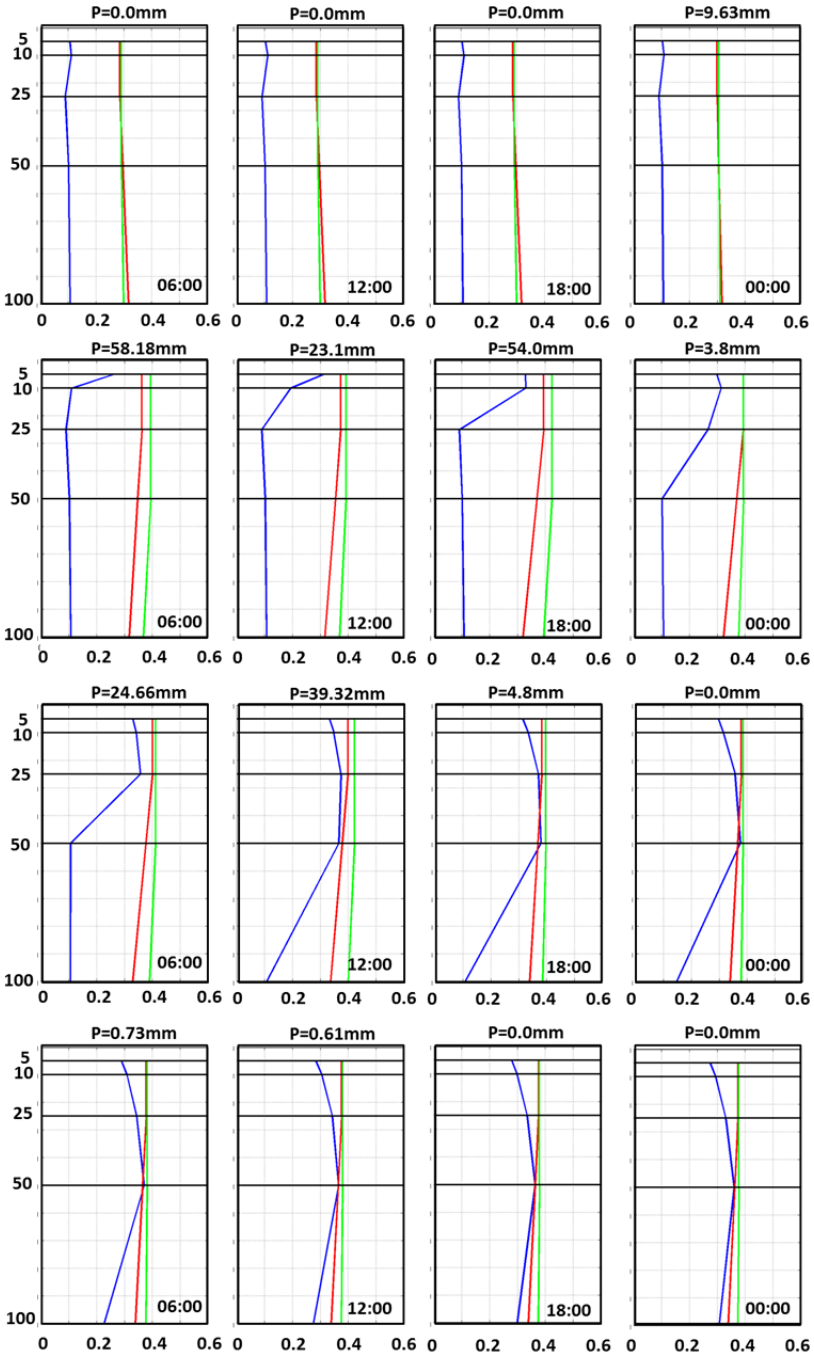

Figure 6-10 Simulated and observed soil moisture profile at the Cemetery location for 10/22/2015 to 10/25/2015 rainfall event (observed (blue), MPE-forced rainfall (green), and CASA-forced rainfall (red))

Chapter 7 Hydrologic and hydraulic models used

In this chapter, the hydrologic model and hydraulic model used in this work are described. The hydrologic model was used for streamflow and soil moisture content simulation and the hydraulic model was applied for the derivation of stage–discharge relation (rating curve) in 5 catchment outlets within the study area

7.1 Hydrologic model

The NWS distributed hydrologic modeling system, Hydrology Laboratory Research Distributed Hydrologic Model (HLRDHM), was used for hydrologic modeling. HLDRHM, has been used in several research studies and has been reported as one of the best distributed hydrologic models for streamflow prediction (Reed et al., 2004; Smith et al., 2012). Tang et al., (2007) used HLRDHM for an analysis of sensitivity to the model parameters and showed that storage variation, spatial trends in forcing, and cell proximity factors control RDHM's behavior. Yilmaz et al., (2008) evaluated HLRDHM at the watershed outlet and showed that diagnostic evaluation has the potential to provide a powerful and intuitive basis for deriving consistent estimates of the parameters. van Werkhoven (2008) used HLRDHM and demonstrated that the information content of streamflow is a dynamic property and that distributed model identification methodologies should consider the impact of spatiotemporal rainfall dynamics. Lee et al., (2011) assimilated streamflow observations and in-situ soil moisture data into HLRDHM to improve streamflow prediction. Fares et al., (2014) evaluated HLRDHM in a tropical watershed. They demonstrated that the streamflow prediction improved with finer resolution of input data and that HLRDHM is applicable for flood forecasting in tropical watersheds. Rafieeinasab et al., (2015a) successfully applied HLRDHM to five urban catchments, ranging in size from 3.4 to 54.6 km^2, and assessed the sensitivity of streamflow simulation to hydrologic modeling. Koren et al., (2008) used the soil moisture observation and improved parameter consistency of HL-RDHM. In addition to the research applications, HLRDHM is operational at 13 NWS River Forecast Centers (RFCs) to provide daily stage forecasts at over 4,000 points.

HL-RDHM is a grid-based model with a default spatial resolution of 4 km × 4 km, which corresponds to the grid of the Hydrologic Rainfall Analysis Project (HRAP, Greene and Hudlow 1982). HL-RDHM uses the Sacramento soil moisture accounting model (SAC, Burnash et al., 1973) with heat transfer, or SAC-HT (Koren et al., 2014) for soil moisture accounting (i.e., rainfall-runoff), and kinematic-wave routing (Koren et al., 2004) for channel and hillslope routing.

SAC-HT is an extension of the Sacramento Soil Moisture Accounting (SAC-SMA) model, and uses the conceptual water storages at a soil column and converts them to soil moisture states via a physically-based heat-moisture transfer model (Koren et al., 1999). Since SAC-HT and SAC-SMA have the same structure with two additional parameters; the parameters of SAC-SMA are valid for SAC-HT (Table 7-1, Anderson et al., 2006; Koren et al., 2008).

SAC-SMA is a lumped conceptual rainfall-runoff model of a soil column. SAC-SMA divides a soil column into two distinct layers (i.e. upper zone and lower zone), and each layer consists of free water and tension water storages. Free water storage is that volume of water which can move laterally and/or horizontally in the soil column due to gravity, and the tension water storage is that amount of water bound to soil particles that can be removed only by evaporation or evapotranspiration. The free water storage in the lower zone is partitioned into primary free water storage and supplemental free water storage, enabling simulation of the baseflow recessions observed in nature. The primary free water storage provides baseflow over a long period of time, and the supplemental free water storage supplements the baseflow during and after a rainfall event.

Table 7-1 SAC-HT model parameters, units and their description

Parameters	Units	Description
UZTWM	mm	Upper Zone Tension Water Maximum storage
UZFWM	mm	Upper Zone Free Water Maximum storage
LZTWM	mm	Lower Zone Tension Water Maximum storage
LZFSM	mm	Lower Zone Free water Supplementary Maximum storage
LZFPM	mm	Lower Zone Free water Primary Maximum storage
UZK	day^{-1}	Upper zone free water withdrawal rate
LZSK	day^{-1}	Lower Zone Supplementary withdrawal rate
LZPK	day^{-1}	Lower Zone Primary withdrawal rate
ZPERC		Maximum percolation rate under dry condition
REXP		Percolation equation exponent
PFREE	%	percent going directly to lower zone free water
PCTIM	%	% permanent impervious area
ADIMP	%	% area contributing as impervious when saturated
RIVA	%	% area affected by riparian vegetarian, streams and lakes
SIDE	%	Ratio of deep percolation from lower layer free water storages
RSERV	%	Fraction of lower layer free water not transferable to lower layer
TBOT	°C	Climatological annual air temperature
STXT		Soil texture of the upper layer

In SAC-SMA, partitioning of rainfall into runoff is determined by the upper zone storages and the percolation potential of the lower zone storage. Once the upper zone tension water is filled, the runoff generation process is controlled by the available water in the upper zone free water storage and the deficiency of water in the lower zone free and tension water storages. Free water storage in both the lower and upper zones can produce runoff, using upper zone and lower zone depletion coefficients. The available water storage in the soil column will then be converted to the soil moisture states of SAC-HT via the basic heat transfer model (Koren 1999):

$$c(\theta, \theta_c)\frac{\partial T}{\partial t} = \frac{d}{dz}\left[K(\theta, \theta_{ice})\frac{\partial T}{\partial z}\right] + \rho L\frac{\partial \theta_{ice}}{\partial t} \qquad (7\text{-}1)$$

where *c* is the volumetric heat capacity, *T* is soil temperature, *K* is the thermal conductivity of soil, θ is the volumetric soil moisture content, θ_{ice} is the volumetric ice content, *ρ* is the density of water, *z* is depth, and *t* is time. SAC-HT uses the soil texture of the upper layer and the climatological annual air temperature parameters.

7.1.1 Derivation of 11 a priori SAC-SMA parameters at higher resolution

Koren et al., (2000 and 2003) developed a set of relationships to derive 11 a priori SAC parameters (highlighted in Table 7-1) from soil properties (i.e. saturated moisture content, field capacity, wilting point, saturated hydraulic conductivity, and specific yield) and land cover and land cover data. They used the State Soil Geographic Database (STATSGO, Miller and White 1998) and assumed uniform land use and land cover for the derivation of the 11 a priori SAC parameters. STATSGO is a Geographic Information System (GIS)-based soil property dataset with the resolution of 1:250,000. Anderson et al., (2006) improved the SAC-SMA a priori parameter estimates by using a finer-scale database of soil data, the SSURGO database, and a high-resolution land cover and land use database, NLCD. The SSURGO-based and the STASGO-based gridded a priori model parameters used in 63 basins across the United States, range from 30 km^2 to 5224 km^2 to simulate the streamflow and soil moisture (Zhang et al., 2012). Results showed that use of the SSURGO-based parameters can improve soil moisture and streamflow simulations more than the use of STATSGO-based parameters. The Hydrology Laboratory of the NWS office of Hydrologic Development (NWS/OHD) developed an automated approach for deriving gridded a priori SAC-SMA parameters from SSURGO and NLCD datasets based on Koren et al. (2000 and 2003) and Anderson et al., (2006) a priori SAC parameters derivation (Zhang et al., 2011).

The spatial resolution of the gridded a priori SAC-SMA parameters, available for the continental US from NWS/OHD, are on the HRAP grid (i.e. 4 km × 4 km, Koren et al., 2000; Anderson et al., 2006; Zhang et al., 2011; and Zhang et al., 2012). Within a large urban area such as the DFW area, the spatial variability of imperviousness may vary greatly; consequently, it is expected that the available a priori SAC parameters at the resolution of 4 km × 4 km cannot sufficiently represent the variation of the imperviousness, and hence the variability of resulting runoff. Moreover, the available a priori SAC parameters from the NWS/OHD cannot reflect the land cover and land use changes over the years. In order to take into account the variations of the land cover and land use changes over the years in the a priori SAC parameters, the automated NWS/OHD model of the a priori SAC-SMA parameters derivation was modified, and the 11 a priori SAC parameters at 1, 1/2, 1/4, 1/8, and 1/16 HRAP resolutions were derived. The NLCD 2001, NLCD 2006, and NLCD 2011 were processed along with the SSURGO data, and the a priori SAC parameters were derived. It should be noted that with the derivation of a priori SAC parameters at higher resolutions, the impact of finer-scale soil properties on the a priori SAC parameters is also considered. Figure 7-1 toFigure 7-3 shows the variation of the Upper Zone Free Water Maximum within the study area, derived from SSURGO and NLCDs of 2001, 2006 and 2011. The upper bound of 1/16 HRAP is based on extensive visual examination of the land cover images in various parts of the DFW. It was observed that most large features associated with imperviousness may be resolved on a 1/16HRAP grid (Rafieeinasab et al., 2015a).

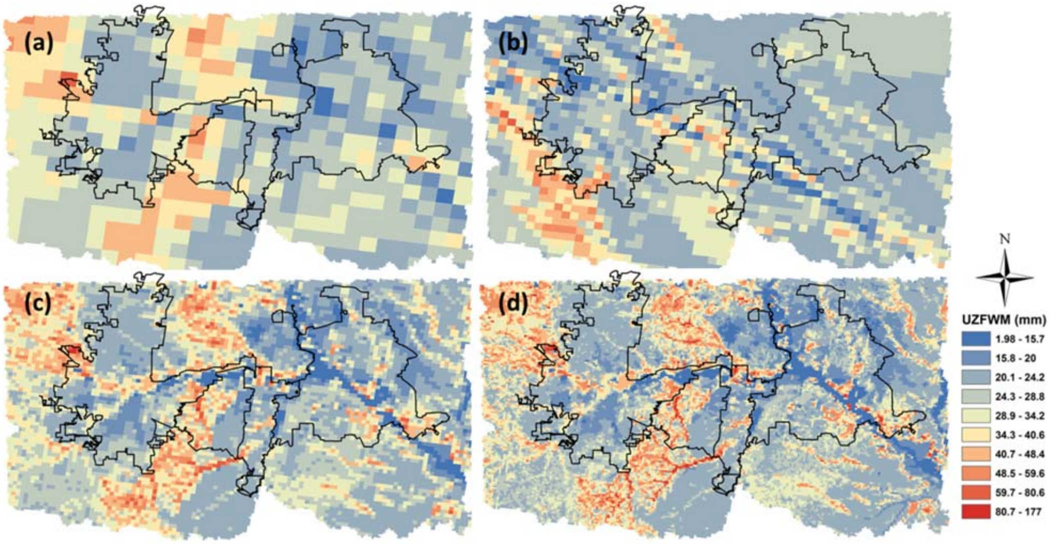

Figure 7-1 UZFWM map within the study area at full HRAP (a), at 1/2HRAP (b), at 1/4HRAP (c) and at 1/8HRAP (d) resolutions, derived from SSURGO and NLCD 2001

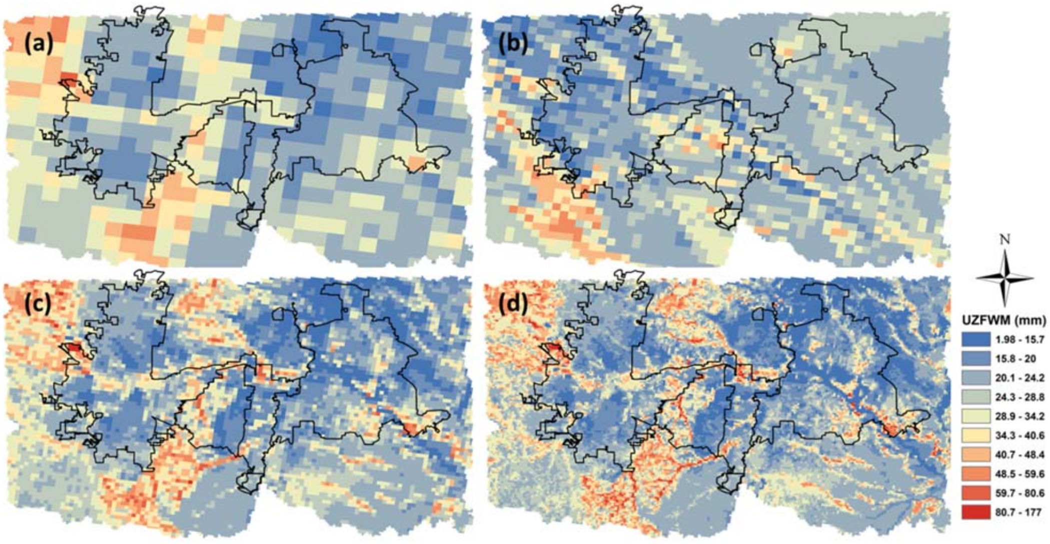

Figure 7-2 UZFWM map within the study area at full HRAP (a), at 1/2HRAP (b), at 1/4HRAP (c) and at 1/8HRAP (d) resolutions, derived from SSURGO and NLCD 2006

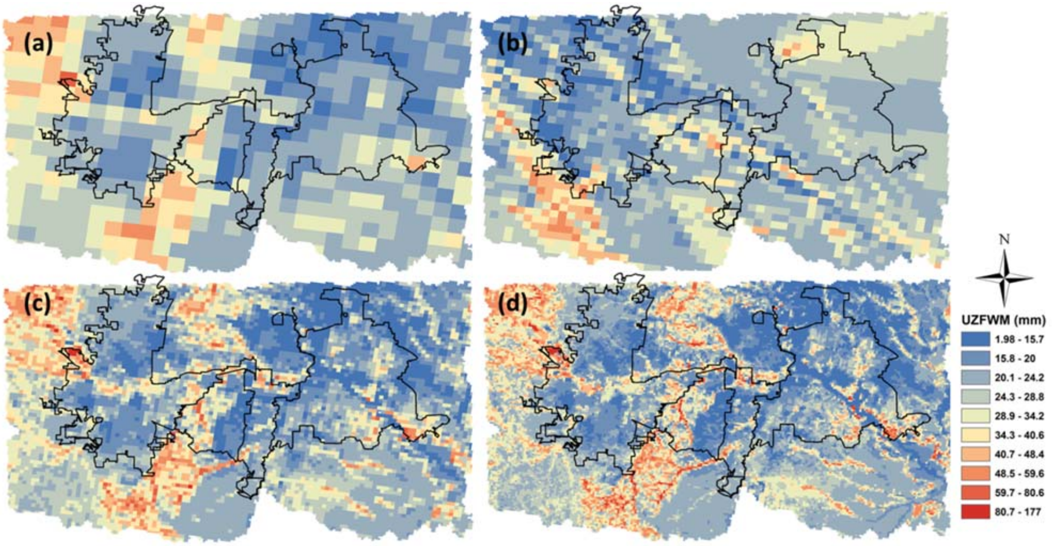

Figure 7-3 UZFWM map within the study area at full HRAP (a), at 1/2HRAP (b), at 1/4HRAP (c) and at 1/8HRAP (d) resolutions, derived from SSURGO and NLCD 2011

7.1.2 Derivation of permanent impervious area (PCTIM)

The Permanent Impervious Area (PCTIM) was derived at higher resolutions corresponding to the resolutions of the derived a priori SAC parameters. (PCTIM in SAC refers to areas in the watershed that are impervious and are directly connected to the channel system; HL-RDH Manual 2012.) Four different sources of land use and land cover datasets (i.e. NLCD 2001, NLCD 2006, NLCD 2011 and GIS layers) were used. GIS layers, obtained from the Cities of Fort Worth, Arlington, Grand Prairie, and Dallas, TX, represent the impervious area within the city boundaries; however, NLCDs covered the areas where the impervious GIS layers were not available. All available layers were combined, and the percent of impervious cover, defined as the percentage of the impervious area within a grid box, was calculated for each pixel, ranging from 1/16 HRAP (~250 m) to 1/2 HRAP (~2 km). Because the GIS layers used in this work do not account for all the sources of imperviousness, the calculated PCTIM from this source is likely to be an underestimate. Figure 7-4 shows the PCTIM maps within the study area at 1/16HRAP resolution from different available sources of land cover and land use datasets.

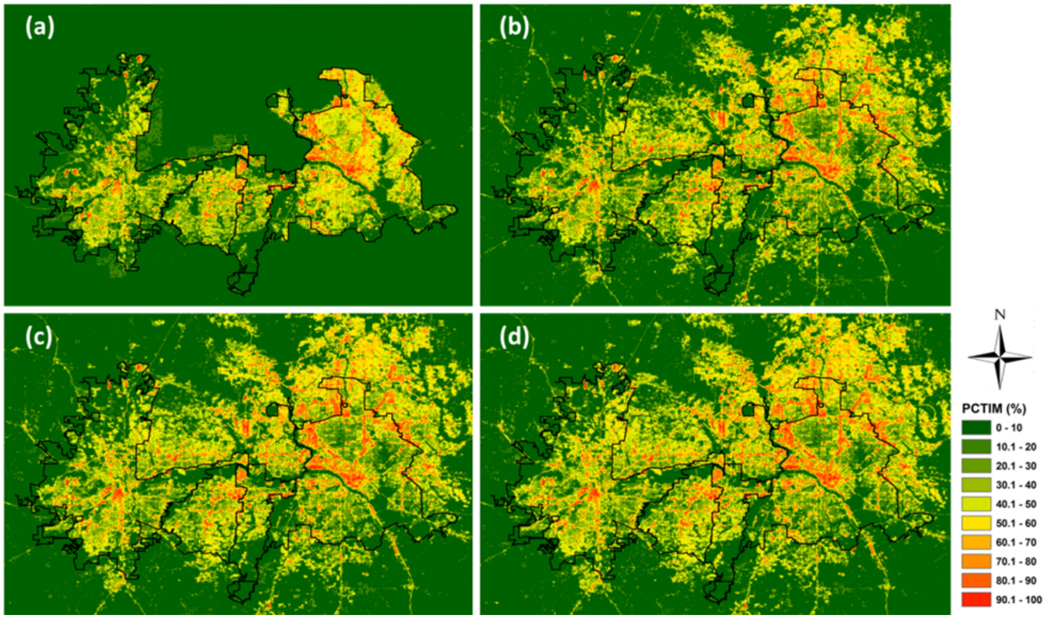

Figure 7-4 PCTIM map within the study area at 1/16HRAP resolution, derived from GIS layers (a), NLCD2001 (b), NLCD2006 (c) and NLCD 2011 (d)

Hillslope and channel routing in HLRDHM is performed using kinematic-wave routing (Chow et al., 1988; Koren et al., 2004). HLRDHM routes runoff through the natural channels identifiable from the digital elevation model (DEM) by the Cell Outlet Tracing with an Area Threshold (COTAT) algorithm (Reed, 2003).Within each cell, fast runoff is first routed over conceptual hillslopes, and then the combination of channel inflow from hillslope routing, slow (i.e. subsurface or ground) runoff, and inflow from upstream cells is routed via channel routing (Koren et al., 2004). A conceptual hillslope consists of multiple uniform hillslopes, the number of which depends on the stream channel density specified for the cell. The conceptual channel that transfers water from one cell to another usually represents the highest order stream in the cell selected. The cell-to-cell connectivity is used to transfer water from upstream to downstream cells and to the basin outlets. For hillslope routing, discharge per unit area of hillslope (q_h) was given by (Koren et al., 2004):

$$q_h = 2k_q D \frac{\sqrt{S_h}}{n_h} h^{5/3} \tag{7-2}$$

where k_q denotes the unit transformation coefficient, D denotes the stream channel density in km^{-1}, S_h denotes the hillslope slope, n_h denotes the hillslope roughness coefficient, and h denotes the average depth of water on the hillslope. For channel routing, the discharge for each cell, Q_c, is a power function of the wetted cross sectional area, A:

$$Q_c = q_o A^{q_m} \tag{7-3}$$

where q_0 denotes the specific discharge, i.e., discharge per unit channel cross section area, and q_m denotes the exponent in the power-law relationship. The specific discharge may be evaluated if A and Q_c are known. Mean annual flow may be derived from the mean average annual runoff data over the continental US available from the United States Geological Survey (USGS, Slack and Landwehr 1992). The wetted channel cross section, A, may be obtained from A=Q/V where V denotes the mean velocity, which may be evaluated using the empirical equation developed by Jobson (1996):

$$V = 0.094 + 0.0143 \left(\frac{D_a^{1.25}\sqrt{g}}{Q}\right)^{0.919} S^{0.159} \frac{Q}{D_a} \tag{7-4}$$

where D_a denotes the upstream drainage area calculated by using the flow direction and cell size grids, g denotes the gravitational acceleration, and S denotes the channel slope. The two kinematic-wave channel routing parameters, q_0 and q_m, were derived by using the above relationships and the National Elevation Dataset (NED) with 30 meter resolution from the NHDPlus Version 2 dataset (David et al., 2014).

7.2 Hydraulic model

Streamflow observations are necessary for calibration and validation of hydrologic models used for flash flood forecasting in urban areas. Streamflow at a cross-section is typically estimated using the stage-discharge relationship or rating curve, describing the relationship between the observed streamflows and the corresponding water levels. Based on the definition, the rating curve consists of long historical-paired measurements of stage and discharge and a fitted curve to the stage-discharge data (Rantz, 1982a, 1982b, Kean and Smith 2010). Streamflow measurement is more time consuming and expensive than water level measurement, particularly in urban watersheds, where the streamflow changes rapidly in rainfall conditions (Garth et al., 2011 and Nathanson et al., 2012). While water levels are observed in many urban streams, estimation of streamflow from them is impossible due to the lack of a stage-discharge relationship.

There are different indirect methods for developing the rating curve and estimating streamflow from the recorded observed water levels. The most widely-used methods to estimate the streamflow when the direct flow measurement is not available are the Manning equation and step-backward models, for instance Hydrologic Engineering Centers River Analysis System (HEC-RAS, Rantz, 1982b, Brunner 2010). These methods are less accurate than the direct streamflow measurements, because they are subjected to the uncertainties due to the estimation of the empirical roughness coefficient (Kim et al., 1995; Lopez et al., 2007).

Kean and Smith (2004, 2005, 2010) proposed a fluid mechanically-based model to derive the stage-discharge relationship. The proposed model determines the channel roughness from field measurements of channel geometry and dominant bed materials. The approach is applicable to geomorphically stable channels and consists of two parts: 1) procedures for quantifying various contributions to the total flow resistance in the channel and 2) a flow model that incorporates the results from the above procedures. The technique models streamflow in a channel reach by solving the Saint-Venant equation (Chow et al., 1988) for steady non-uniform flow in one dimension. The mass and momentum balance equations are given by (Kean and Smith 2005):

$$\frac{\partial \mathrm{Q}}{\partial \mathrm{x}} = 0 \tag{7-5}$$

$$\frac{1}{2}\frac{\partial(\mathrm{u}^2)_{\mathrm{av}}}{\partial \mathrm{x}} + \mathrm{g}\frac{\partial \mathrm{E}}{\partial \mathrm{x}} + \frac{1}{\rho}\frac{(\tau_{\mathrm{b}})_{\mathrm{av}}}{\mathrm{R}} = 0 \tag{7-6}$$

where Q denotes the channel flow, x denotes the direction of flow, $(u^2)_{av}$ denotes the square of the downstream velocity averaged over the cross section,$(\tau_{\mathrm{b}})_{\mathrm{av}}$ denotes the perimeter-averaged shear stress (N/m^2), *E* denotes the elevation of the water surface (m), and *R* denotes the hydraulic radius (m).The physical roughness of the channel bed is related to the particle size of the bed material via z_o=0.1D_{84} (m), where D_{84} denotes the 84th percentile of the grain size distribution. The channel roughness is estimated from the channel geometry, the physical roughness of the channel bed, banks, and floodplain, and the vegetation density on the banks and floodplain. Using the Kean and Smith approach to derive the rating curve requires channel and floodplain cross-section data, which can be time intensive and laborious to obtain. High-resolution airborne light detection and ranging (LiDAR) data has been proposed as an alternate to prescribe the fixed boundary conditions (Garth et al., 2011; Nathanson et al., 2012).

The Kean and Smith approach was applied to five locations within the study area and derived the stage-discharge relation for them. The five selected locations are located at the outlet of the catchments, ranging from 54.6 km^2 to 3.4 km^2 (Figure 7-5). Water level observations were available every 15 minutes from the pressure transducer-type water level sensor.

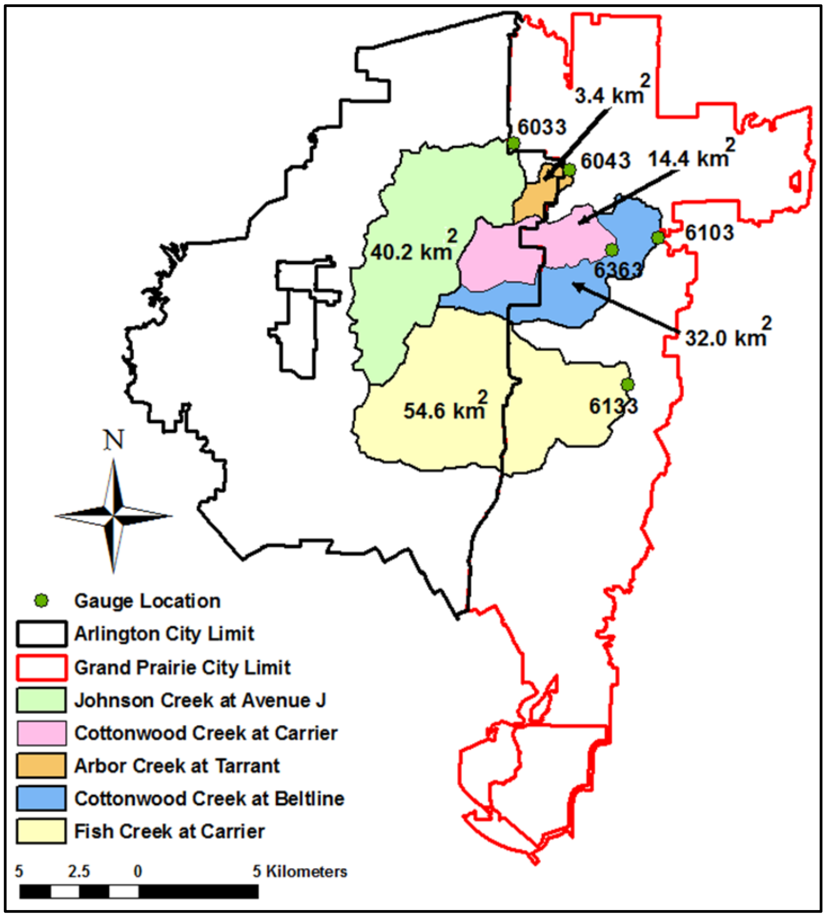

Figure 7-5 Selected locations for the rating curve derivation

The historical water level time series were visually examined at the five locations selected for rating curve derivation. Figure 7-6 shows the water level time series at the outlet of Cottonwood Creek at Carrier (6363).

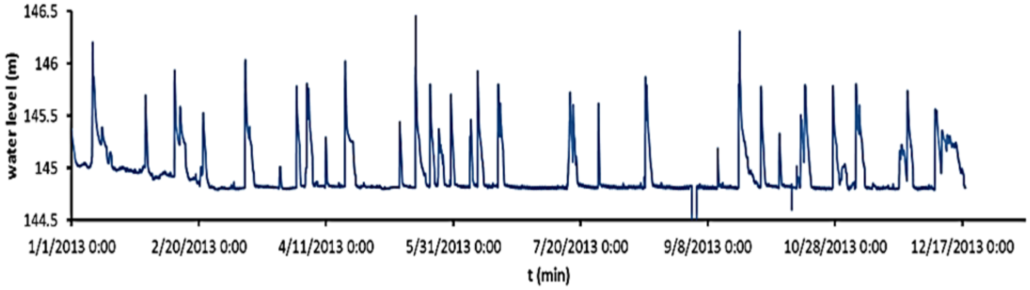

Figure 7-6 Water level time series (01/01/2013-12/18/2013) at the outlet of Cottonwood Creek catchment (6363), Grand Prairie, TX

7.2.1 Channel Geometry

High-resolution (0.7 m) LiDAR data was used to delineate the channel geometry of the stream and derive the channel cross sections at the locations of interest (Figure 7-7). The derived channel cross sections were transferred to the river flow and riverbed variation analysis solver, Flow and Sediment Transport with Morphological Evolution of Channels (FastMECH, Nelson and McDonald 1996, Nelson et al., 2003), to construct a mesh (Figure 7-8). The resulting mesh was then used to calculate the bed slope of the channel, the velocity field for a given cross section, stage, and water surface slope using the ray-isovel approach of Kean and Smith (2004).

Table 7-2 Datum, length of the reach, bed slope and the number of mesh in longitudinal and traverse direction at each location

Location	Datum (m)	Length (m)	Bed slope (m/m)	Number of mesh	
				Longitudinal	Traverse
6033	147.4	250	0.0008	463	113
6043	147.73	130	0.0024	271	141
6103	134.0	130	0.0031	121	101
6133	140.3	220	0.0024	355	251
6363	144.75	180	0.0008	370	200

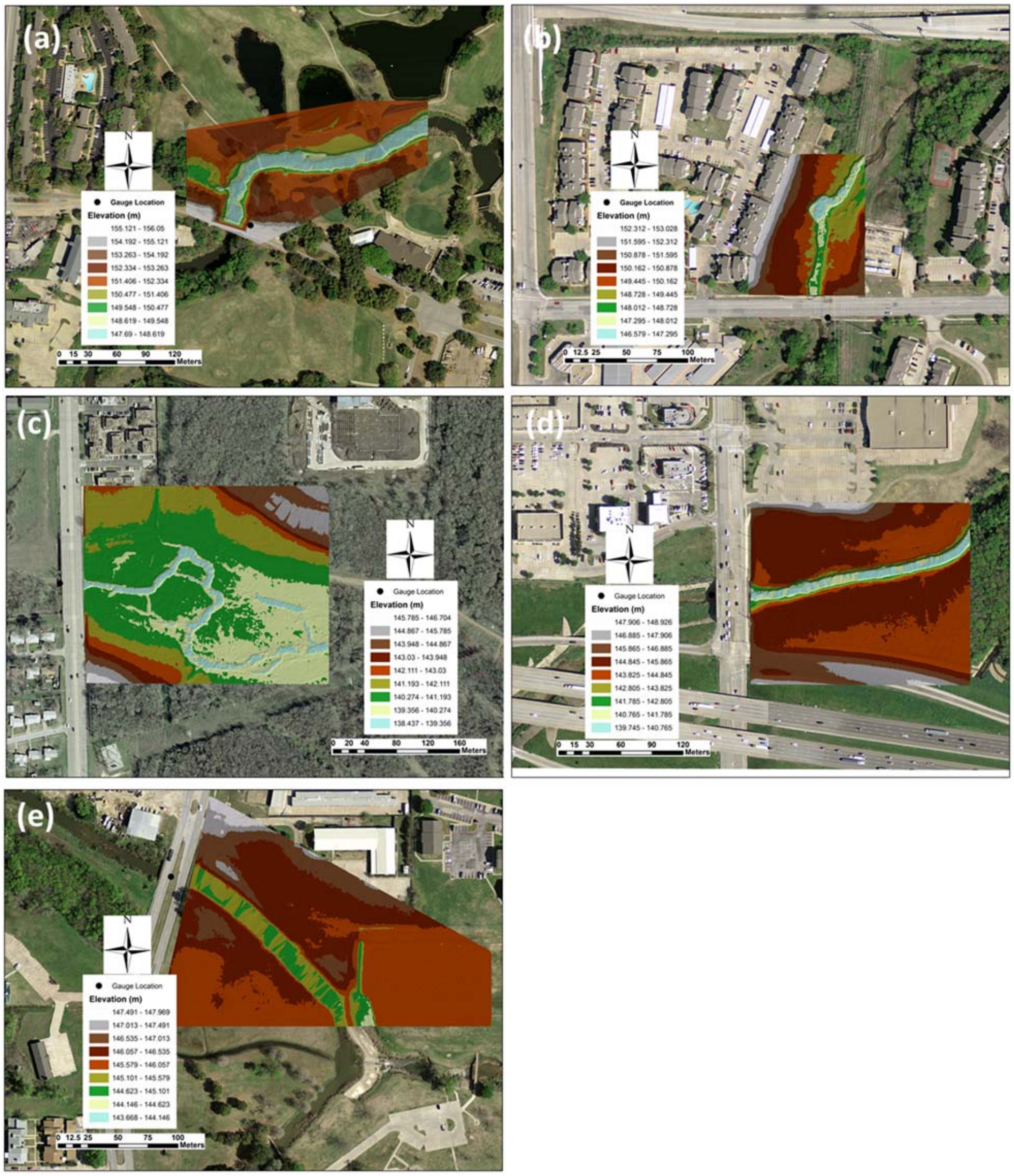

Figure 7-7 Plan view of the channels at 6033(a), 6043 (b), 6103 (c), 6133 (d) and 6363 (e) derived from high-resolution LIDAR data

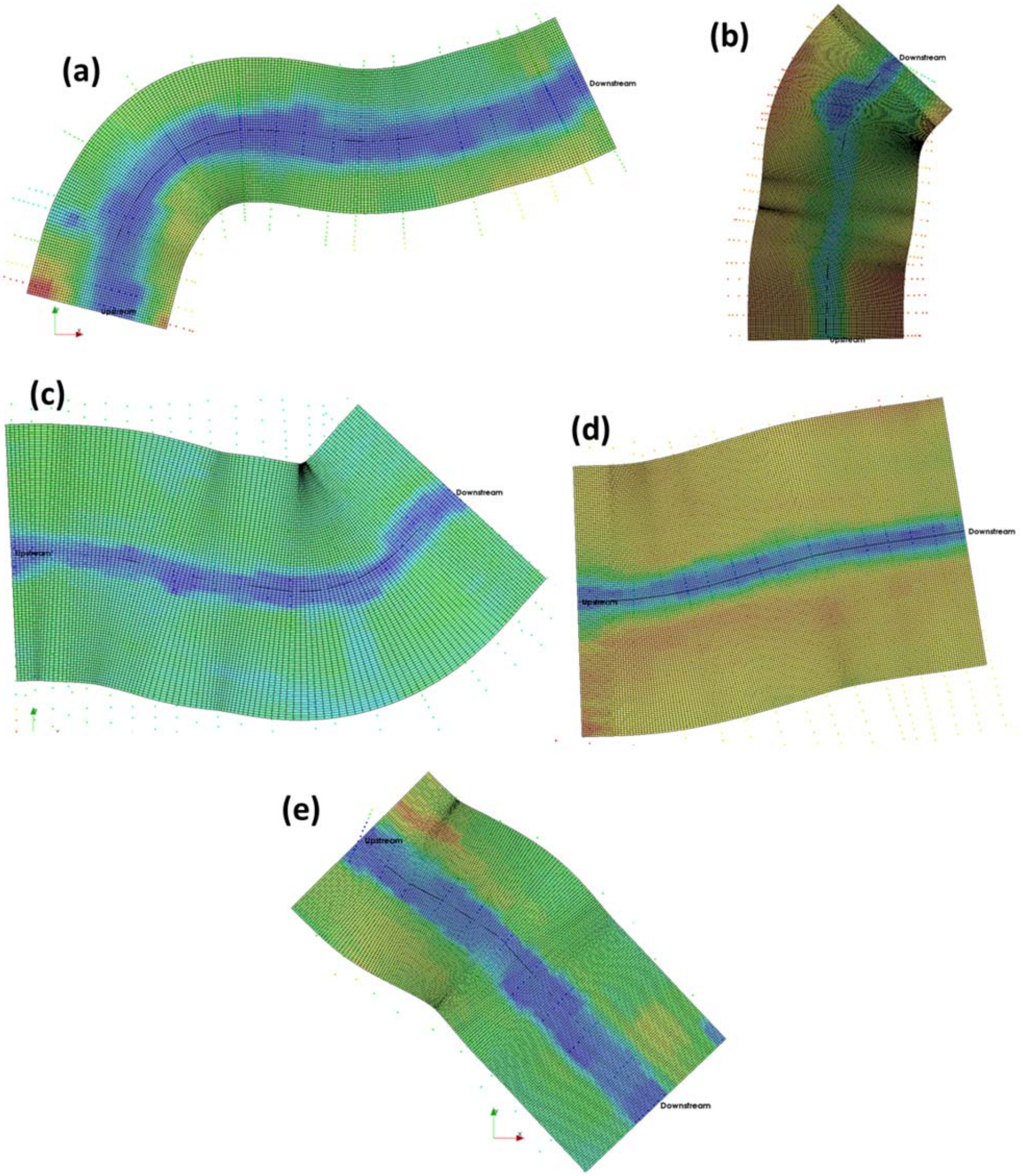

Figure 7-8 Generated mesh using the Flow and Sediment Transport with Morphological Evolution of Channels (FastMECH) at (a) 6033, (b) 6043, (c) 6103, (d), 6133, and (e) 6363

7.2.2 *Relative bed roughness*

The grain size distribution of channel beds was obtained from the Cities of Grand Prairie and Fort Worth to determine D_{84} and the relative bed roughness, z_o (Table 5-1). The physical bed roughness (D_{84}) was used for estimation of the relative bed roughness at the locations of interest.

7.3 Stage-discharge relation

7.3.1 *Rating curve estimation at the outlet of five selected catchment areas*

The stage-discharge relationships at the water level sensor locations were derived by solving Eqs.7-5 and 7-6. Given the prescribed downstream water level, Eq. 7-6 was solved iteratively to estimate the flow. This procedure was repeated over the desired range of water level. It was noted that all available grain size distributions were used for the stage-discharge relation derivation at each location. Figure 7-9 shows the derived rating curves at 6363 (Figure 7-5), using all available grain size distributions.

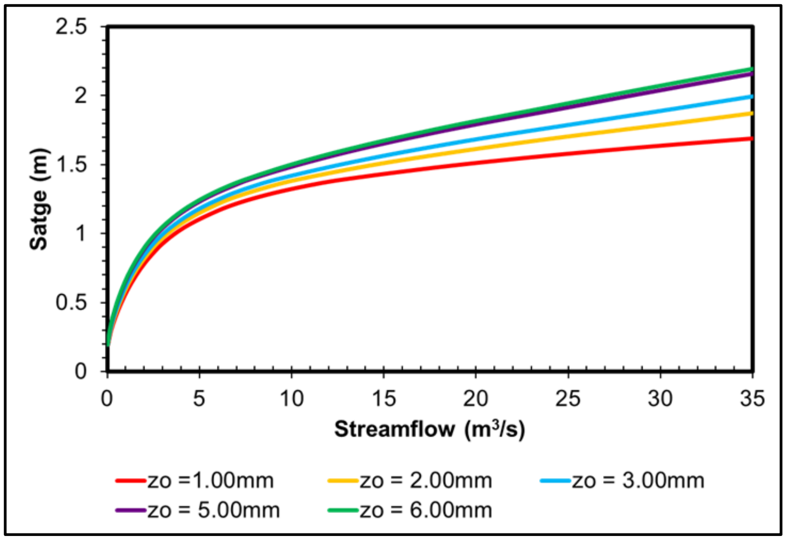

Figure 7-9 Estimated stage-discharge relation at 6363 using different relative bed roughness ranging from 1.00 to 6.00 mm

7.3.2 Evaluation of estimated rating curves

Due to the lack of observed streamflow, the derived rating curves were evaluated by the empirical rating curves derived from the observed stage vs. the HL-RDHM-simulated flow. Streamflow was simulated using the MPE estimates at 1/8-HRAP and 15-min resolution, in which the 1-HRAP 1-hr MPE estimates were uniformly disaggregated onto the 1/8-HRAP grid and into 15-min subintervals. The 15-min subinterval corresponded to the sampling interval of stage observations. The following stage-discharge relationship (Herschy 1993) was then fitted:

$$Q = c\ (h + a)^n \tag{7-7}$$

where Q denotes the discharge (m^3/s), h denotes the stage (m), c and n denote the parameters to be estimated, and a denotes the stage (m) at zero flow. The datum correction, a, represents the stage corresponding to zero discharge. To minimize the effects of resolution-dependent timing errors in estimating the parameters in Eq. 7-7), only the marginal statistics of mean, variance and maximum flow in the curve fitting were considered. The two independently-derived rating curves showed good agreement at all locations (Figure 7-10 toFigure 7-14), which provides confidence that the fluid mechanically-derived rating curves may be used for validation, calibration and real-time assimilation.

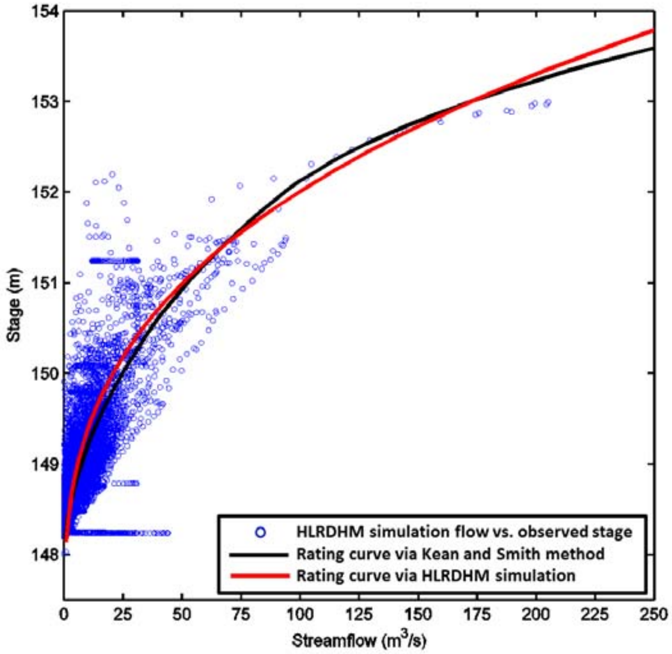

Figure 7-10 Rating curves derived via the Kean and Smith method and HLRDHM at 6033

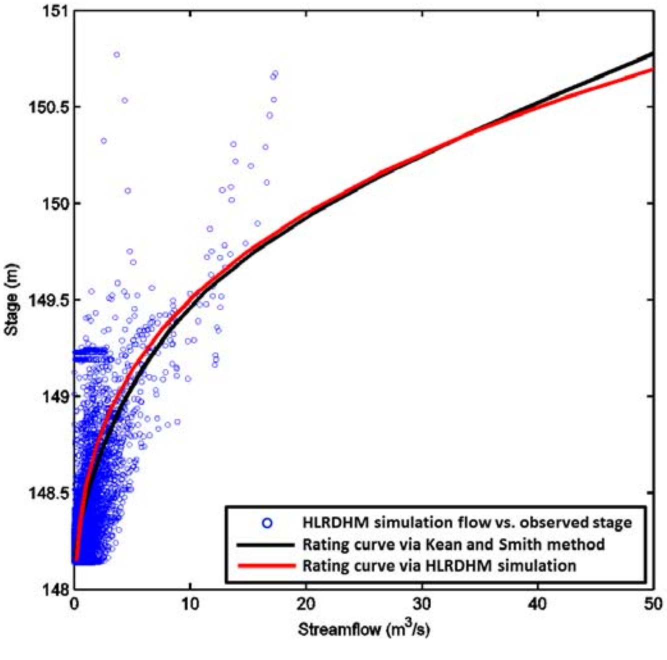

Figure 7-11 Rating curves derived via the Kean and Smith method and HLRDHM at 6043

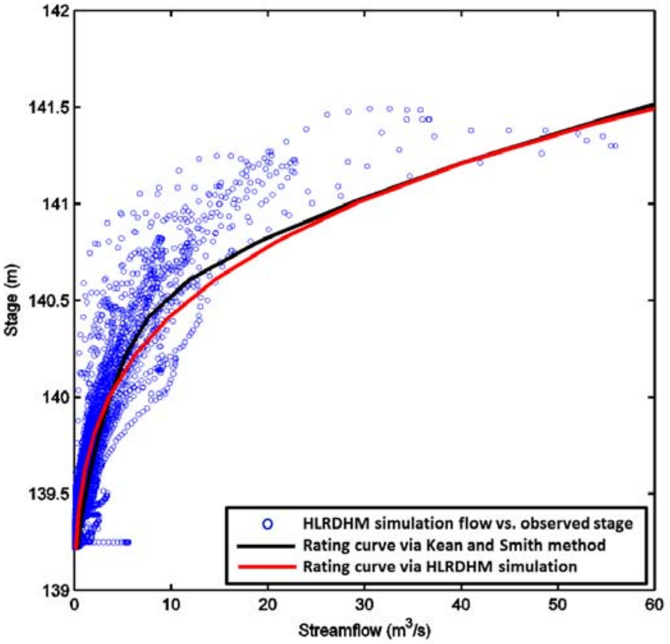

Figure 7-12 Rating curves derived via the Kean and Smith method and HLRDHM at 6103

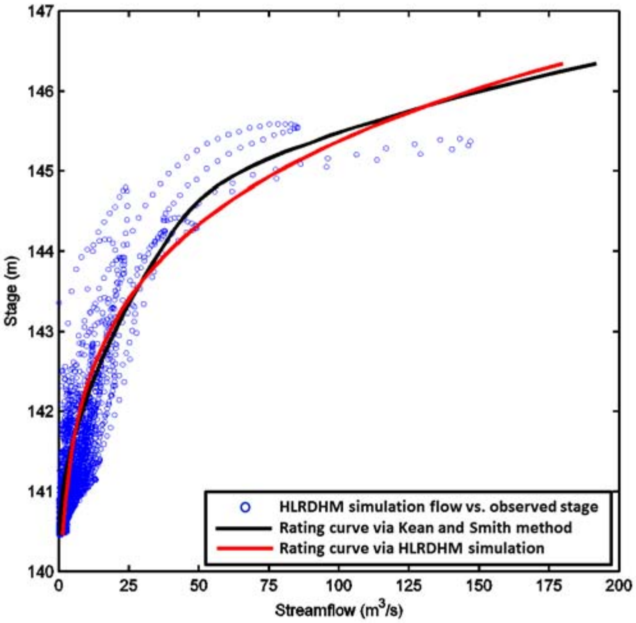

Figure 7-13 Rating curves derived via the Kean and Smith method and HLRDHM at 6133

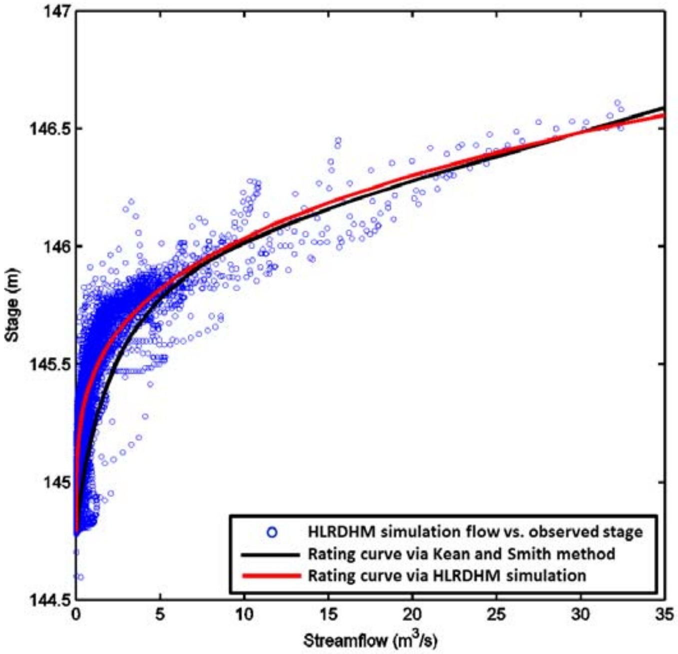

Figure 7-14 Rating curves derived via the Kean and Smith method and HLRDHM at 6363

Chapter 8 Evaluation of high-resolution hydrologic modeling

In this chapter, the sensitivity of simulated streamflow and soil moisture to the spatial resolution of a priori model parameters and rainfall input is assessed. Streamflow and soil moisture simulations were carried out based on Table 4-1. For the assessment, mean square error (MSE) decomposition was used.

MSE can be decomposed in three terms as follows (Murphy and Winkler 1987; Nelson et al. 2010):

$$MSE = \sum_{i=1}^{N}(f_n - o_n)^2 = (m_f - m_o)^2 + (\sigma_f - \sigma_o)^2 + 2\sigma_f\sigma_o(1-\rho) \qquad (8\text{-}1)$$

where f_n and o_n denote the n-th forecast and verifying observation, respectively; N denotes the number of pairs of forecast and verifying observation; m_f and m_o denote the mean of forecast and that of verifying observation, respectively; σ_f and σ_o denote the standard deviation of forecast and that of verifying observation, respectively; and ρ denotes the correlation between the forecast and the verifying observation.

For evaluation of the streamflow simulations, the streamflow observations, obtained from water level measurements via estimated rating curves, were used. The water level data for 2015 area was available from 10/09/2015. To quality control the data, the time series of all water level observations from 10/9/2015 to 12/31/2015 were visually examined, and two locations in Arlington and Grand Prairie (6043 and 6363, Figure 7-5) were selected. For evaluation of the soil moisture simulations, the soil moisture observations obtained from the CELB, Bridge, and Cemetery locations (Figure 6-4) were used.

8.1 Sensitivity analysis of simulated streamflow

Figure 8-1 toFigure 8-4 show the MSE decomposition of CASA- and MPE-forced simulations at 6043 and 6363. Comparisons between MSE decomposition of CASA-forced and MPE-forced simulations at 6043 and 6363 showed, using of CASA QPE improved the streamflow simulation at all resolutions of rainfall input and model parameters. However, the results did not show a clear relationship between the simulation accuracy and the resolutions of rainfall input and model parameters. This was due to the errors in QPEs and hydrologic models (rainfall-runoff routing), to which small catchments are susceptible. For simulations using CASA-forced rainfall input and model parameters, biases in mean and standard deviation are generally smaller for 1/16 HRAP resolution than for those of other resolutions (Figure 8-1 and Figure 8-2). However the strength of covariation did not change significantly for different resolutions.

Streamflow simulations forced by MPE showed larger sensitivity to the resolution of the rainfall input than to the model parameters. Given the small size of 6043 and 6363 (3.4 and 14.4 km^2, respectively), this may be due to the variations in catchment delineation. Among MPE-forced simulations, the 1/16 HRAP resolution showed slightly smaller biases in mean and standard deviation and lower strength of covariation than those of the other resolutions, except at the resolution of 1/8HRAP for catchment 6363.

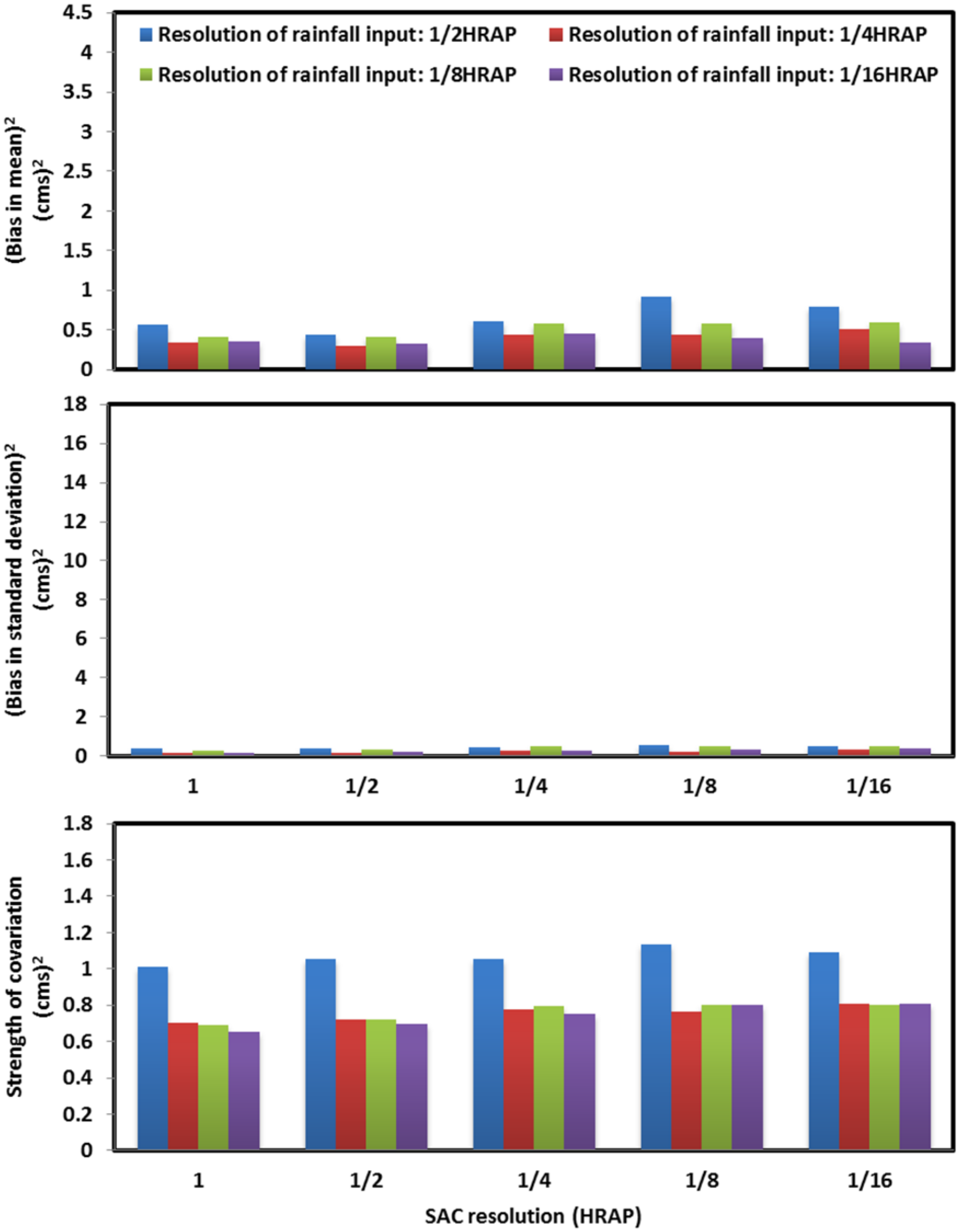

Figure 8-1 MSE decomposition of CASA-forced streamflow simulation at 6043

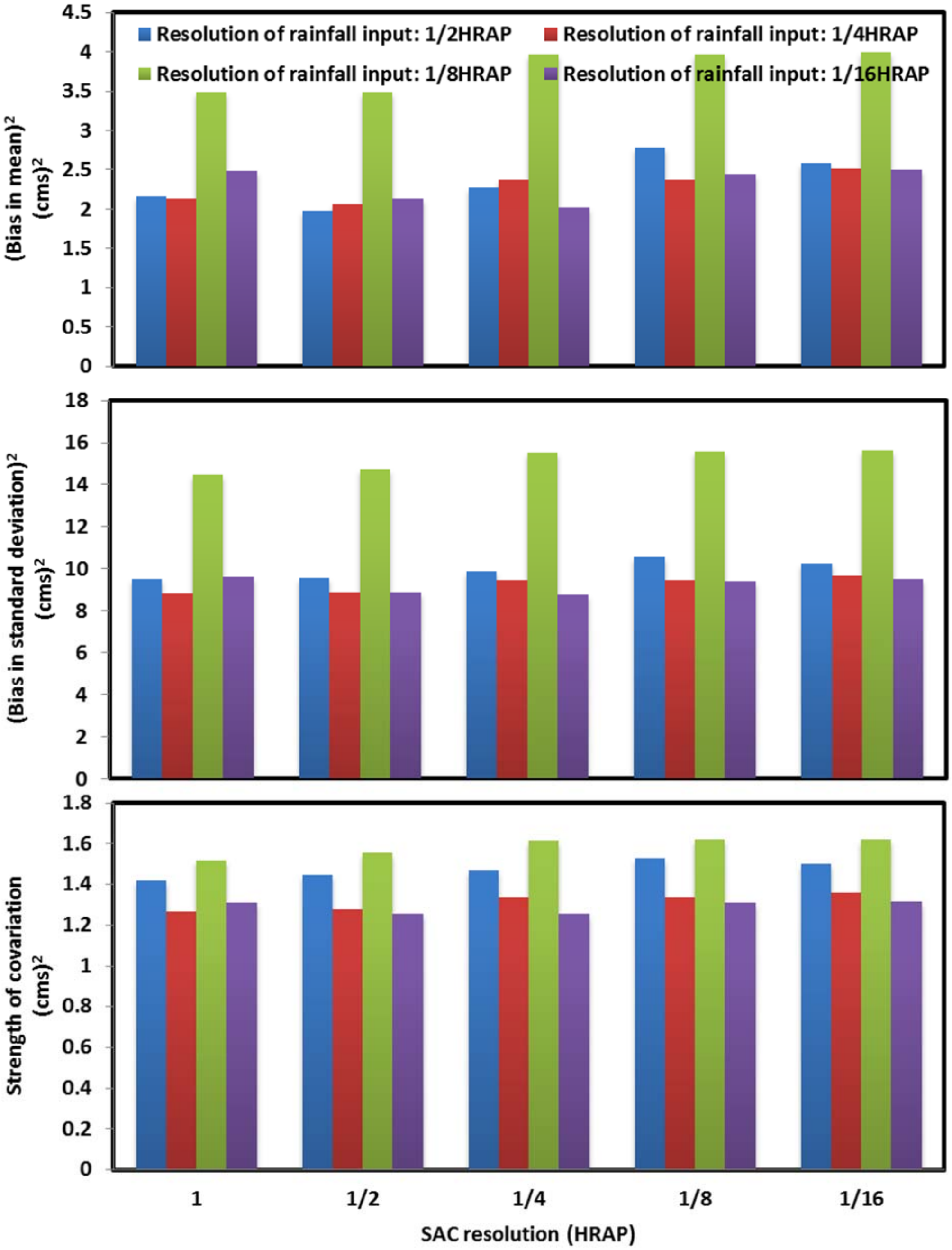

Figure 8-2 MSE decomposition of MPE-forced streamflow simulation at 6043

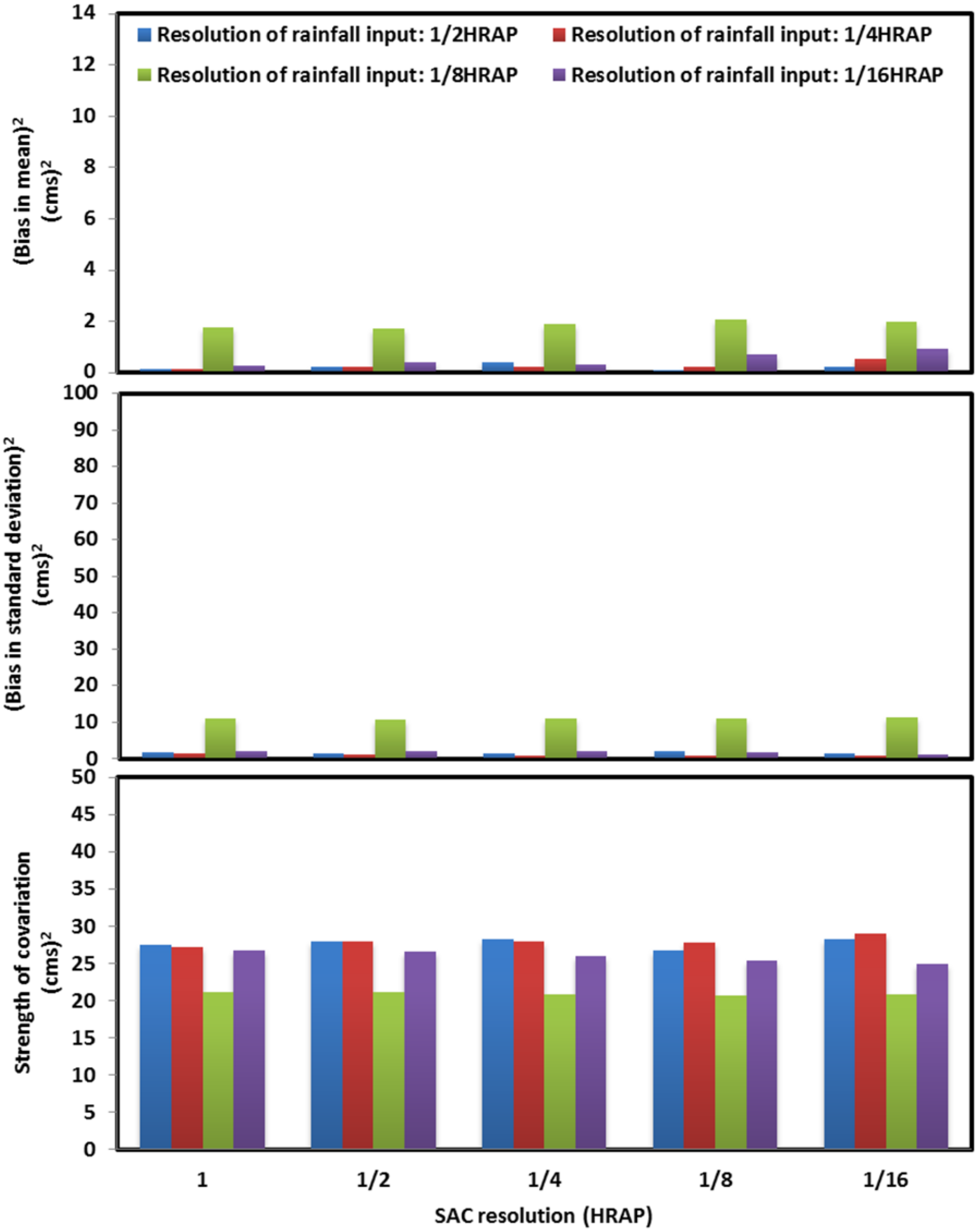

Figure 8-3 MSE decomposition of CASA-forced streamflow simulation at 6363

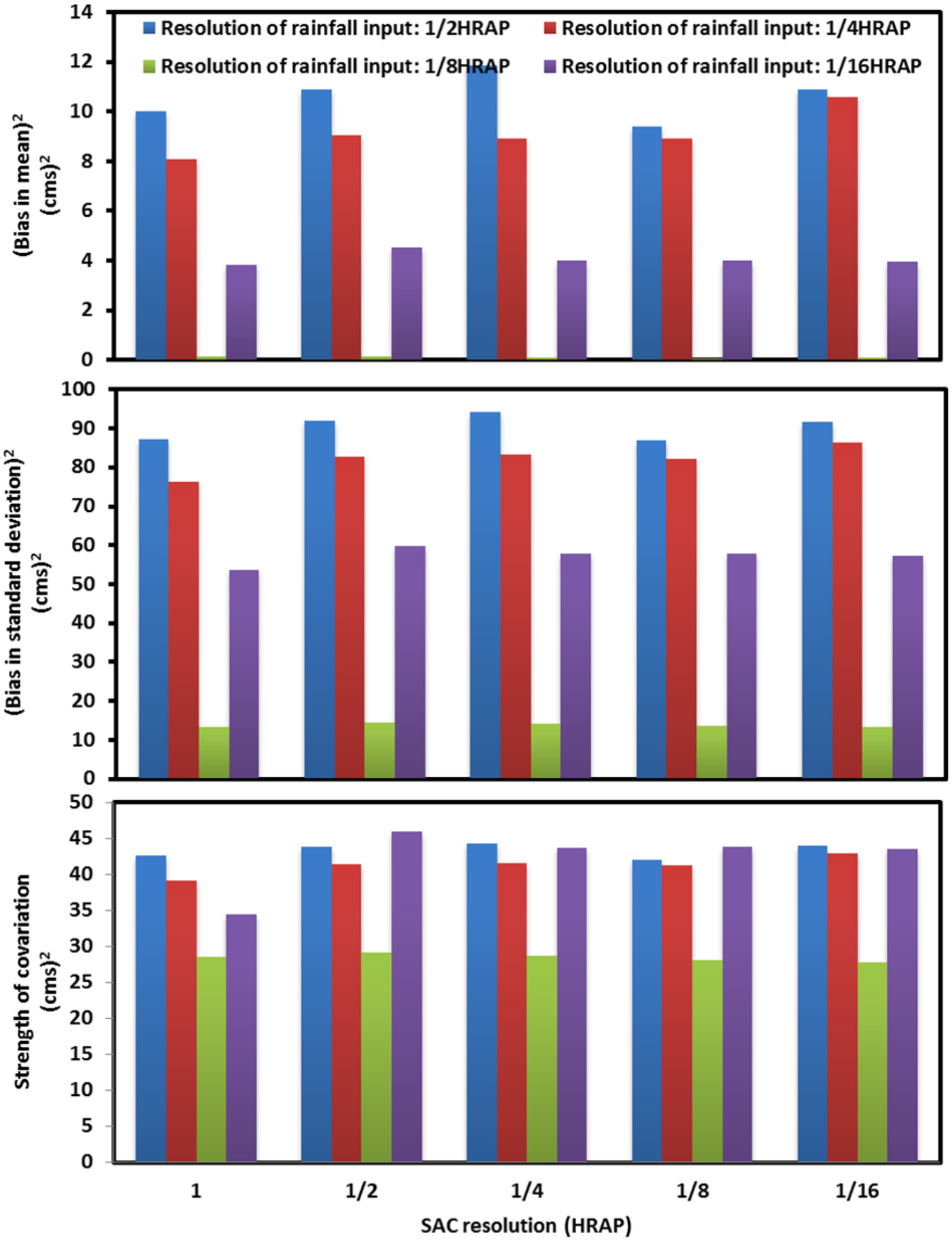

Figure 8-4 MSE decomposition of MPE-forced streamflow simulation at 6363

Comparison of the time series of CASA-forced and MPE-forced streamflow simulations with the streamflow observations showed that there was a significant difference between the MPE-forced simulation and streamflow observations for the first rainfall event within the evaluation period (Oct. 22, 2015, see Appendix B). This may be due to the long dry period prior to the rainfall event. Based on MPE-forced simulation, the soil reached the saturated condition much faster than the CASA-forced simulation (Figure 8-5). The figure also shows that the soil became saturated within a few hours after the rain began. While based on CASA-forced simulation, the soil reached the saturated condition after nearly one day, when the rainfall was lighter. For other rainfall events, due to the soil moisture condition, the observed and simulated streamflows were in better agreement.

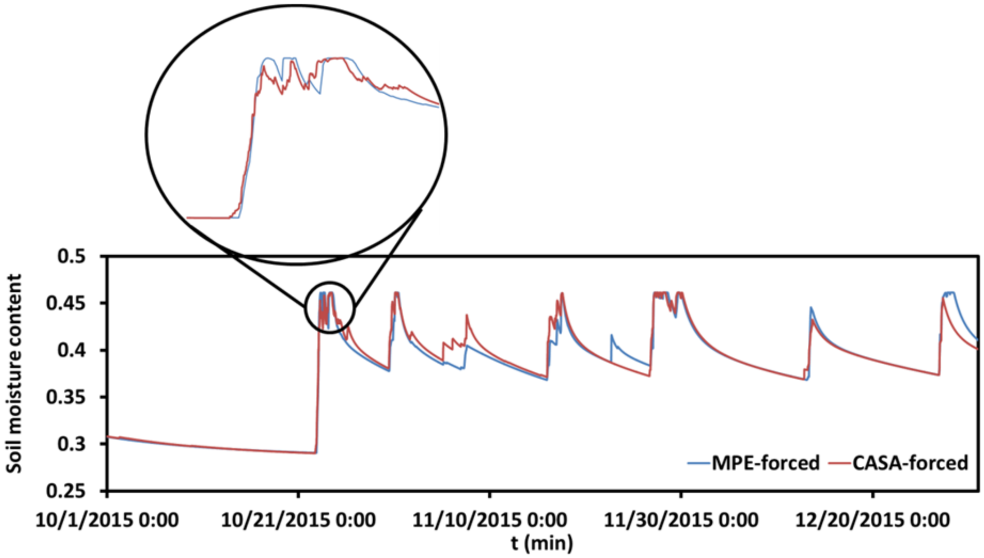

Figure 8-5 Spatially-averaged soil moisture content in 6363

8.2 Sensitivity analysis of simulated soil moisture

Figure 8-6 toFigure 8-11 show the MSE decomposition of CASA-forced and MPE-forced soil moisture simulations at Bridge, CELB, and Cemetery locations at the depth of 5 cm. The MPE-forced simulation shows smaller biases in mean and standard deviation and lower strength of covariation than the CASA-forced simulation at all three locations. The simulated soil moisture did not improve with an increase in the a priori model parameters and rainfall input; therefore, no clear relationship was seen between simulation accuracy and the resolutions. SAC-HT, in general, was not able to simulate the soil moisture with accuracy, which may be due to errors in QPEs, model physics, and/or lack of soil information.

Figure 8-6 and Figure 8-7 show that MSE decomposition for rainfall resolution of 1/2HRAP is larger than the MSE decomposition of rainfall resolution at 1/4, 1/8 and 1/16 HRAP resolution at the Bridge location. The main reason is presumably due to a large difference between the percentage of impervious area at 1/2HRAP resolution and the percentage of impervious areas at 1/4, 1/8 and 1/16 HRAP resolutions at this location. Based on the impervious cover maps of 1/2, 1/4, 1/8 and 1/16 HRAP resolutions, the PCTIMs are 42%, 56%, 57% and 70%, respectively.

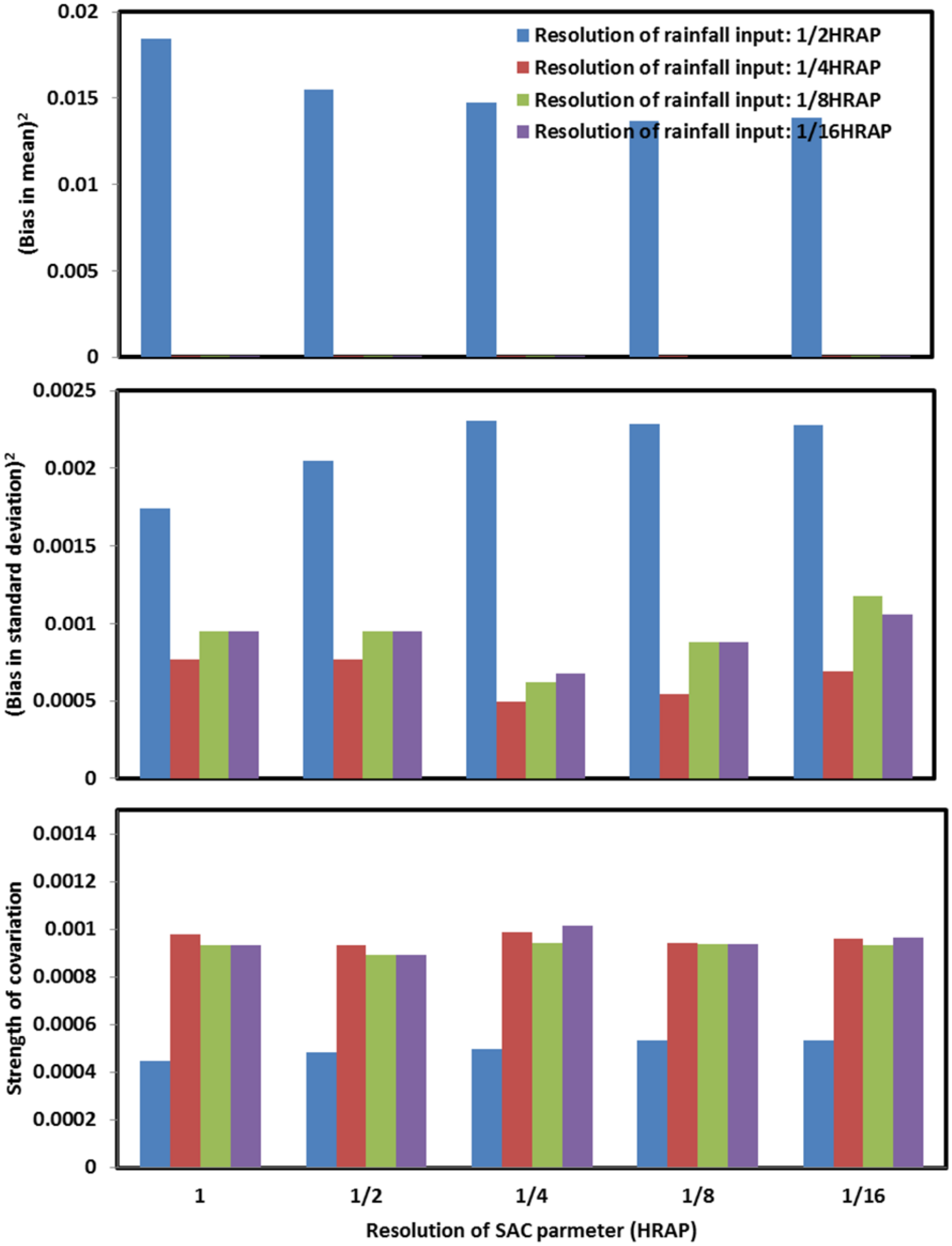

Figure 8-6 MSE decomposition of CASA-forced soil moisture simulation at Bridge location at D = 5 cm

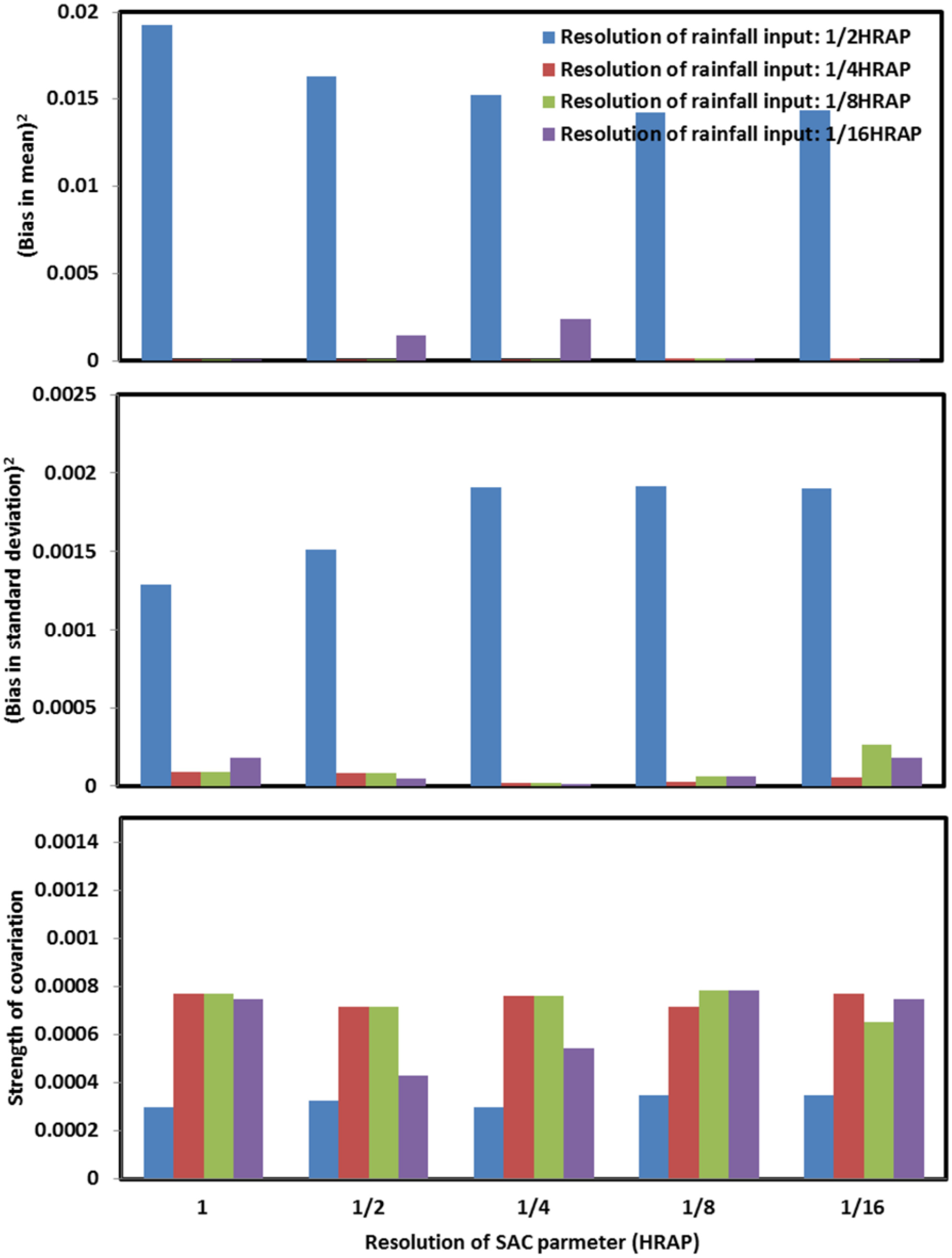

Figure 8-7 MSE decomposition of MPE-forced soil moisture simulation at Bridge location at D = 5 cm

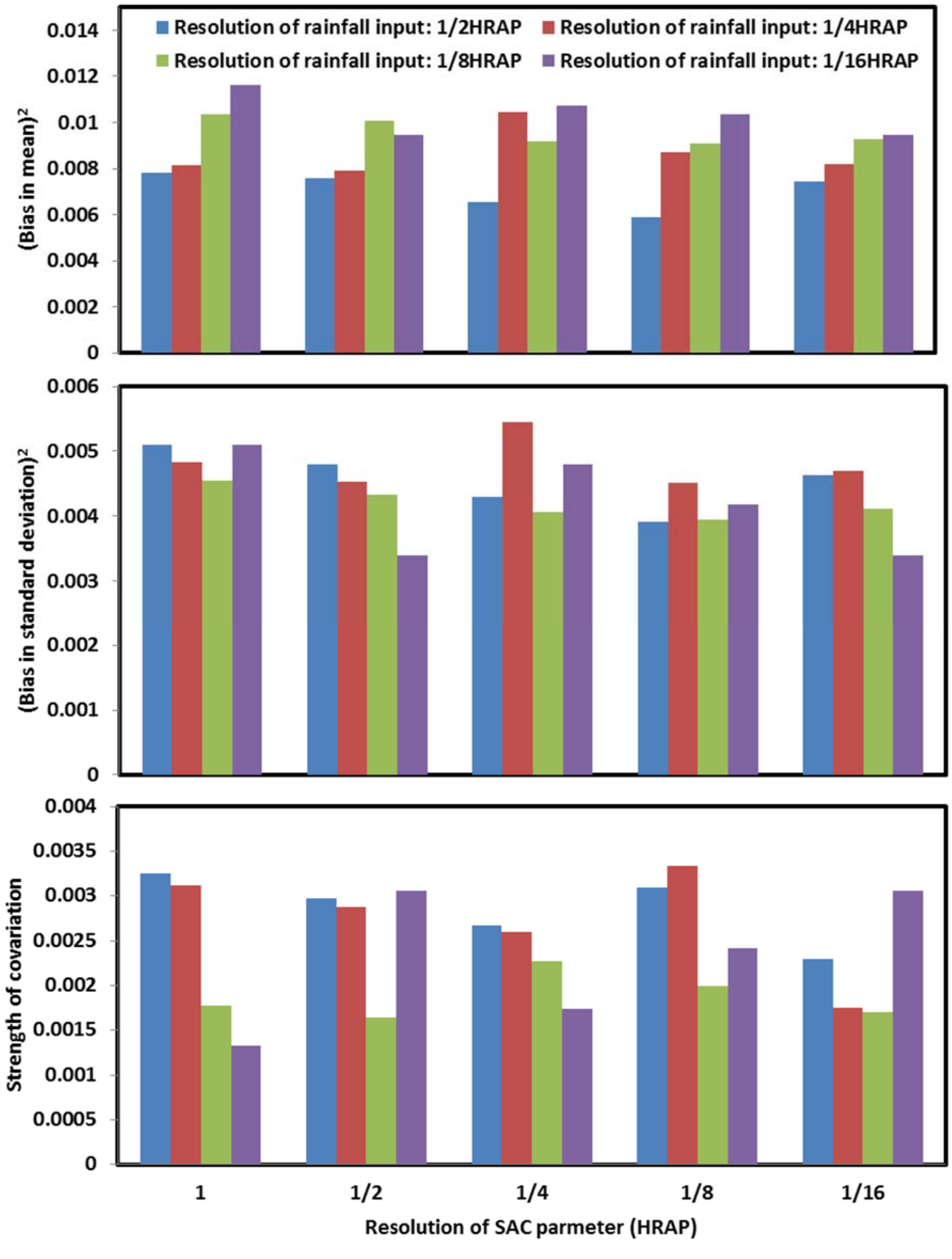

Figure 8-8 MSE decomposition of CASA-forced soil moisture simulation at CELB location at D = 5 cm

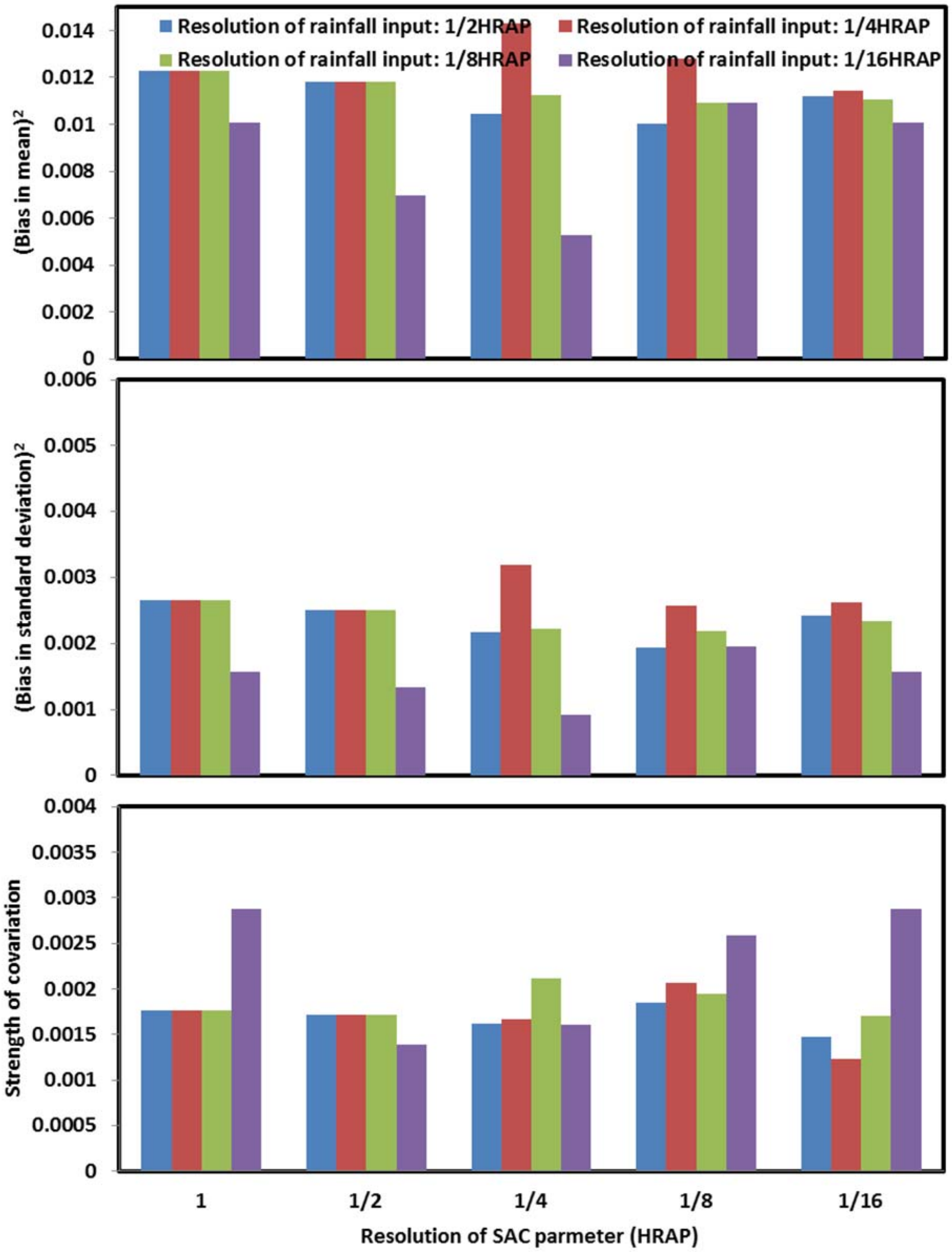

Figure 8-9 MSE decomposition of MPE-forced soil moisture simulation at CELB location at D = 5 cm

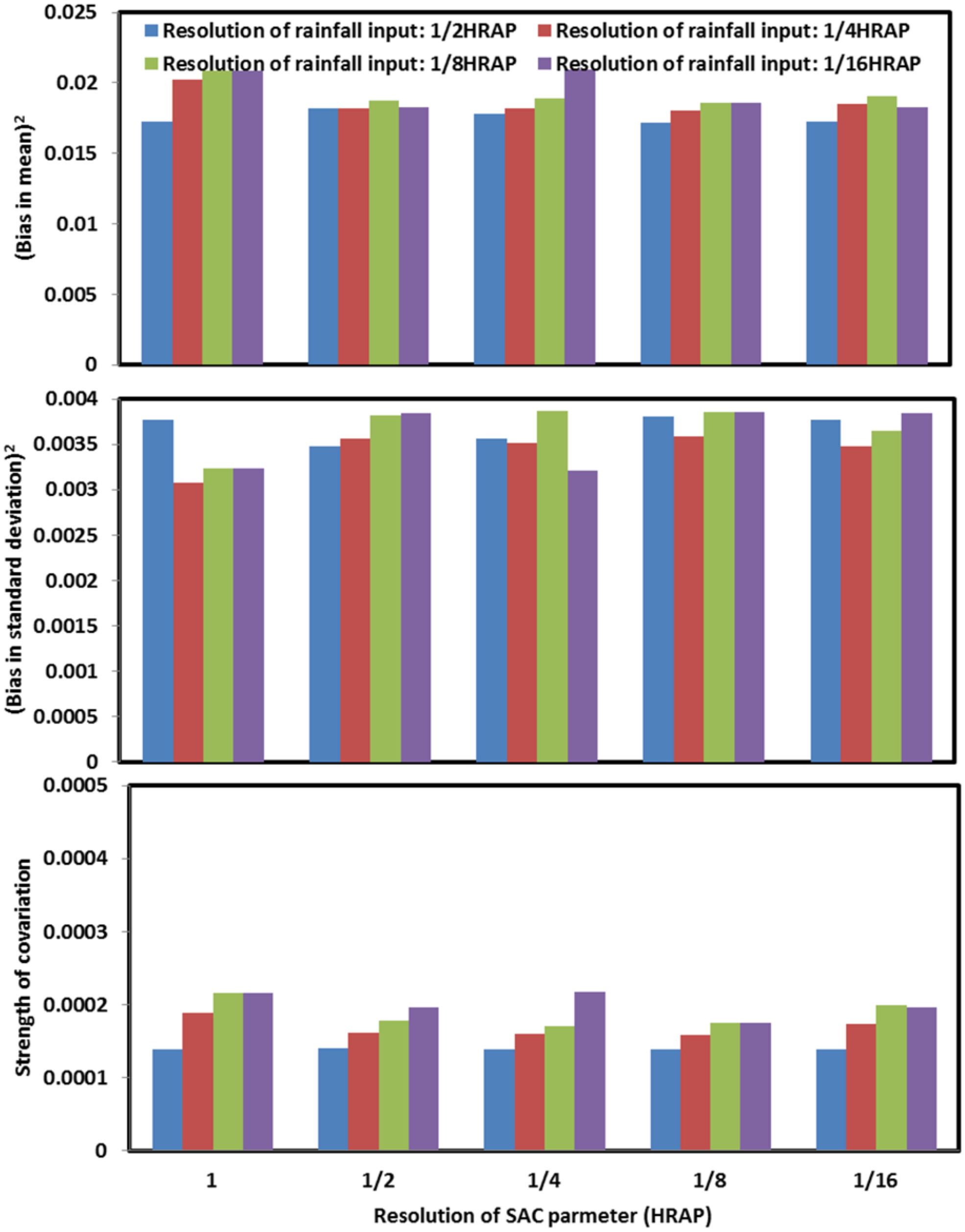

Figure 8-10 MSE decomposition of CASA-forced soil moisture simulation at Cemetery location at D = 5 cm

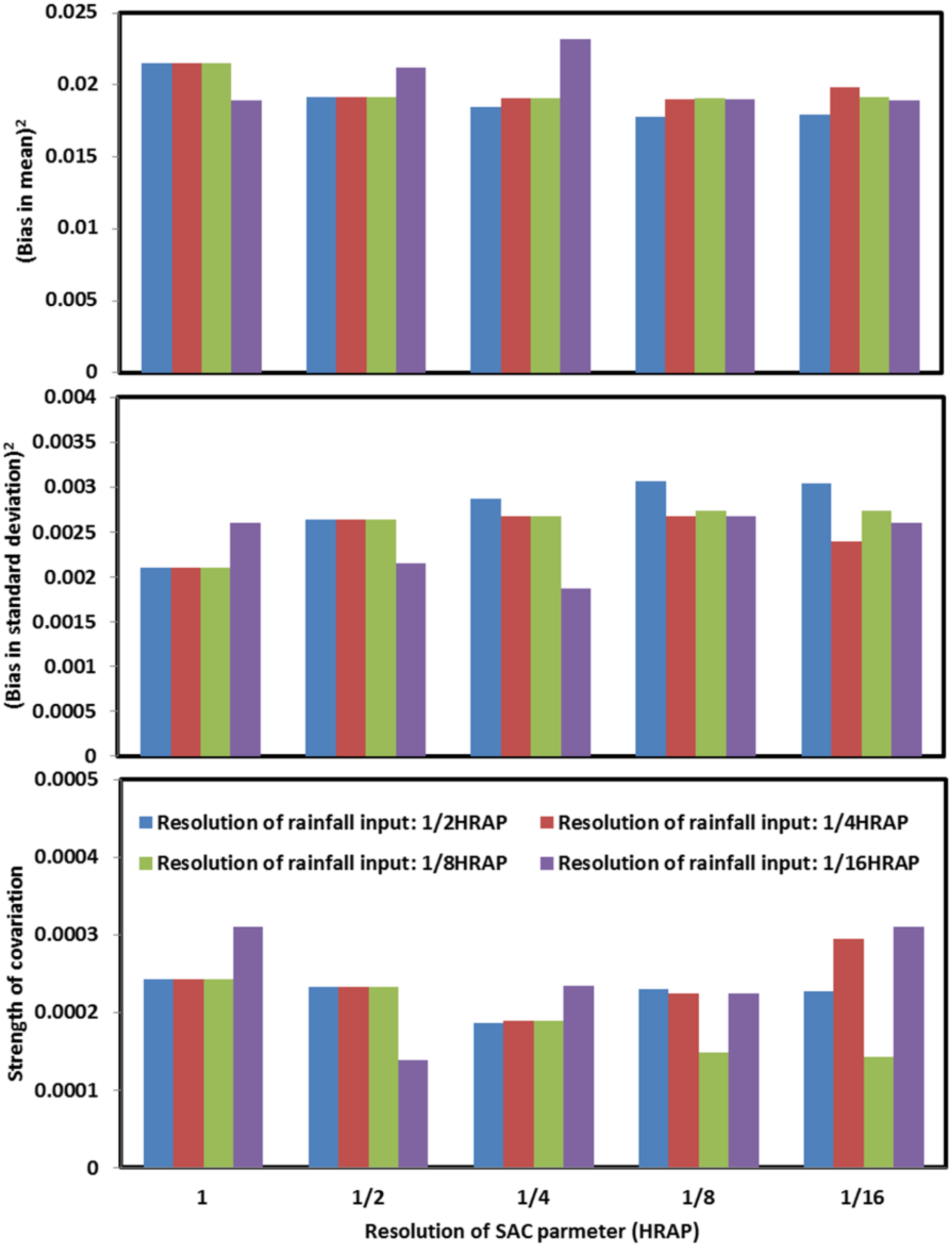

Figure 8-11 MSE decomposition of MPE-forced soil moisture simulation at Cemetery location at D = 5 cm

Chapter 9 Impact of land cover changes on streamflow response

Three sets of a priori SAC parameters, derived from SSURGO data and NLCD2001, NLCD2006 and NLCD2011 at 1/16HRAP resolution, were used for the streamflow simulation of the modeling domain to investigate the impact of land cover changes on streamflow simulation. Using MPE-forced rainfall, the simulated streamflow was analyzed for the five urban catchments (Figure 7-5).

The rainfall events of 2015 were isolated, and the corresponding flood hydrograph was extracted for each rainfall event. Three measures, percentage of relative difference of simulated peak flow (PRDP); percentage of relative difference of simulated runoff volume (PRDV); and percentage of difference of time-to-peak relative to the time-to-peak of the catchment (PRDT) as a function of total rainfall were considered for the assessments. The percentage of relative difference of simulated peak flow, runoff volume, and time-to-peak are given by:

$$PRDP = \frac{Peak\ flow_{i+1} - Peak\ flow_{i}}{Peak\ flow_{i+1}} \times 100 \tag{9-1}$$

$$PRDV = \frac{Volume\ flow_{i+1} - Volume\ of\ flow_{i}}{Volume\ of\ flow_{i+1}} \times 100 \tag{9-2}$$

$$PRDT = \frac{time-to-peak_{i} - time-to-peak_{i+1}}{time-to-peak} \times 100 \tag{9-3}$$

where *i* represents the year for which the a priori SAC parameters are available.

Land cover changes from 2001 to 2011 at these five catchments were analyzed prior to assessing the impact of land cover changes on the simulated streamflow.

9.1 Analysis of the PCTIM maps at five subcatchment areas in the modeling domain

Examination of the 1/16HRAP resolution (Figure 9-1) at the five catchment locations showed that the fractional impervious area varied between 0.5% and 98%.

Analysis of the percentage of impervious areas for each catchment was carried out by using empirical cumulative distribution functions (ECDF) of the percent of impervious areas at each catchment (Figure 9-2 toFigure 9-6).

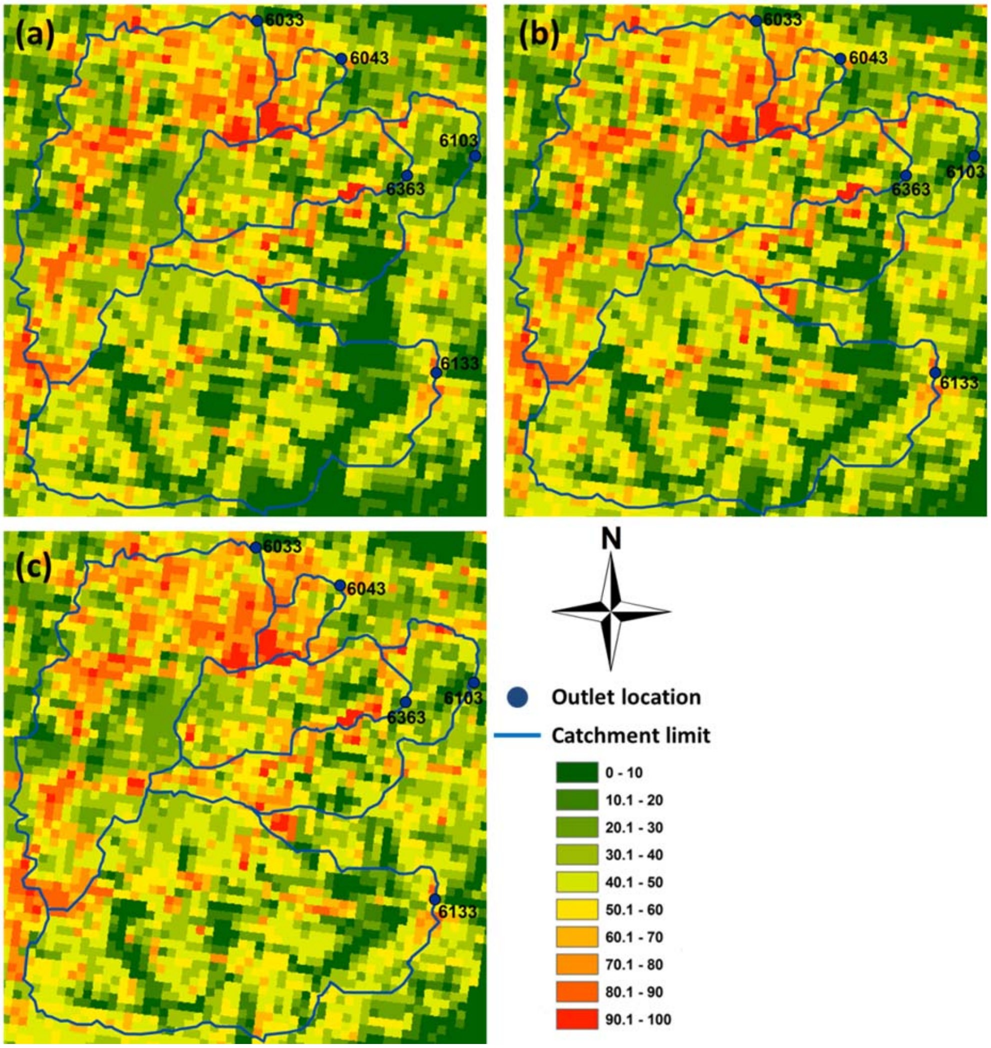

Figure 9-1 Percent of impervious area at five catchment areas within the modeling domain based on NLCD2001 (a), NLCD2006 (b) and NLCD2011 (c)

Figure 9-2 shows that the percent of impervious area varied between 20% to 80% percent at this catchment. The land cover changed more between 2006 and 2011 than between 2001 and 2006. Also the figure shows that the land cover changes between 2006 and 2011 was larger than land cover changes from 2001 to 2006. Figure 9-1 shows that significant land cover changes at 6033 occurred close to the outlet, after construction of a sport complex and its parking lots. The land cover changes reached 60 percent at this location.

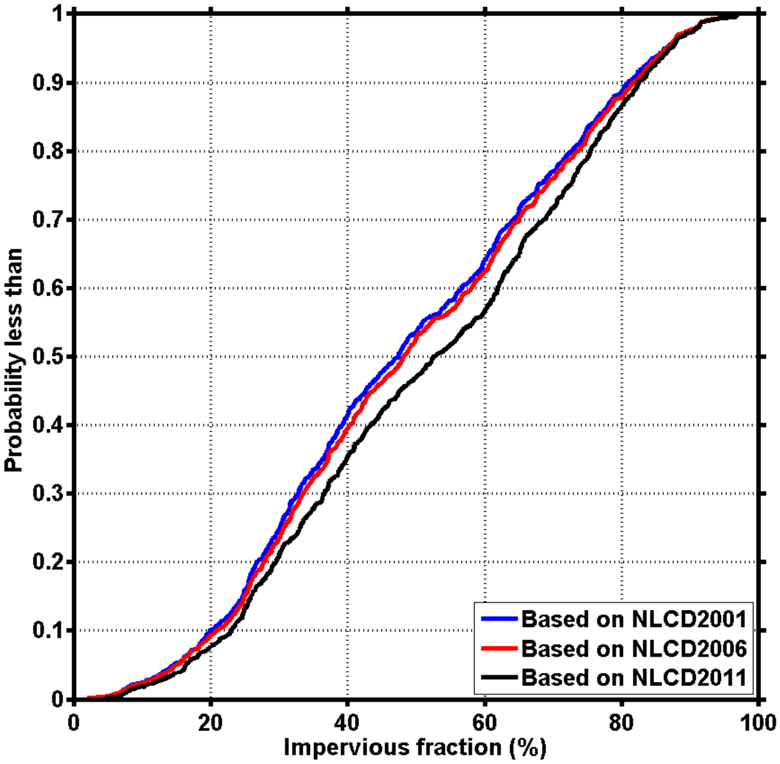

Figure 9-2 Empirical cumulative probability distribution function (ECDF) of impervious fractions in 6033

Catchment 6043 is the smallest and most impervious catchment of the selected catchments. Figure 9-3 shows that the land cover did not change significantly from 2001 to 2011 at 6043, because ECDFs based on NLCD2001 and NLCD 2011 are close to one another. The largest difference between ECDFs of 2001 and 2011, which is between 60 to 85 percent (Figure 9-3), occurred close to the outlet (Figure 9-1).

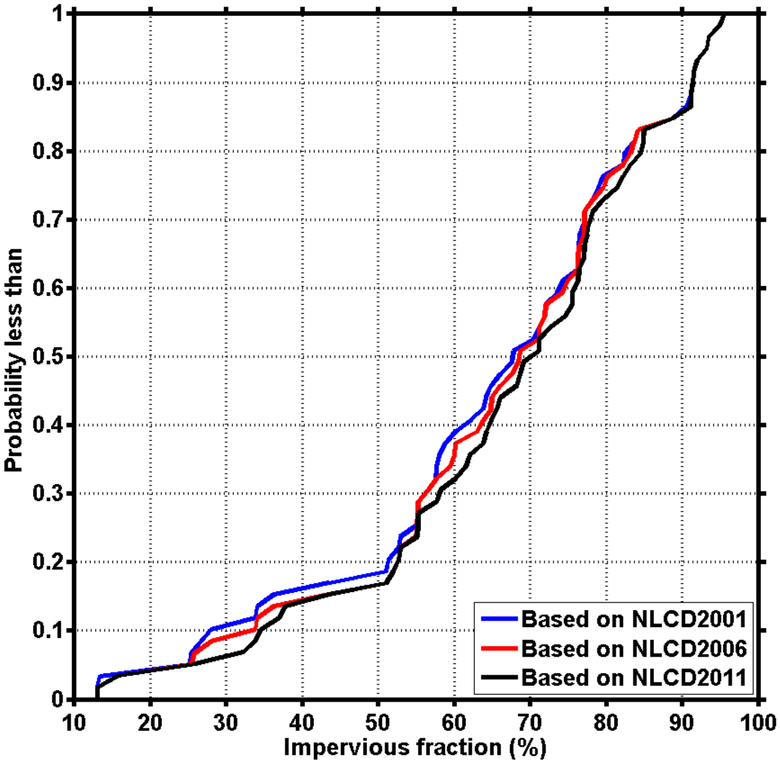

Figure 9-3 Empirical cumulative probability distribution function (ECDF) of impervious fractions in 6043

The spatially-averaged impervious fractions, based on NLCD 2001, NLCD 2006, and NLCD 2011 for 6103, are 40.21%, 41.97%, and 45.58%, respectively, showing 11.8% land cover changes from 2001 to 2011. Figure 9-4 shows that the largest difference between land covers of 2001 and 2011 occurred between 0 to 60 percent at

6103, and smaller land cover changes can be seen between 60 to 80 percent. Figure 9-1 shows that most of changes occurred in the midstream and downstream of the catchment.

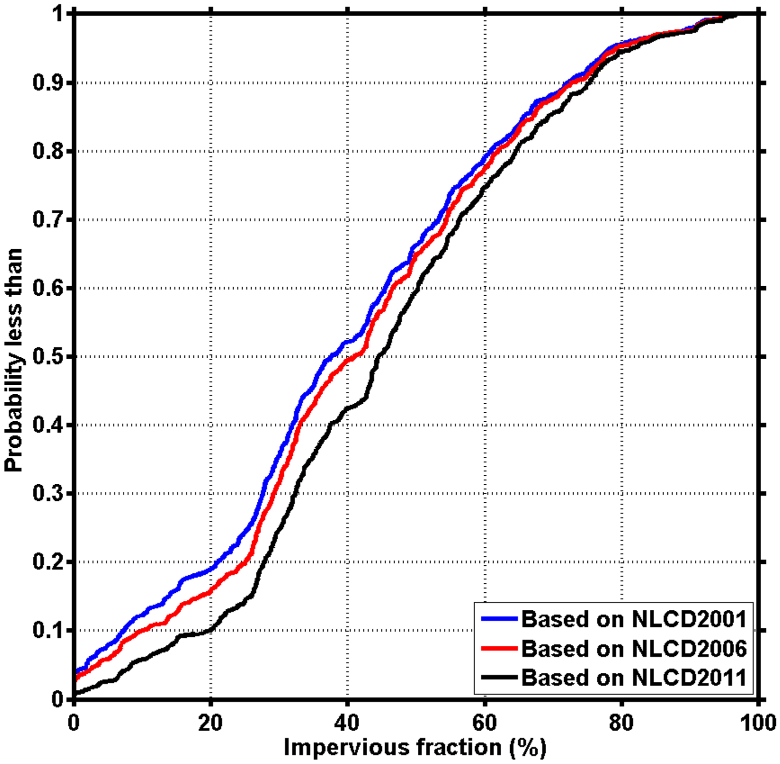

Figure 9-4 Empirical cumulative probability distribution function (ECDF) of impervious fractions in 6103

Catchment 6133, with 54.6 km^2, is the largest of the selected catchments. The spatially-averaged impervious area in this catchment based on NLCD 2001, NLCD 2006, and NLCD 2011 are 32.9, 35.2 and 38.4 percent respectively. The land cover changes from 2001 to 2011 at 6133 were 16.7%. Figure 9-6 shows that the largest land cover changes occurred between 0 to 60 percent, and smaller land cover changes occurred between 60 to 78 percent, approximately.

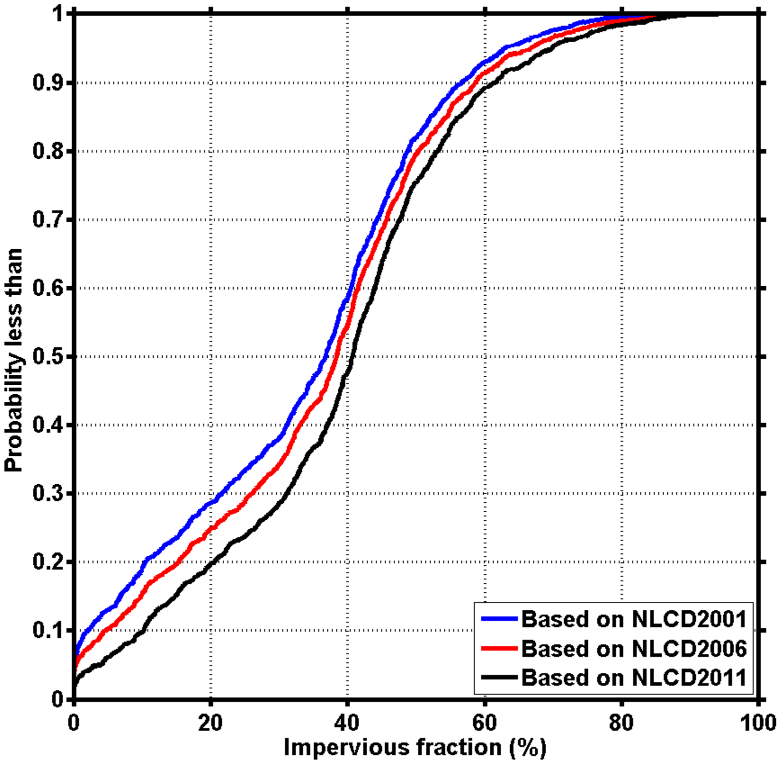

Figure 9-5 Empirical cumulative probability distribution function (ECDF) of impervious fractions in 6133

The spatially-averaged impervious areas at 6363 from NLCD 2001, NLCD 2006, and NLCD 2011 are 42.85%, 44.76%, and 47.29%, respectively, showing 10.36% land cover changes from 2001 to 2011. Figure 9-6 shows that the largest land cover changes occurred between 10 to 60 percent, and smaller land cover changes occurred between 60 to 78 percent, approximately. Also Figure 9-6 shows that increasing the impervious fraction between 25 to 30 percent from 2001 to 2006 were larger than that of 2006 and 2011.

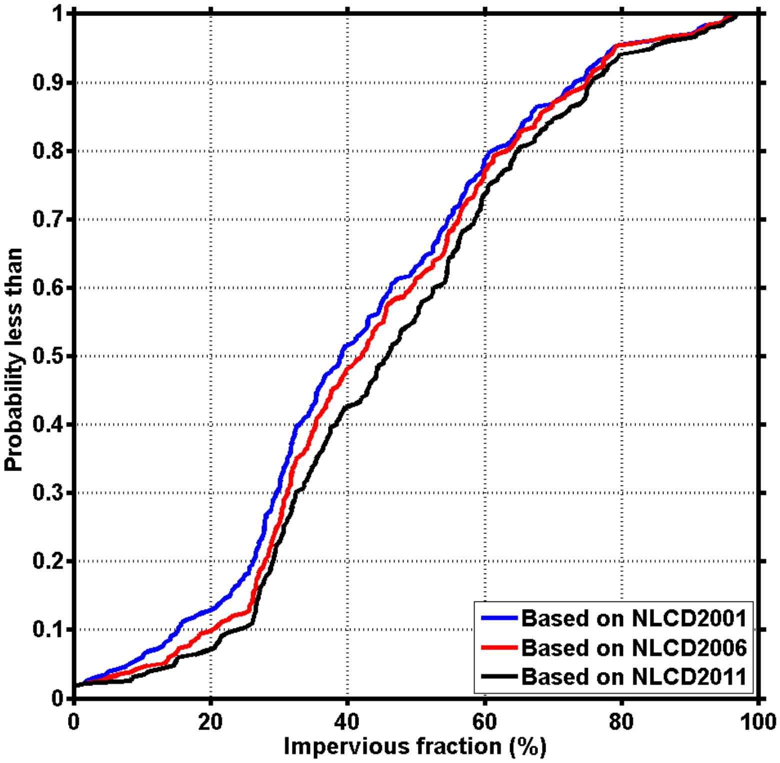

Figure 9-6 Empirical cumulative probability distribution function (ECDF) of impervious fractions in 6363

9.2 Impact of land cover changes on peak flow

After completing the streamflow simulation, by using a priori SAC parameters of 2001, 2006, and 2011, the rainfall events of 2015 were isolated and the corresponding flood hydrographs in the selected catchments were extracted. Time-to-peak, runoff volume, and peak flow of the flood hydrographs were then estimated. The number of rainfall events and flood hydrographs at 6033, 6043, 6103, 6133, and 6363 were 38, 43, 41, 40, and 41, respectively.

The impact of land cover changes on peak flow showed approximately the same pattern, but with different magnitudes in five urban catchments (Figure 9-7 toFigure 9-11).

The results showed that the impact of land cover changes on peak flow at 6103 and 6133 was greater than the impact of land cover changes on peak flow at 6033, 6043 and 6363. This is due to the significant land cover changes from 2001 to 2011 at 6103and 6133. The relative difference of peak flow between 2001 and 2011 for rainfall depths greater than 100 mm in five urban catchments was close to zero, indicating that the pervious areas in these catchments, for rainfall events greater than 100 mm, saturated and performed as impervious areas. Therefore, there was no significant difference between peak flows of simulated streamflow based on NLCD 2001, NLCD 2006, and NLCD 2011 for rainfall events greater than 100 mm.

Figure 9-7 shows the percent of relative difference of peak flow in 6033. The figure shows that the percent of relative difference between peak flows of 2001 and 2006 is greater than that of 2006 and 2011, which may due to the land cover changes at a limited area in 6033. While the land cover changes from 2001 to 2006 is more scattered.

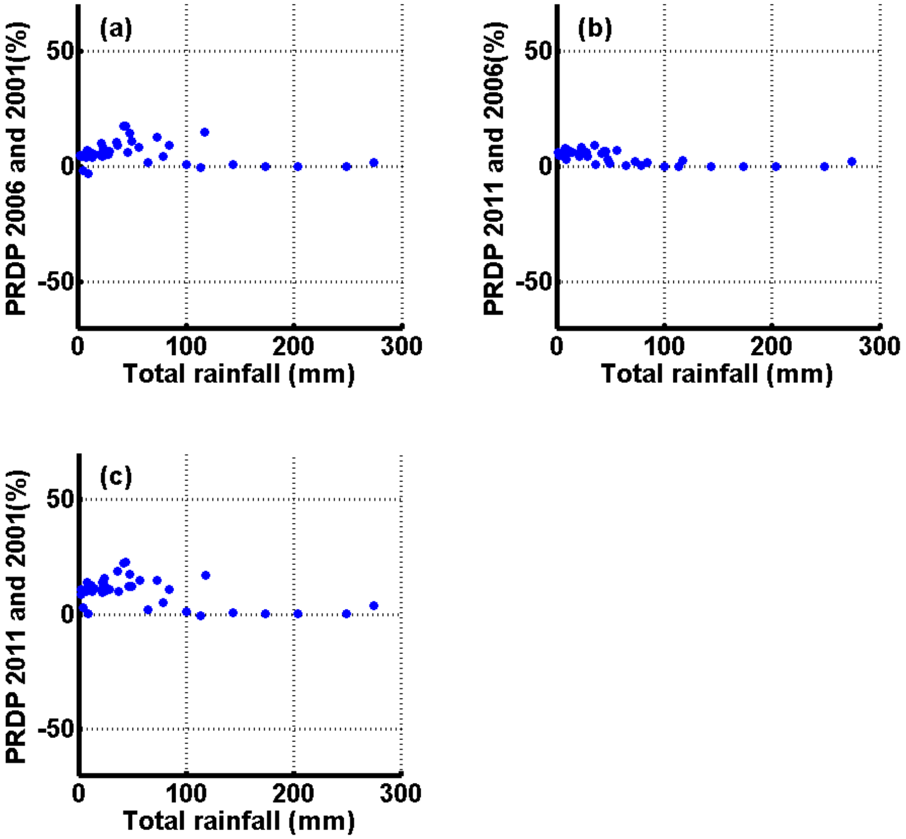

Figure 9-7 (a) Percent of Relative Difference of Peak flow (PRDP) of 2006 and 2001, (b) PRDP of 2011 and 2006, and (c) PRDP of 2011 and 2001 at 6033

Figure 9-8 shows the percent of relative difference of peak flow at 6043. The figure shows that there is no significant difference between PRDP of 2001 and 2006 and PRDP of 2006 and 2011, due to small land cover changes between these years. Figure 9-8c shows that the peak flows of 2001 are not significantly different with the peak flows of 2011, except in a rainfall events, in which the relative difference between peak flow of 2001 and 2011 is not more than 15 percent.

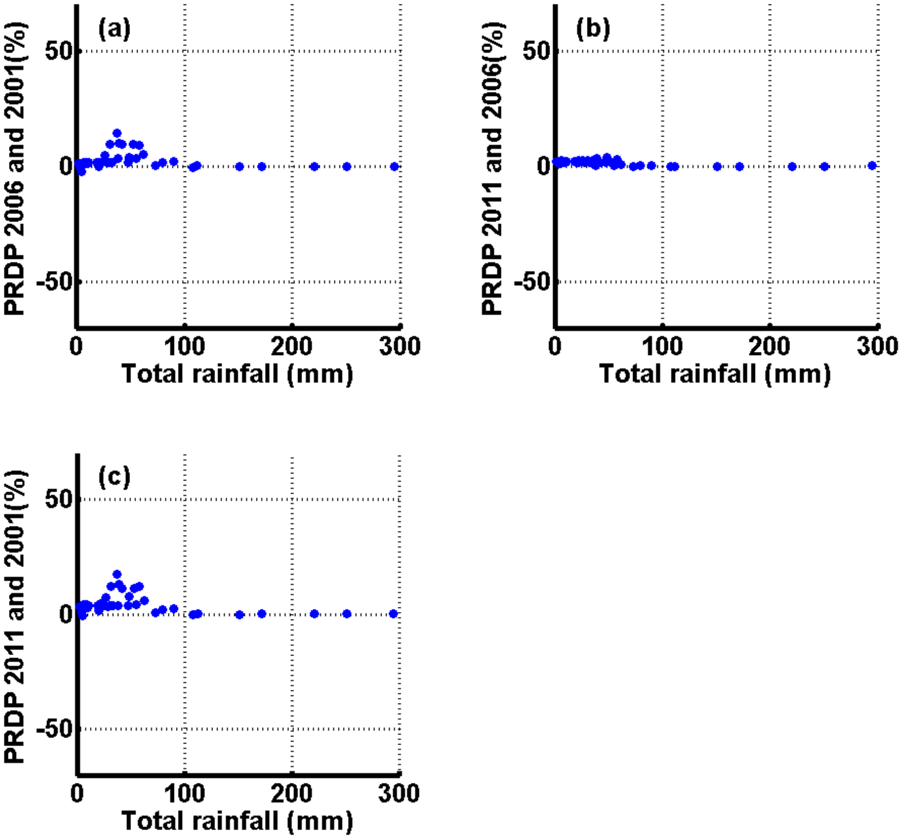

Figure 9-8 (a) Percent of Relative Difference of Peak flow (PRDP) of 2006 and 2001, (b) PRDP of 2011 and 2006, and (c) PRDP of 2011 and 2001 at 6043

Figure 9-9 shows that there is a small difference between the percent of relative difference of peak flow of 2001 and 2006 and that of 2006 and 2011, which may be due to the similar land cover changes between 2001 and 2006 and 2006 and 2011 (Figure 9-4). Figure 9-9c shows significant changes between peak flows of 2001 and 2011, which is due to the significant land cover changes between 2001 and 2011 at 6103.

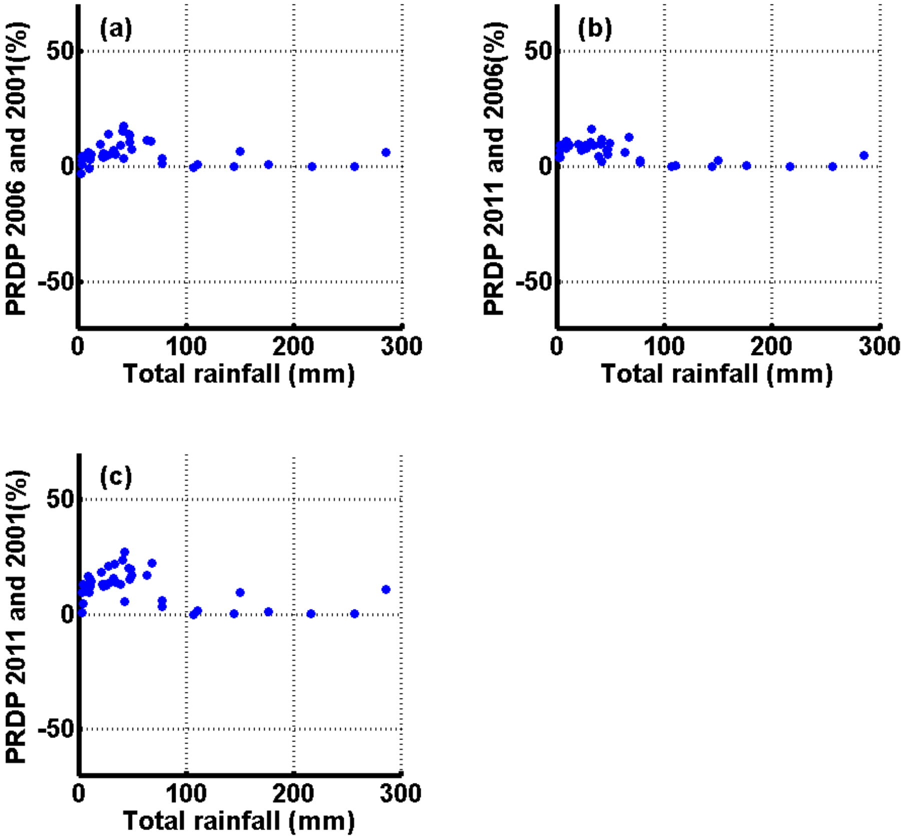

Figure 9-9 (a) Percent of Relative Difference of Peak flow (PRDP) of 2006 and 2001, (b) PRDP of 2011 and 2006, and (c) PRDP of 2011 and 2001at 6103

Significant differences between land cover changes from 2001 and 2011 led to significant changes in peak flows from 2001 to 2011 for rainfall events less than 100 mm (Figure 9-10). Also the figure shows that for rainfall events greater than 100 mm the percent of relative difference of peak flow is close to zero, except for one rainfall event.

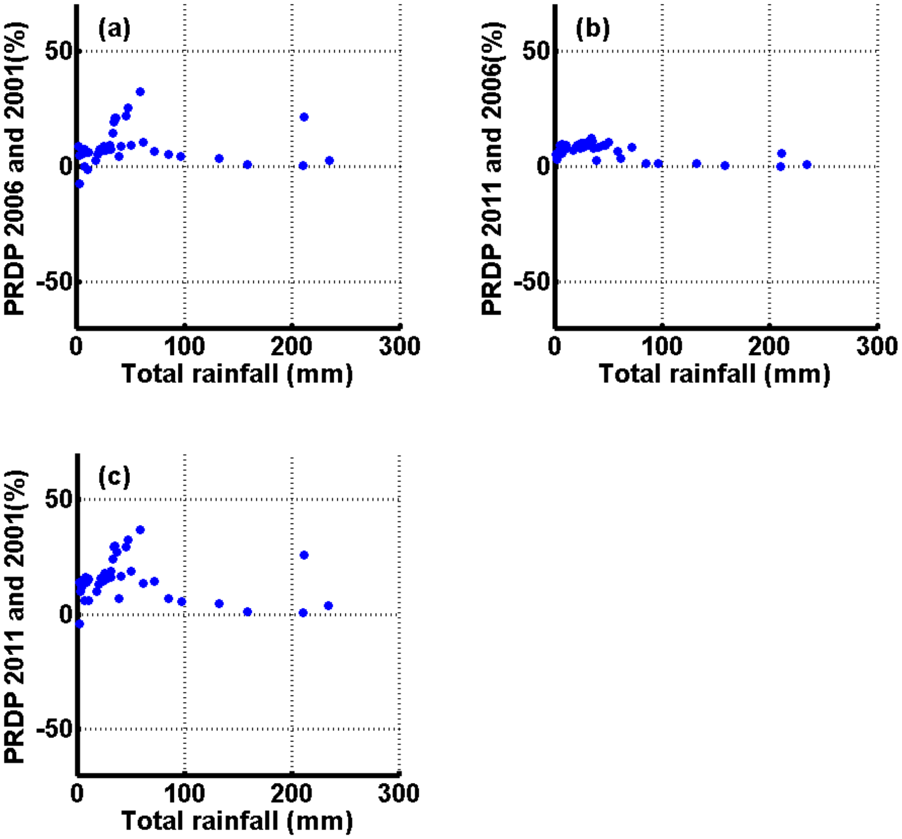

Figure 9-10 (a) Percent of Relative Difference of Peak flow (PRDP) of 2006 and 2001, (b) PRDP of 2011 and 2006, and (c) PRDP of 2011 and 2001at 6133

Figure 9-11 shows that the percent of relative difference of peak flows between 2001 and 2006 is greater than that of 2006 and 2011 at 6363, which may be due to the larger difference between percent of impervious area of 2001 and 2006 and 2006 and 2011 between 0 to 35 percent (Figure 9-6). Also Figure 9-11 shows that the relative difference of peak flow for rainfall events greater than 100 mm is close to zero.

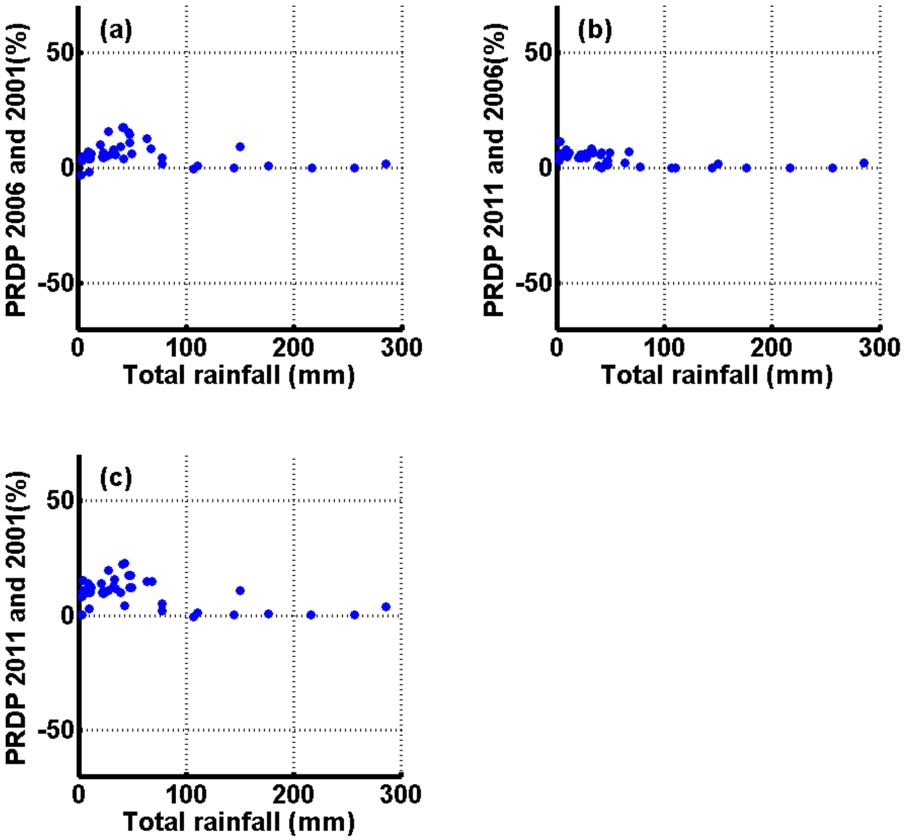

Figure 9-11 (a) Percent of Relative Difference of Peak flow (PRDP) of 2006 and 2001, (b) PRDP of 2011 and 2006, and (c) PRDP of 2011 and 2001 at 6363

As mentioned earlier, the impact of land cover changes on those peak flows associated with rainfall events greater than 100 mm in five urban catchments was close to zero. However the rainfall event in 6133 was an exception. This rainfall event occurred from Oct. 22, 2015 to Oct. 26, 2015. The total rainfall based on MPE data was greater than 200 mm, and the relative difference between peak flows of 2001 and 2011 was approximately 35%. This may be due to significant increasing of impervious area, or decreasing pervious area, from 2001 to 2011 at 6133. Comparing the spatially-averaged soil moisture content, simulated based on NLCD 2001 and NLCD 2011 at depths of 0.05

and 0.25 m, showed that prior to the rainfall event, the soil moisture was 0.28. After the rain began, the soil moisture, based on NLCD 2011, reached the saturated condition at the depth of 0.05 m faster than that based on NLCD 2001 (Figure 9-12). Based on the soil texture maps used by SAC-HT, soil texture at 6133 is clay, and its saturated soil moisture content is 46 percent. This makes a significant difference between peak flows of 2001 and 2011 for the Oct. 22, 2015 rainfall event (Figure 9-13).

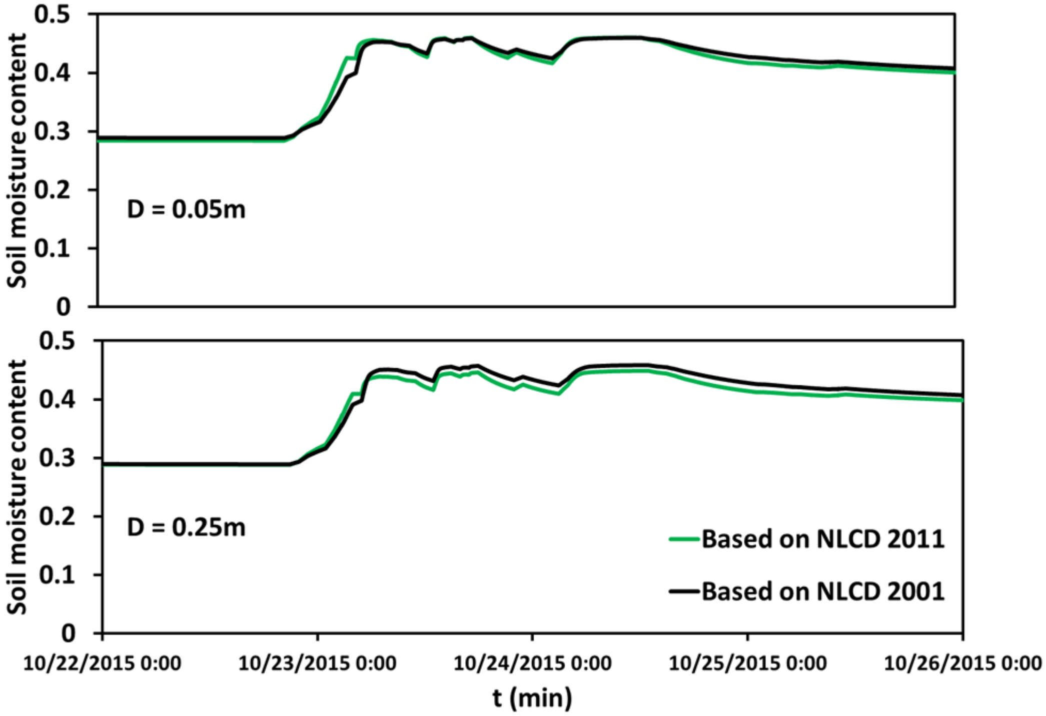

Figure 9-12 Spatially-averaged soil moisture content at 6133 due to Oct. 22, 2015 rainfall event at depths of 0.05 and 0.25 m

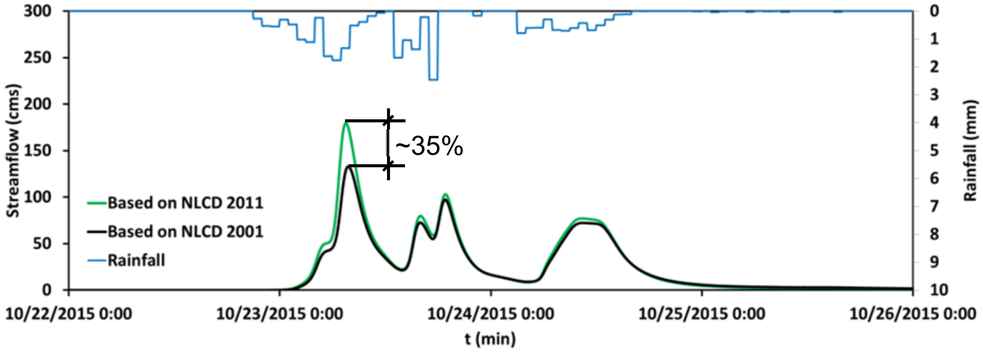

Figure 9-13 Simulated streamflow due to at 6133 Oct. 22, 2015 rainfall event

For the same rainfall event in other catchments (i.e. 6033, 6043, 6103 and 6363), there was no significant difference between peak flow of 2001 and 2011, due to the soil moisture content at these catchments.

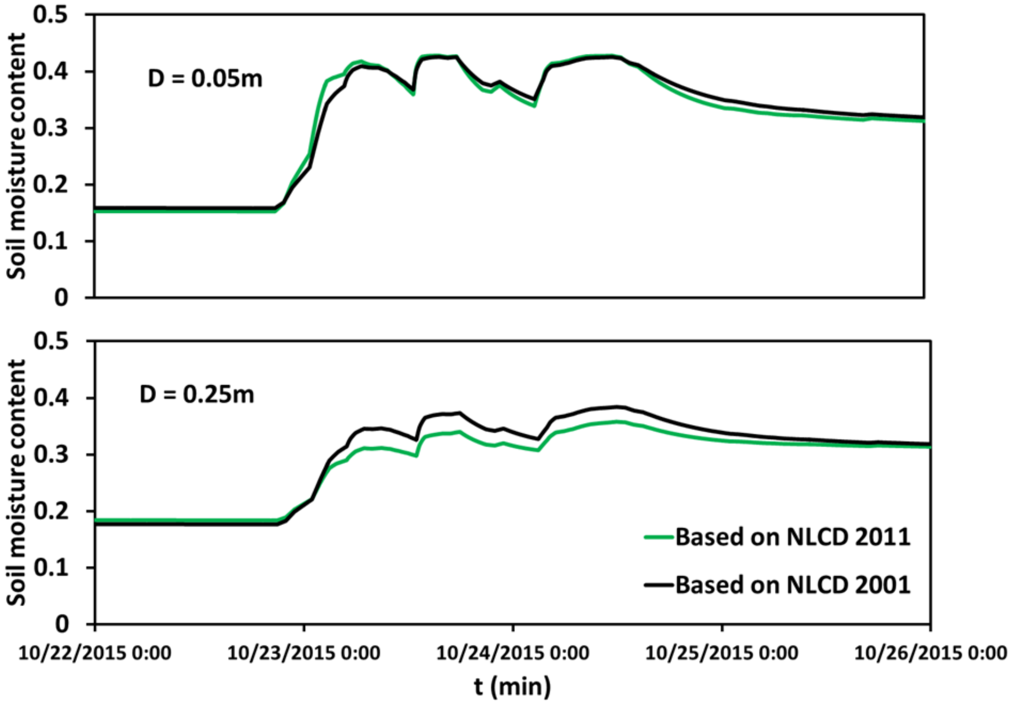

Figure 9-14 Spatially-averaged soil moisture content at 6033 due to Oct. 22, 2015 rainfall event at depths of 0.05 and 0.25 m

Figure 9-14 shows the spatially-averaged soil moisture content at 6033 due to Oct. 22, 2015 rainfall events at depths of 0.05 and 0.25 m. Based on the soil moisture texture, used by SAC-HT, catchment 6033 located on sandy loam with the saturated soil moisture of 42 percent. Although, the soil moisture content based on NLCD 2011 reached to saturated condition faster than that of based on NLCD 2001, the difference between them, particularly at the beginning of the rainfall is not significant. Also the figure shows that the soil moisture content at the depth of 0.25 m did not reach to the fully saturated condition. Therefore, the difference between peak flow based on NLCD 2001 and peak flow based on NLCD 2011 is 7 percent (Figure 9-15).

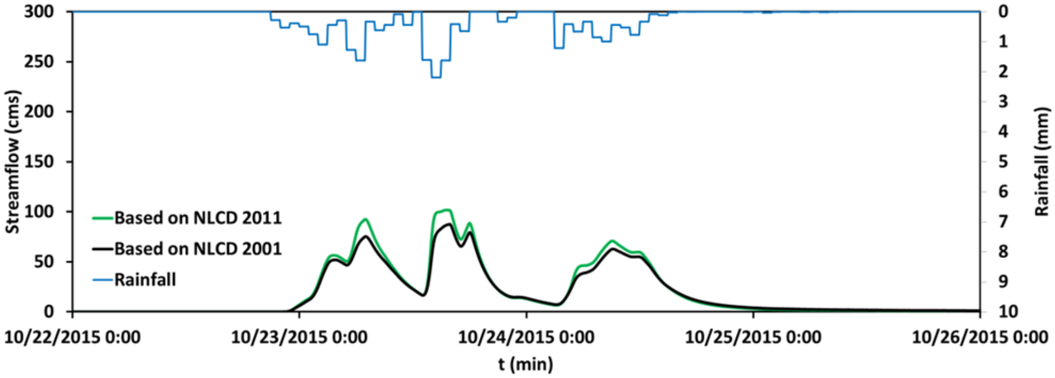

Figure 9-15 Simulated streamflow due to at 6033 Oct. 22, 2015 rainfall event

Figure 9-16 shows the spatially-averaged soil moisture content at 6043 due to Oct. 22, 2015 rainfall events at depths of 0.05 and 0.25 m. Based on the soil moisture texture, used by SAC-HT, catchment 6033 located on clay with the saturated soil moisture of 46 percent. At this location, soil moisture content based on NLCD 2011 reached to the saturated condition faster than that of based on NLCD 2001; however due to the small length of the stream and also small size of the catchment, the difference between peak flows of 2001 and 2011 is minor (Figure 9-17).

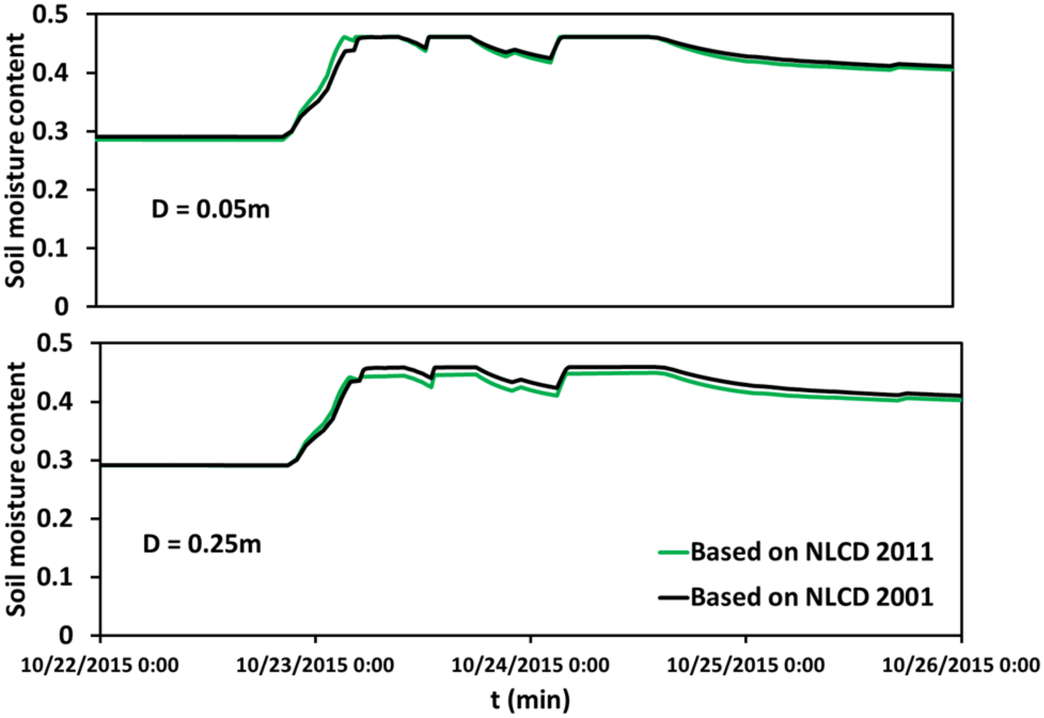

Figure 9-16 Spatially-averaged soil moisture content at 6043 due to Oct. 22, 2015 rainfall event at depths of 0.05 and 0.25 m

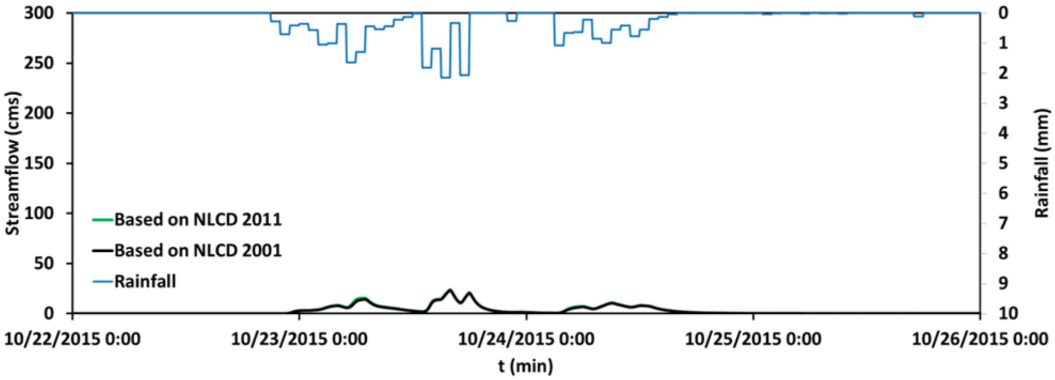

Figure 9-17 Simulated streamflow due to at 6043 Oct. 22, 2015 rainfall event

Figure 9-18 shows the spatially-averaged soil moisture content at 6103 due to Oct. 22, 2015 rainfall events at depths of 0.05 and 0.25 m. Based on the soil moisture texture, used by SAC-HT, catchment 6033 located on clay with the saturated soil moisture of 46 percent. The figure shows that the simulated soil moisture content based on NLCD 2001 and NLCD 2011 reached to the saturated condition at the same time, and the difference between them is very small. Therefore, the difference between peak flows based on NLCD 2001 and NLCD 2011 is minor.

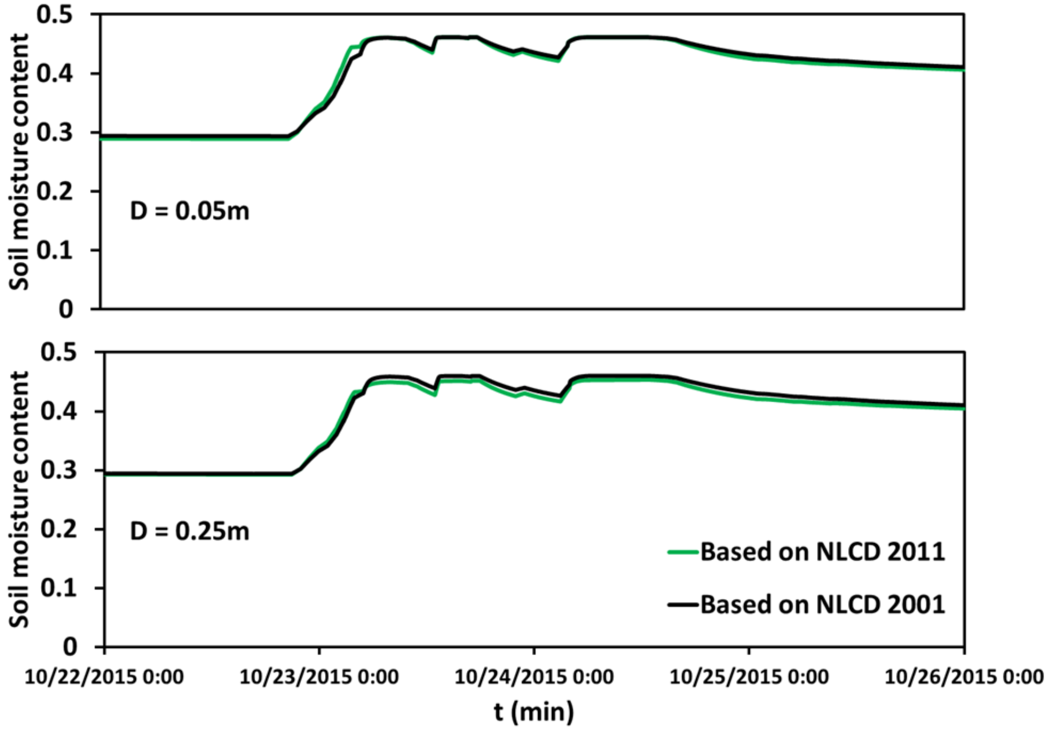

Figure 9-18 Spatially-averaged soil moisture content at 6103 due to Oct. 22, 2015 rainfall event at depths of 0.05 and 0.25 m

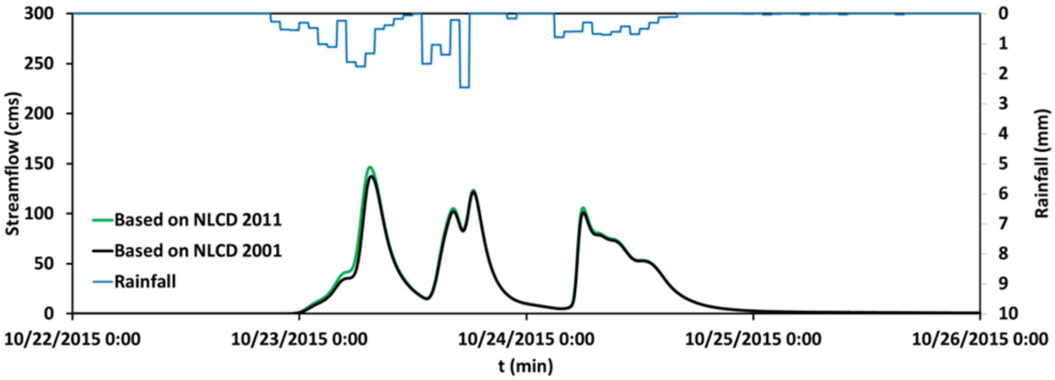

Figure 9-19 Simulated streamflow due to at 6103 Oct. 22, 2015 rainfall event

Figure 9-20 shows the spatially-averaged soil moisture content at 6363 due to Oct. 22, 2015 rainfall events at depths of 0.05 and 0.25 m. Based on the soil moisture texture, used by SAC-HT, catchment 6033 located on clay with the saturated soil moisture of 46 percent. The figure shows that the simulated soil moisture content based on NLCD 2001 and NLCD 2011 reached to the saturated condition at the same time, and the difference between them is very small. Therefore, the difference between peak flows based on NLCD 2001 and NLCD 2011 is small.

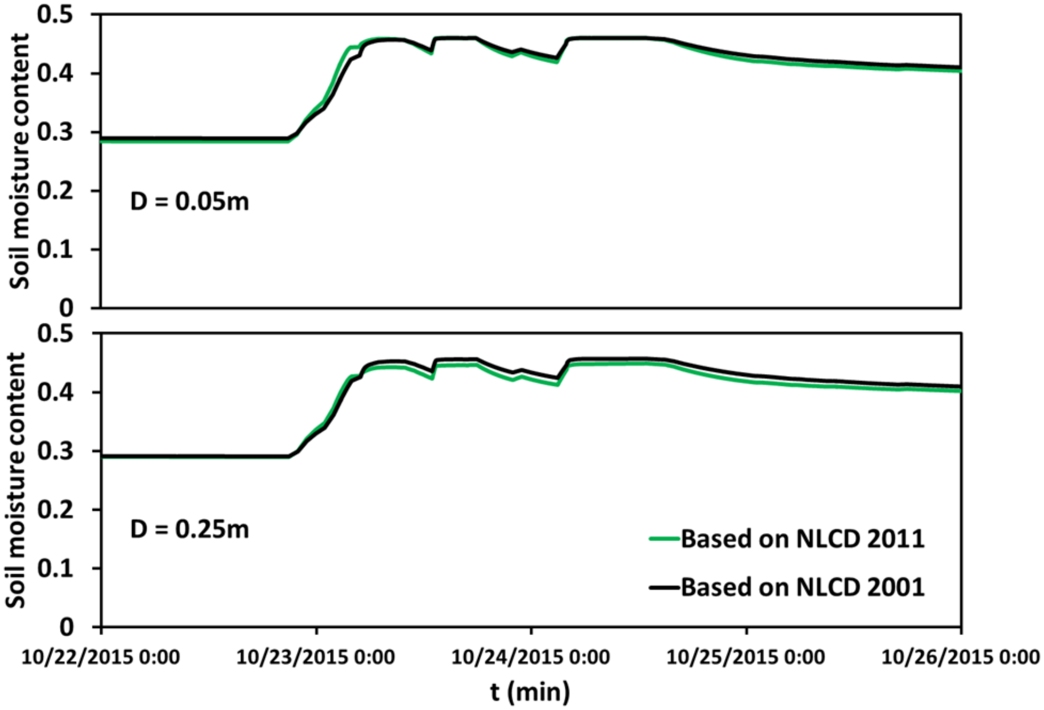

Figure 9-20 Spatially-averaged soil moisture content at 6363 due to Oct. 22, 2015 rainfall event at depths of 0.05 and 0.25 m

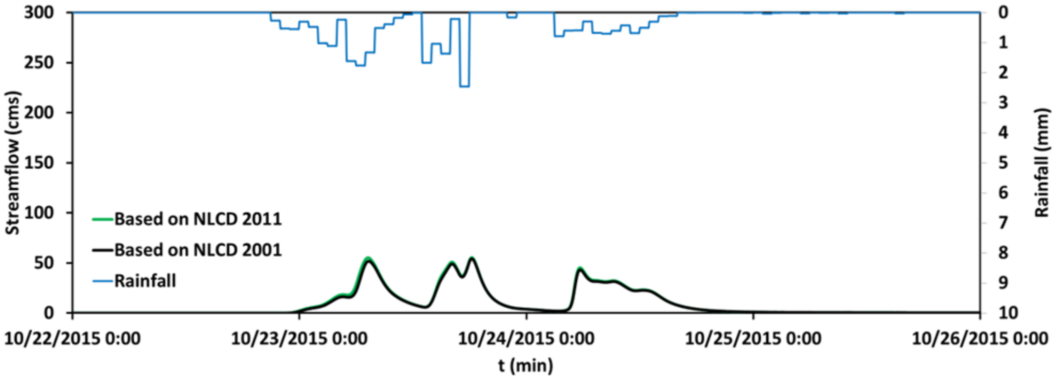

Figure 9-21 Simulated streamflow due to at 6363 Oct. 22, 2015 rainfall event

9.3 Impact of land cover changes on runoff volume

Figure 9-22 toFigure 9-26 show the relative difference of runoff volume in 2006 and 2001, 2011 and 2006, and 2011 and 2001 for subcatchments 6033, 6043, 6103, 6133, and 6363. The relative difference of runoff volume plots showed that increasing impervious fractional areas increases the runoff volume. The most significant changes in the runoff volume against the land cover changes occurred in subcatchment 6133 (Figure 9-25), where the relative difference of runoff volume reached approximately 20%. In catchments 6103 (Figure 9-24) and 6363 (Figure 9-26), the maximum relative difference of peak flow was approximately 15 percent for rainfall events less than 100 mm, and in 6033 (Figure 9-22) and 6043 (Figure 9-23) this varied between 5 to 10 percent for rainfall events less than 100 mm. The magnitude of relative difference of runoff volume was close to zero for rainfall events greater than 100 mm in five urban subcatchments. This showed that rainfall events greater than 100 mm saturate the pervious areas in the subcatchments, converting rainfall to runoff. Therefore, the difference between the runoff volume based on NLCD 2001 and NLCD 2011 is close to zero.

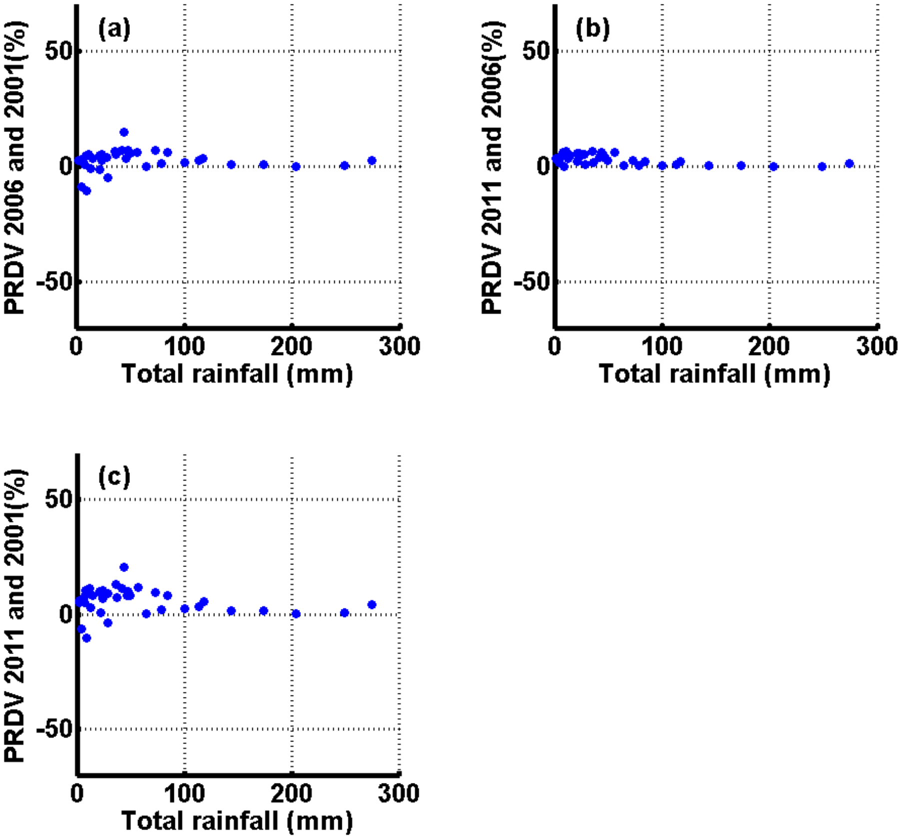

Figure 9-22 (a) Percent of Relative Difference of Runoff Volume (PRDV) of 2006 and 2001, (b) PRDV of 2011 and 2006, and (c) PRDV of 2011 and 2001 at 6033

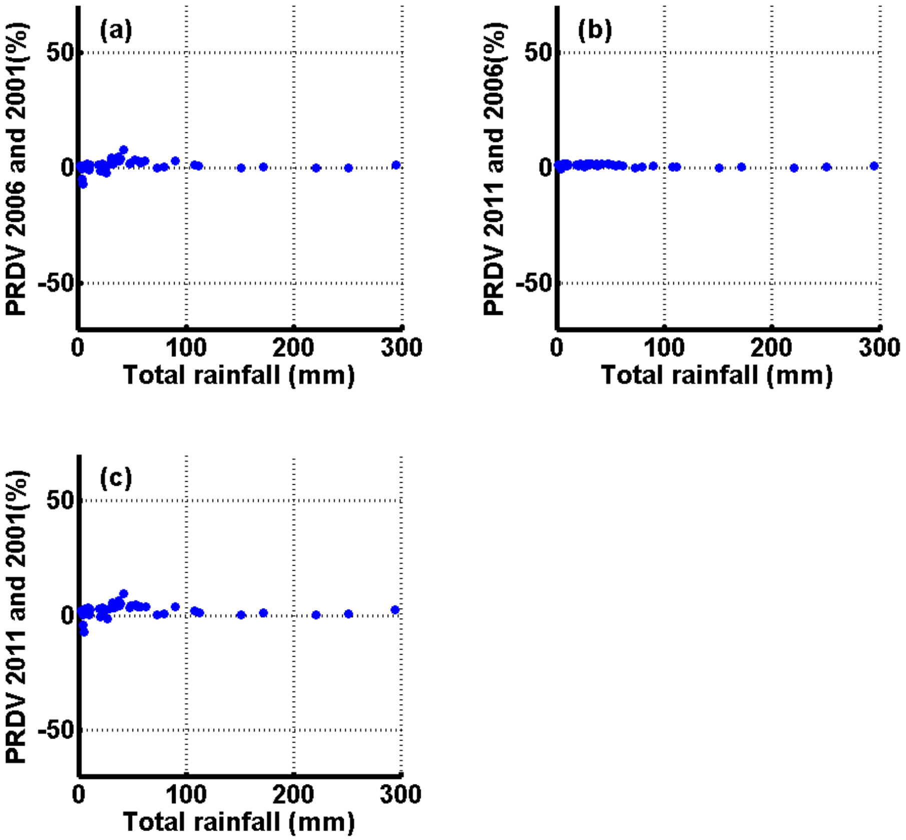

Figure 9-23 (a) Percent of Relative Difference of Runoff Volume (PRDV) of 2006 and 2001, (b) PRDV of 2011 and 2006, and (c) PRDV of 2011 and 2001 at 6043

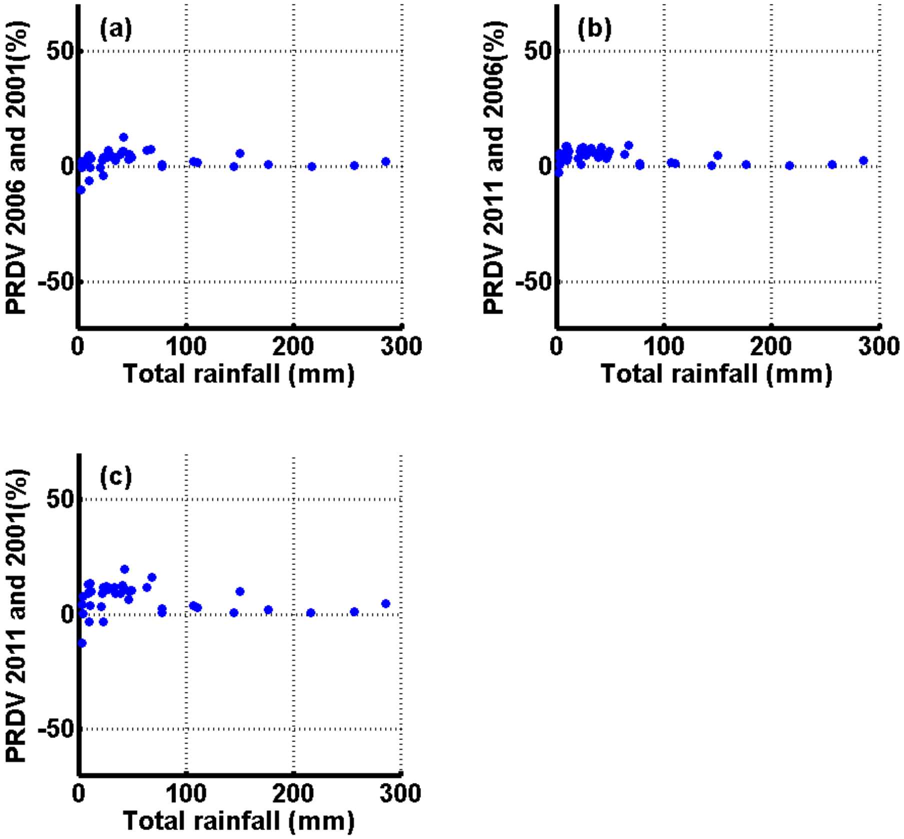

Figure 9-24 (a) Percent of Relative Difference of Runoff Volume (PRDV) of 2006 and 2001, (b) PRDV of 2011 and 2006, and (c) PRDV of 2011 and 2001 at 6103

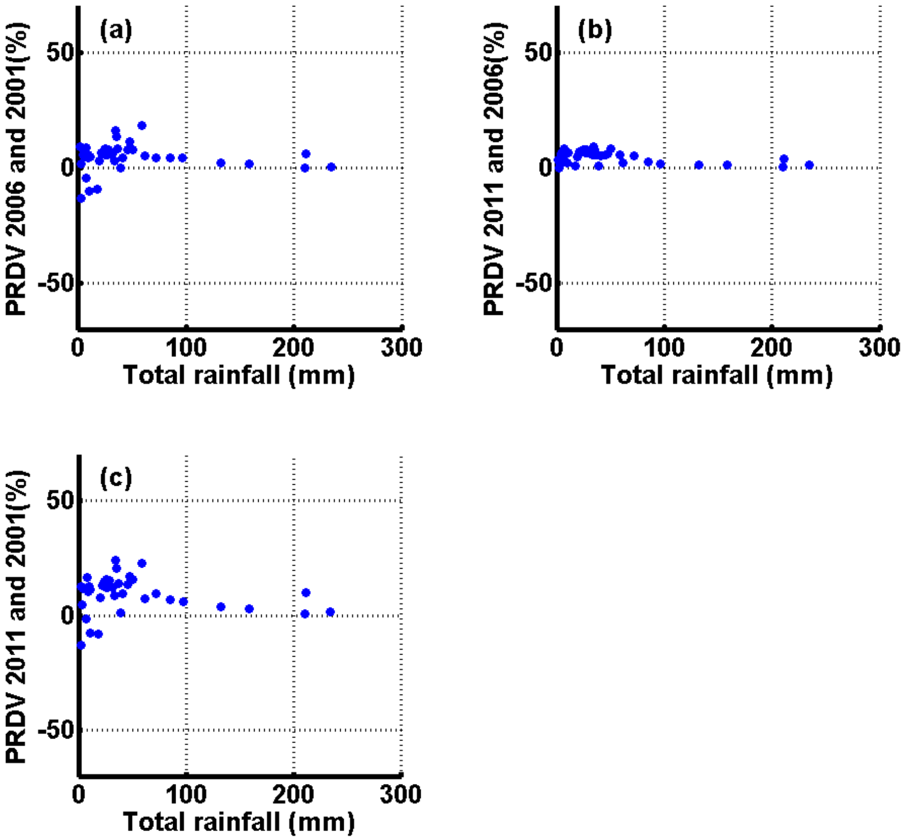

Figure 9-25 (a) Percent of Relative Difference of Runoff Volume (PRDV) of 2006 and 2001, (b) PRDV of 2011 and 2006, and (c) PRDV of 2011 and 2001 at 6133

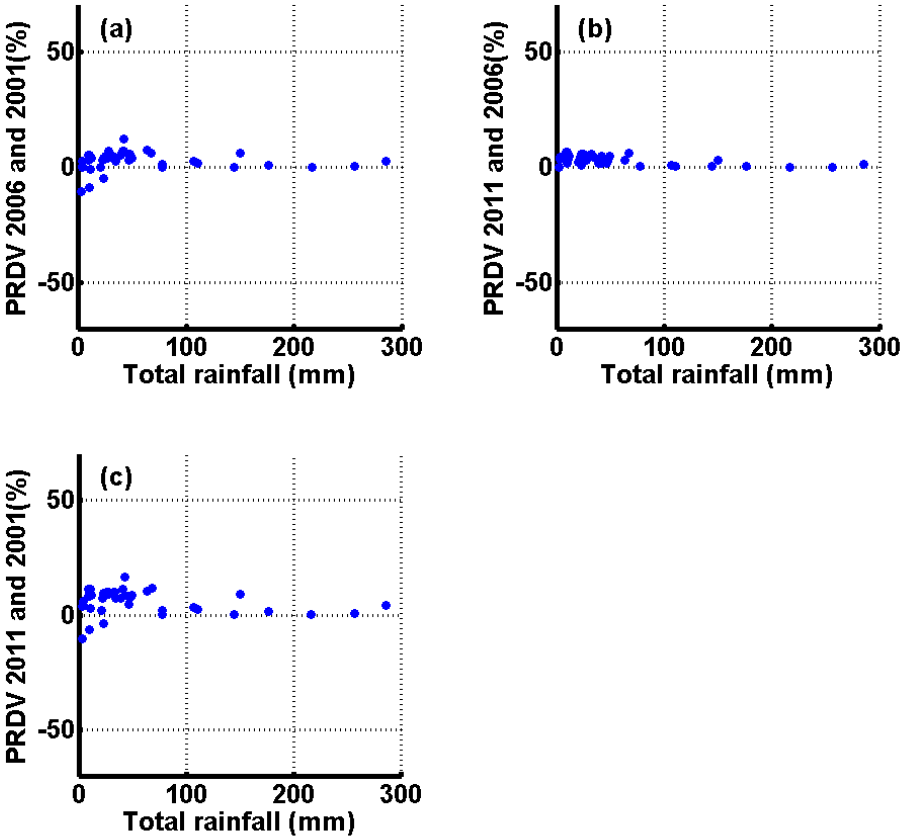

Figure 9-26 (a) Percent of Relative Difference of Runoff Volume (PRDV) of 2006 and 2001, (b) PRDV of 2011 and 2006, and (c) PRDV of 2011 and 2001 at 6363

9.4 Impact of land cover changes on time-to-peak

The response time of each subcatchment was required to assess the impact of land cover changes on time-to-peak of five urban subcatchments. Rafieeinasab et al. (2015a) estimated the time-to-peak of each catchment by using an empirical unit hydrograph (UHG). Based on their estimation, the time-to-peak of 6033, 6043, 6103, 6133, and 6363 were 0.75, 0.75, 3, 2.75, and 1.5 hrs, respectively (Figure 9-27).

The impact of land cover changes on time-to-peak varied from catchment to catchment (Figure 9-28 toFigure 9-32). The difference of time-to-peak of 2001 and 2011 relative to the time-to-peak of the five urban catchments for rainfall events greater than 100 mm was close to zero. In catchment 6043 (Figure 9-28), a few rainfall events were less than 100 mm, and the relative difference in time-to-peak was greater than zero, but never exceeded 10 percent. The maximum difference in time-to-peak relative to time-to-peak of the catchment from 2001 to 2011 in 6103 (Figure 9-29), 6133 (Figure 9-30), and 6363 (Figure 9-30) was 10, 15, and 15 percent, respectively.The impact of land cover changes on time-to-peak in catchment 6033 from 2001 to 2011 was remarkably higher than for the other four subcatchments.

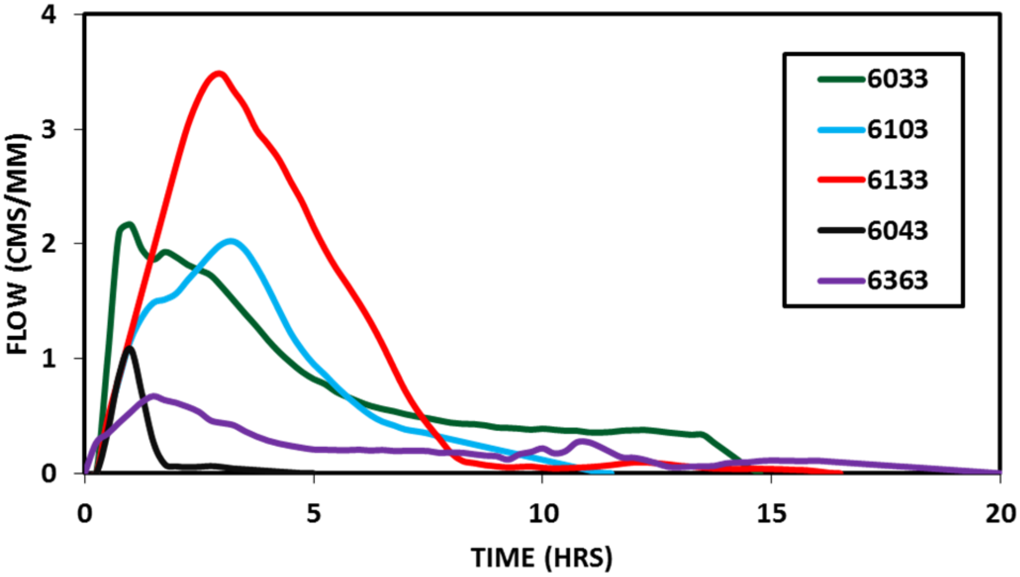

Figure 9-27 Derived empirical unit hydrographs (UHG) of the study catchments (Rafieeinasab et al., 2015a)

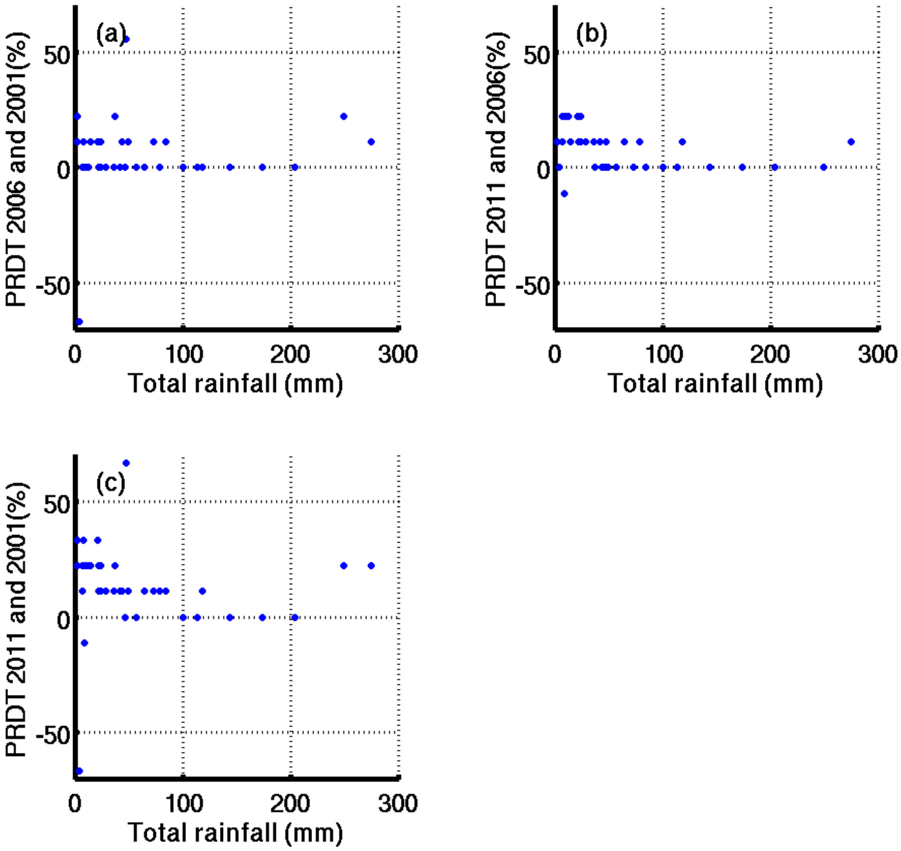

Figure 9-28 (a) Percent of Difference of Time-to-Peak Relative to the Time-to-Peak of the catchment (PRDT) of 2006 and 2001, (b) PRDT of 2011 and 2006, and (c) PRDT of 2011 and 2001 at 6033

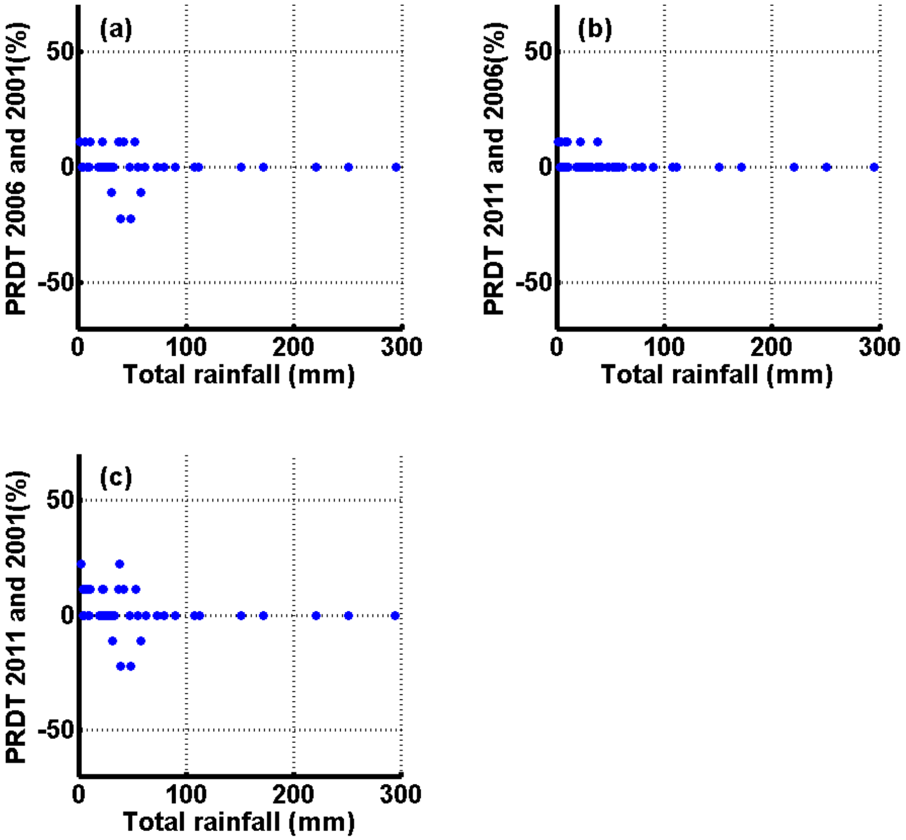

Figure 9-29 (a) Percent of Difference of Time-to-Peak Relative to the Time-to-Peak of the catchment (PRDT) of 2006 and 2001, (b) PRDT of 2011 and 2006, and (c) PRDT of 2011 and 2001 at 6043

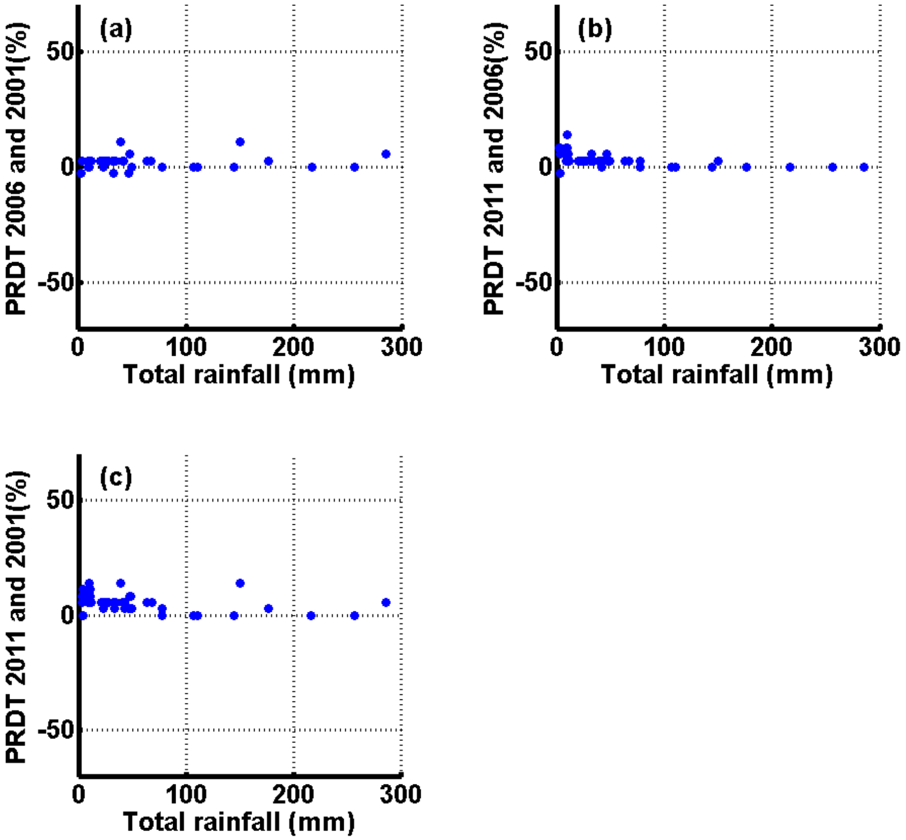

Figure 9-30 (a) Percent of Difference of Time-to-Peak Relative to the Time-to-Peak of the catchment (PRDT) of 2006 and 2001, (b) PRDT of 2011 and 2006, and (c) PRDT of 2011 and 2001 at 6103

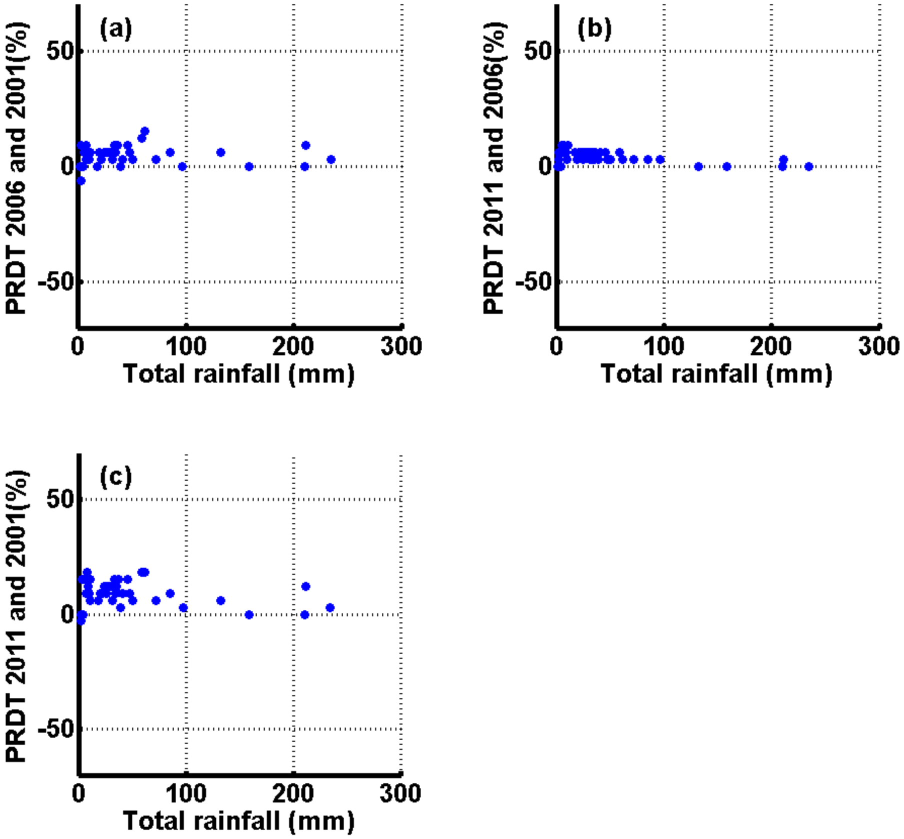

Figure 9-31 (a) Percent of Difference of Time-to-Peak Relative to the Time-to-Peak of the catchment (PRDT) of 2006 and 2001, (b) PRDT of 2011 and 2006, and (c) PRDT of 2011 and 2001 at 6133

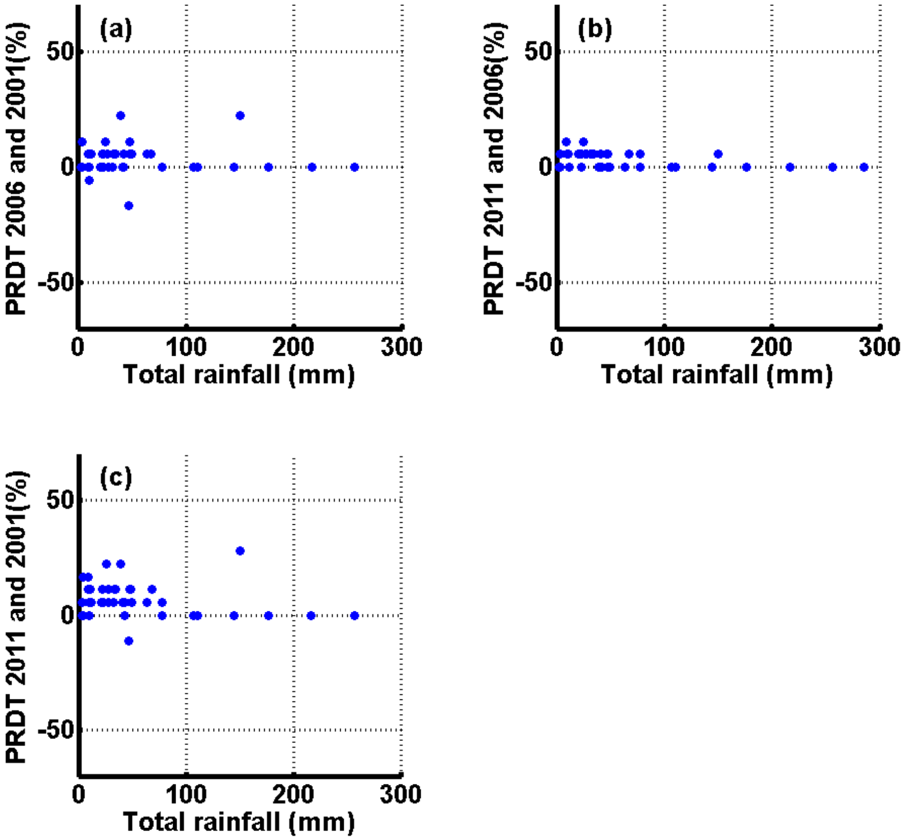

Figure 9-32 (a) Percent of Difference of Time-to-Peak Relative to the Time-to-Peak of the catchment (PRDT) of 2006 and 2001, (b) PRDT of 2011 and 2006, and (c) PRDT of 2011 and 2001 at 6363

Figure 9-28 shows that in a rainfall event of less than 50 mm at 6033, the relative difference in time-to-peak reached 65 percent of the time-to-peak. This rainfall event occurred from Nov. 15 to Nov. 18, 2015. The rainfall map, based on MPE QPE, (Figure 9-33) showed that a large part of the rainfall event occurred close to the outlet and at a location where the relative difference of land cover changes from 2001 to 2011 was approximately 58% (encircled in Figure 9-34). Therefore, the time-to-peak of 2011 associated to this rainfall event was reduced 30 min relative to the time-to-peak of 2001 (Figure 9-35).

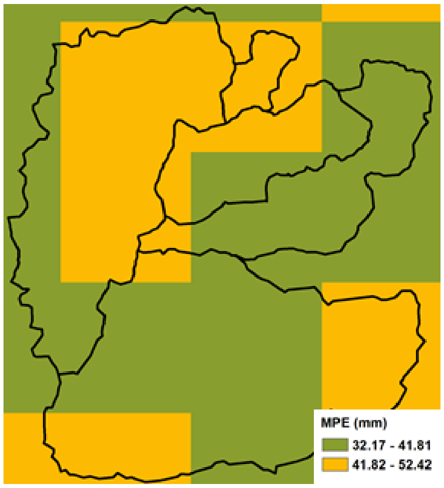

Figure 9-33 Total rainfall map based on MPE QPE over five urban catchments for rainfall event of Nov. 15, 2015

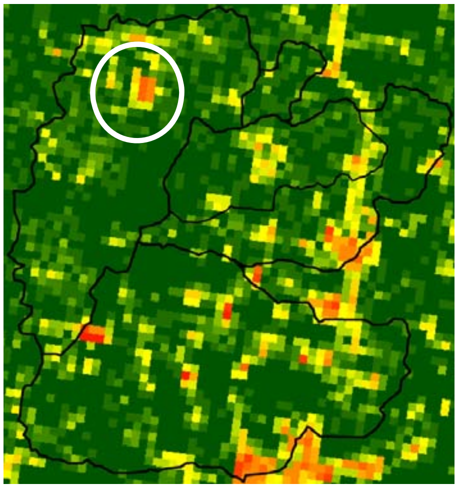

Figure 9-34 Difference of impervious area between 2001 and 2011

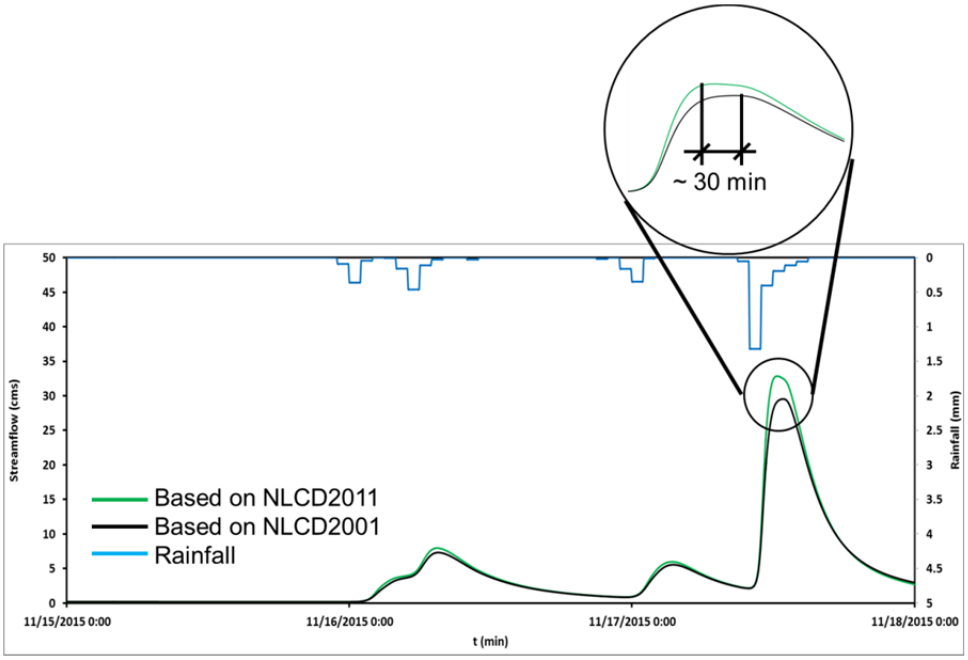

Figure 9-35 Streamflow simulation based on NLCD 2001 and NLCD 2011 at 6033 for rainfall event of Nov. 15, 2015

Chapter 10 Conclusions and future recommendations

The four primary objectives of this work are to: 1) advance understanding of the sources of variability of areal runoff in large urban areas and their dependence on spatial scale, 2) advance understanding of the runoff generation processes in urban areas based on soil moisture observations, 3) assess the sensitivity of streamflow and soil moisture simulations to the spatial resolution of precipitation input and the a priori parameters of the hydrologic models in the NWS Hydrology Laboratory Research Distributed Hydrologic Model (HLRDHM, Koren et al. 2004), and 4) assess the impact of land cover changes on streamflow and soil moisture simulations in large urban areas. The study area of this work is the Dallas-Fort Worth (DFW) Metroplex in North Central Texas.

In Part I of this work, a simple spatial stochastic model was developed for translation of rainfall to areal runoff in urban areas, climatological mean and variance of mean areal runoff (MAR) were then evaluated over a range of catchment scales and translated into runoff frequency as a proxy for flood frequency, and sensitivity of runoff frequency to precipitation, imperviousness and soil, and their changes was assessed. The results show that the variability of MAR in urban areas depends significantly on the catchment scale and magnitude of precipitation, and that precipitation, soil, and land cover all exert influences of varying relative importance in shaping the frequency of MAR, and hence flood frequency, for different sizes of urban areas. The findings indicate that, due to large sensitivity of MAR frequency to multiple hydrometeorological and physiographic factors, estimation of flood frequency for urban catchments is inherently more uncertain, and that the approach developed in this work may be useful in developing bounds for flood frequencies in urban areas under nonstationary conditions arising from climate change and urbanization.

In Part II of this work, the current limits of high-resolution hydrologic modeling for real-time forecasting were tested by assessing the sensitivity of streamflow and soil moisture simulations in urban catchments to the spatial resolution of the rainfall input and the a priori hydrologic model parameters. The hydrologic model used is HLRDHM which uses the Sacramento model (SAC, Burnash et al. 1979) for soil moisture accounting (i.e., rainfall-runoff) and kinematic-wave model (Chow et al. 1988) for channel and hillslope routing. HLRDHM is a grid-based model with a default spatial resolution of 4 km × 4 km, which corresponds to the Hydrologic Rainfall Analysis Project grid (HRAP, Greene and Hudlow 1982). SAC has 11 soil- and land cover-related a priori parameters which are available at a 1 HRAP resolution for CONUS. In this work, the 11 parameters were derived at resolutions of 1/2, 1/4, 1/8, and 1/16 HRAP using the Soil Survey Geographic Database (SSURGO) and the National Land Cover Database (NLCD) 2011. HLRDHM was then applied at spatial resolutions ranging from 250 m to 2 km for the precipitation input and from 250 m to 4 km for the a priori model parameters. The rainfall input used were the CASA QPE available at a resolution of 1/8 HRAP and 1 min and the MPE product available at a resolution of 1 HRAP and 1 hr. The temporal resolution of the model was fixed at 5 min for both. The streamflow observations used for evaluation were obtained from the water level measurements available from the City of Grand Prairie via the stage-discharge relations estimated from the 1-D steady-state non-uniform fluid mechanically-based model of Kean and Smith (2004, 2005, 2010). The water level observations are available from Oct 10, 2015, to Dec 31, 2015, for the outlets, 6363 and 6042 (see Figure 7-5), whose catchment areas are 14.4 and 3.4 km^2, respectively. The soil moisture simulation results were evaluated at three locations in Arlington where observations are available at depths of 0.05, 0.10, 0.25, 0.50 and 1.00 m. The soil moisture observations were obtained from three Time Domain Transmissometry (TDT) and Time Domain Reflectometry (TDR) sensors newly deployed for this work. Prior to operation, the sensors were tested against gravimetric analysis results. Comparison of in-situ soil moisture content vs. the lab test results showed that the relative difference between the two did not exceed 7% for all three locations.

The streamflow results show that the use of high-resolution QPE improves streamflow simulation significantly, but that, once the resolution of QPE was increased to the scale of the catchment, no clear relationships were seen between the simulation accuracy and the resolution of the QPE or hydrologic modeling, presumably because the errors in QPE and models mask the relationships. The soil moisture results suggest that there are disparate infiltration processes at work within the small area in Arlington where the 3 sensors are deployed, and that, while the near-surface simulation of soil moisture is generally skillful, the heat transfer version of SAC (SAC-HT, Koren et al. 1999, 2006, 2008, 2014, Anderson et al. 2006) in HLRDHM has difficulty in simulating the vertical dynamics of soil moisture. Specifically, the soil moisture observations obtained from Aug. 18, 2015, to Dec. 31, 2015, indicate that infiltration at the CELB, Bridge, and Cemetery locations is largely matric potential-, saturation excess-, and infiltration excess-driven, respectively. The findings point to real-time updating of model states to reduce uncertainties in the initial soil moisture conditions, and the need for a dense observing network to improve understanding of the processes both at point and catchment scales.

To assess the impact of recent land cover changes in the study area and to project what may be expected in the future, in Part III of this work, streamflow and soil moisture were simulated using HLRDHM at 250 m and 5 min resolution with the National Land Cover Data (NLCD) of 2001, 2006 and 2011 for five urban catchments in Arlington and Grand Prairie, TX. The comparison between the derived impervious maps from NLCD 2001 and 2011 over Dallas, Grand Prairie, Arlington and Fort Worth indicates that imperviousness increased about 15% in these four cities from 2001 to 2011. The findings indicate that, in terms of peak flow, time-to-peak and runoff volume, small events are more sensitive to changes in impervious cover than large events, increase in peak flow is more pronounced for catchments with larger increase in impervious cover, increase in peak flow is also impacted by changes in antecedent soil moisture due to increased impervious cover, runoff volume is not significantly impacted by changes in impervious cover, and changes in time-to-peak relative to the response time of the catchment is impacted by the location of the land cover changes relative to the outlet and the time-to-peak itself. In particular, the Johnson Creek Catchment in Arlington (~40 km^2), which has a time-to-peak of only 40 min, shows larger sensitivity in time-to-peak to land cover changes due presumably to the proximity of the area of increased land cover to the catchment outlet. For further evaluation, in addition to the CASA network of X-band polarimetric radars for high-resolution quantitative precipitation information (QPI), dense observation networks for streamflow and soil moisture, such as the Arlington Urban Hydrology Testbed currently under development, are necessary.

Appendix A

Time series of observed and simulated streamflow at 6363 using CASA and MPE data

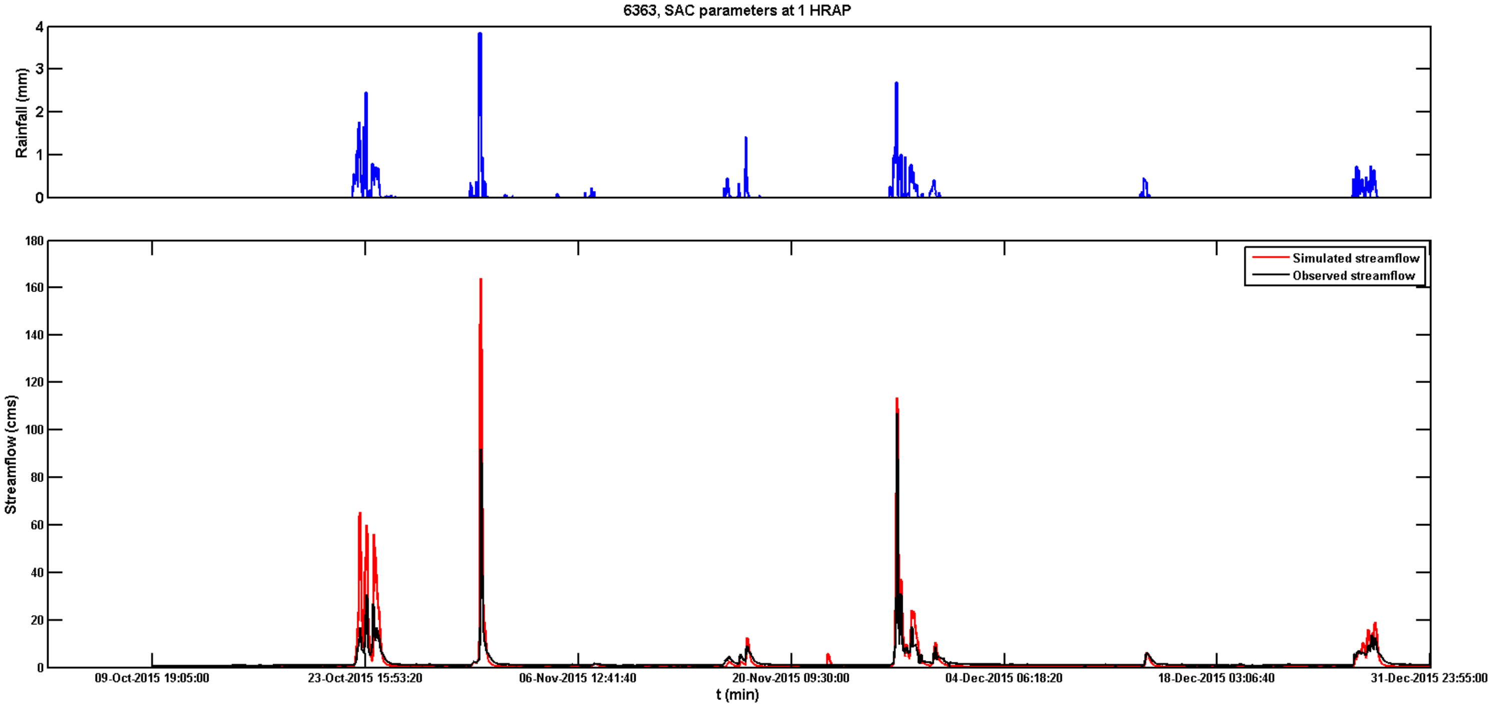

Figure A- 1 Streamflow simulation time series at model resolution of 1/2 HRAP and SAC parameters at 1 HRAP using MPE QPE at 6363

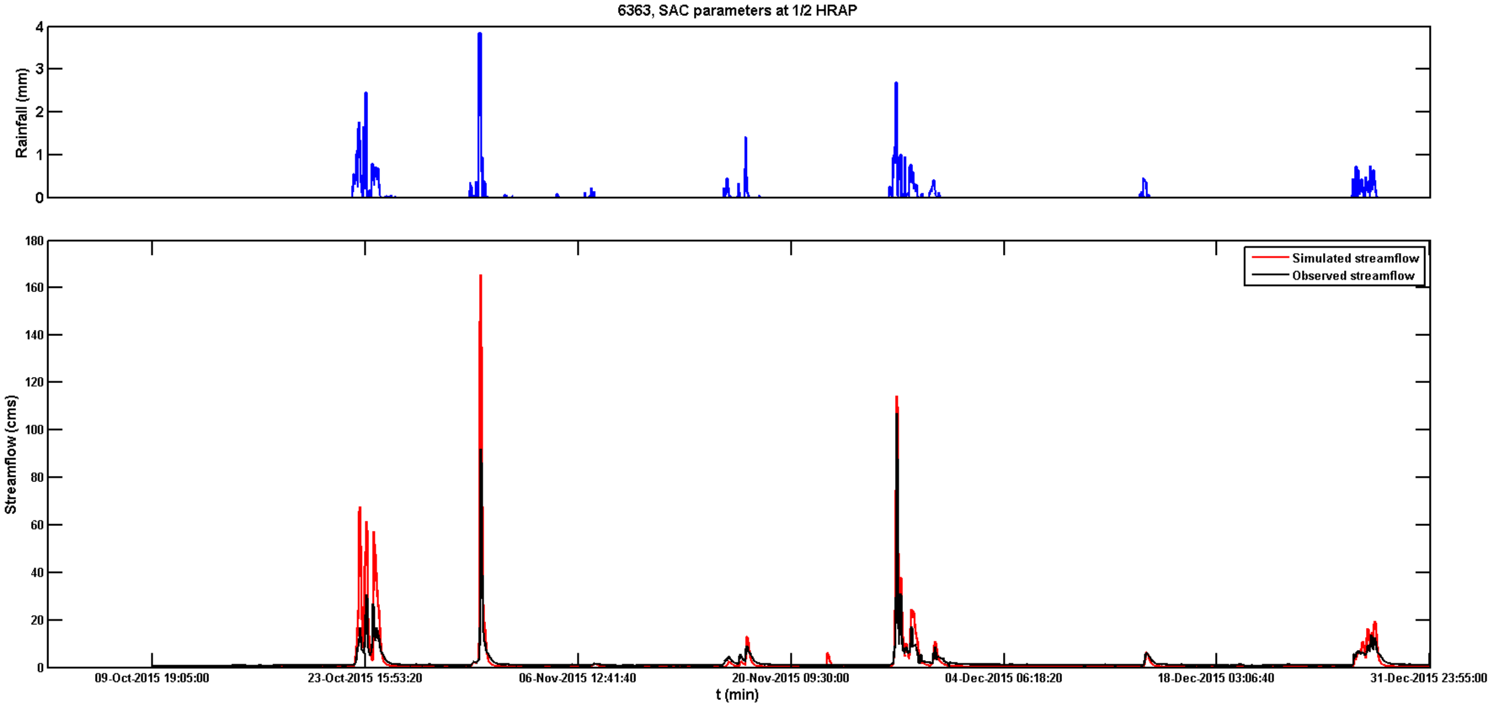

Figure A- 2 Streamflow simulation time series at model resolution of 1/2 HRAP and SAC parameters at 1/2 HRAP using MPE QPE at 6363

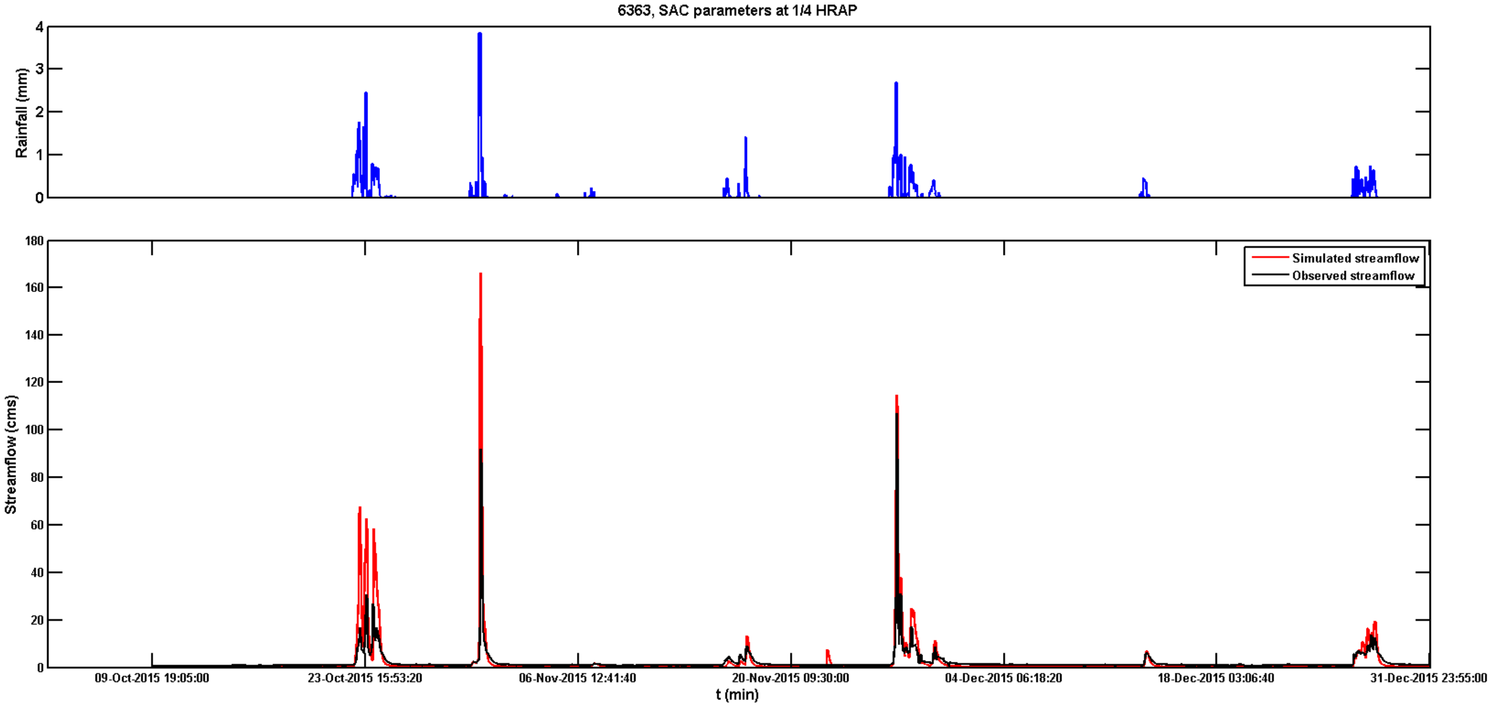

Figure A- 3 Streamflow simulation time series at model resolution of 1/2 HRAP and SAC parameters at 1/4 HRAP using MPE QPE at 6363

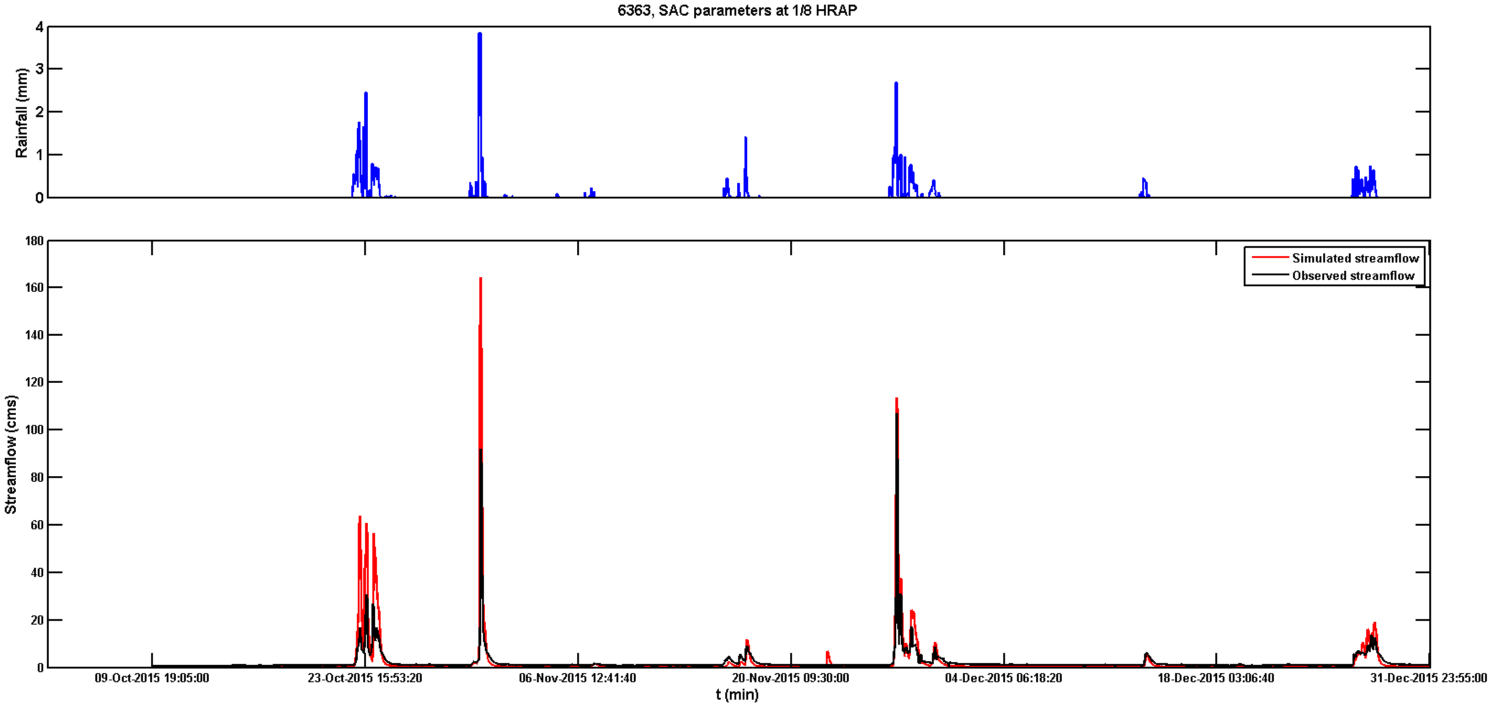

Figure A- 4 Streamflow simulation time series at model resolution of 1/2 HRAP and SAC parameters at 1/8 HRAP using MPE QPE at 6363

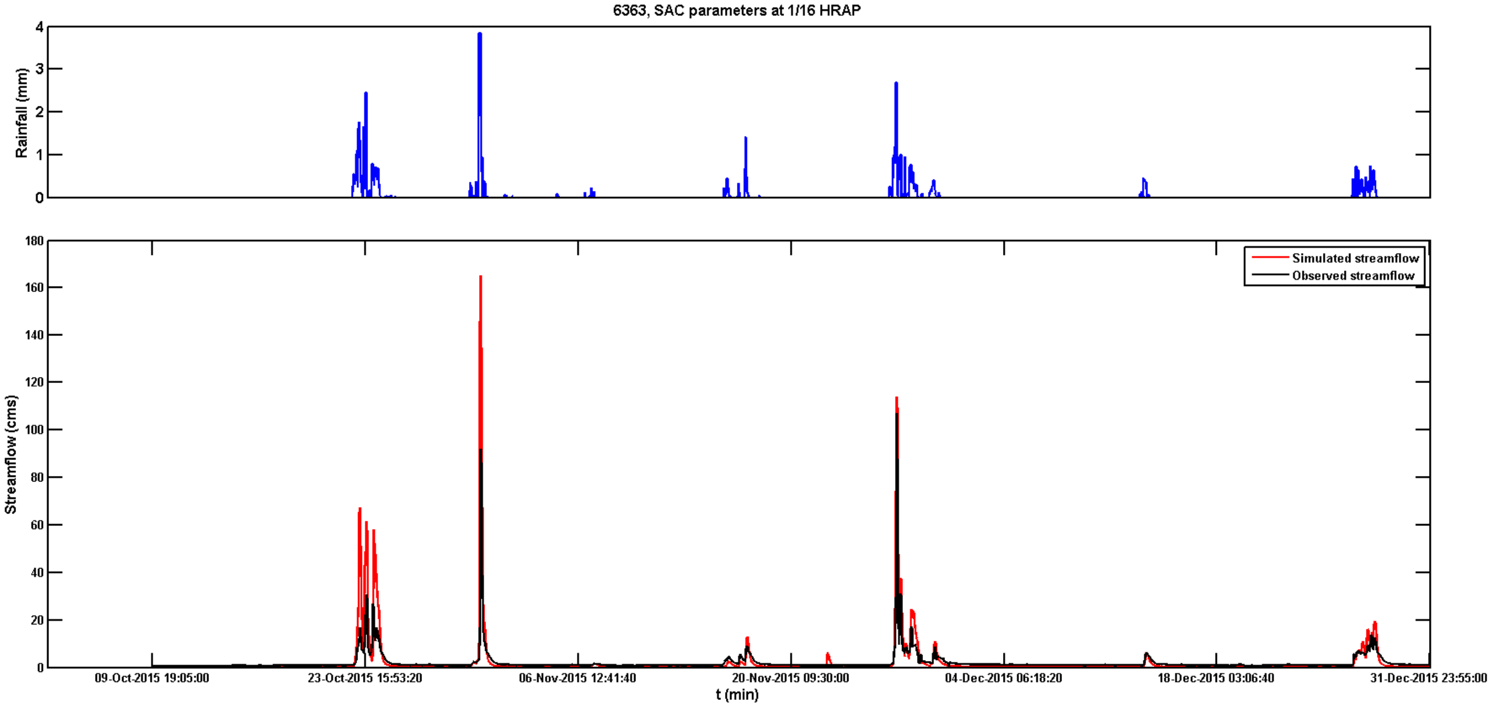

Figure A- 5 Streamflow simulation time series at model resolution of 1/2 HRAP and SAC parameters at 1/16 HRAP using MPE QPE at 6363

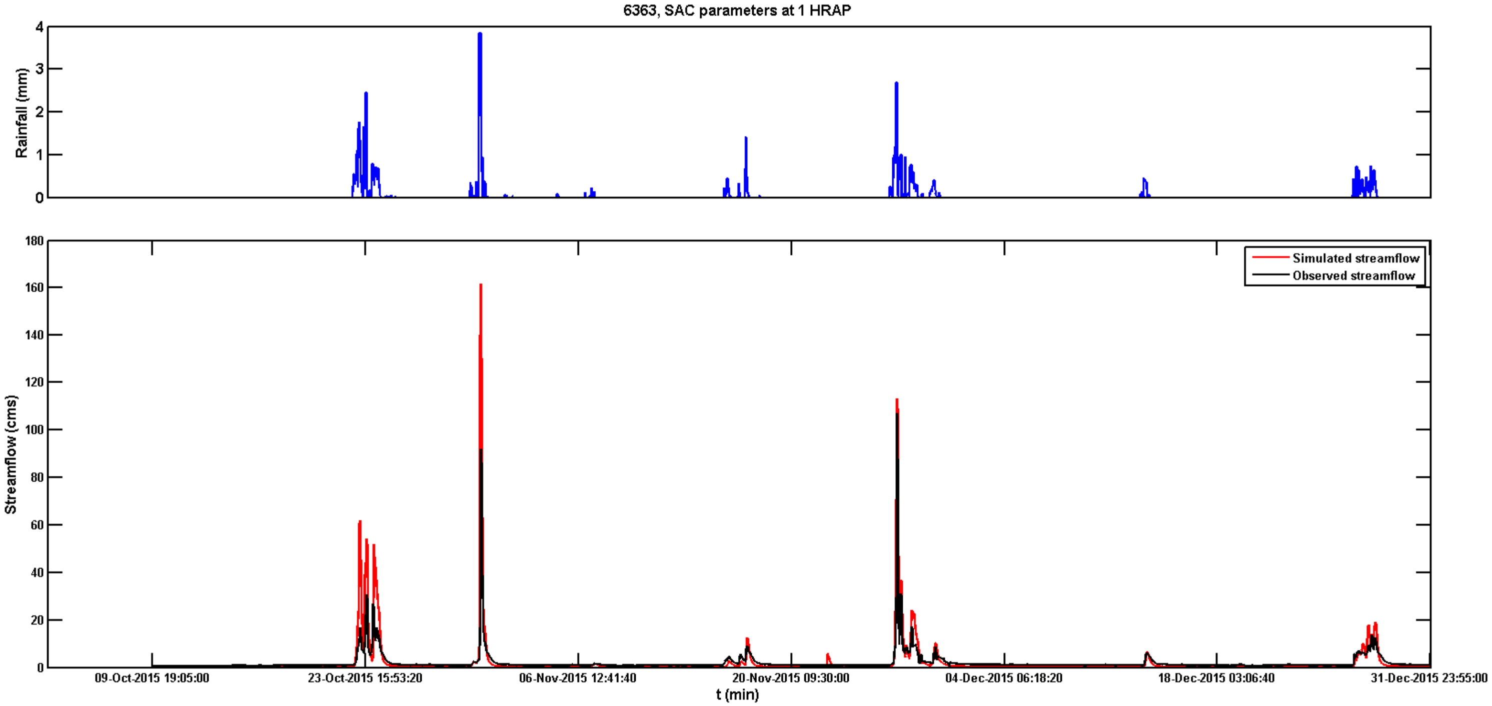

Figure A- 6 Streamflow simulation time series at model resolution of 1/4 HRAP and SAC parameters at 1 HRAP using MPE QPE at 6363

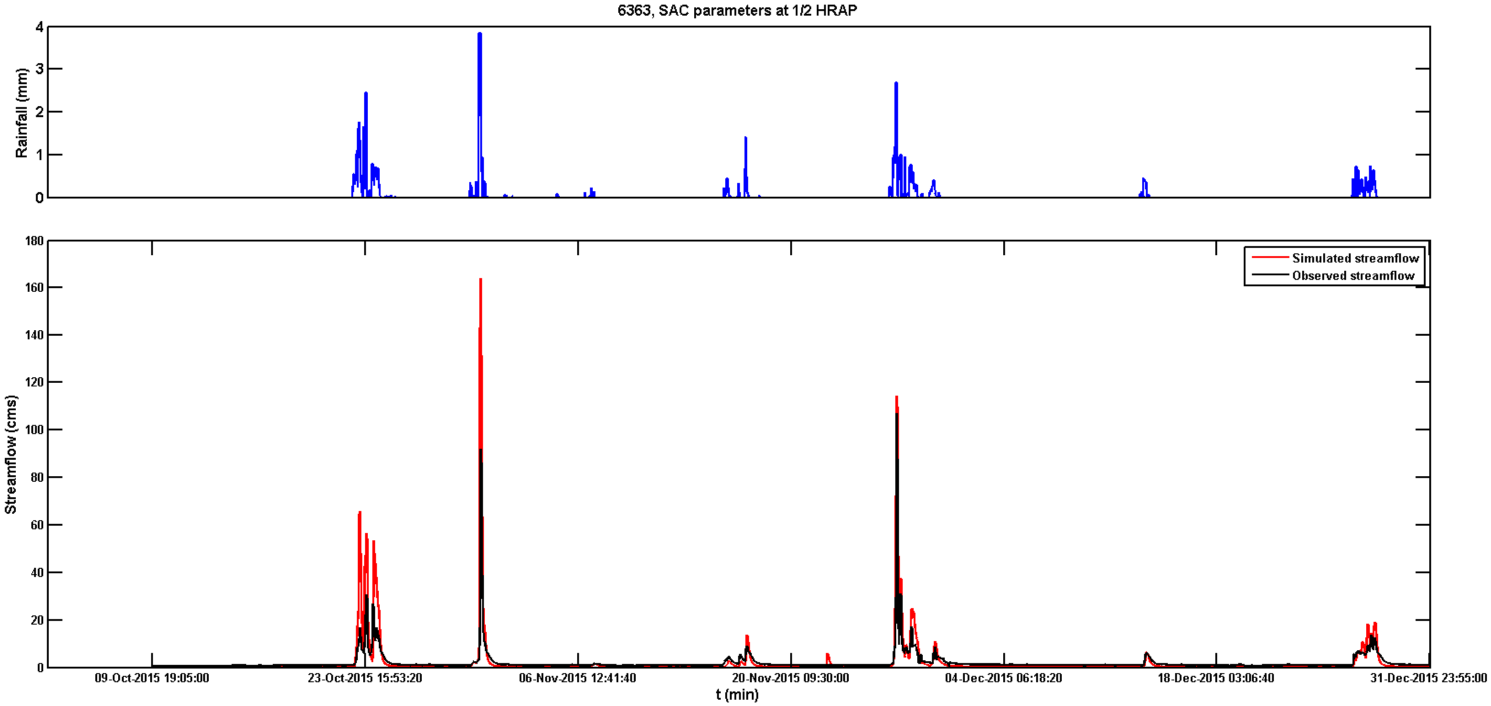

Figure A- 7 Streamflow simulation time series at model resolution of 1/4 HRAP and SAC parameters at 1/2 HRAP using MPE QPE at 6363

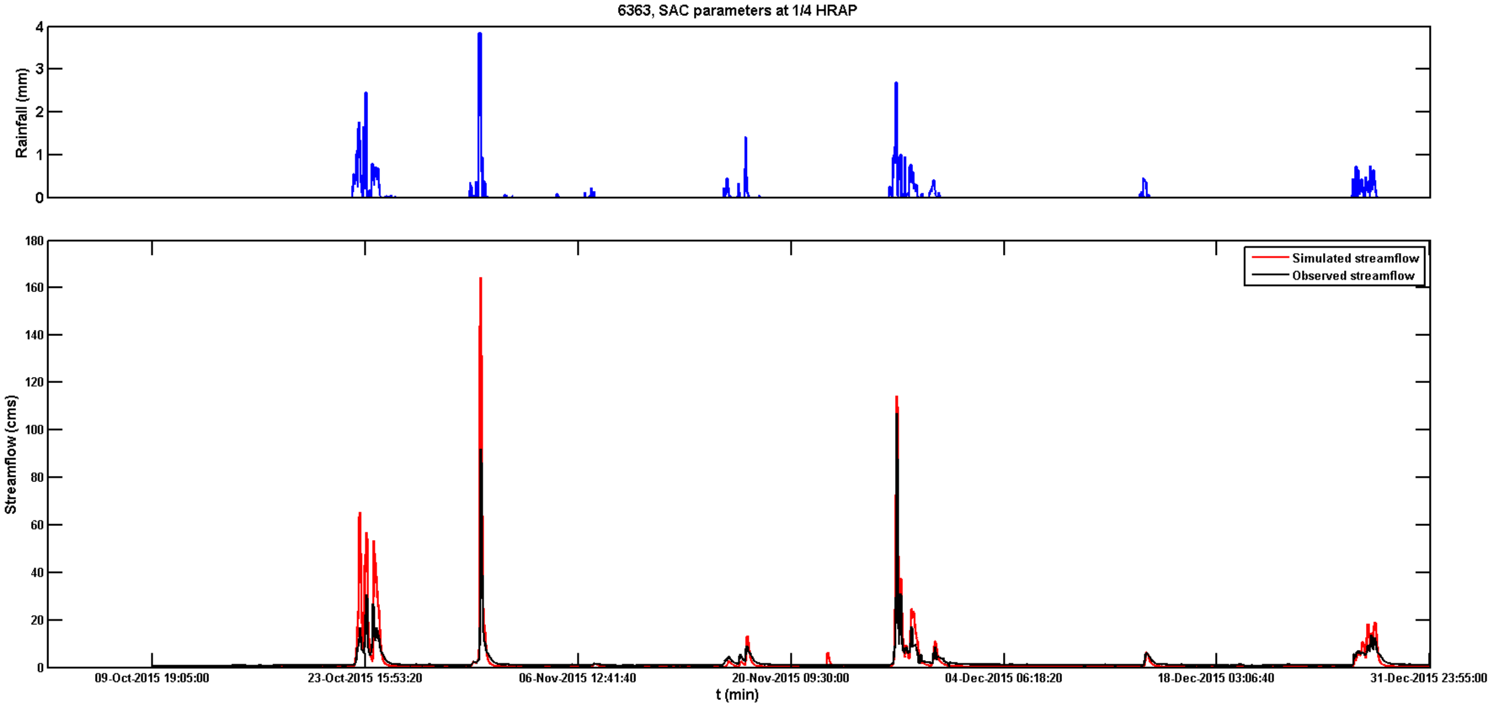

Figure A- 8 Streamflow simulation time series at model resolution of 1/4 HRAP and SAC parameters at 1/4 HRAP using MPE QPE at 6363

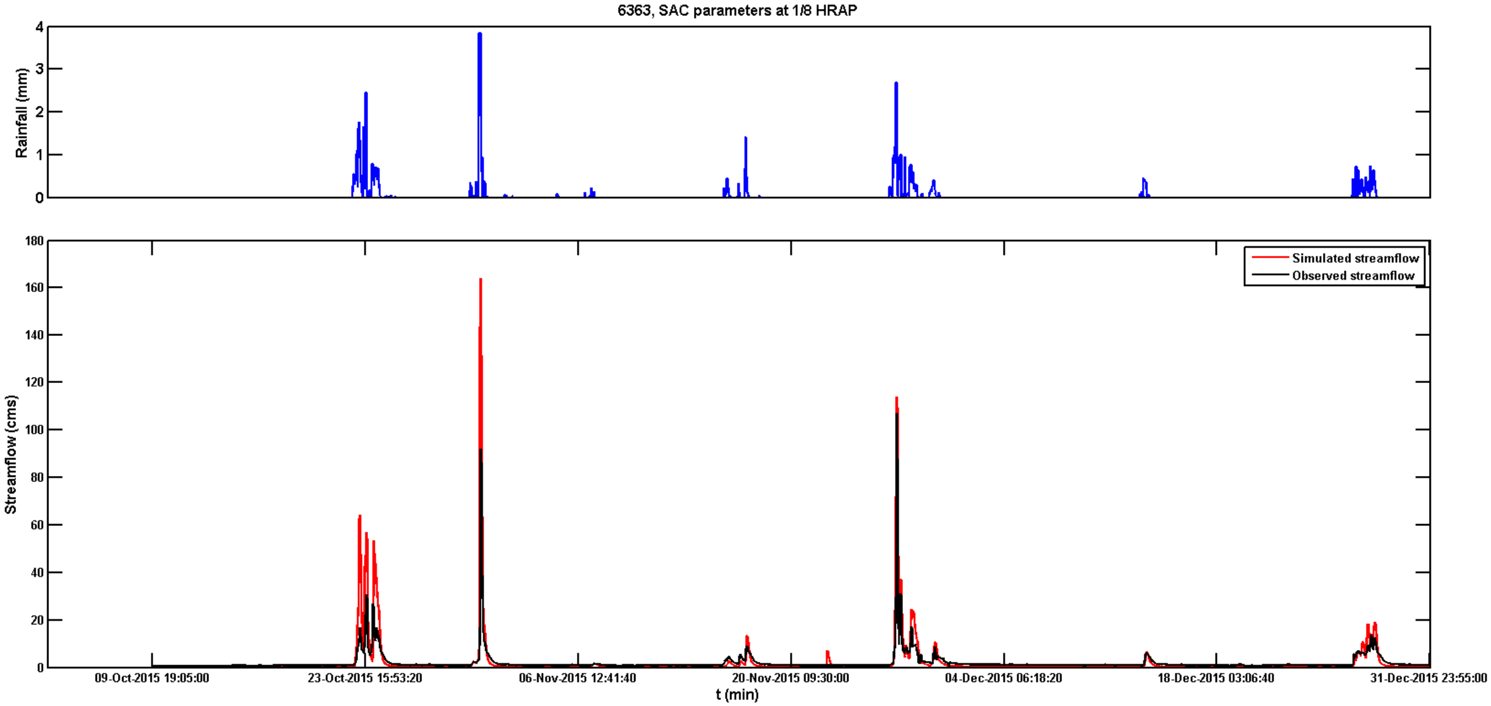

Figure A- 9 Streamflow simulation time series at model resolution of 1/4 HRAP and SAC parameters at 1/8 HRAP using MPE QPE at 6363

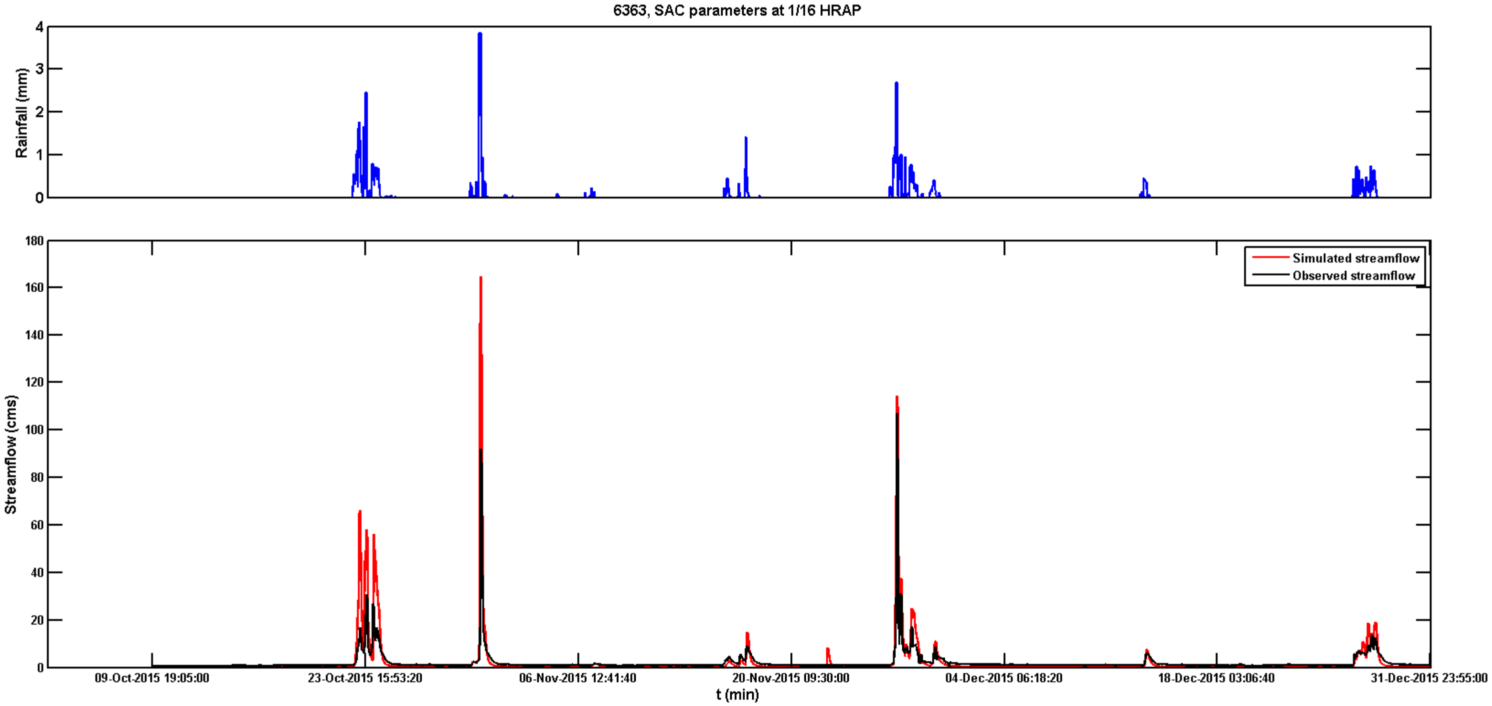

Figure A- 10 Streamflow simulation time series at model resolution of 1/4 HRAP and SAC parameters at 1/16 HRAP using MPE QPE at 6363

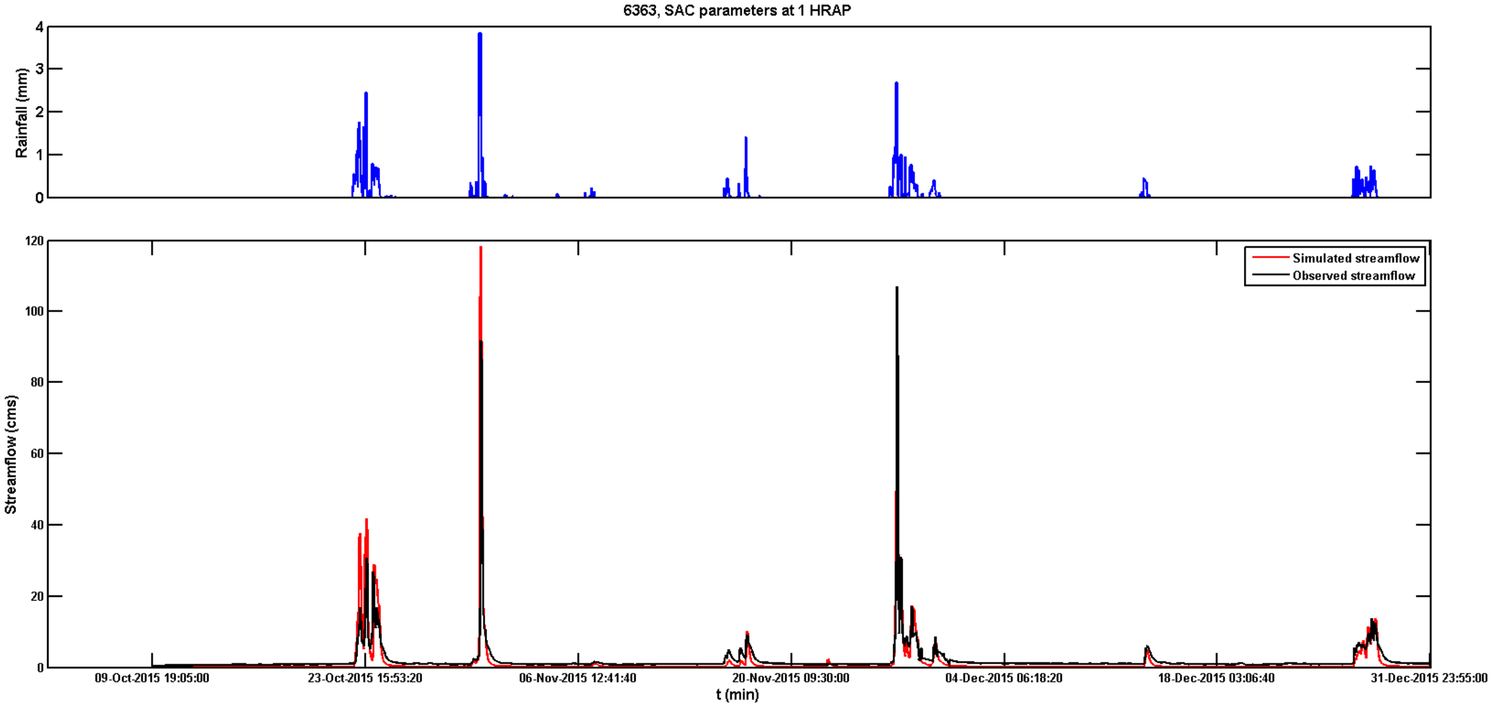

Figure A- 11 Streamflow simulation time series at model resolution of 1/8 HRAP and SAC parameters at 1 HRAP using MPE QPE at 6363

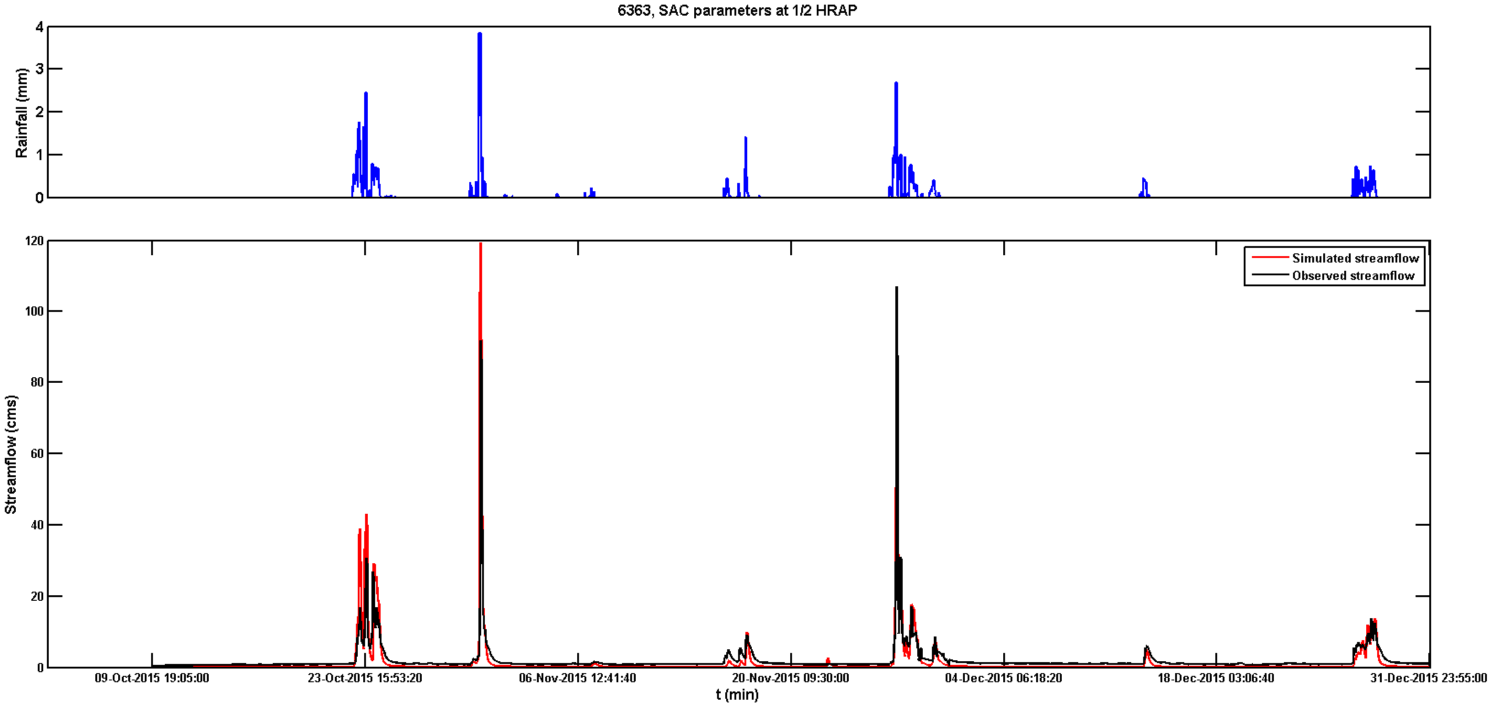

Figure A- 12 Streamflow simulation time series at model resolution of 1/8 HRAP and SAC parameters at 1/2 HRAP using MPE QPE at 6363

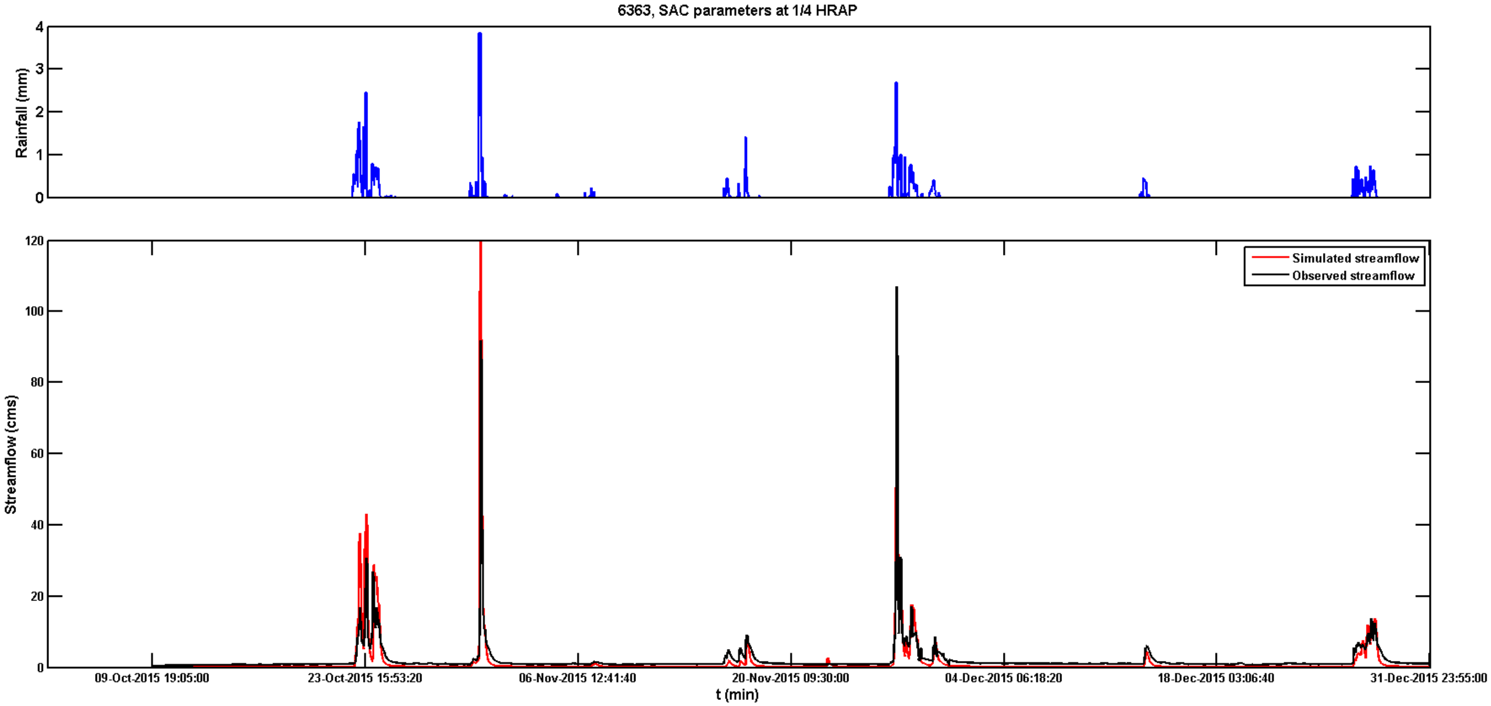

Figure A- 13 Streamflow simulation time series at model resolution of 1/8 HRAP and SAC parameters at 1/4 HRAP using MPE QPE at 6363

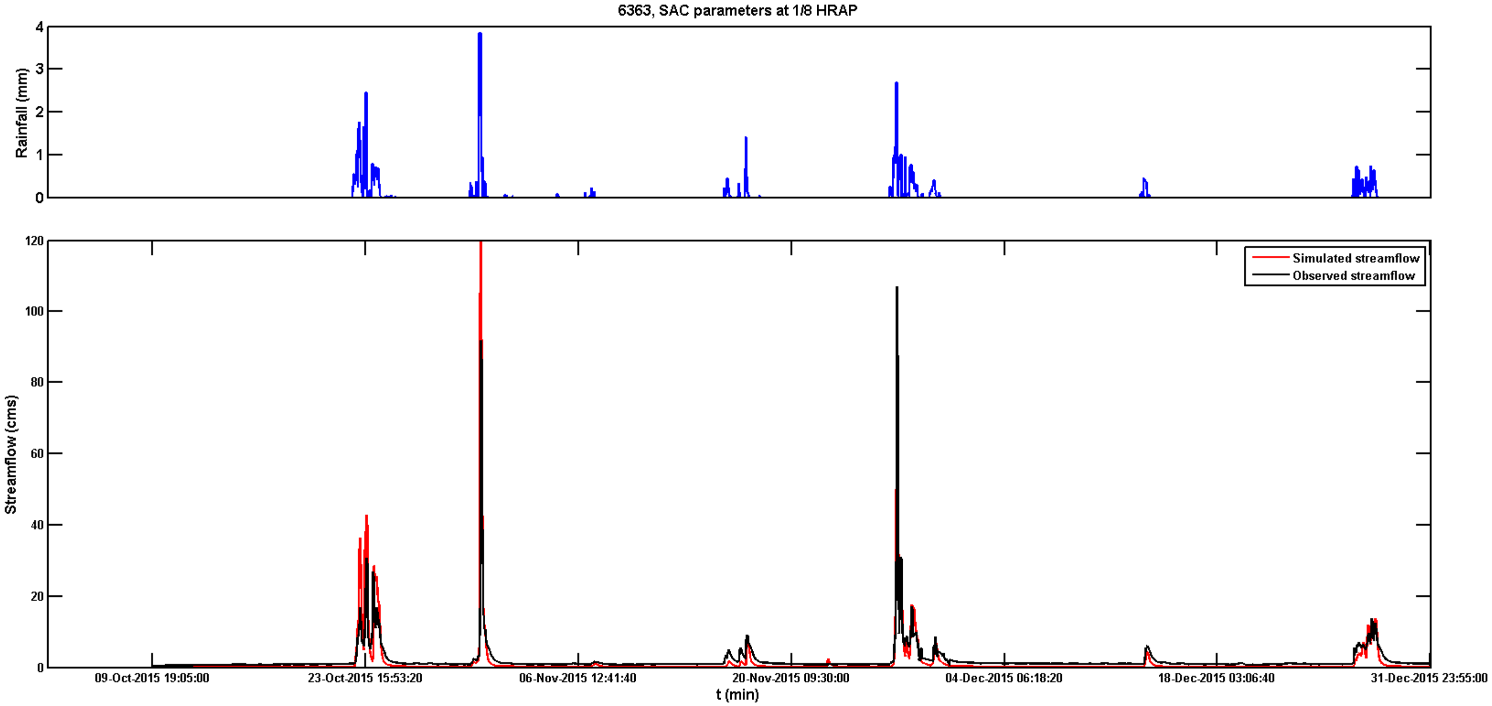

Figure A- 14 Streamflow simulation time series at model resolution of 1/8 HRAP and SAC parameters at 1/8 HRAP using MPE QPE at 6363

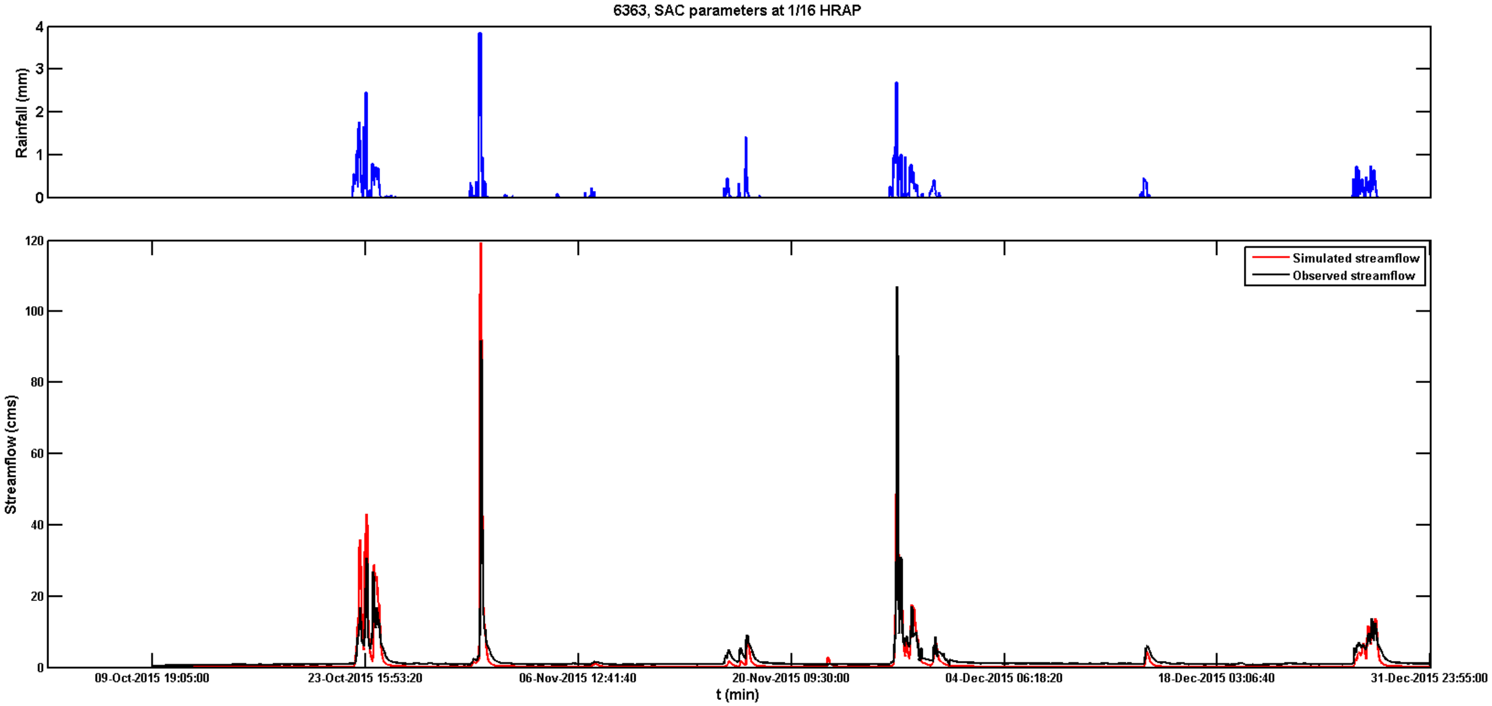

Figure A- 15 Streamflow simulation time series at model resolution of 1/8 HRAP and SAC parameters at 1/16 HRAP using MPE QPE at 6363

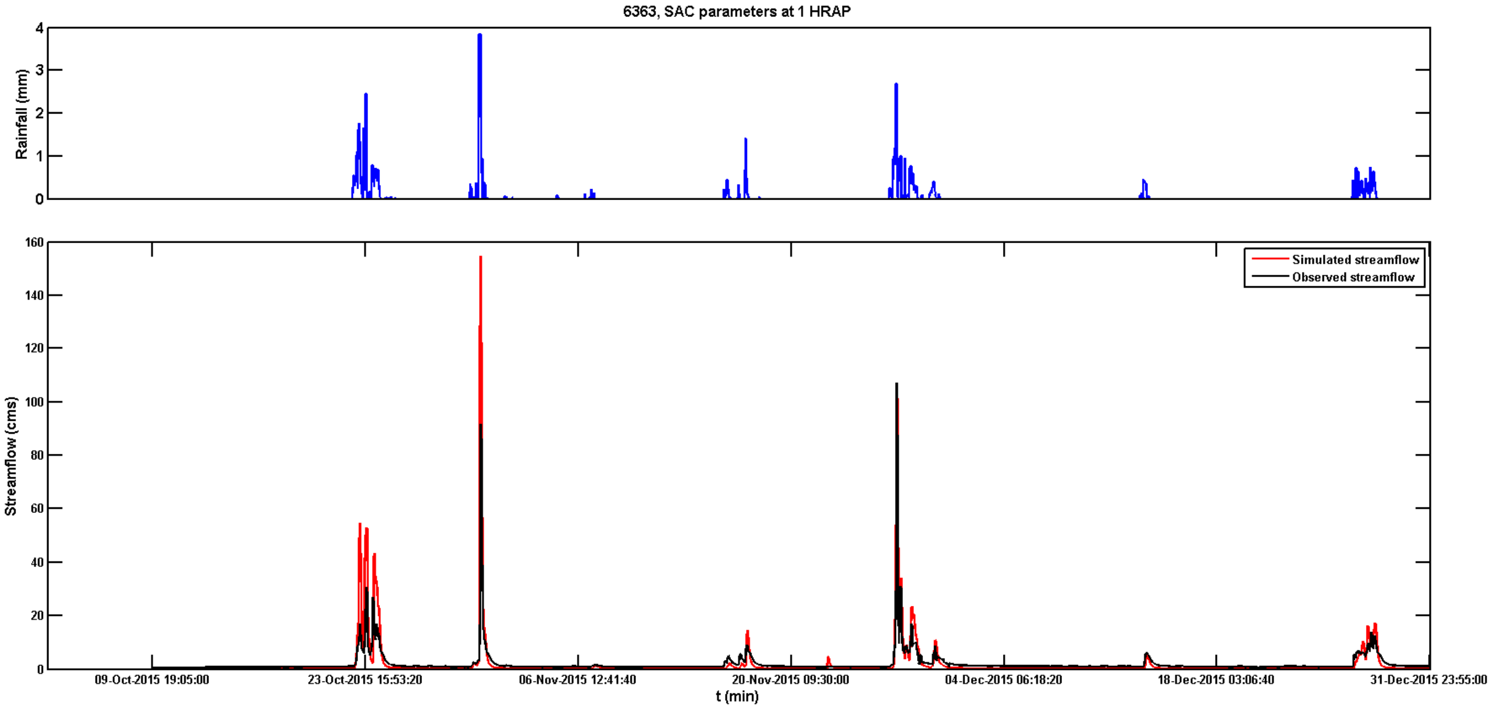

Figure A- 16 Streamflow simulation time series at model resolution of 1/16 HRAP and SAC parameters at 1 HRAP using MPE QPE at 6363

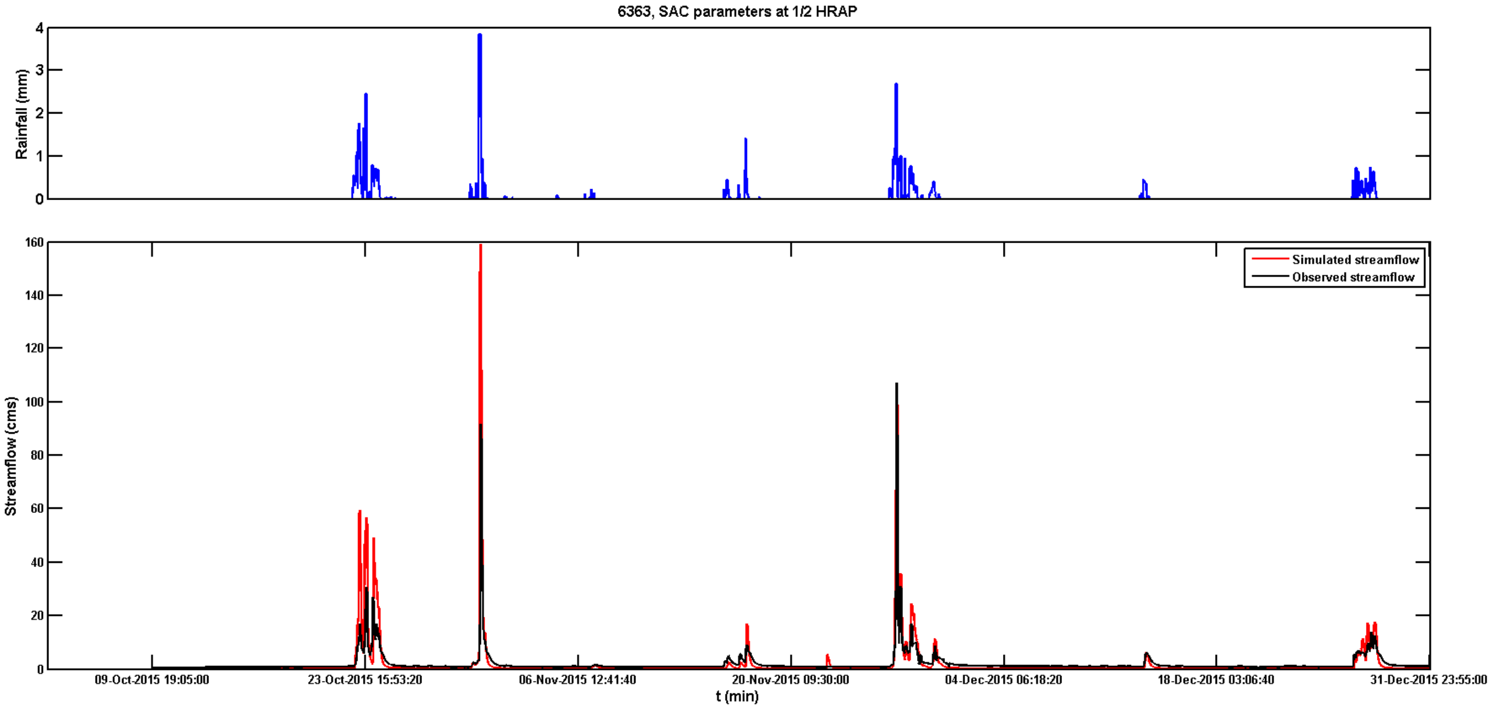

Figure A- 17 Streamflow simulation time series at model resolution of 1/16 HRAP and SAC parameters at 1/2 HRAP using MPE QPE at 6363

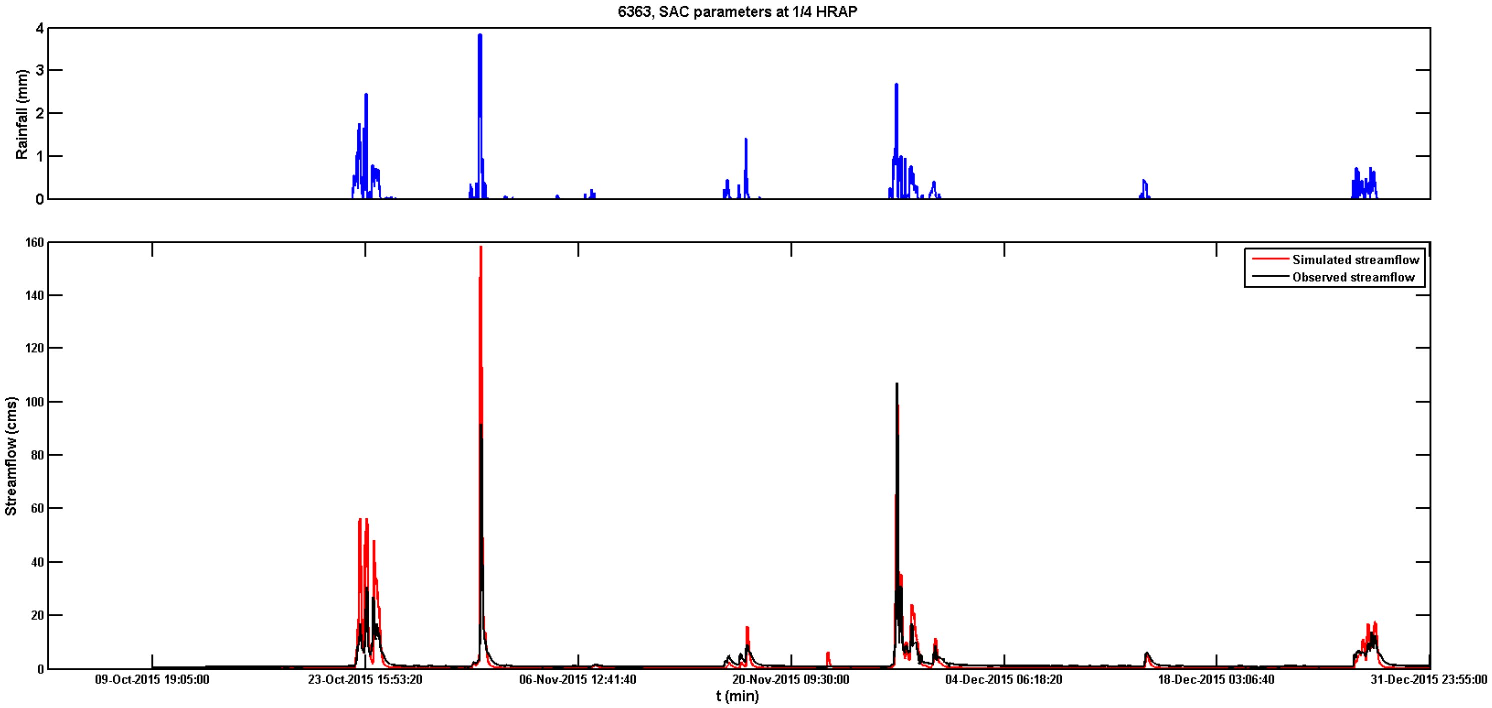

Figure A- 18 Streamflow simulation time series at model resolution of 1/16 HRAP and SAC parameters at 1/4 HRAP using MPE QPE at 6363

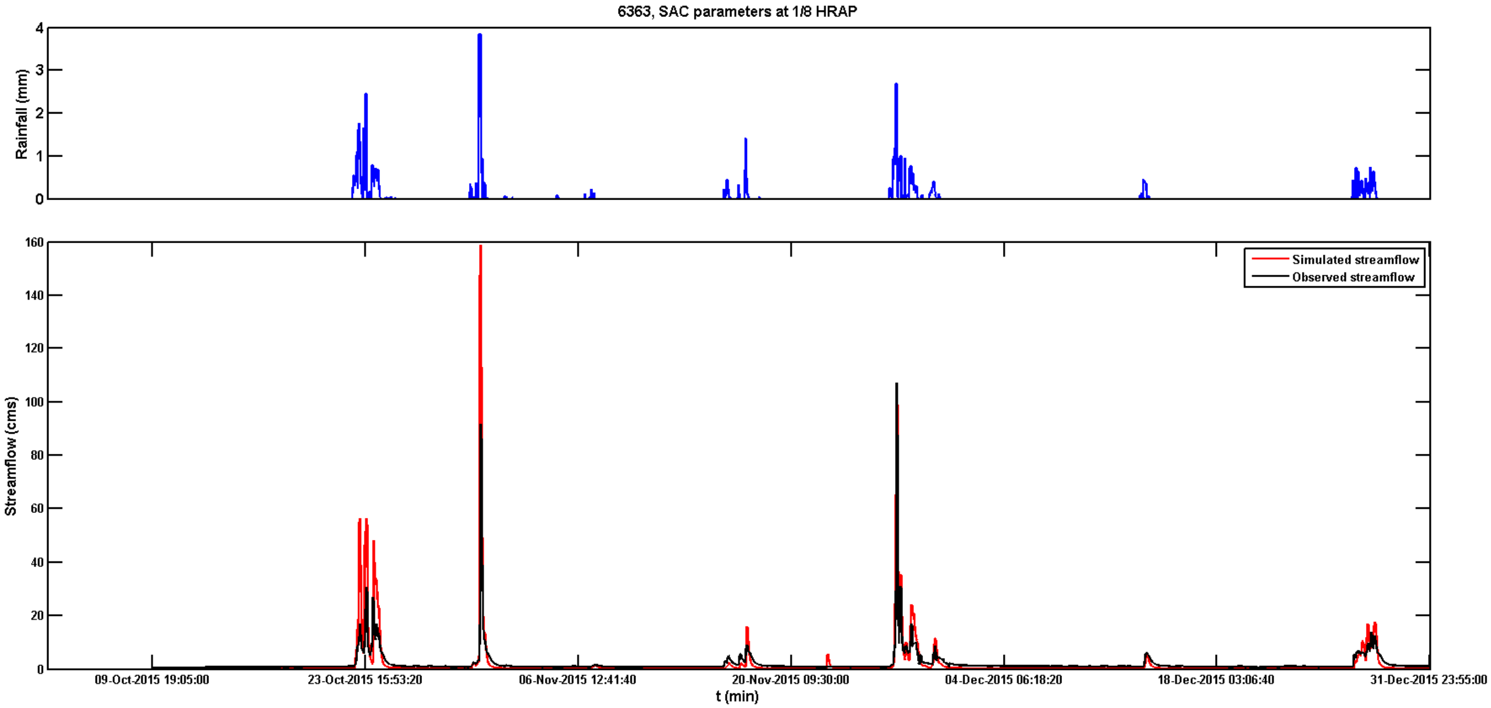

Figure A- 19 Streamflow simulation time series at model resolution of 1/16 HRAP and SAC parameters at 1/8 HRAP using MPE QPE at 6363

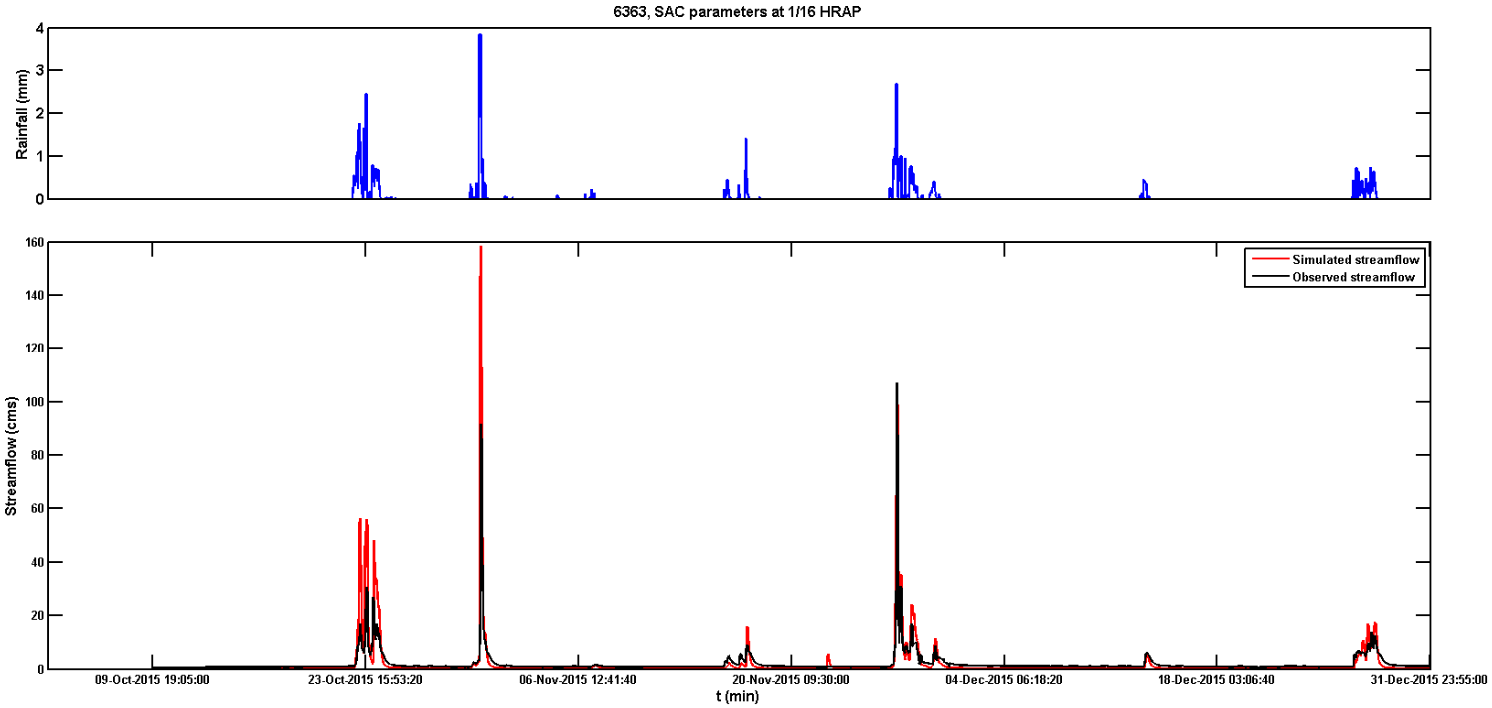

Figure A- 20 Streamflow simulation time series at model resolution of 1/16 HRAP and SAC parameters at 1/16 HRAP using MPE QPE at 6363

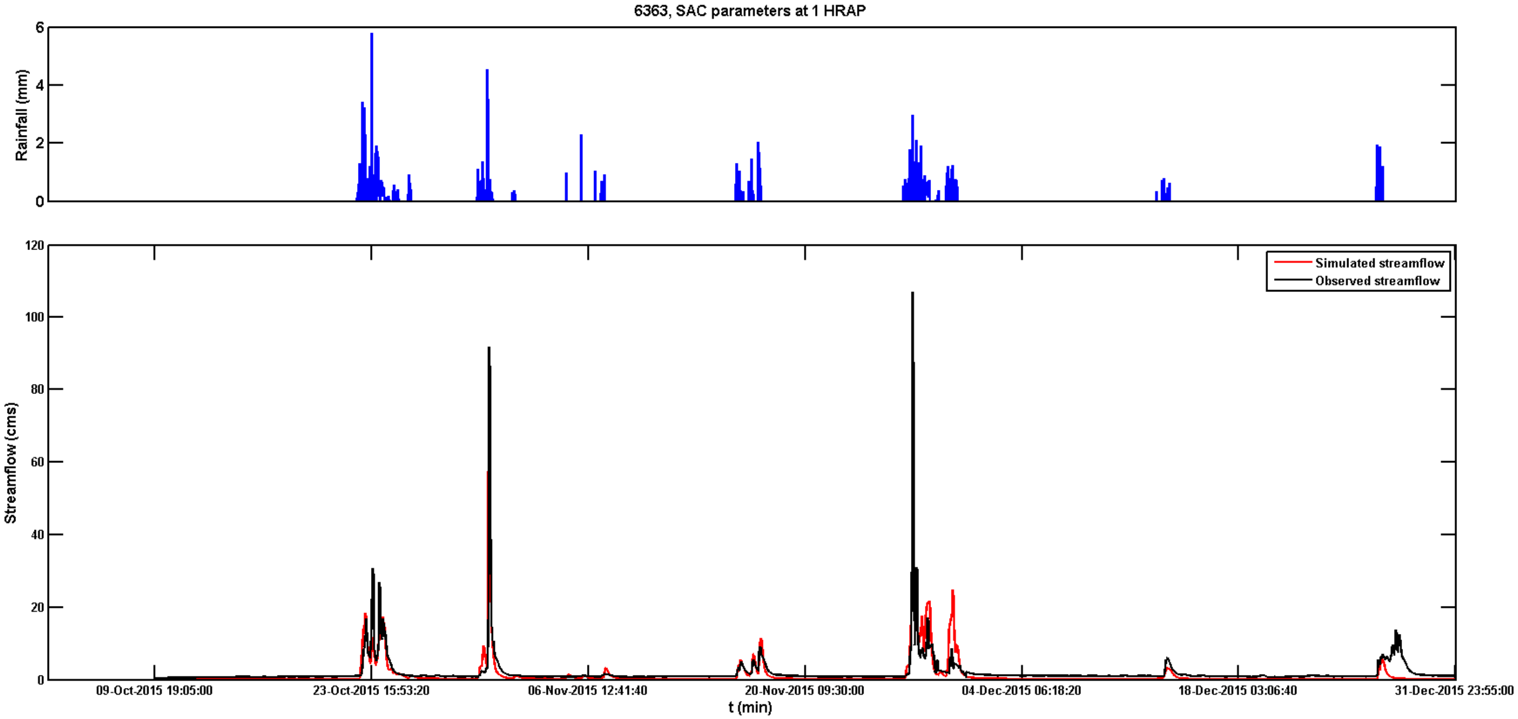

Figure A- 21 Streamflow simulation time series at model resolution of 1/2 HRAP and SAC parameters at 1 HRAP using CASA QPE at 6363

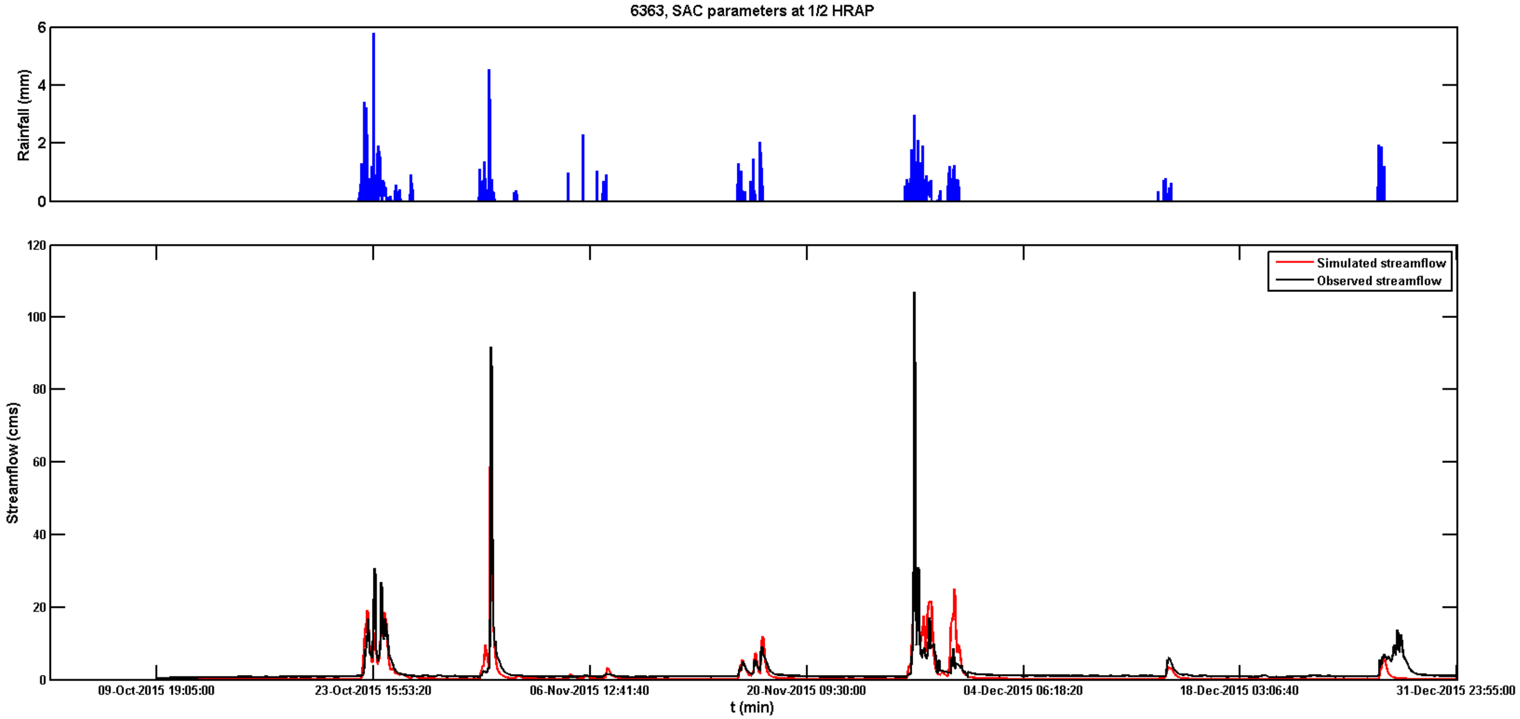

Figure A- 22 Streamflow simulation time series at model resolution of 1/2 HRAP and SAC parameters at 1/2 HRAP using CASA QPE at 6363

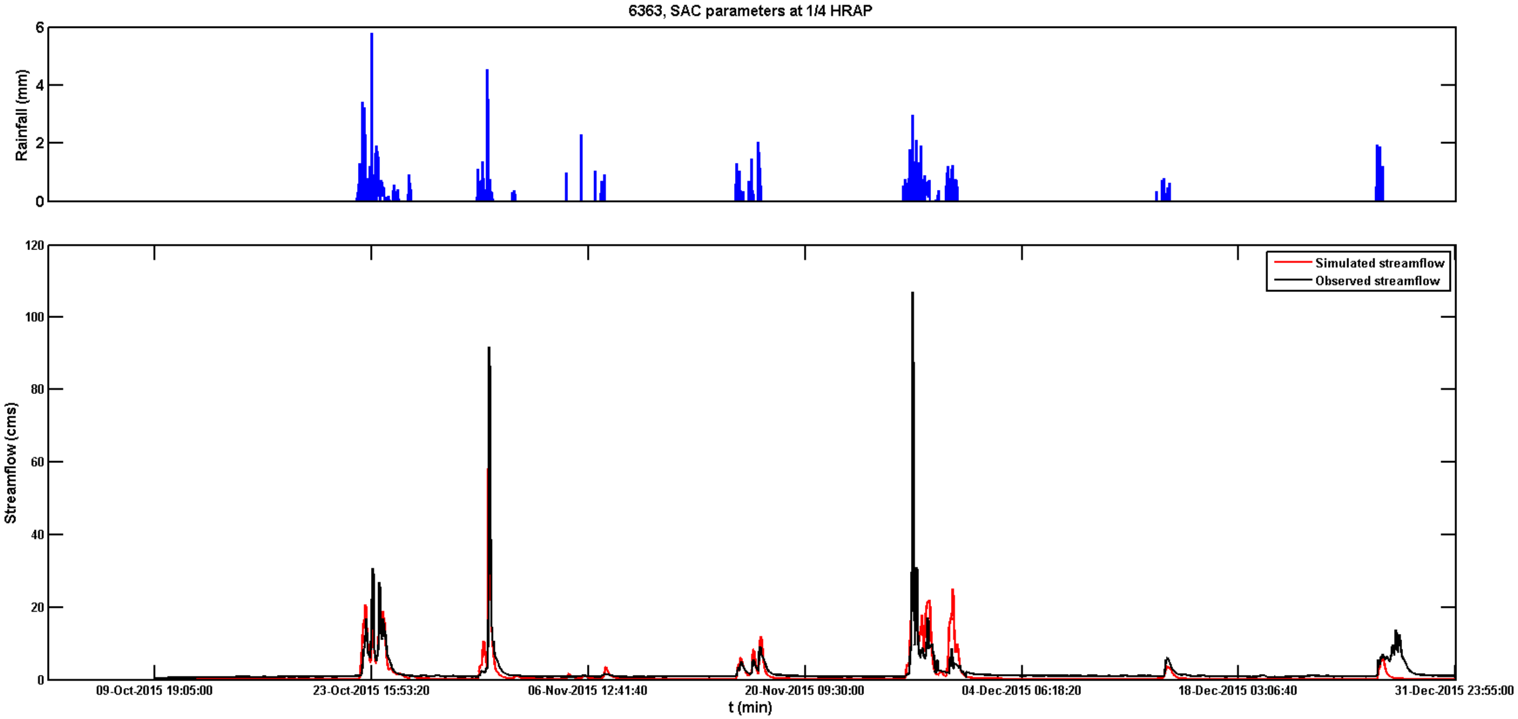

Figure A- 23 Streamflow simulation time series at model resolution of 1/2 HRAP and SAC parameters at 1/4 HRAP using CASA QPE at 6363

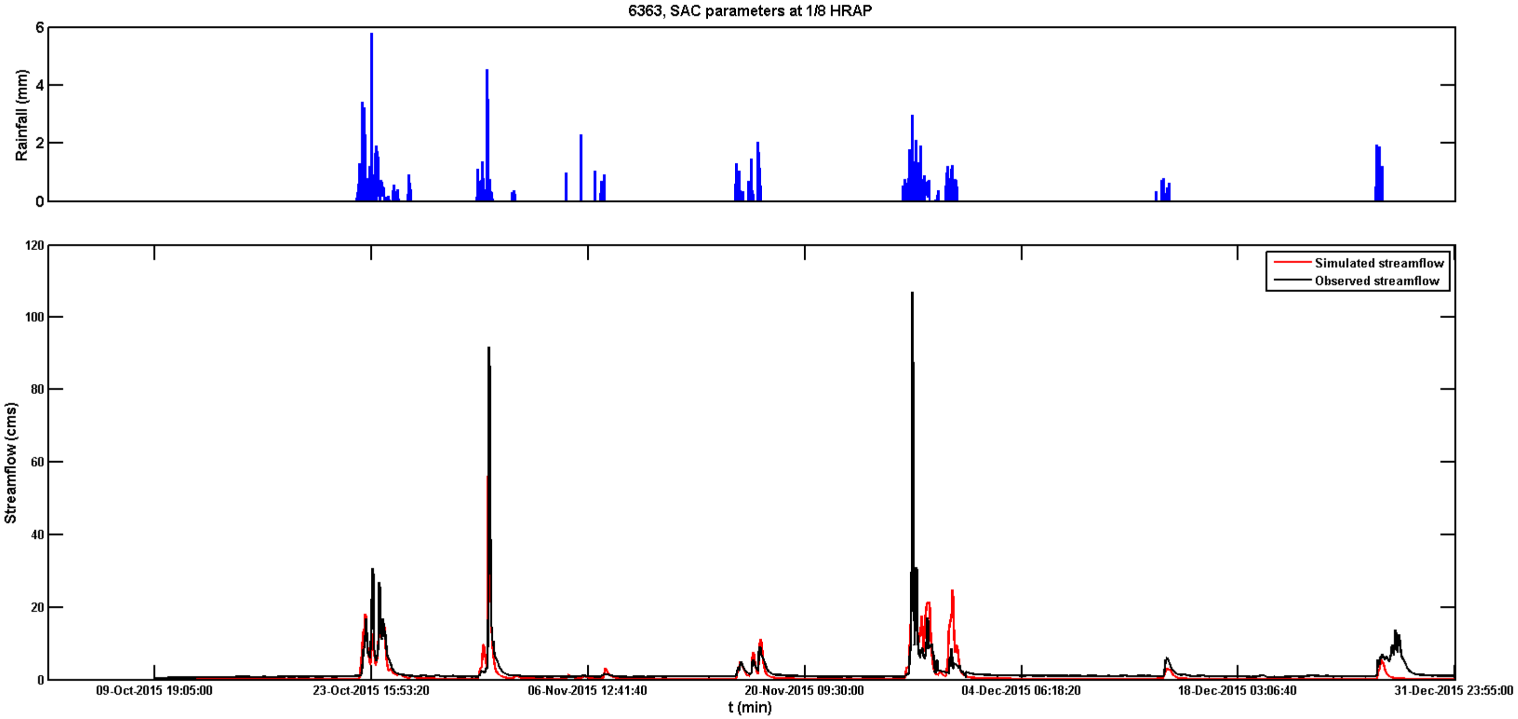

Figure A- 24 Streamflow simulation time series at model resolution of 1/2 HRAP and SAC parameters at 1/8 HRAP using CASA QPE at 6363

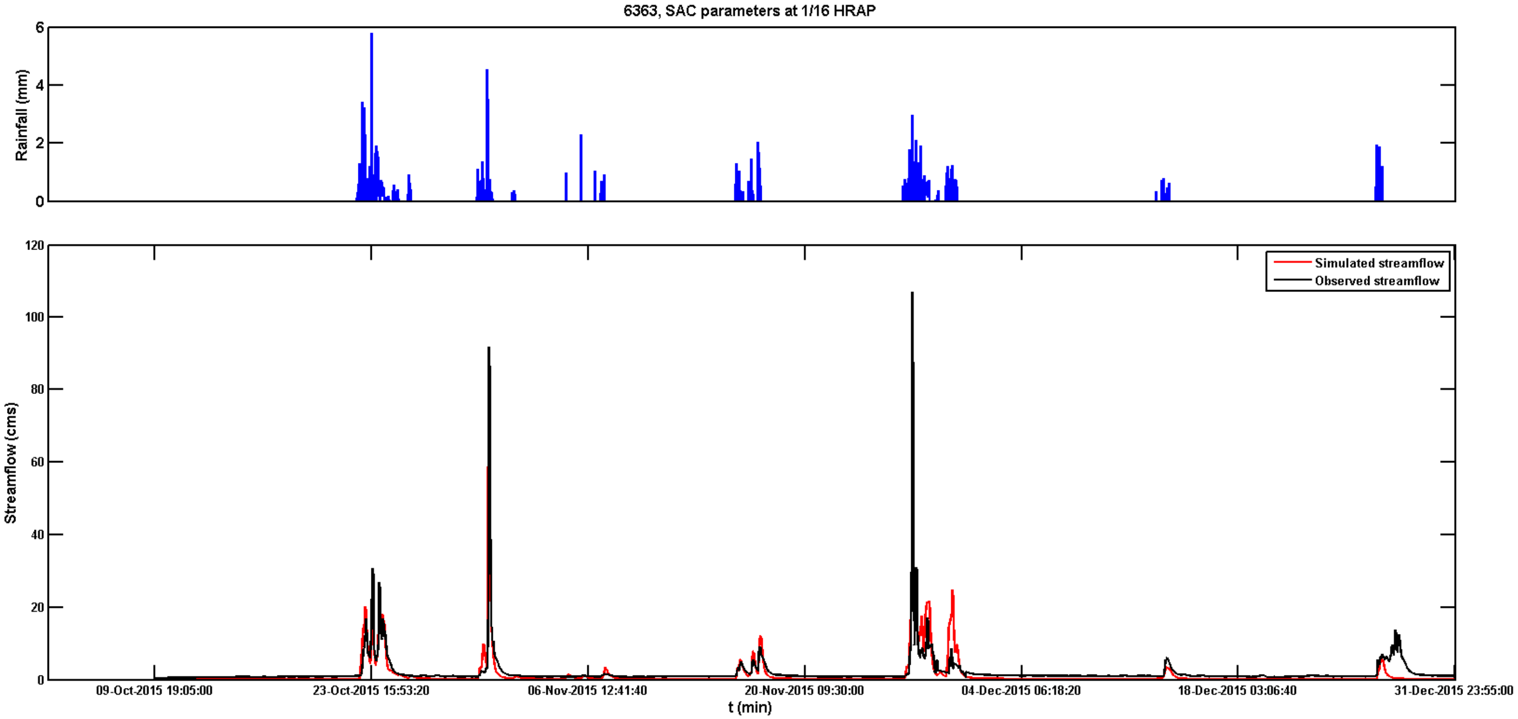

Figure A- 25 Streamflow simulation time series at model resolution of 1/2 HRAP and SAC parameters at 1/16 HRAP using CASA QPE at 6363

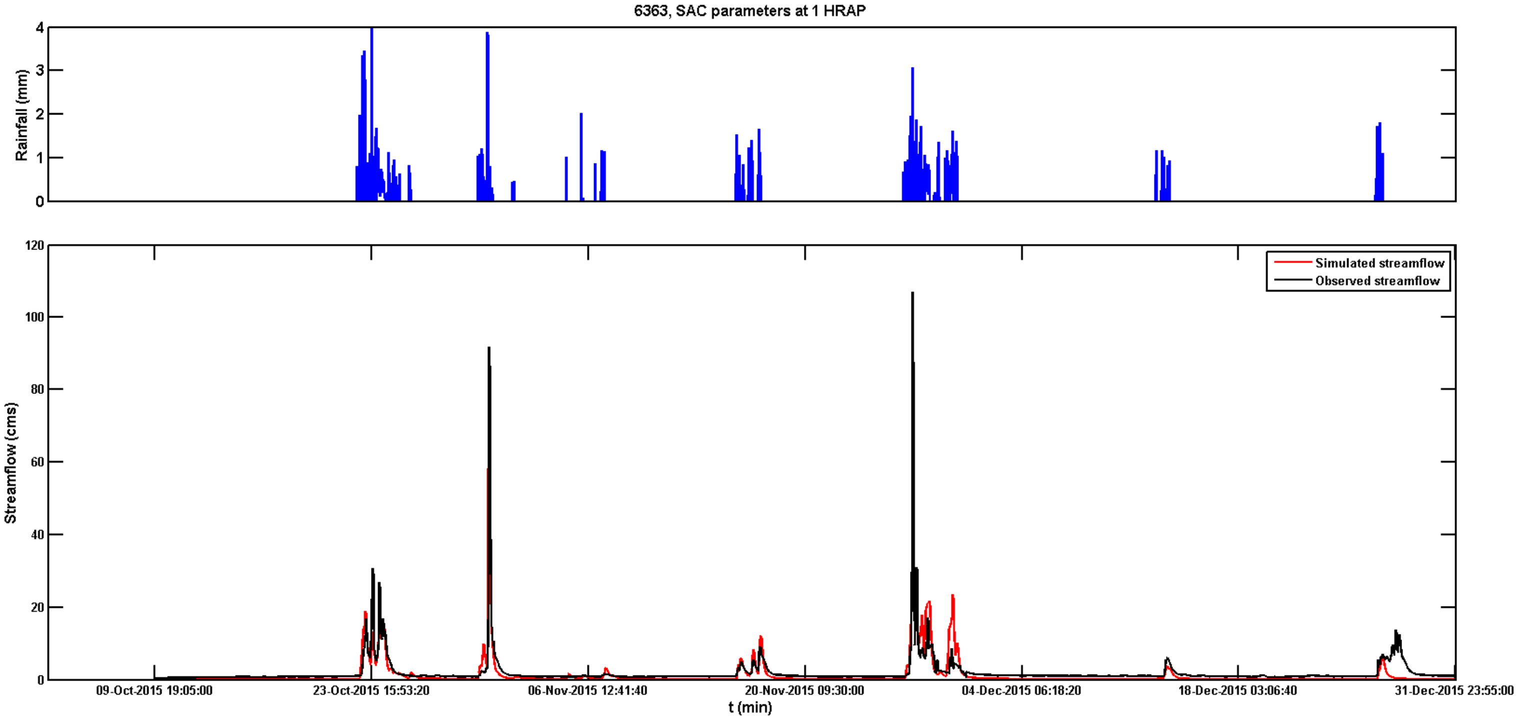

Figure A- 26 Streamflow simulation time series at model resolution of 1/4 HRAP and SAC parameters at 1 HRAP using CASA QPE at 6363

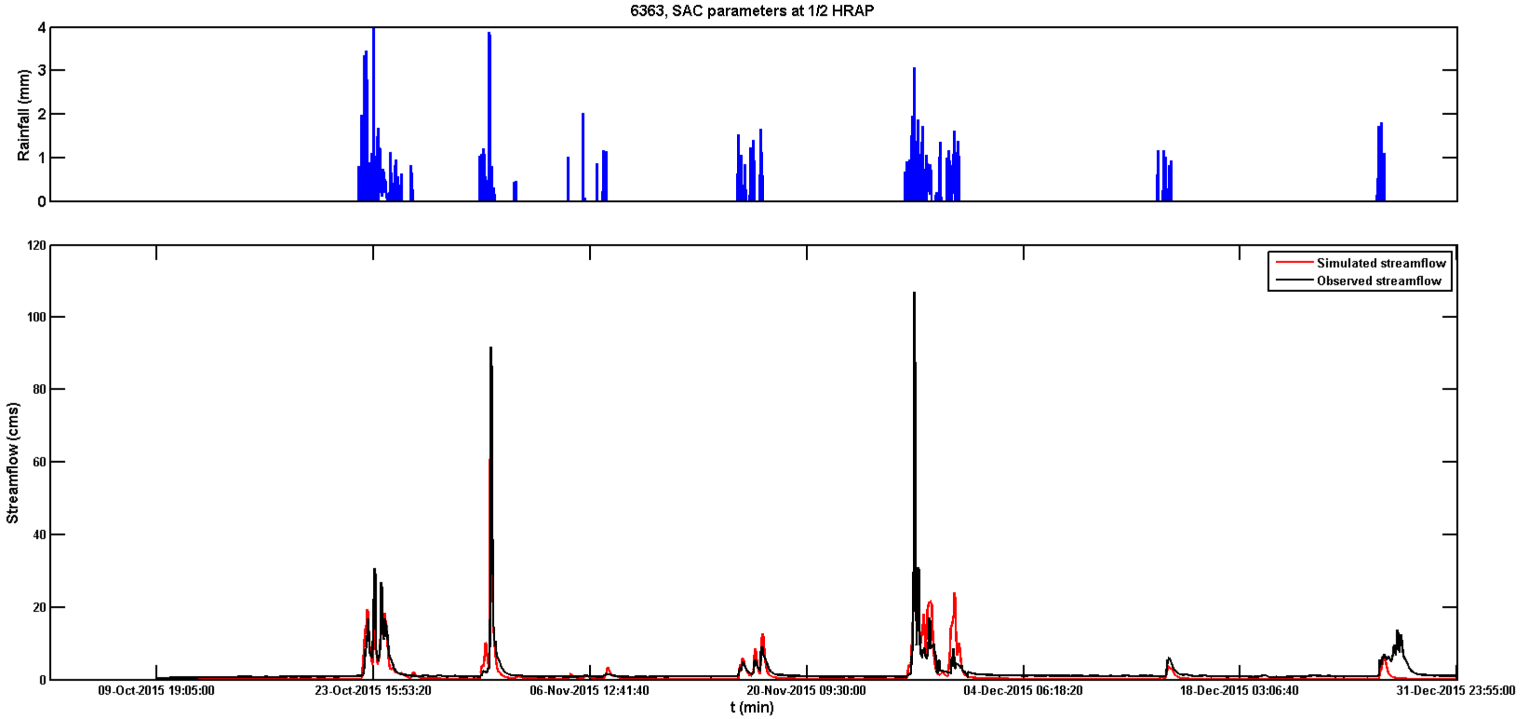

Figure A- 27 Streamflow simulation time series at model resolution of 1/4 HRAP and SAC parameters at 1/2 HRAP using CASA QPE at 6363

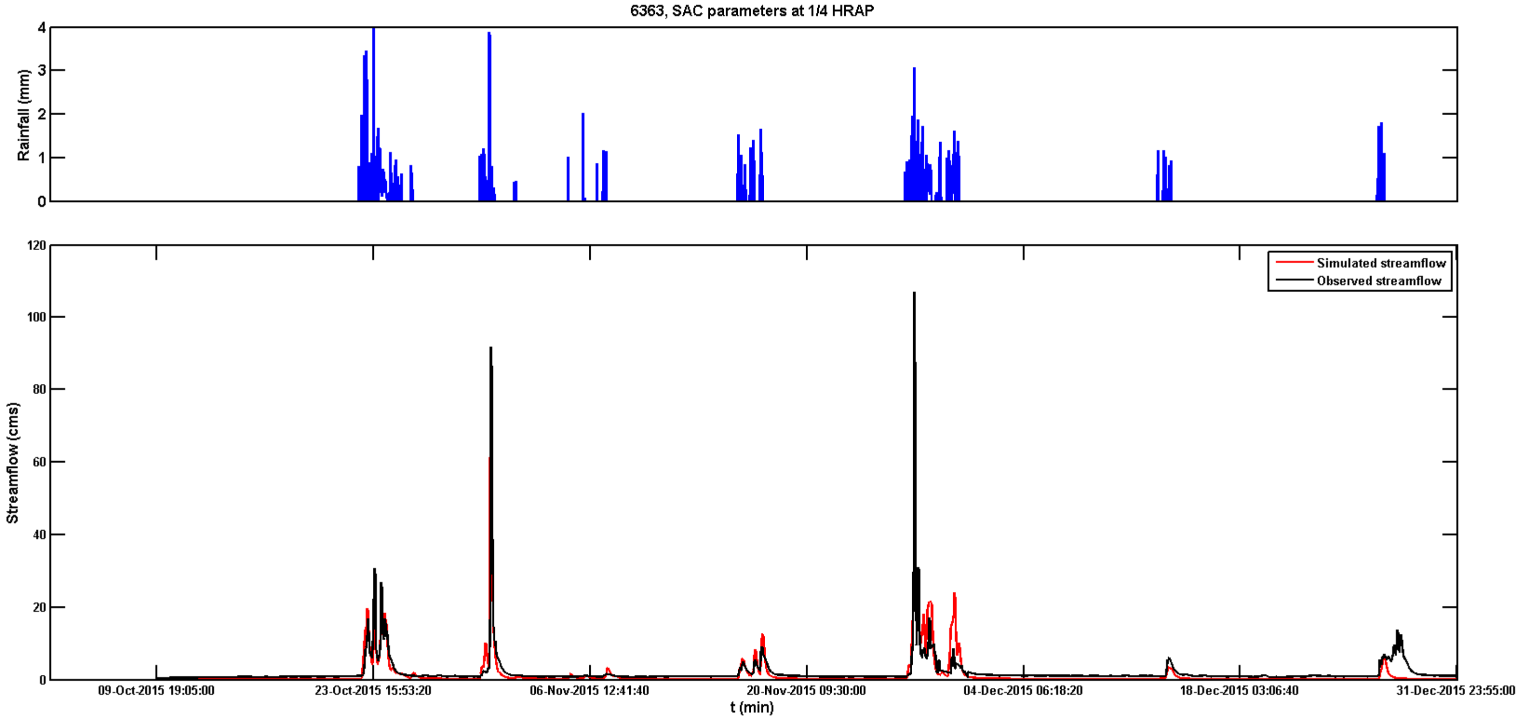

Figure A- 28 Streamflow simulation time series at model resolution of 1/4 HRAP and SAC parameters at 1/4 HRAP using CASA QPE at 6363

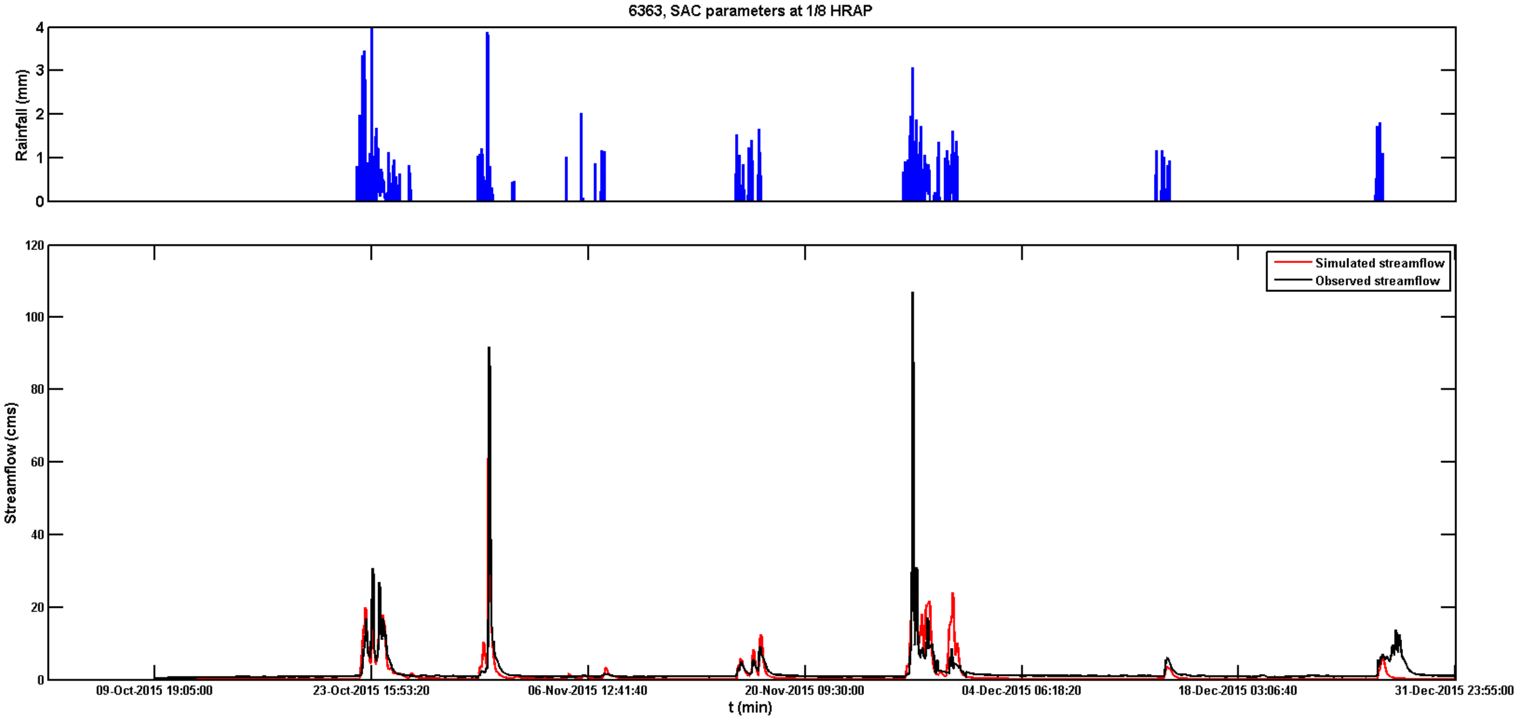

Figure A- 29 Streamflow simulation time series at model resolution of 1/4 HRAP and SAC parameters at 1/8 HRAP using CASA QPE at 6363

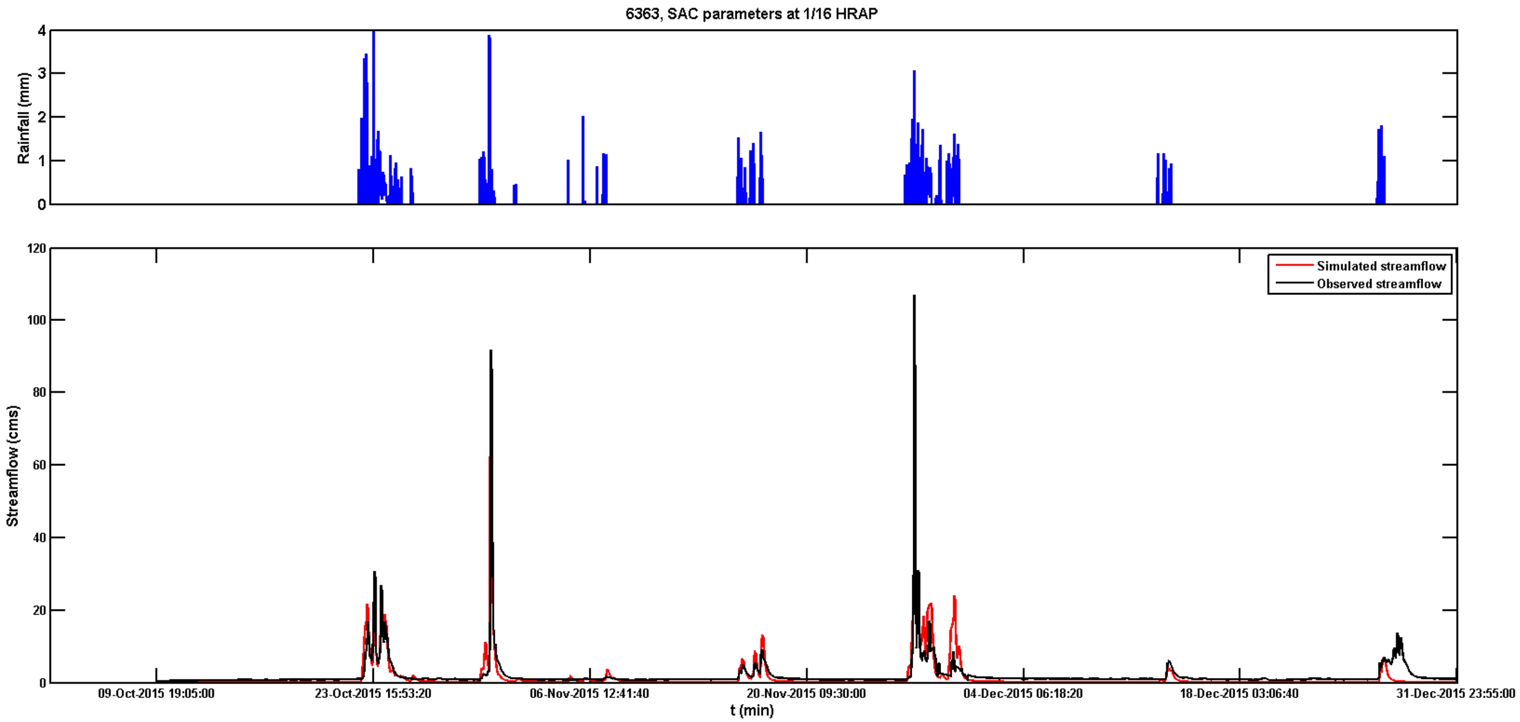

Figure A- 30 Streamflow simulation time series at model resolution of 1/4 HRAP and SAC parameters at 1/16 HRAP using CASA QPE at 6363

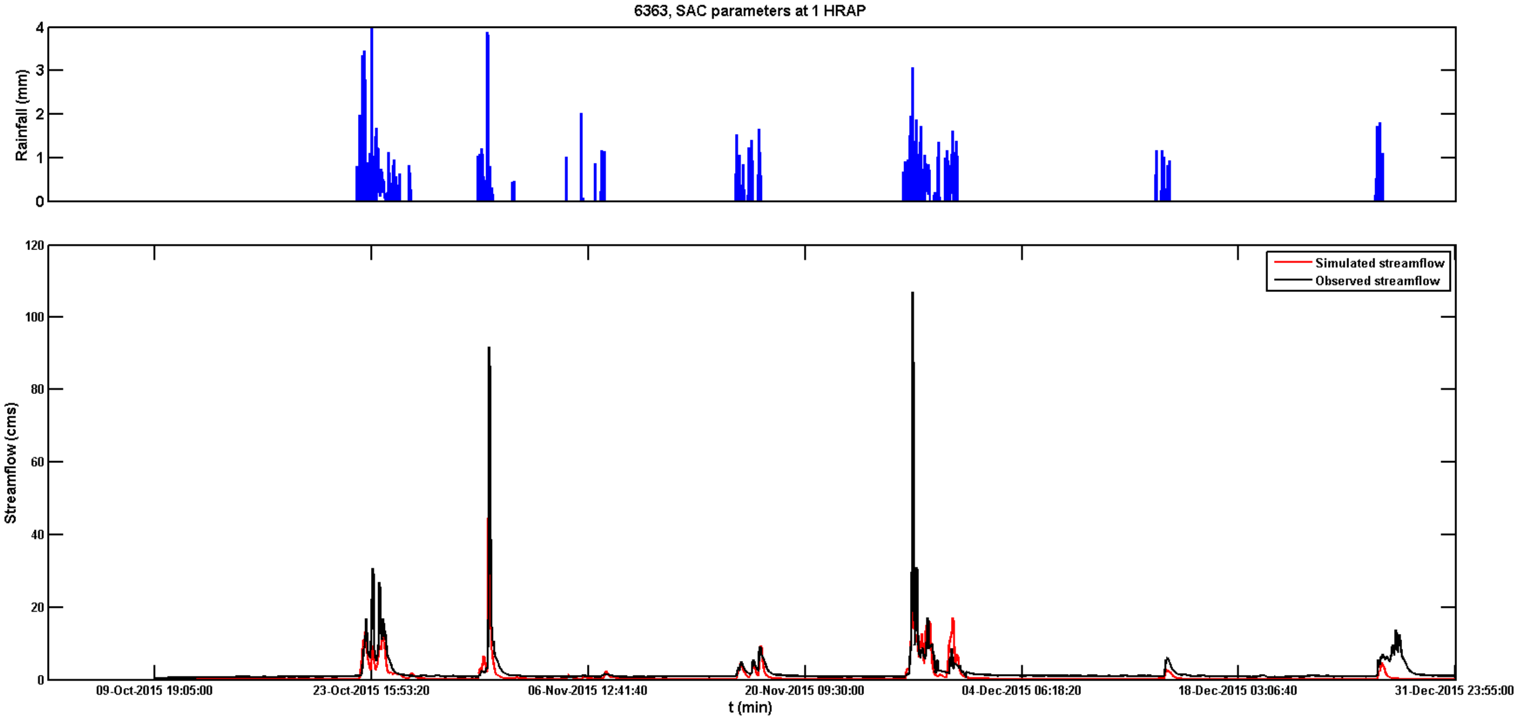

Figure A- 31 Streamflow simulation time series at model resolution of 1/8 HRAP and SAC parameters at 1 HRAP using CASA QPE at 6363

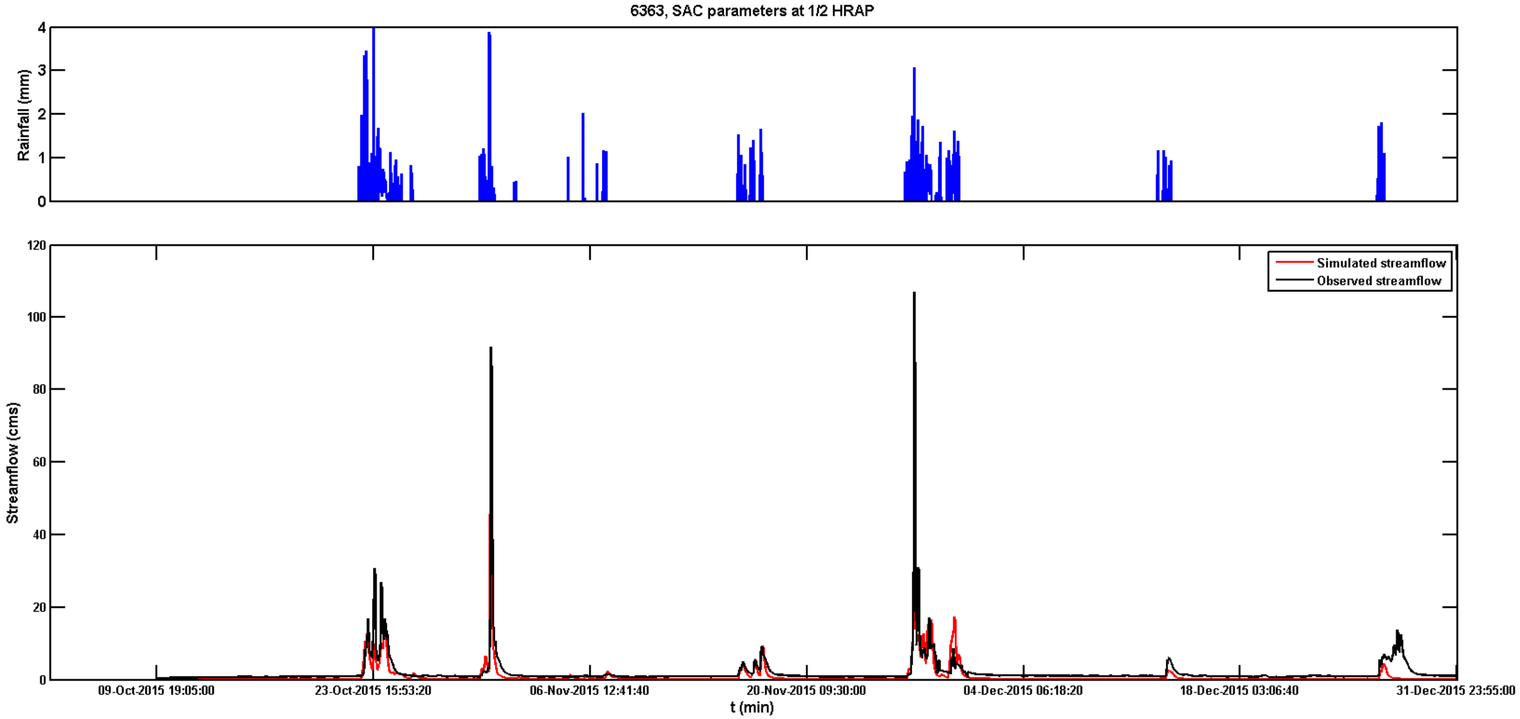

Figure A- 32 Streamflow simulation time series at model resolution of 1/8 HRAP and SAC parameters at 1/2 HRAP using CASA QPE at 6363

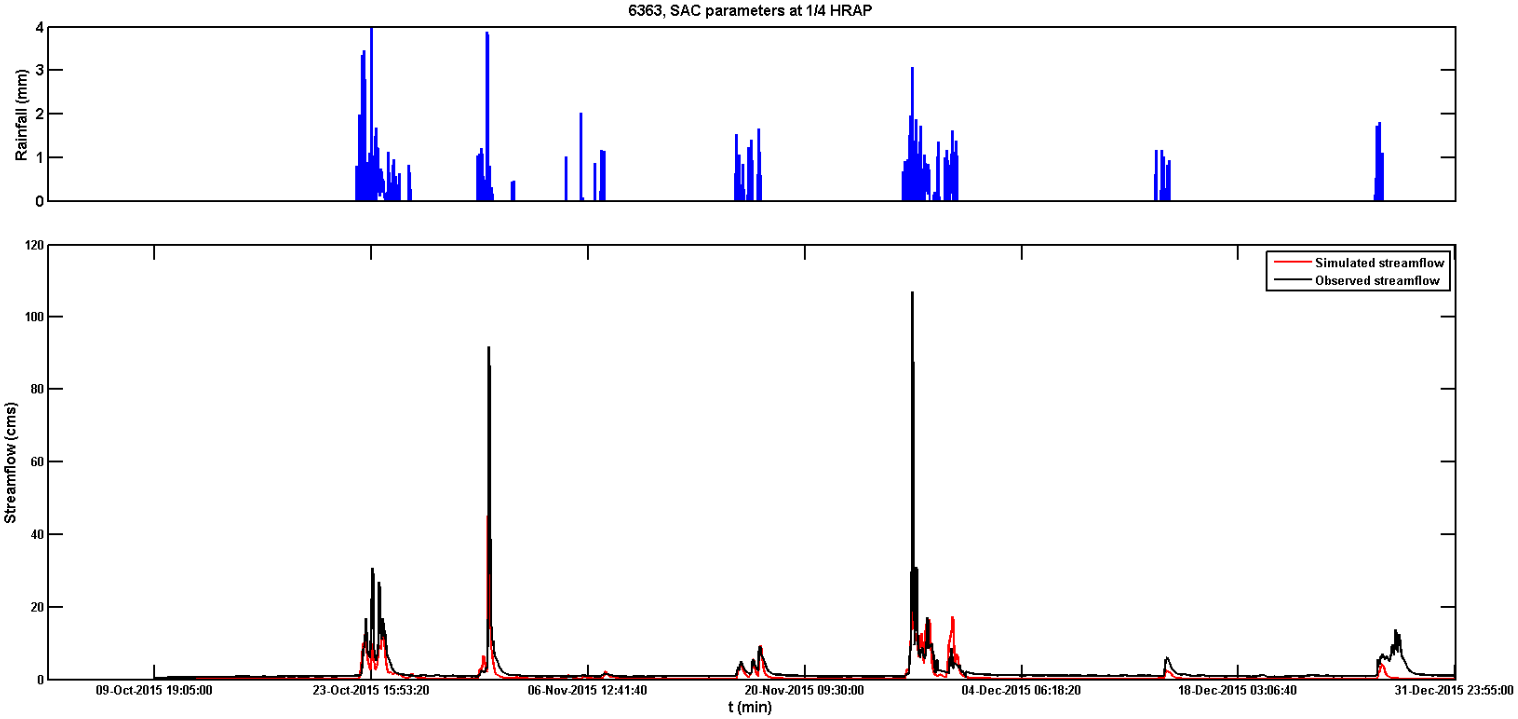

Figure A- 33 Streamflow simulation time series at model resolution of 1/8 HRAP and SAC parameters at 1/4 HRAP using CASA QPE at 6363

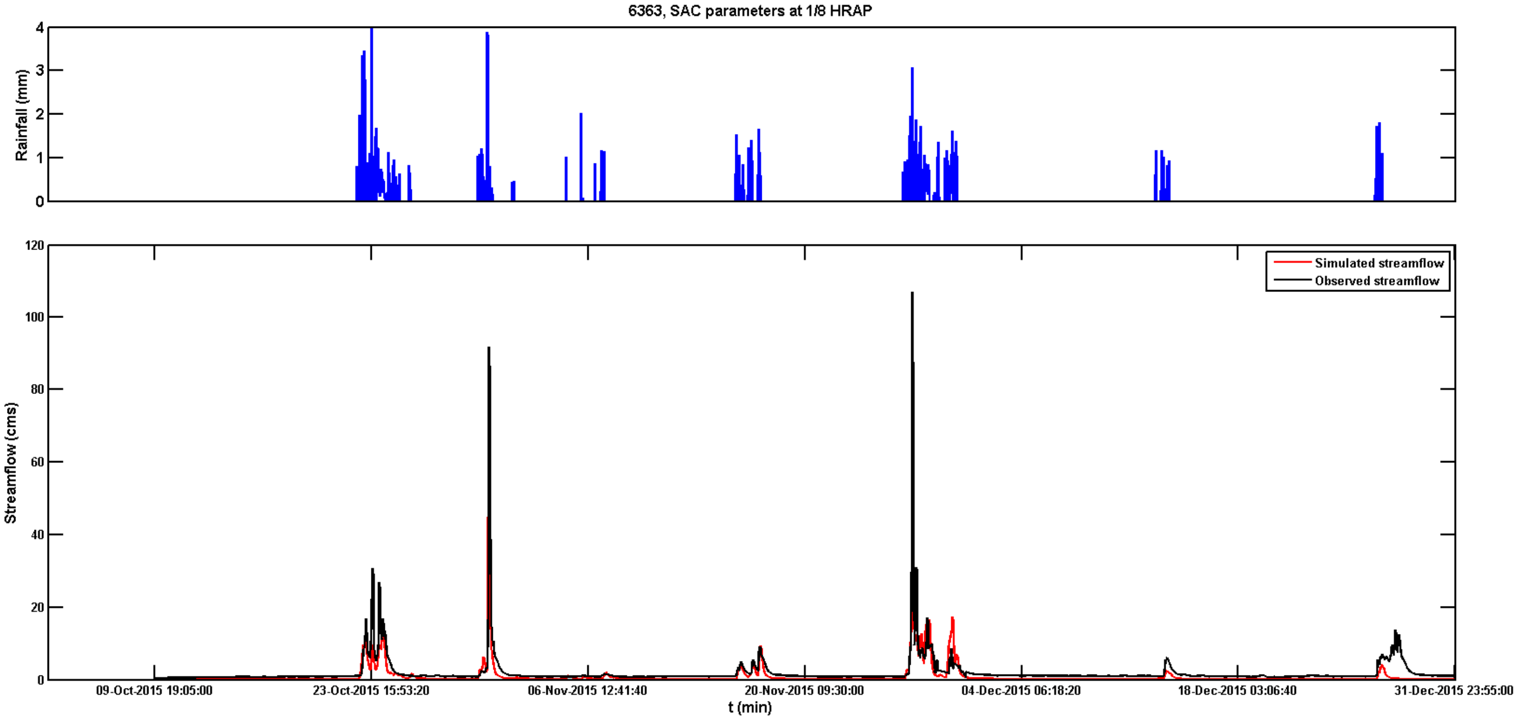

Figure A- 34 Streamflow simulation time series at model resolution of 1/8 HRAP and SAC parameters at 1/8 HRAP using CASA QPE at 6363

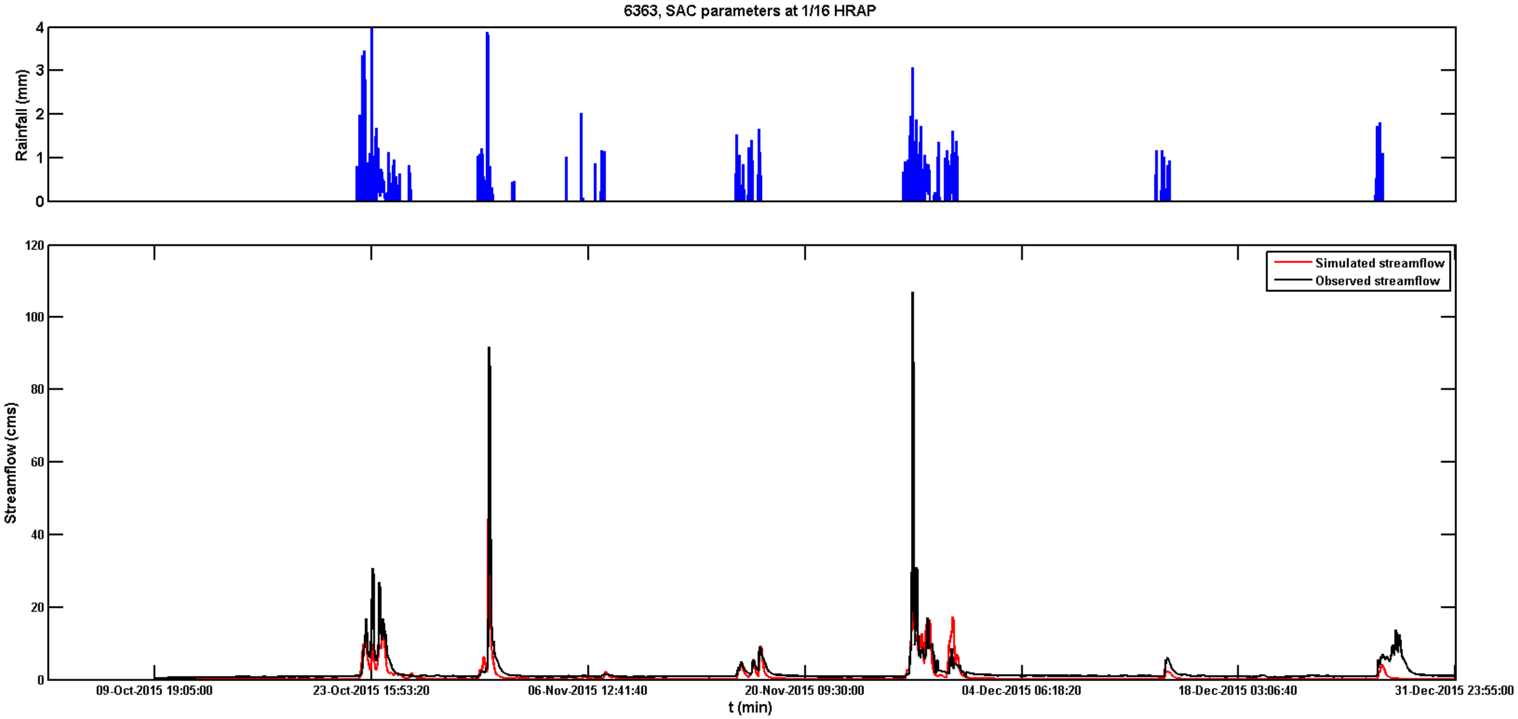

Figure A- 35 Streamflow simulation time series at model resolution of 1/8 HRAP and SAC parameters at 1/16 HRAP using CASA QPE at 6363

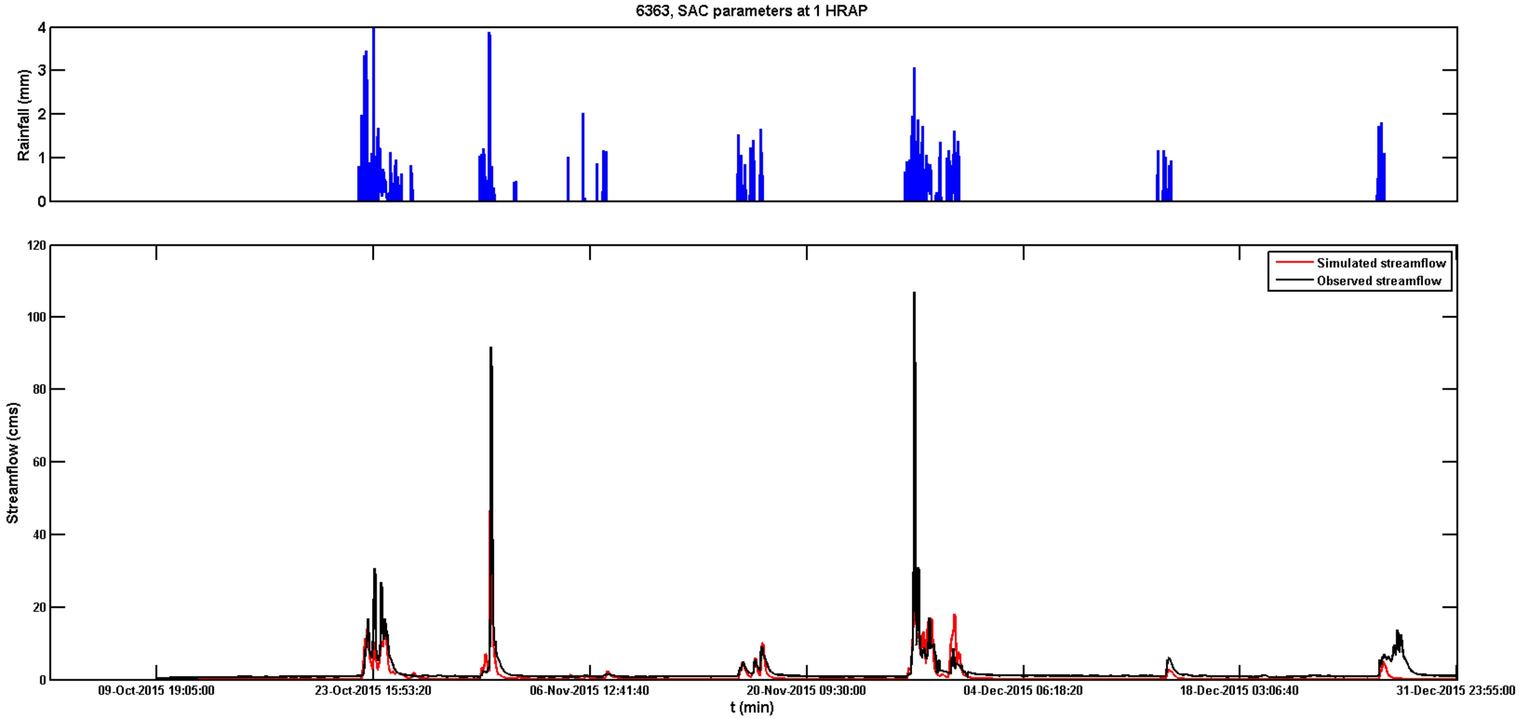

Figure A- 36 Streamflow simulation time series at model resolution of 1/16 HRAP and SAC parameters at 1 HRAP using CASA QPE at 6363

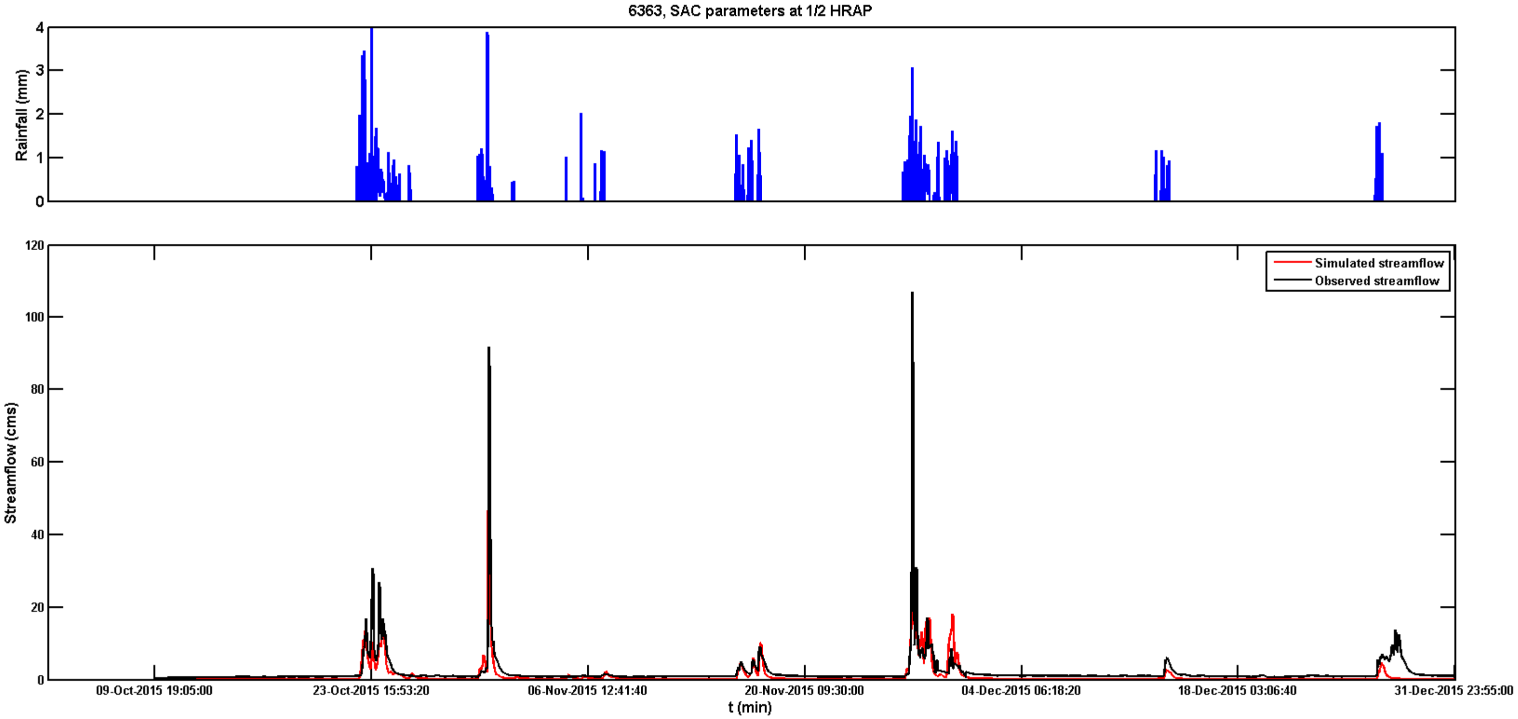

Figure A- 37 Streamflow simulation time series at model resolution of 1/16 HRAP and SAC parameters at 1/2 HRAP using CASA QPE at 6363

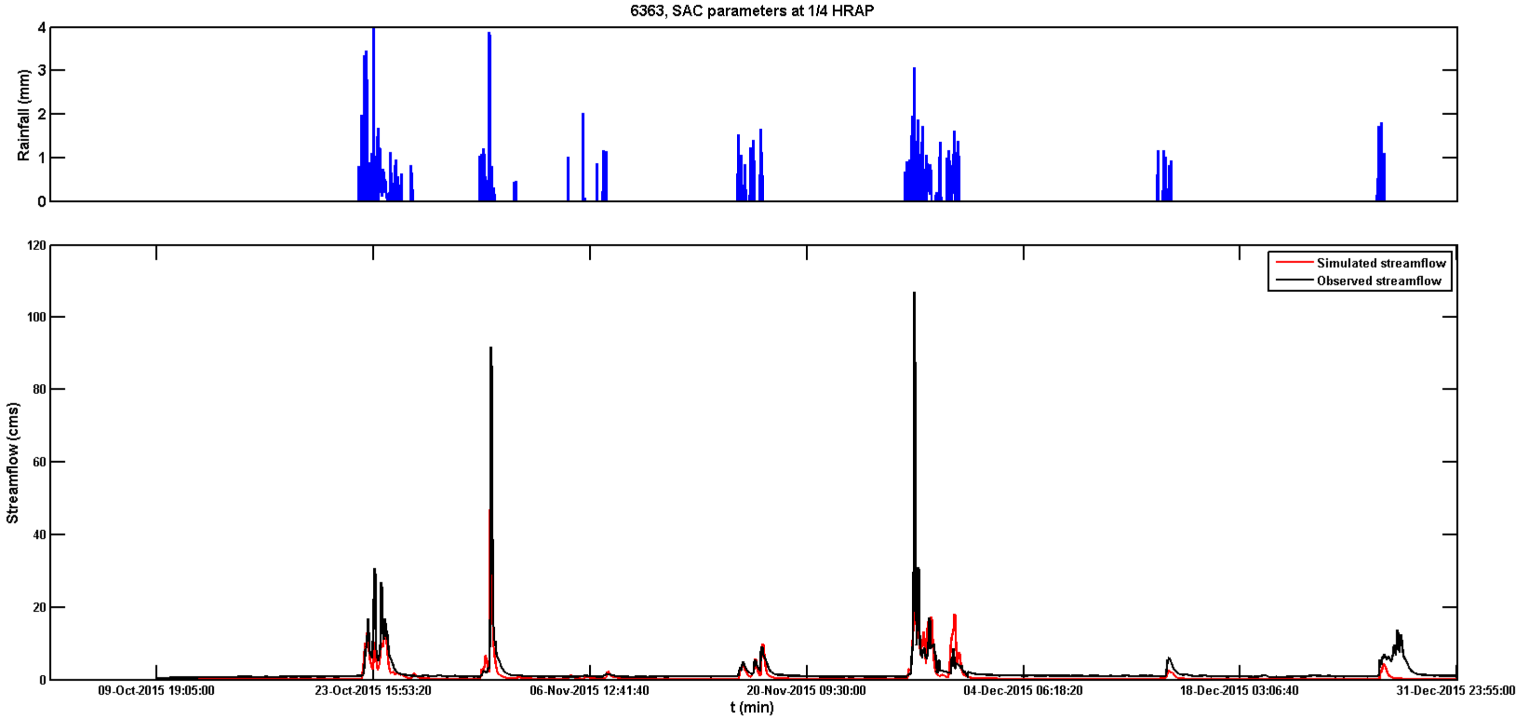

Figure A- 38 Streamflow simulation time series at model resolution of 1/16 HRAP and SAC parameters at 1/4 HRAP using CASA QPE at 6363

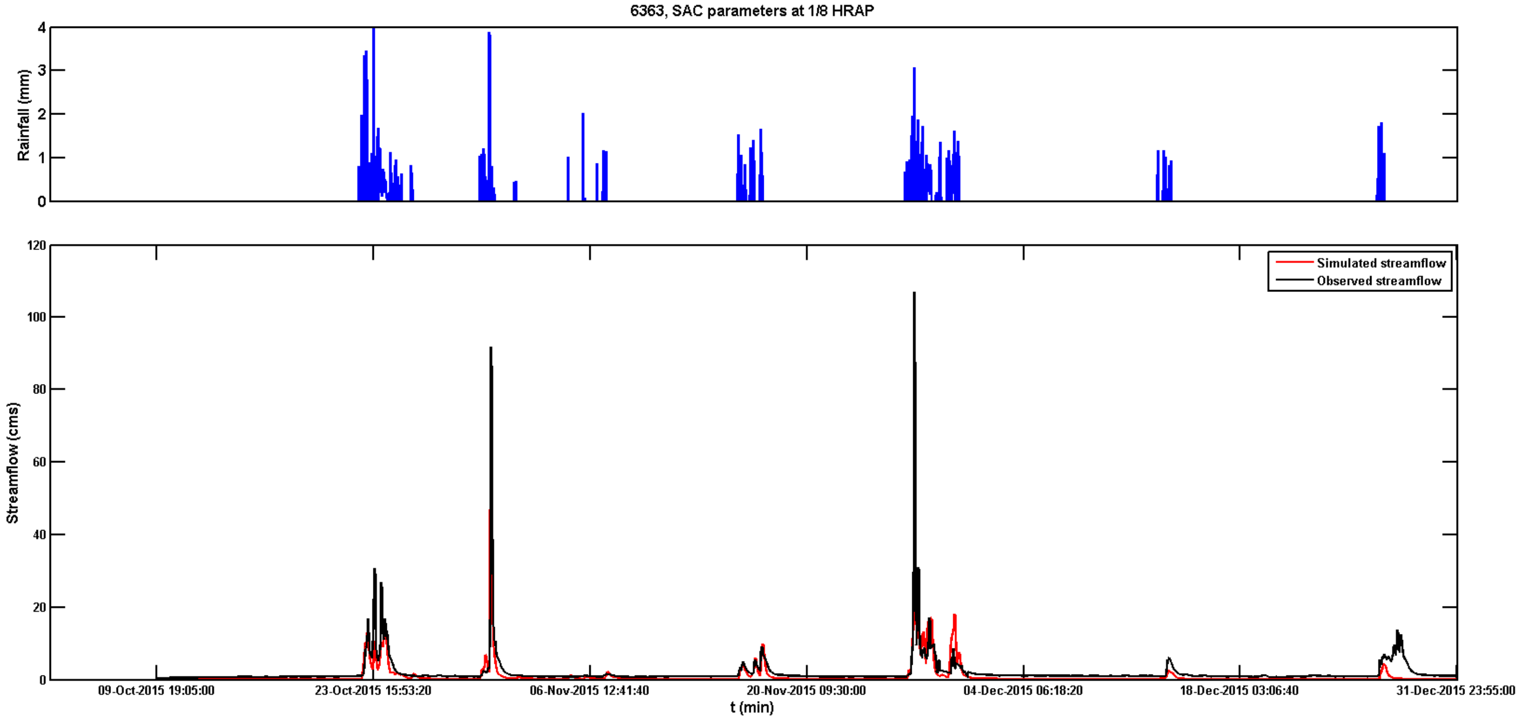

Figure A- 39 Streamflow simulation time series at model resolution of 1/16 HRAP and SAC parameters at 1/8 HRAP using CASA QPE at 6363

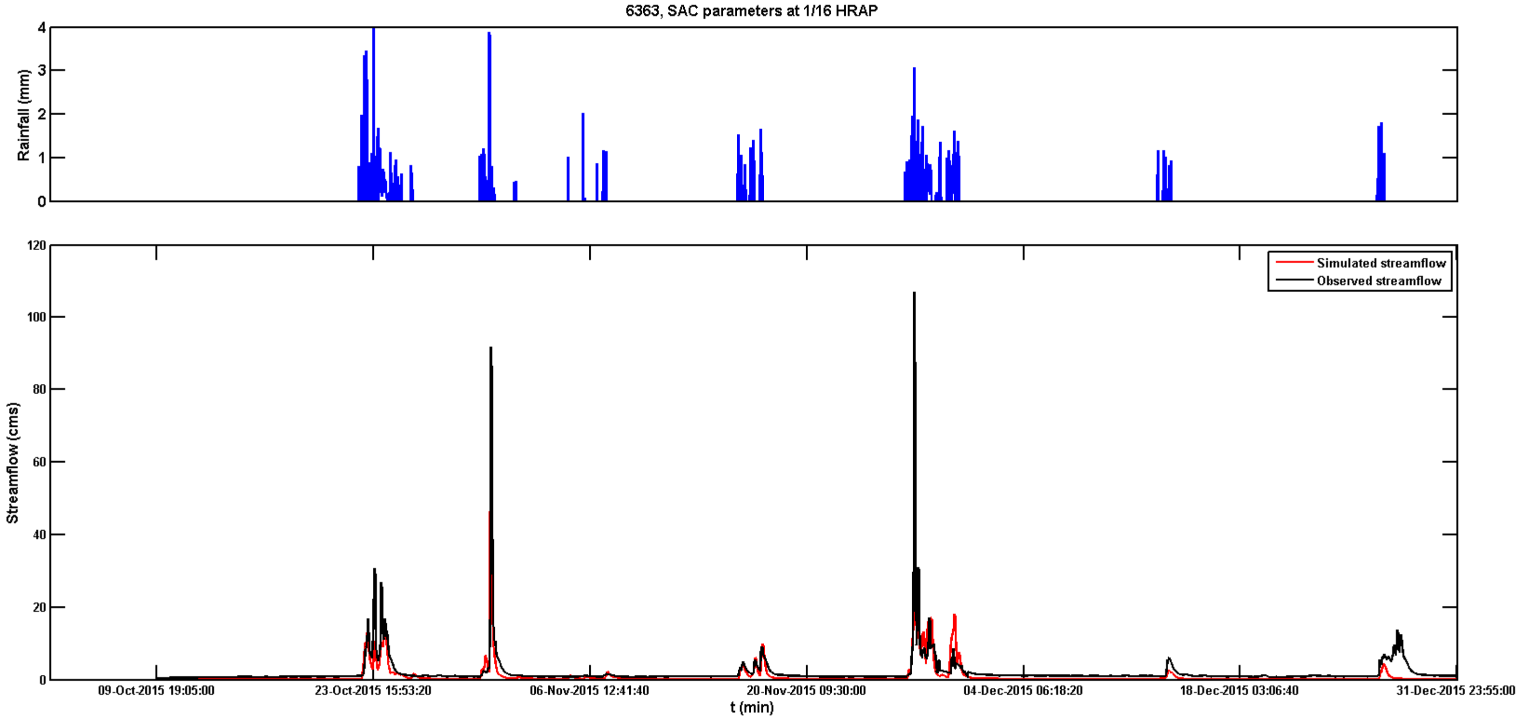

Figure A- 40 Streamflow simulation time series at model resolution of 1/16 HRAP and SAC parameters at 1/16 HRAP using CASA QPE at 6363

Appendix B

Time series of observed and simulated soil moisture content at CELB location

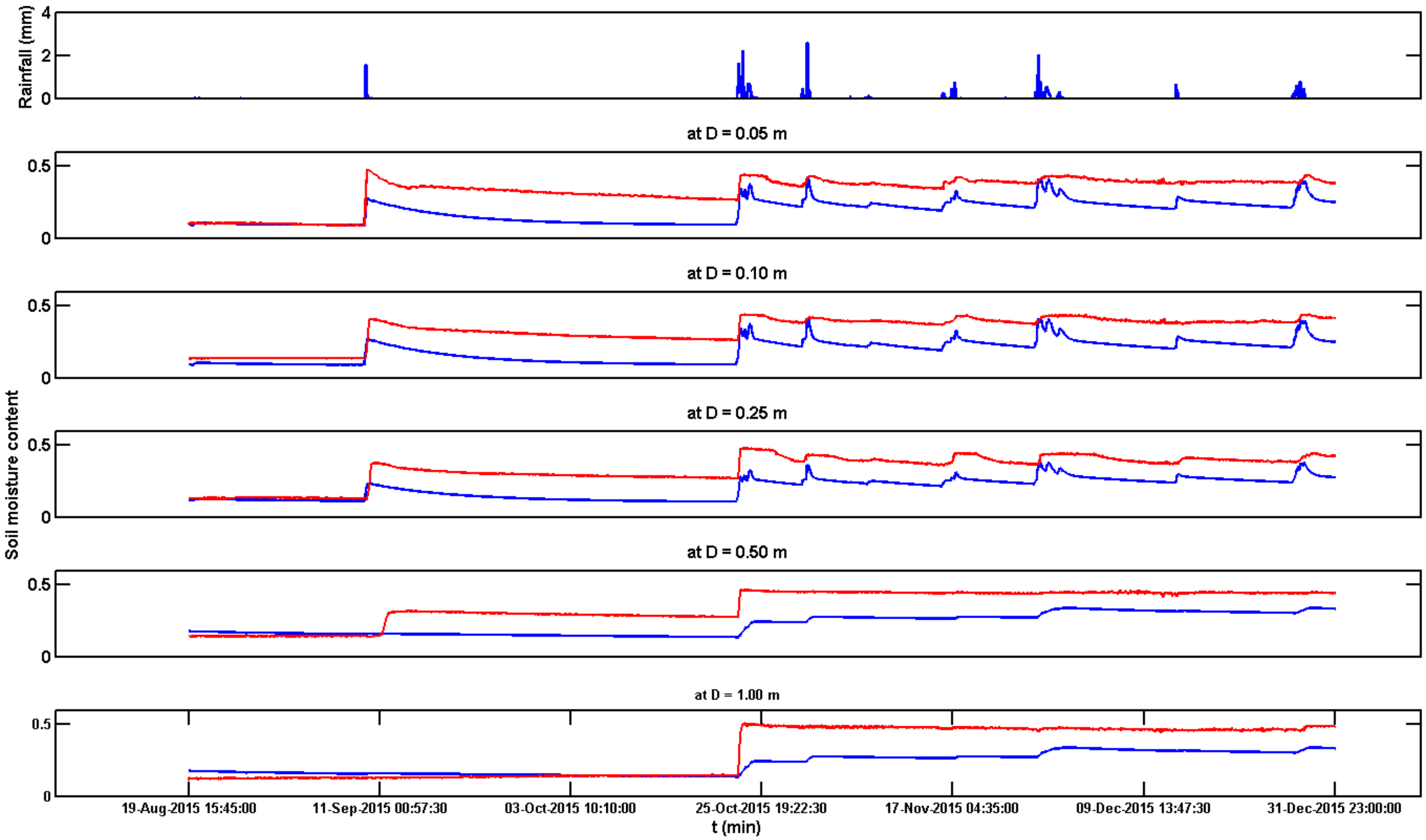

Figure B- 1 Time series of simulated and observed soil moisture content at CELB location using MPE data at 1/2 HRAP resolution and a priori SAC parameters at 1 HRAP resolution. Simulated soil moisture depicted in blue and observed soil moisture depicted in red.

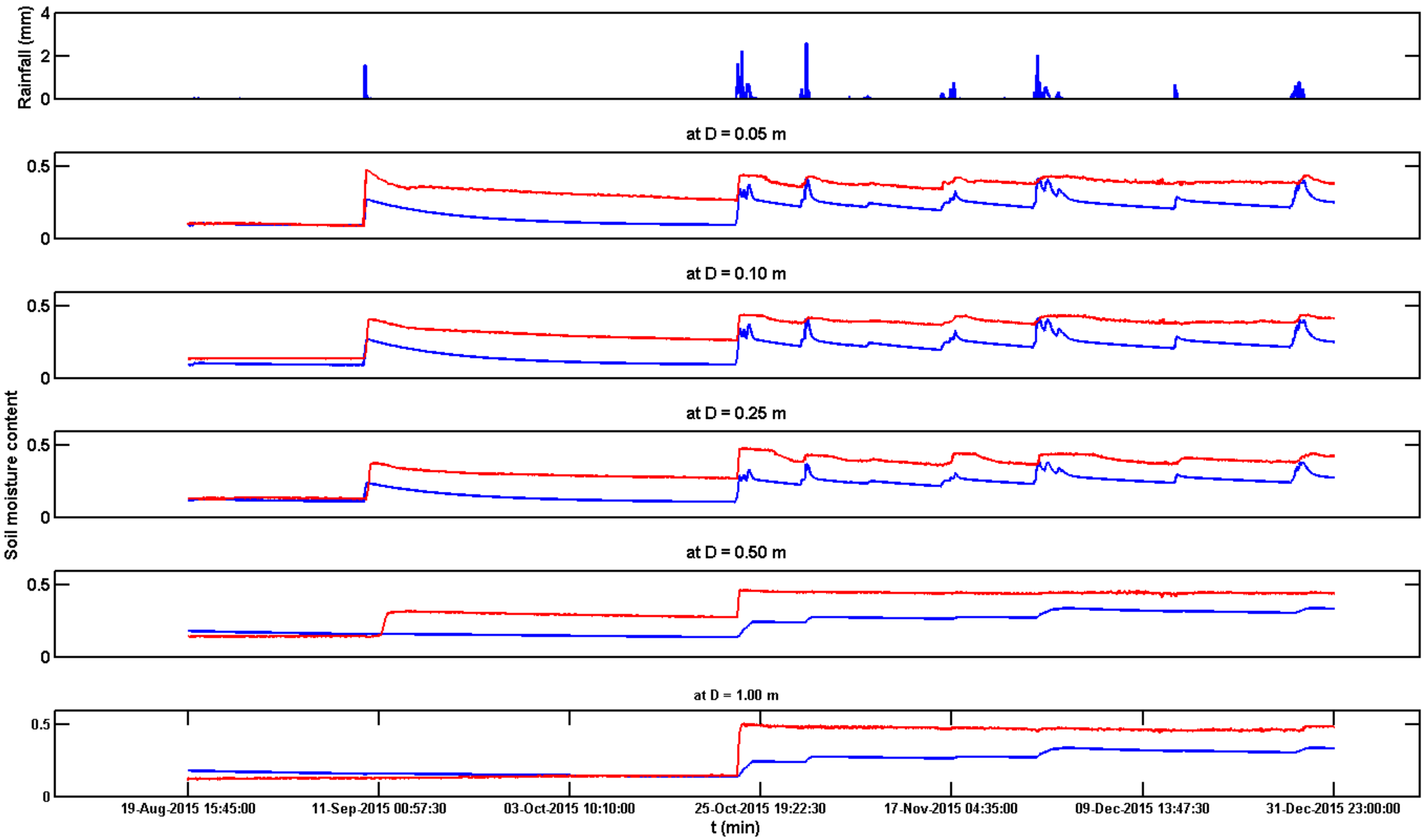

Figure B- 2 Time series of simulated and observed soil moisture content at CELB location using MPE data at 1/2 HRAP resolution and a priori SAC parameters at 1/2 HRAP resolution. Simulated soil moisture depicted in blue and observed soil moisture in red.

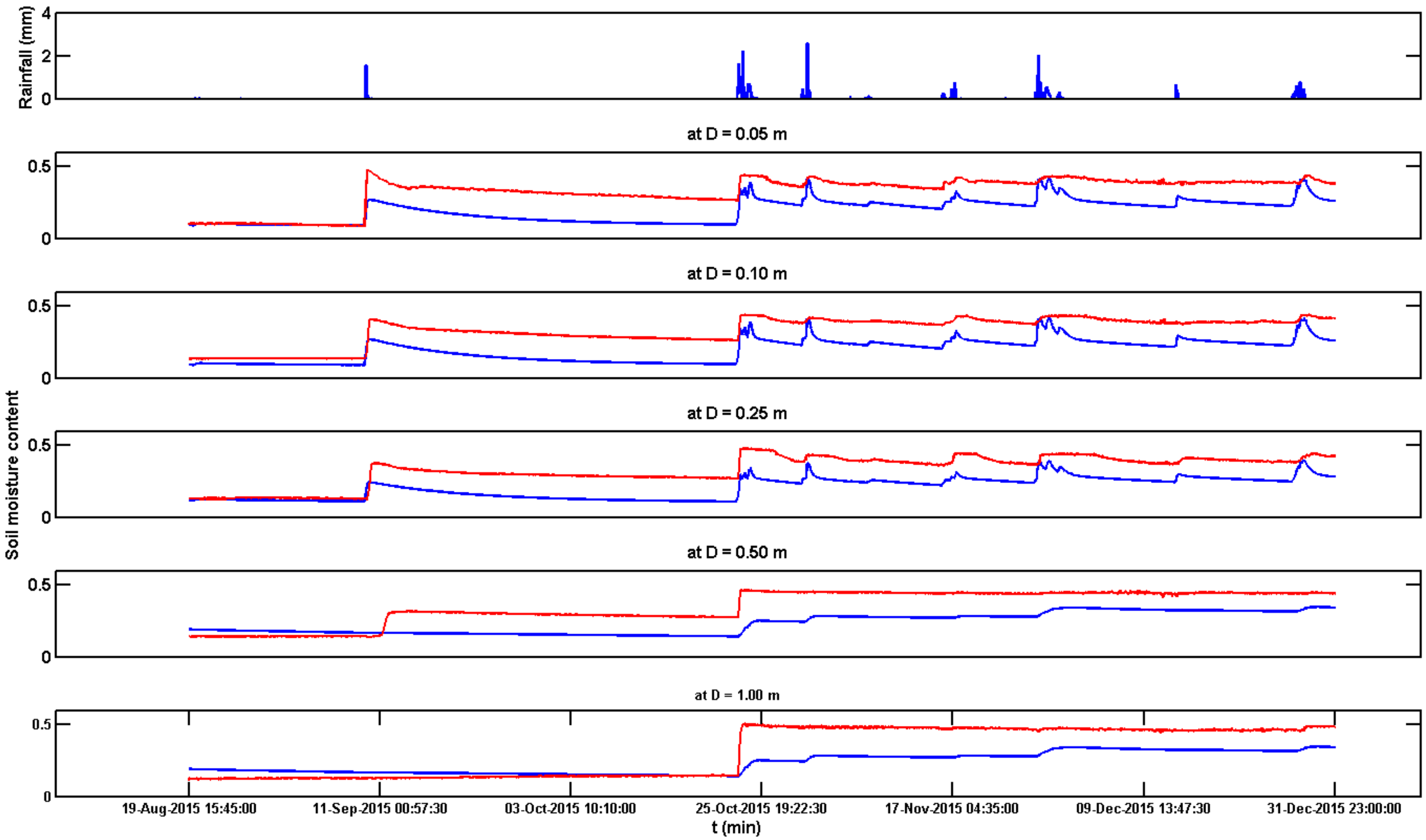

Figure B- 3 Time series of simulated and observed soil moisture content at CELB location using MPE data at 1/2 HRAP resolution and a priori SAC parameters at 1/4 HRAP resolution. Simulated soil moisture depicted in blue and observed soil moisture in red.

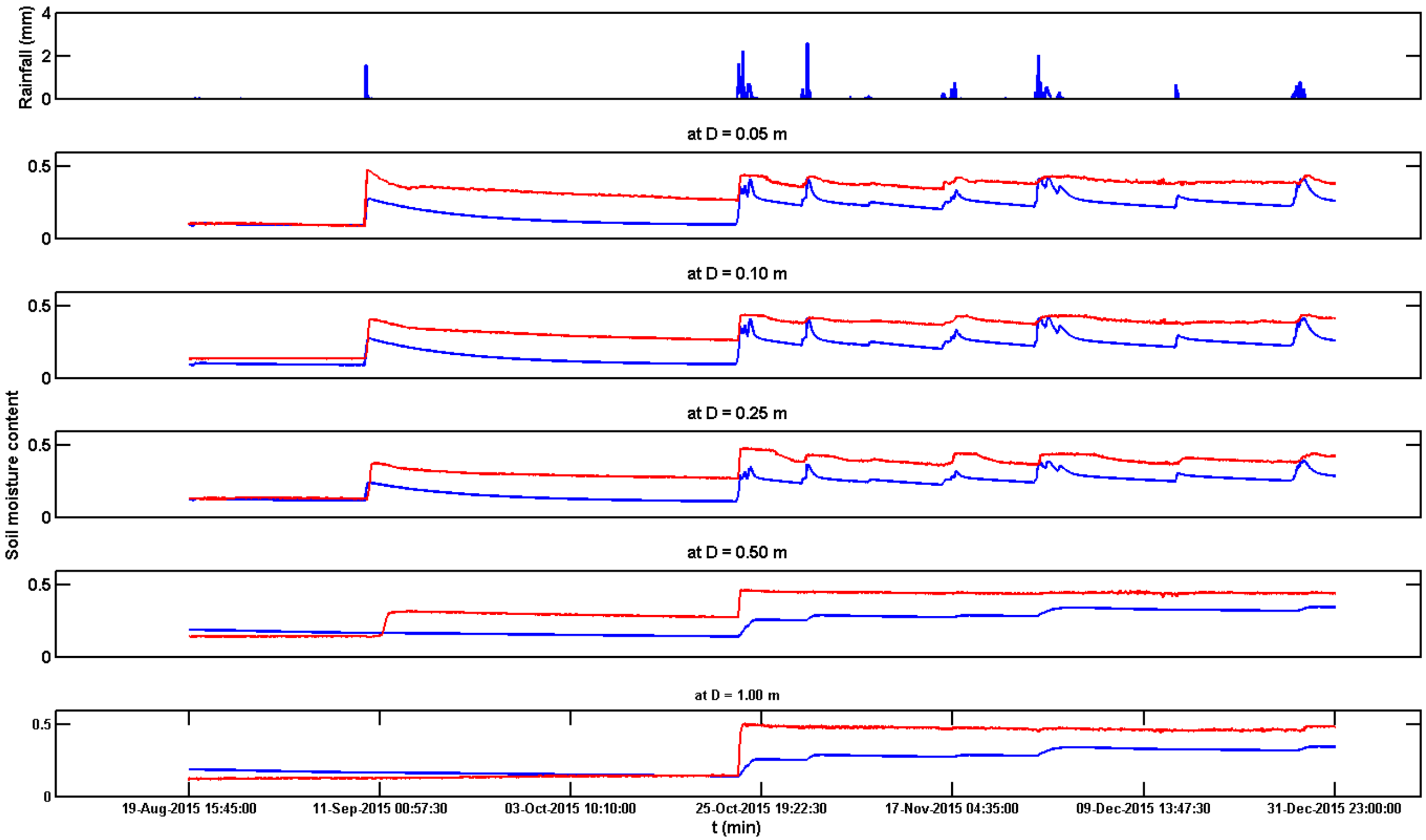

Figure B- 4 Time series of simulated and observed soil moisture content at CELB location using MPE data at 1/2 HRAP resolution and a priori SAC parameters at 1/8 HRAP resolution. Simulated soil moisture depicted in blue and observed soil moisture in red.

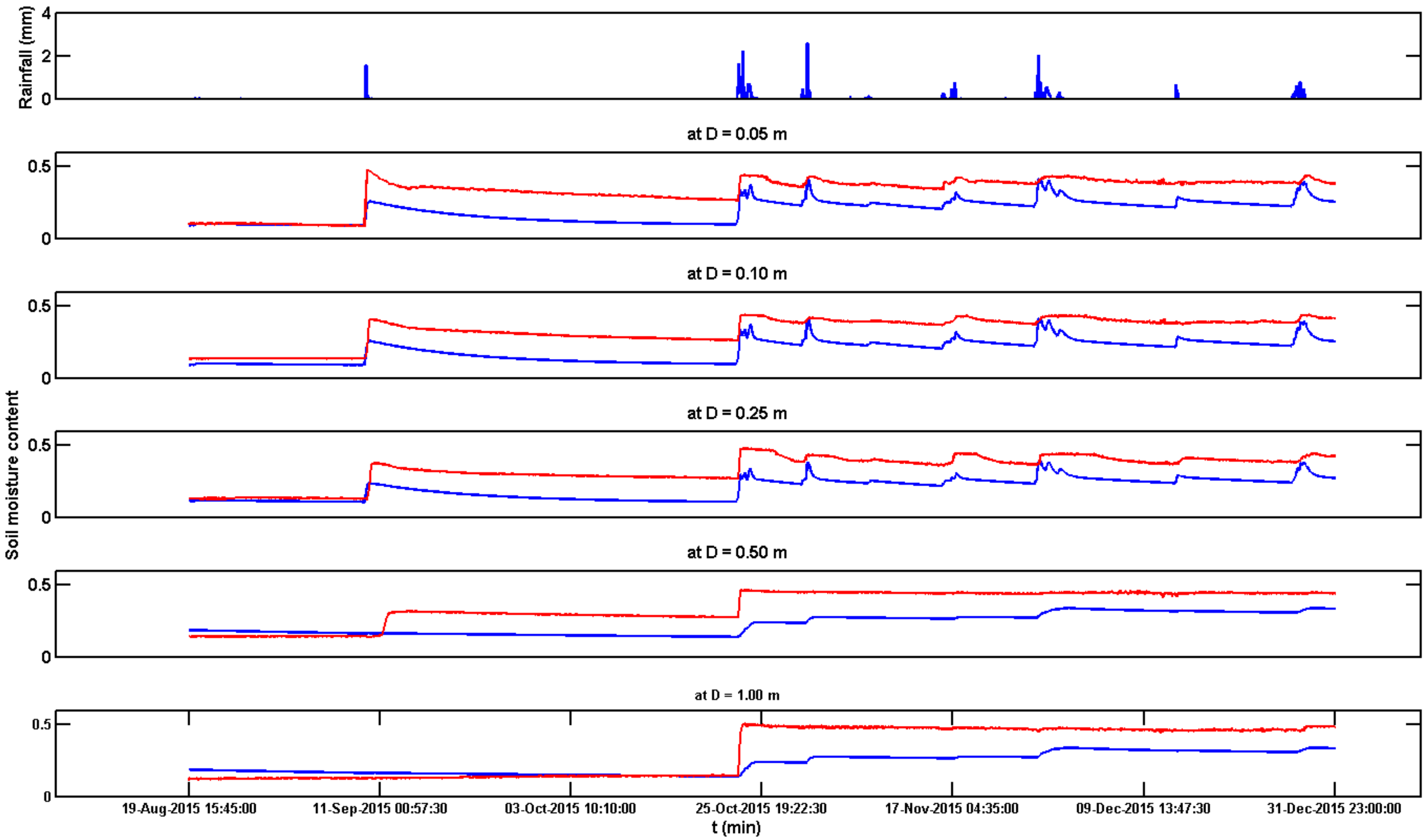

Figure B- 5 Time series of simulated and observed soil moisture content at CELB location using MPE data at 1/2 HRAP resolution and a priori SAC parameters at 1/16 HRAP resolution. Simulated soil moisture depicted in blue and observed soil moisture in red.

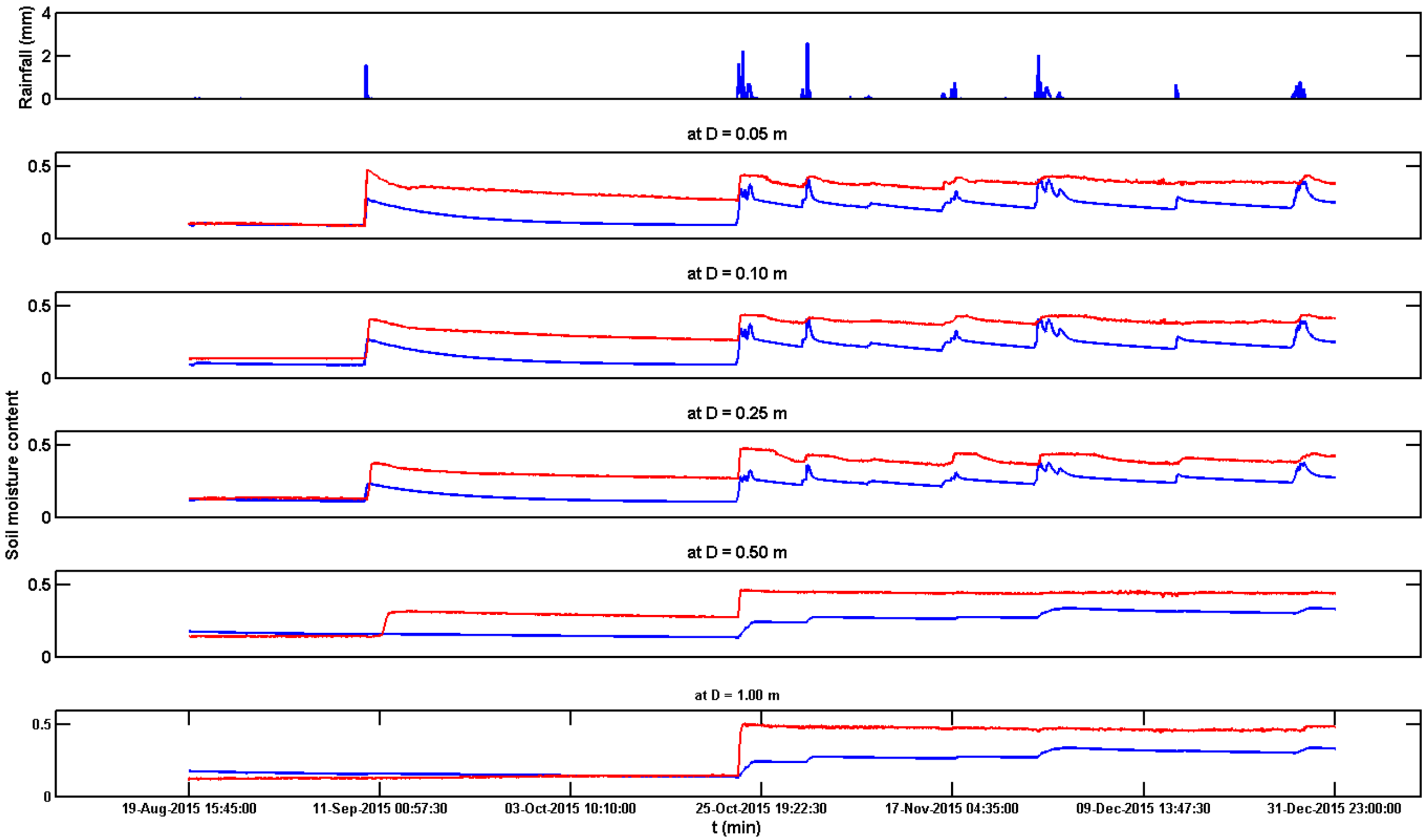

Figure B- 6 Time series of simulated and observed soil moisture content at CELB location using MPE data at 1/4 HRAP resolution and a priori SAC parameters at 1 HRAP resolution. Simulated soil moisture depicted in blue and observed soil moisture in red.

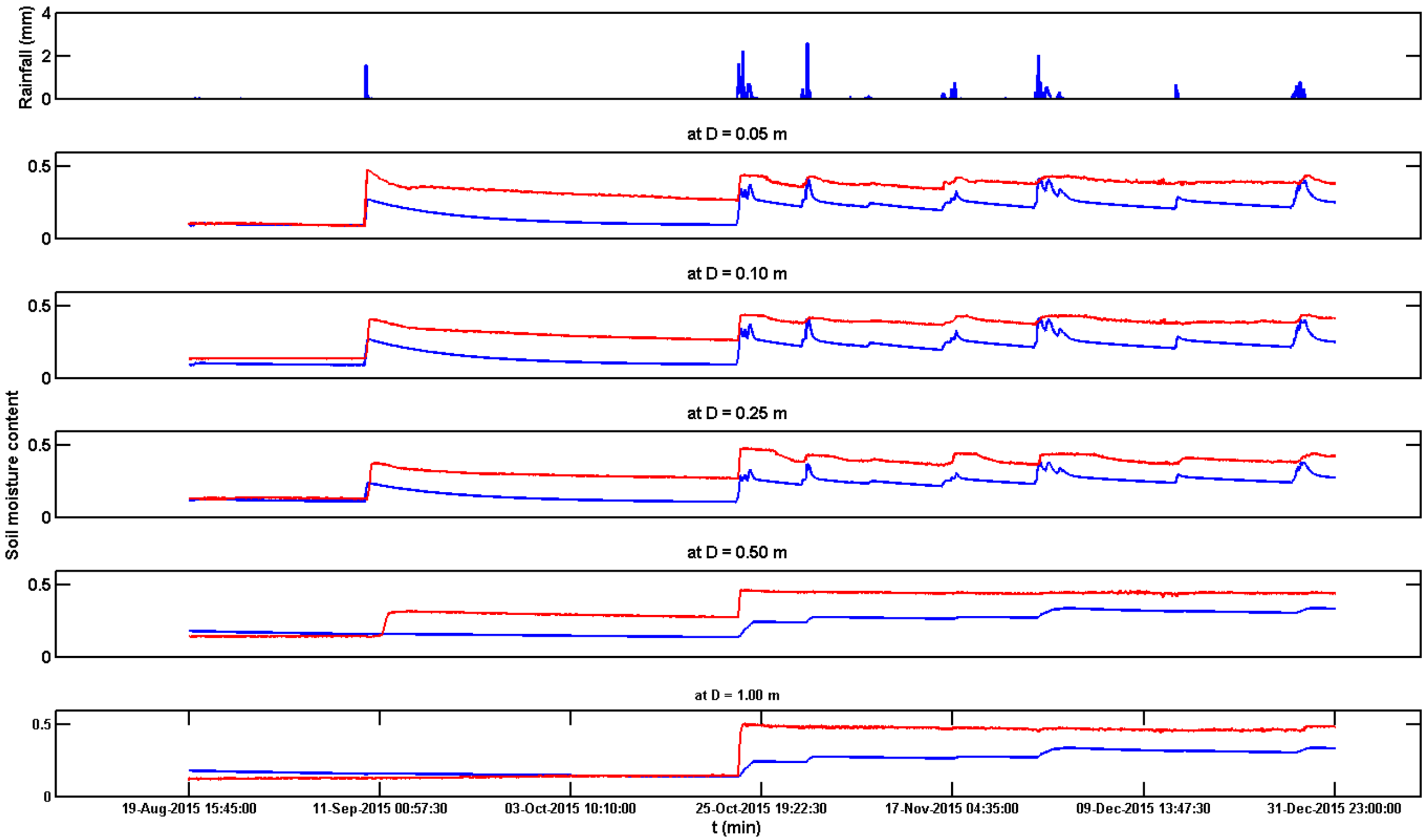

Figure B- 7 Time series of simulated and observed soil moisture content at CELB location using MPE data at 1/4 HRAP resolution and a priori SAC parameters at 1/2 HRAP resolution. Simulated soil moisture depicted in blue and observed soil moisture in red.

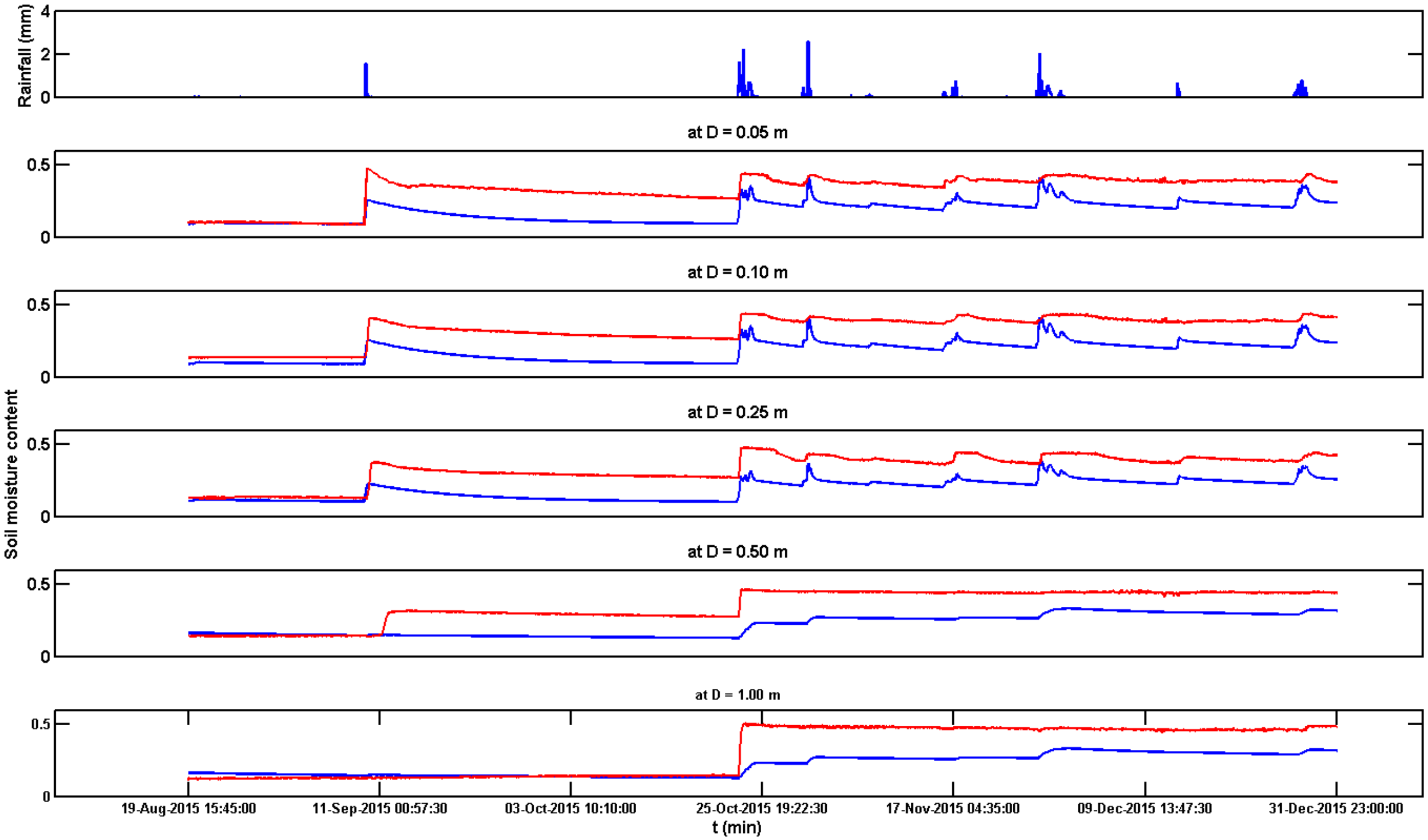

Figure B- 8 Time series of simulated and observed soil moisture content at CELB location using MPE data at 1/4 HRAP resolution and a priori SAC parameters at 1/4 HRAP resolution. Simulated soil moisture depicted in blue and observed soil moisture in red.

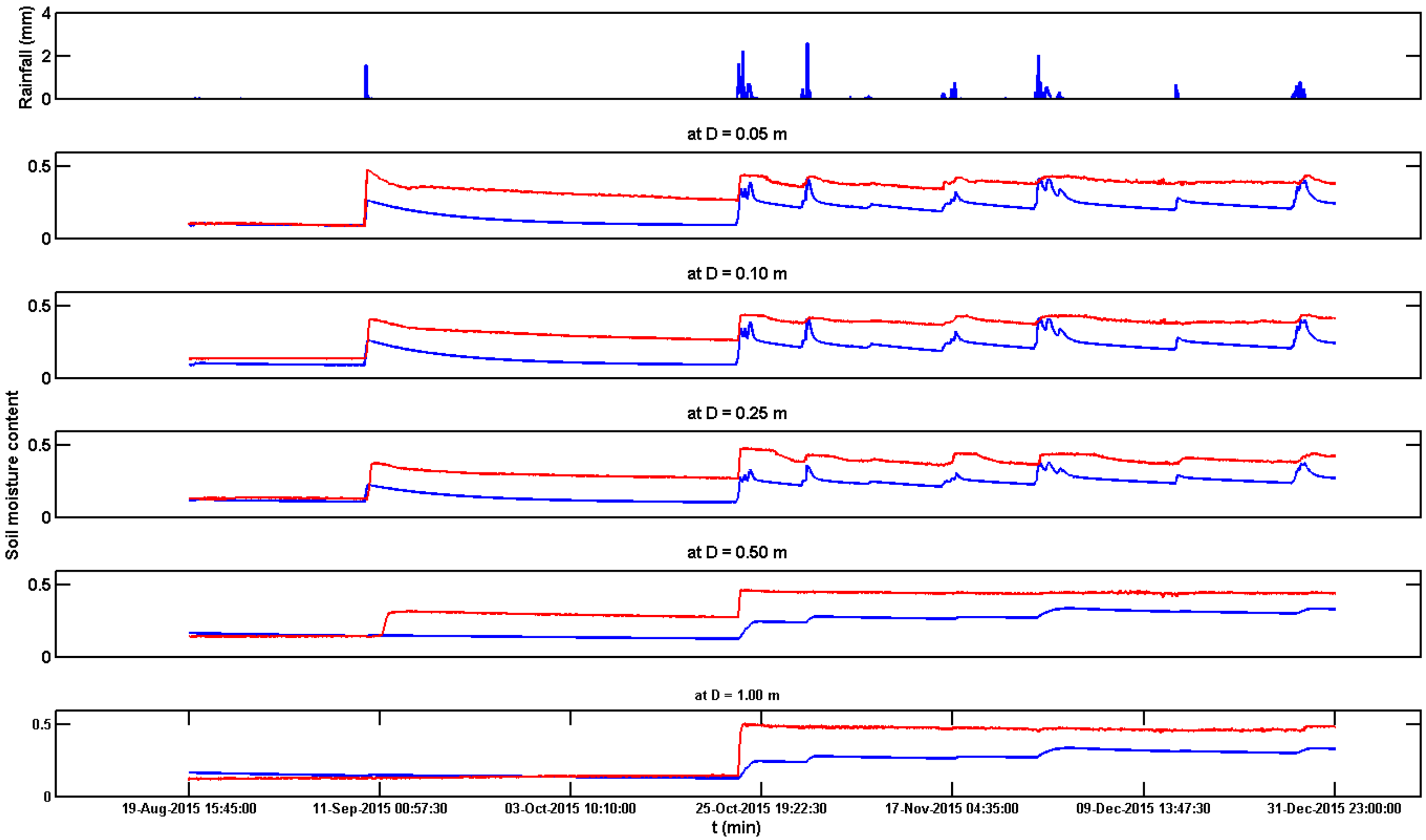

Figure B- 9 Time series of simulated and observed soil moisture content at CELB location using MPE data at 1/4 HRAP resolution and a priori SAC parameters at 1/8 HRAP resolution. Simulated soil moisture depicted in blue and observed soil moisture in red.

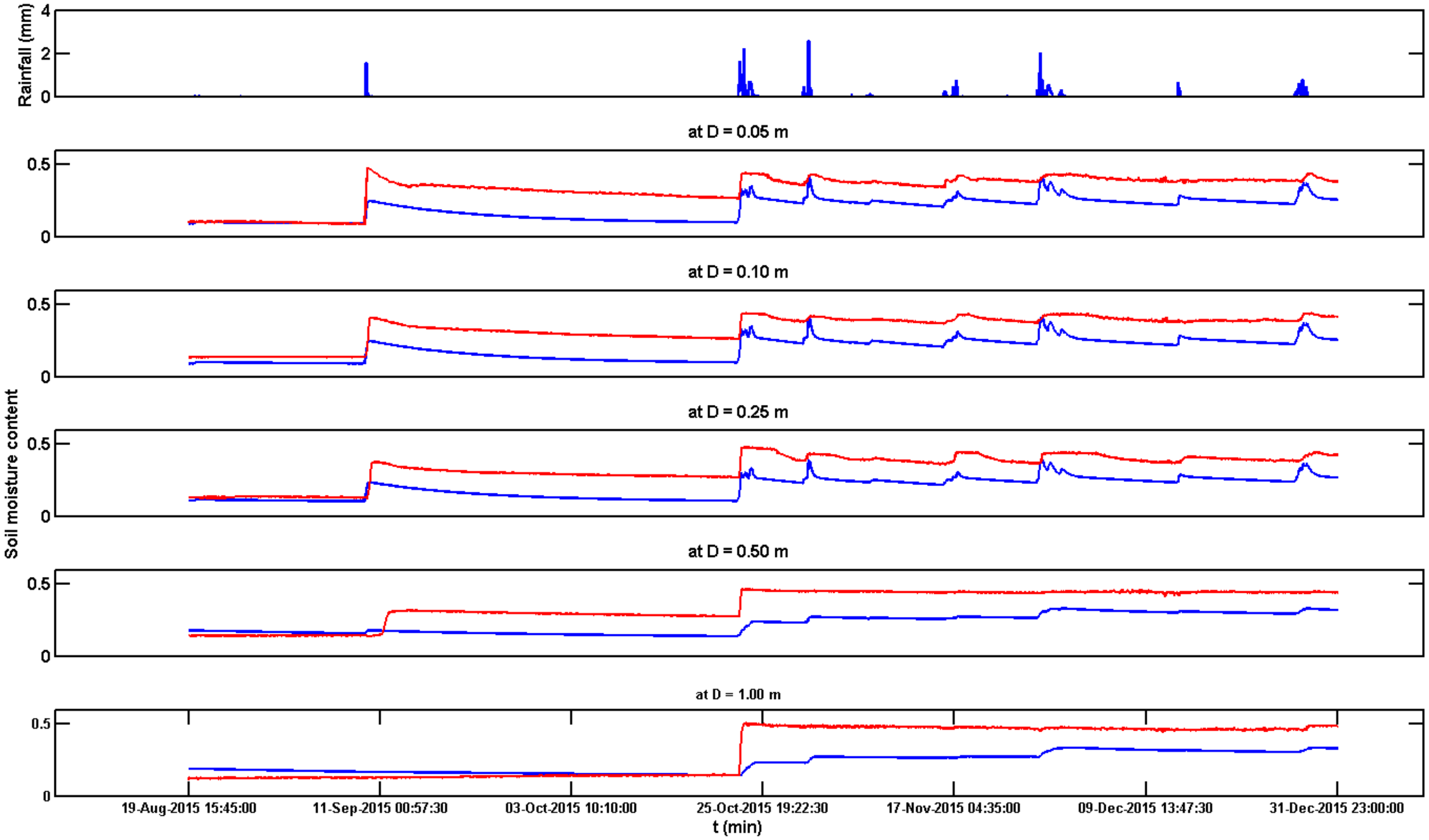

Figure B- 10 Time series of simulated and observed soil moisture content at CELB location using MPE data at 1/4 HRAP resolution and a priori SAC parameters at 1/16 HRAP resolution. Simulated soil moisture depicted in blue and observed soil moisture in red.

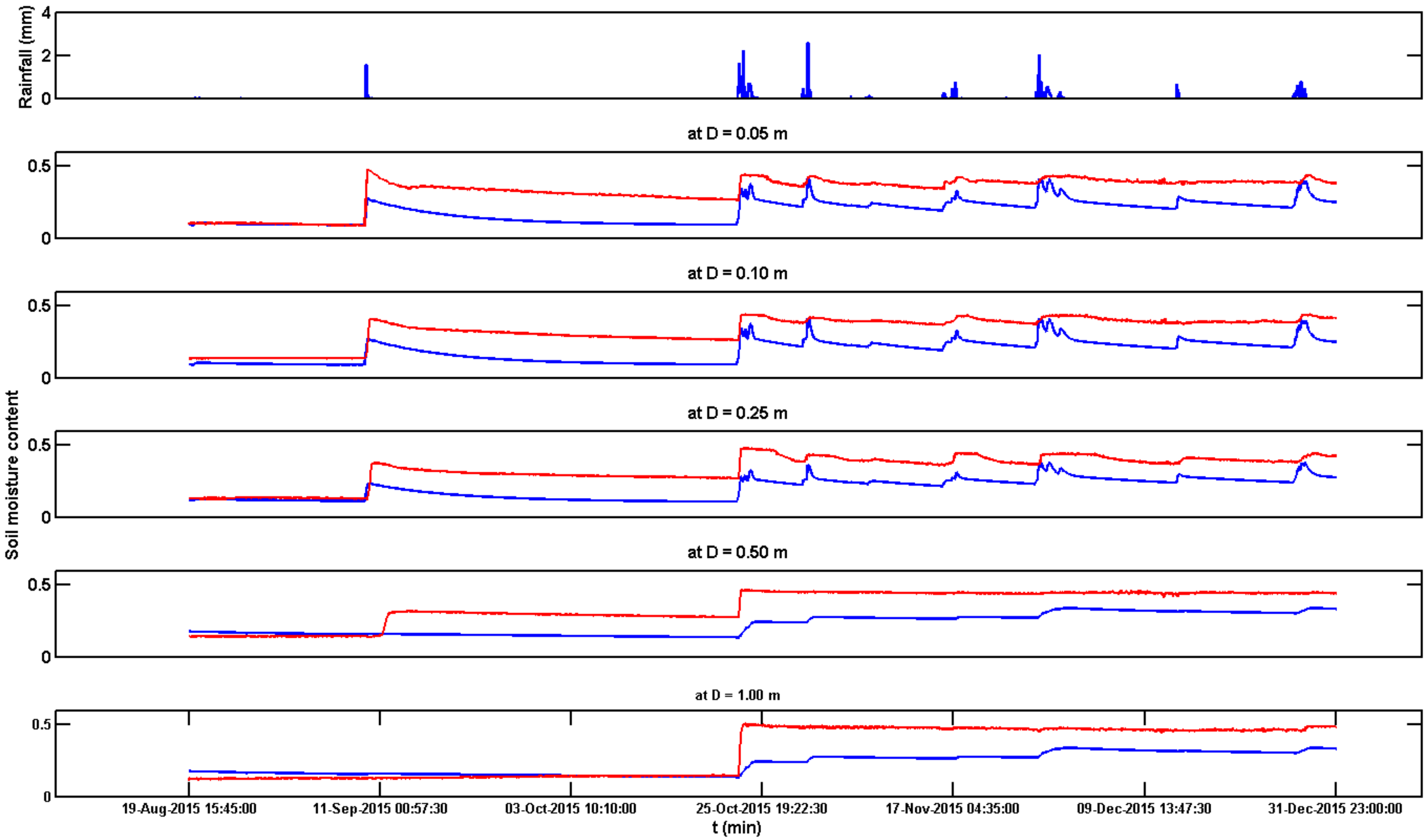

Figure B- 11 Time series of simulated and observed soil moisture content at CELB location using MPE data at 1/8 HRAP resolution and a priori SAC parameters at 1 HRAP resolution. Simulated soil moisture depicted in blue and observed soil moisture in red.

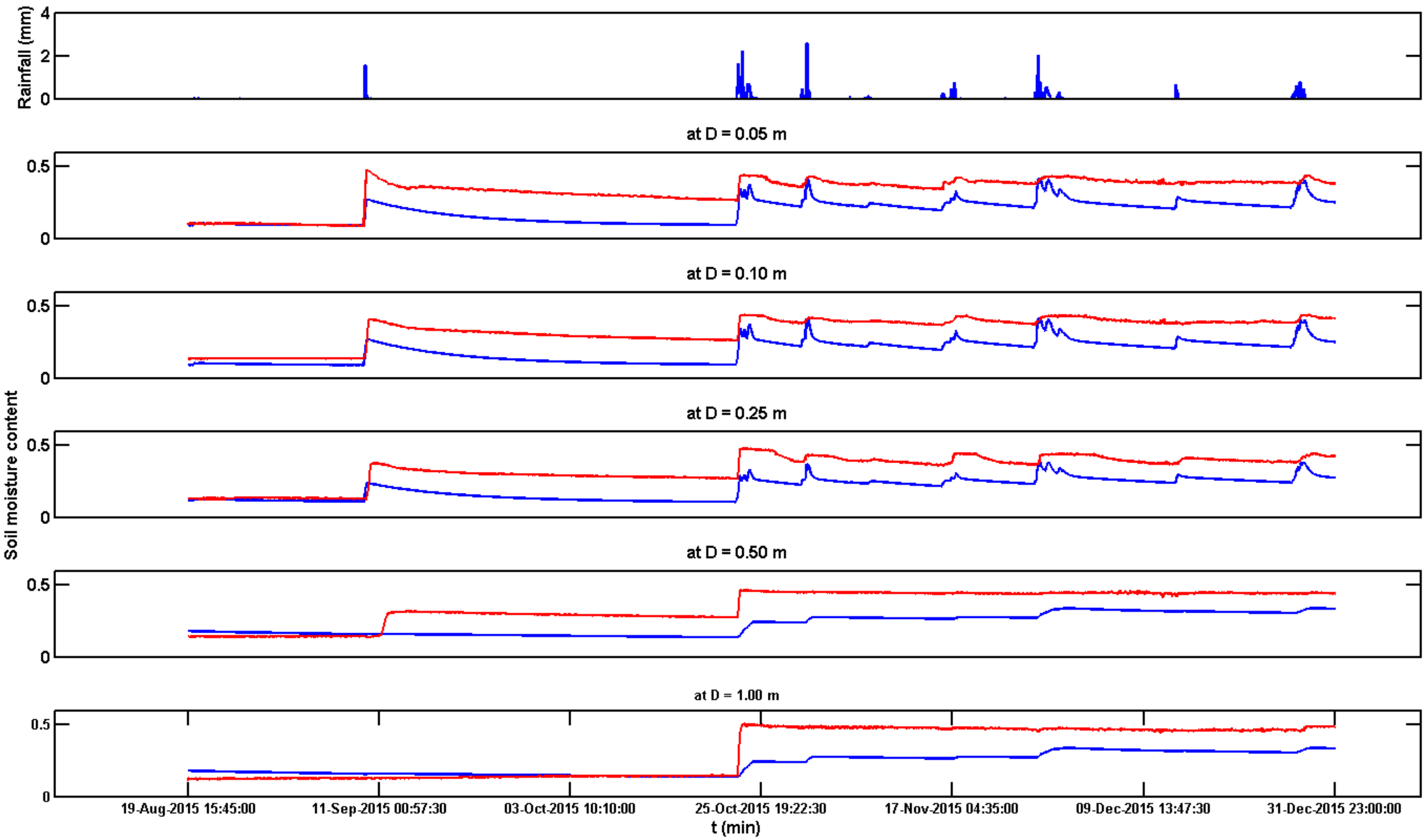

Figure B- 12 Time series of simulated and observed soil moisture content at CELB location using MPE data at 1/8 HRAP resolution and a priori SAC parameters at 1/2 HRAP resolution. Simulated soil moisture depicted in blue and observed soil moisture in red.

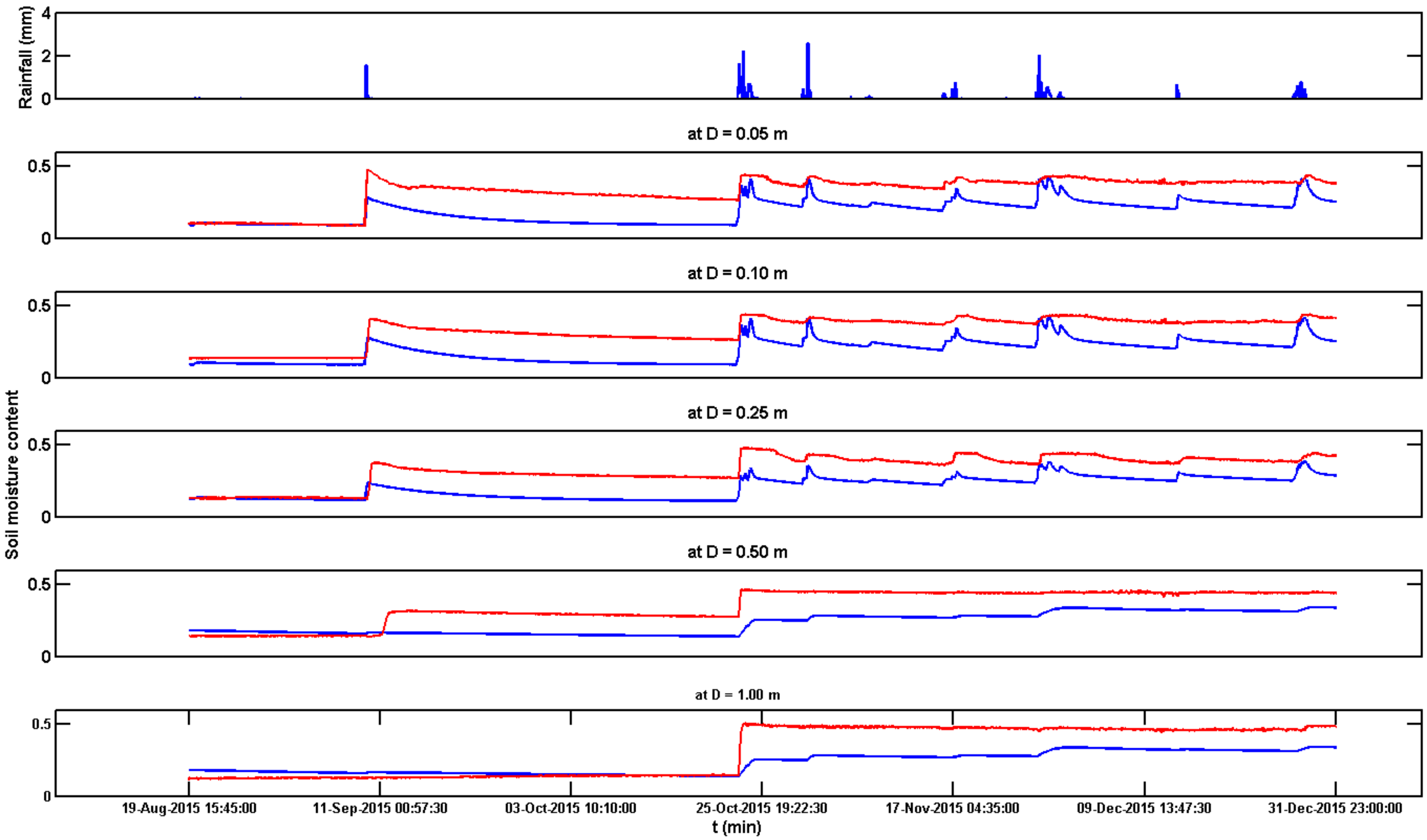

Figure B- 13 Time series of simulated and observed soil moisture content at CELB location using MPE data at 1/8 HRAP resolution and a priori SAC parameters at 1/4 HRAP resolution. Simulated soil moisture depicted in blue and observed soil moisture in red.

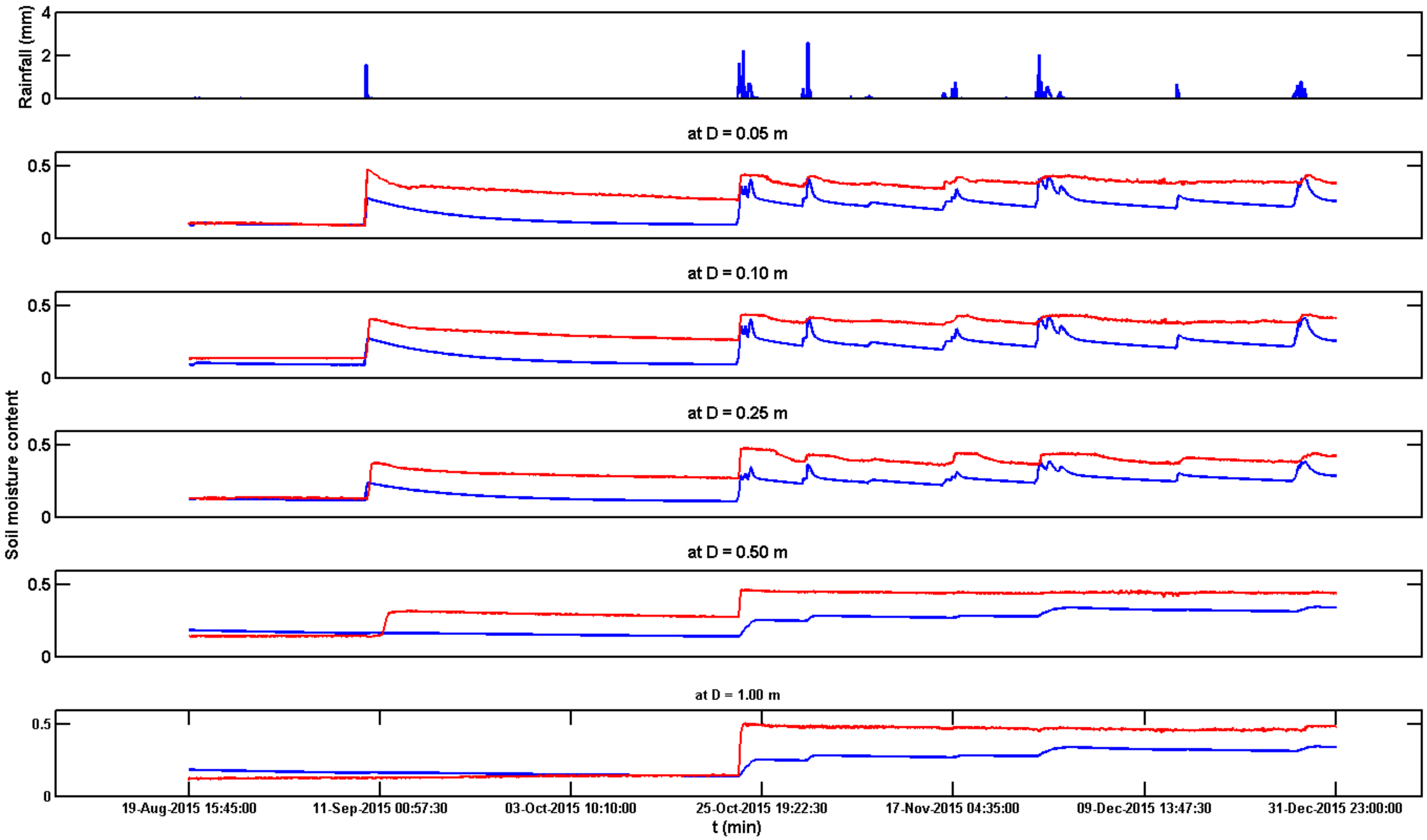

Figure B- 14 Time series of simulated and observed soil moisture content at CELB location using MPE data at 1/8 HRAP resolution and a priori SAC parameters at 1/8 HRAP resolution. Simulated soil moisture depicted in blue and observed soil moisture in red.

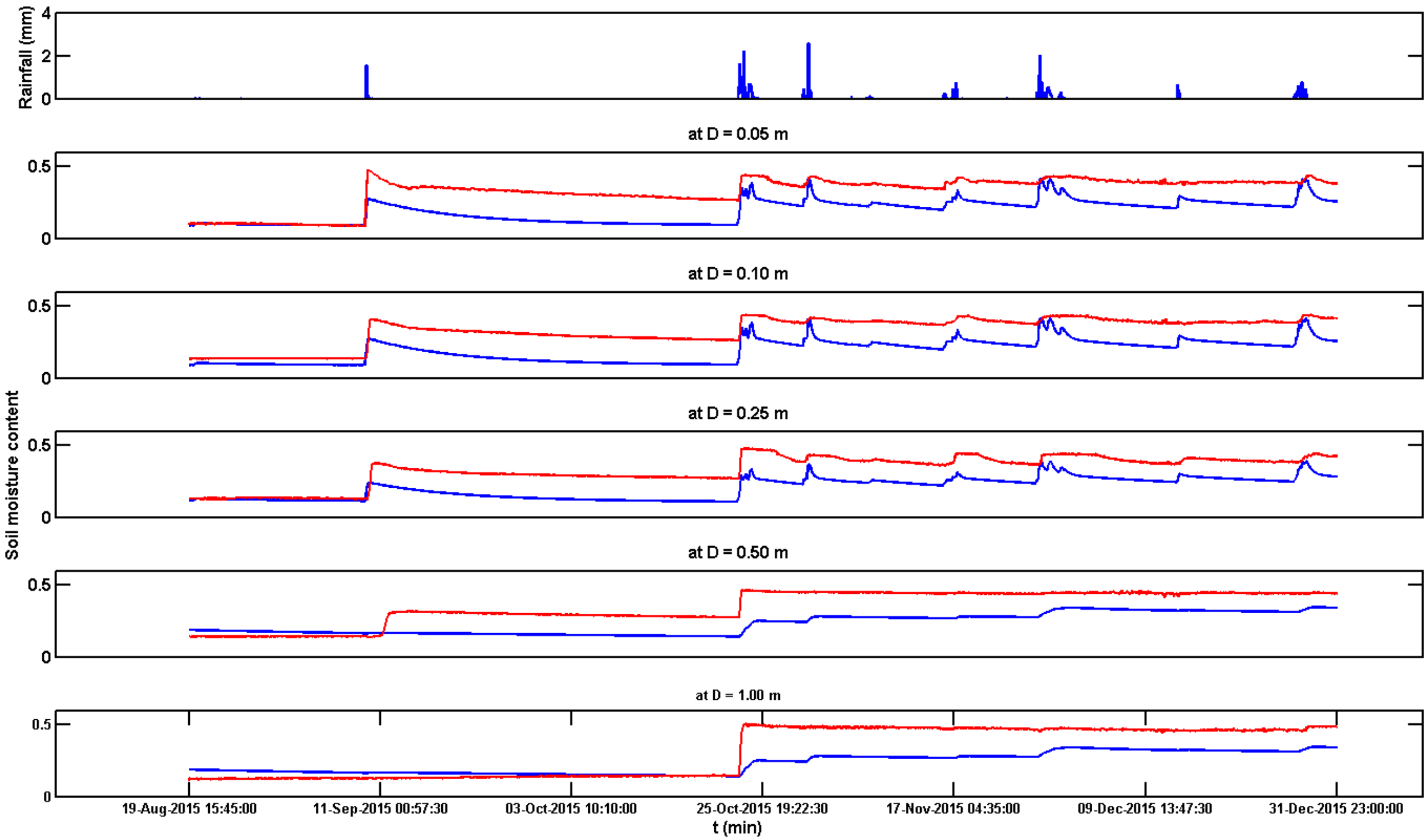

Figure B- 15 Time series of simulated and observed soil moisture content at CELB location using MPE data at 1/8 HRAP resolution and a priori SAC parameters at 1/16 HRAP resolution. Simulated soil moisture depicted in blue and observed soil moisture in red.

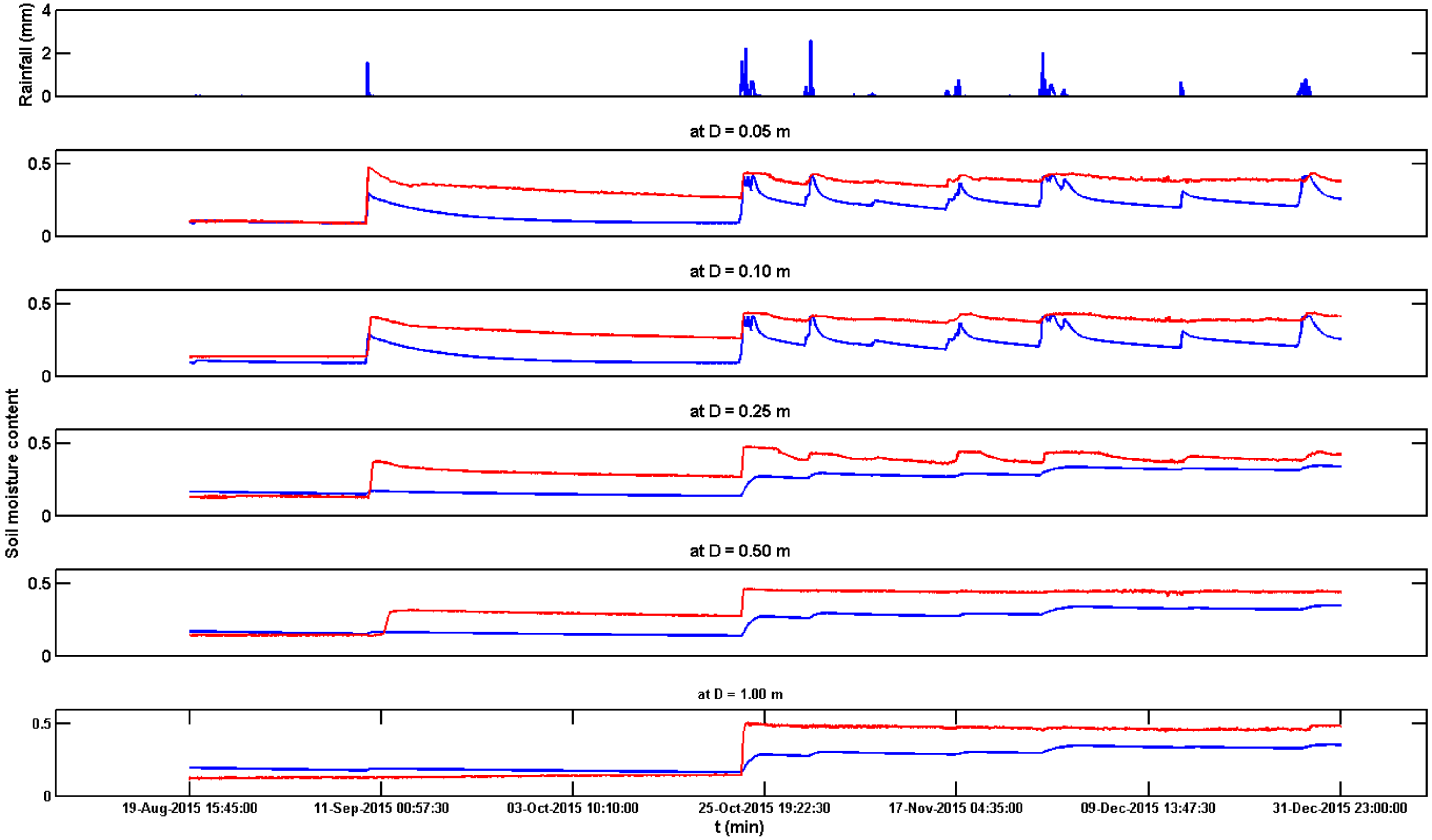

Figure B- 16 Time series of simulated and observed soil moisture content at CELB location using MPE data at 1/16 HRAP resolution and a priori SAC parameters at 1 HRAP resolution. Simulated soil moisture depicted in blue and observed soil moisture in red.

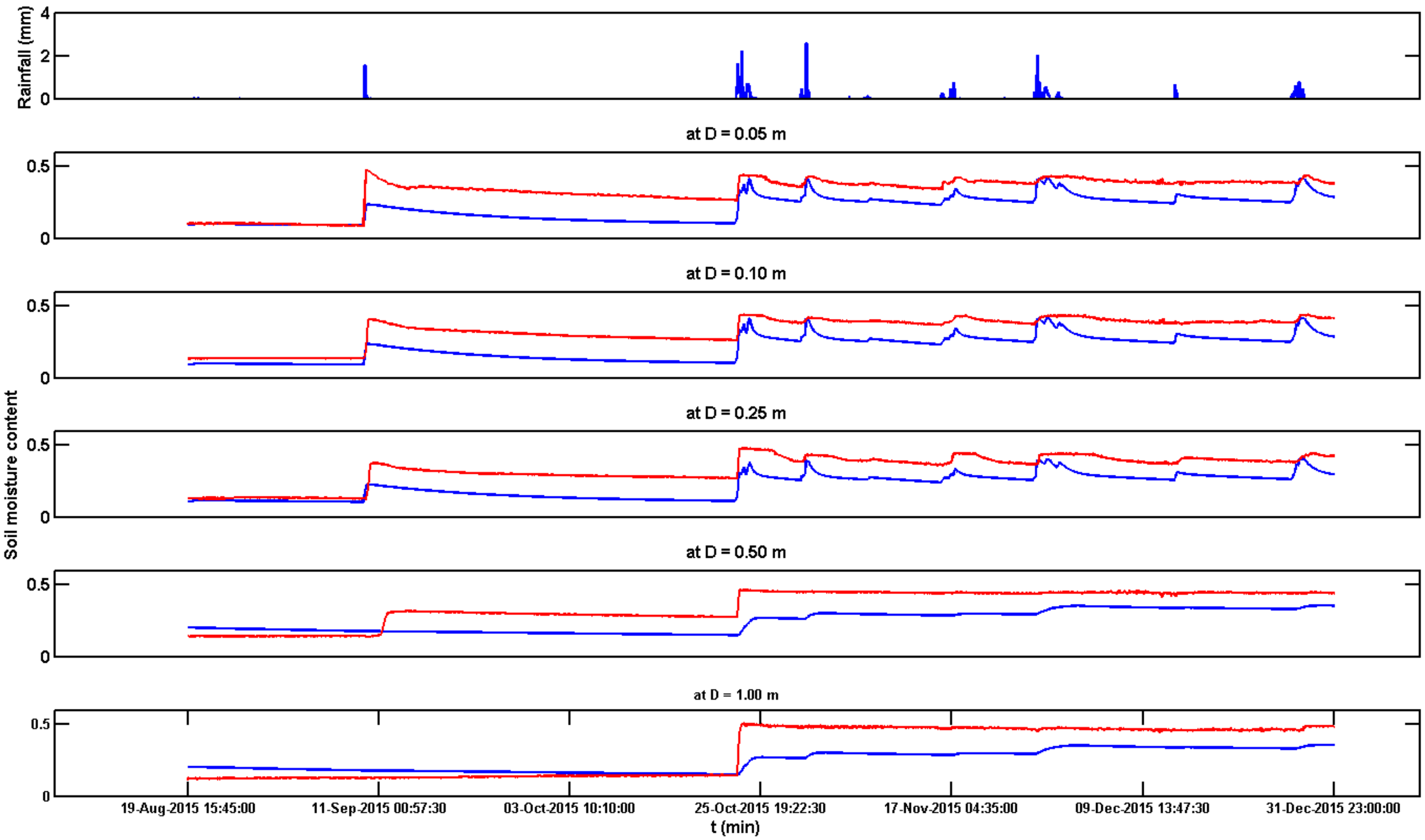

Figure B- 17 Time series of simulated and observed soil moisture content at CELB location using MPE data at 1/16 HRAP resolution and a priori SAC parameters at 1/2 HRAP resolution. Simulated soil moisture depicted in blue and observed soil moisture in red.

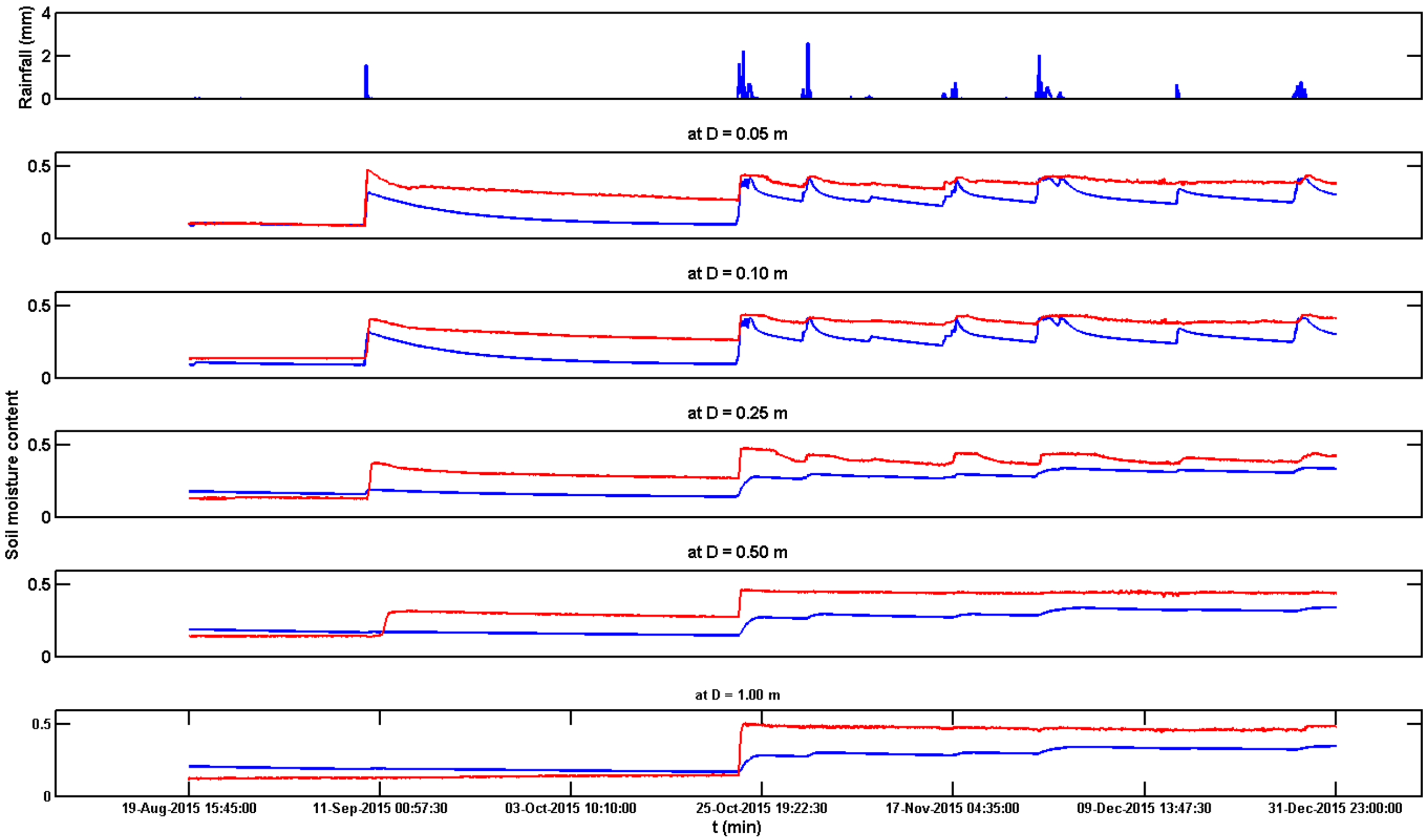

Figure B- 18 Time series of simulated and observed soil moisture content at CELB location using MPE data at 1/16 HRAP resolution and a priori SAC parameters at 1/4 HRAP resolution. Simulated soil moisture depicted in blue and observed soil moisture in red.

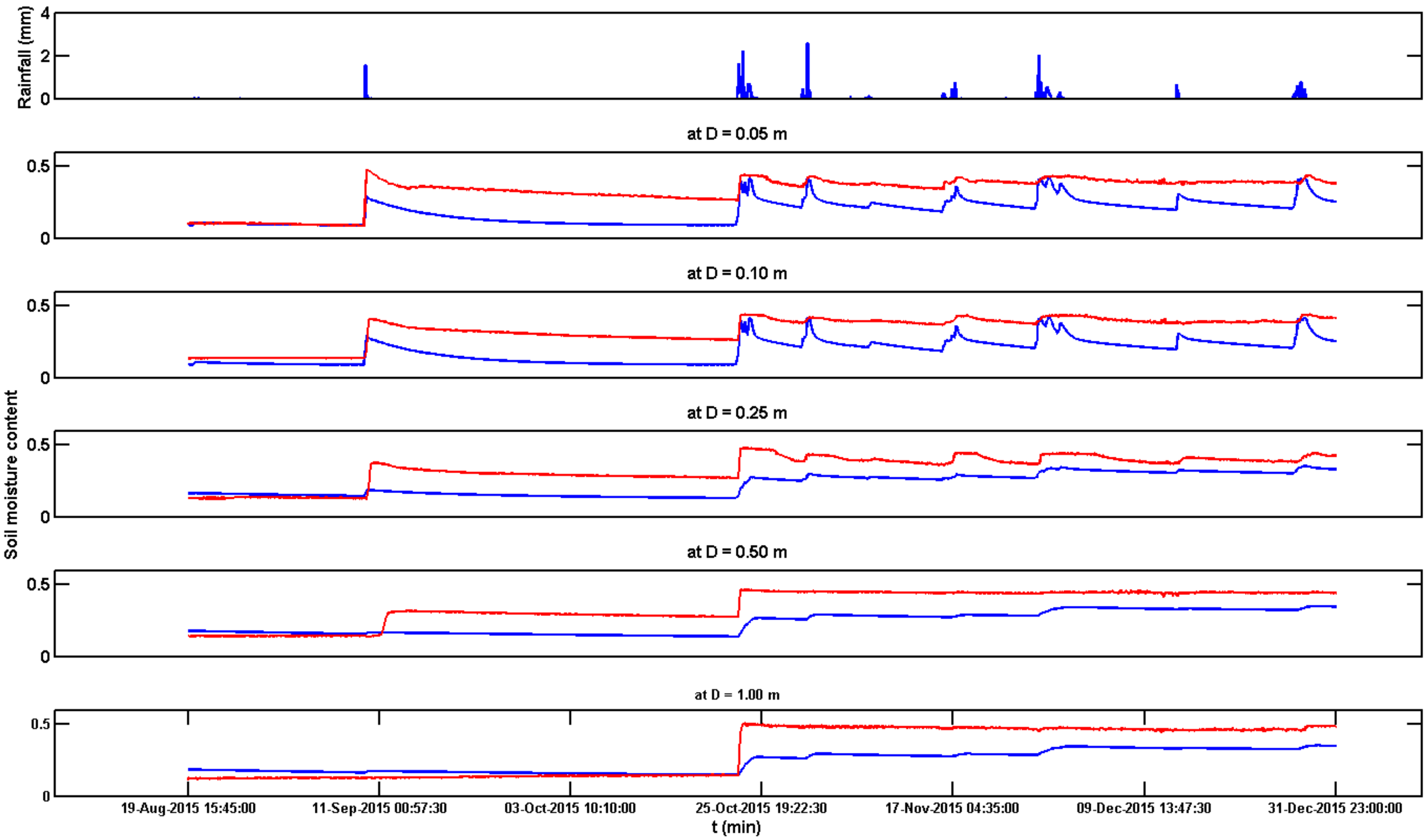

Figure B- 19 Time series of simulated and observed soil moisture content at CELB location using MPE data at 1/16 HRAP resolution and a priori SAC parameters at 1/8 HRAP resolution. Simulated soil moisture depicted in blue and observed soil moisture in red.

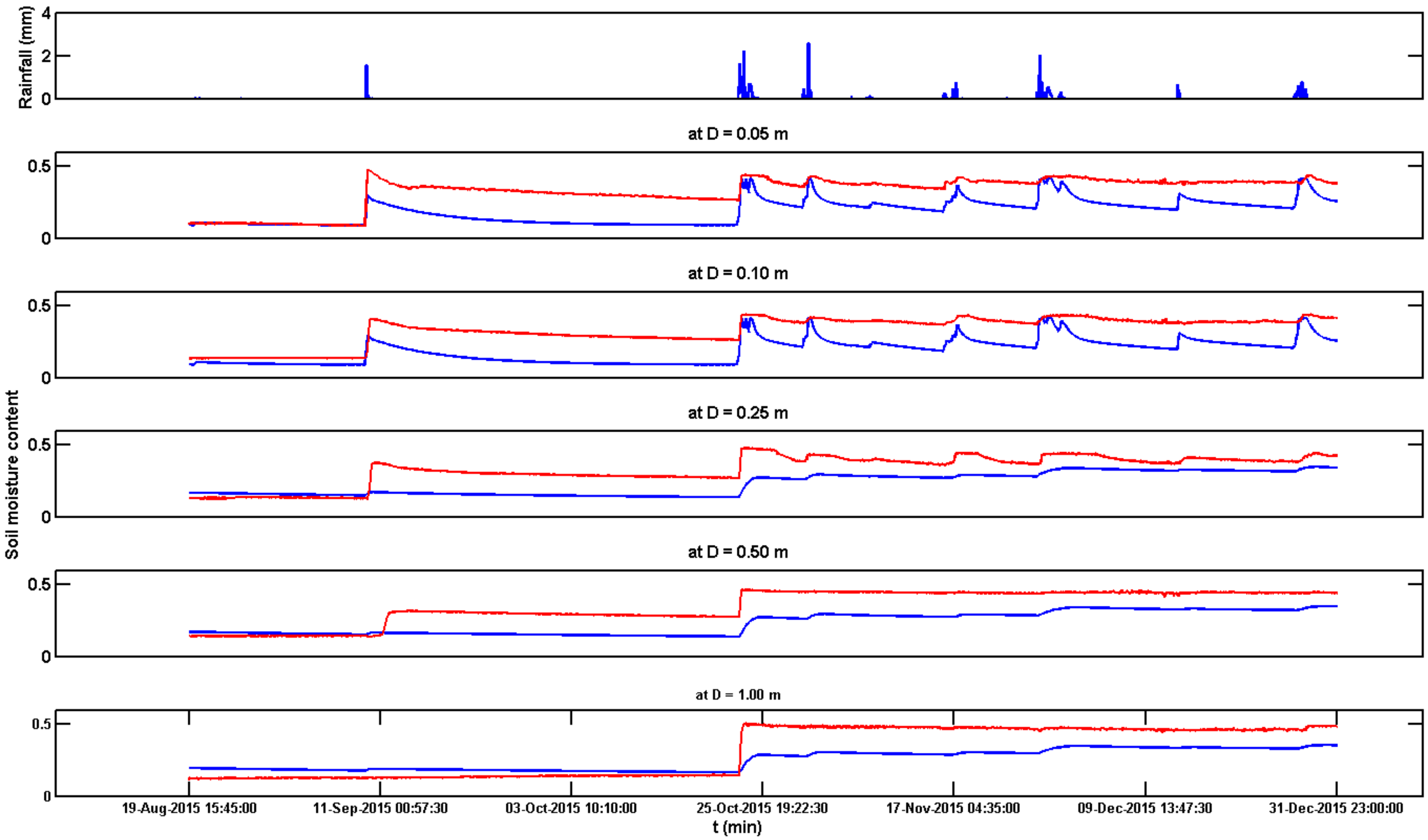

Figure B- 20 Time series of simulated and observed soil moisture content at CELB location using MPE data at 1/16 HRAP resolution and a priori SAC parameters at 1/16 HRAP resolution. Simulated soil moisture depicted in blue and observed soil moisture in red.

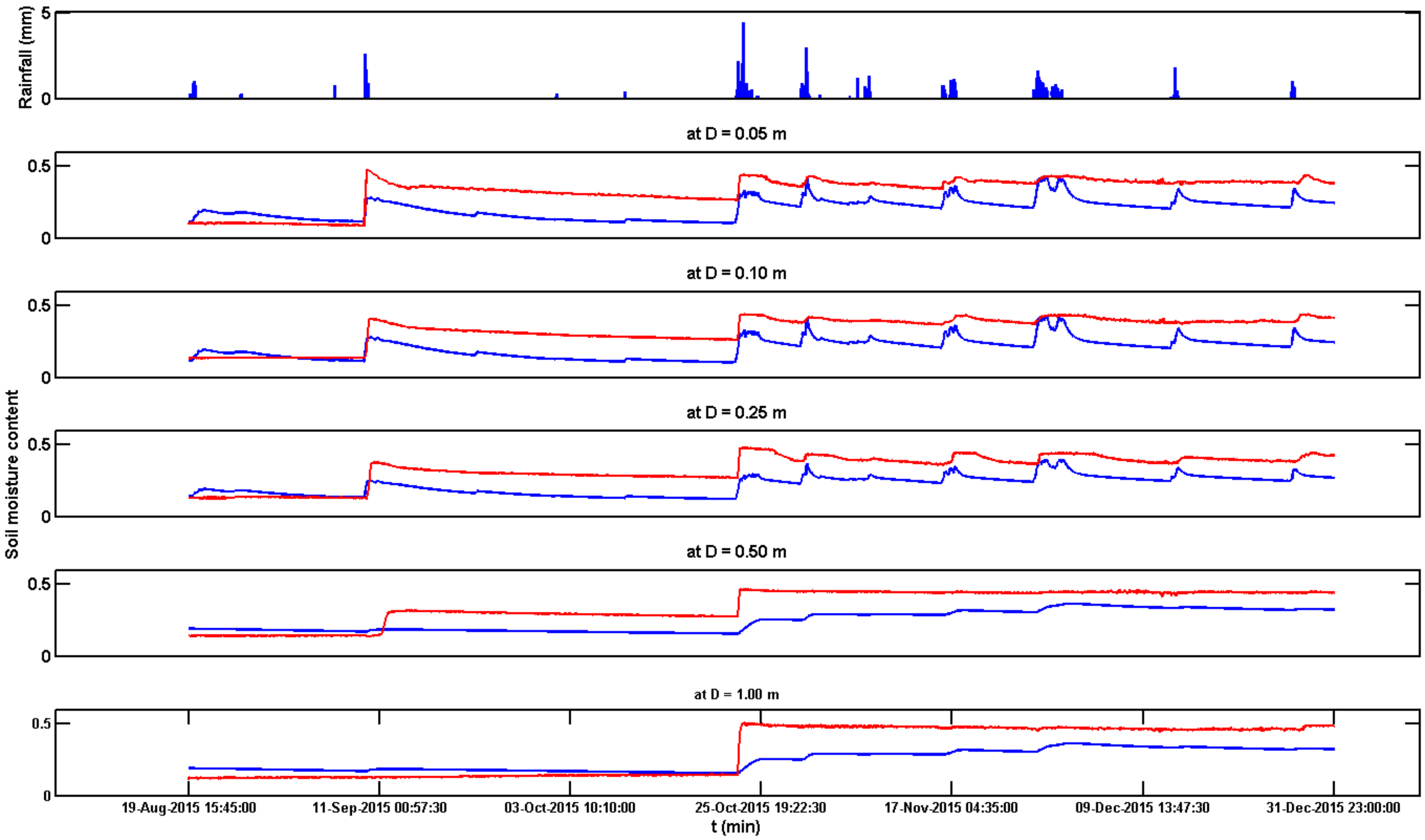

Figure B- 21 Time series of simulated and observed soil moisture content at CELB location using CASA QPE at 1/2HRAP resolution and a priori SAC parameters at 1 HRAP resolution. Simulated soil moisture depicted in blue and observed soil moisture in red.

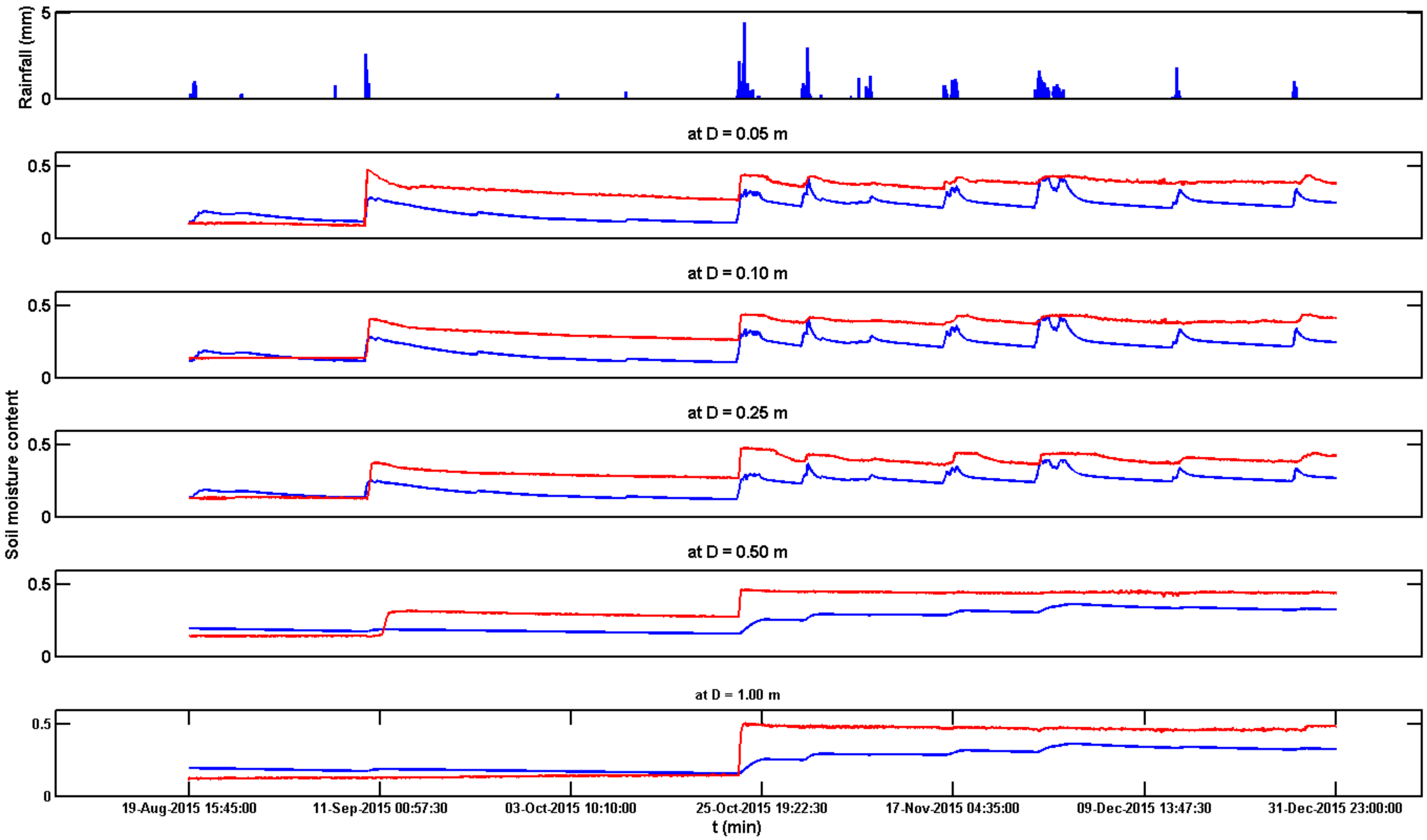

Figure B- 22 Time series of simulated and observed soil moisture content at CELB location using CASA QPE at 1/2HRAP resolution and a priori SAC parameters at 1/2 HRAP resolution. Simulated soil moisture depicted in blue and observed soil moisture in red.

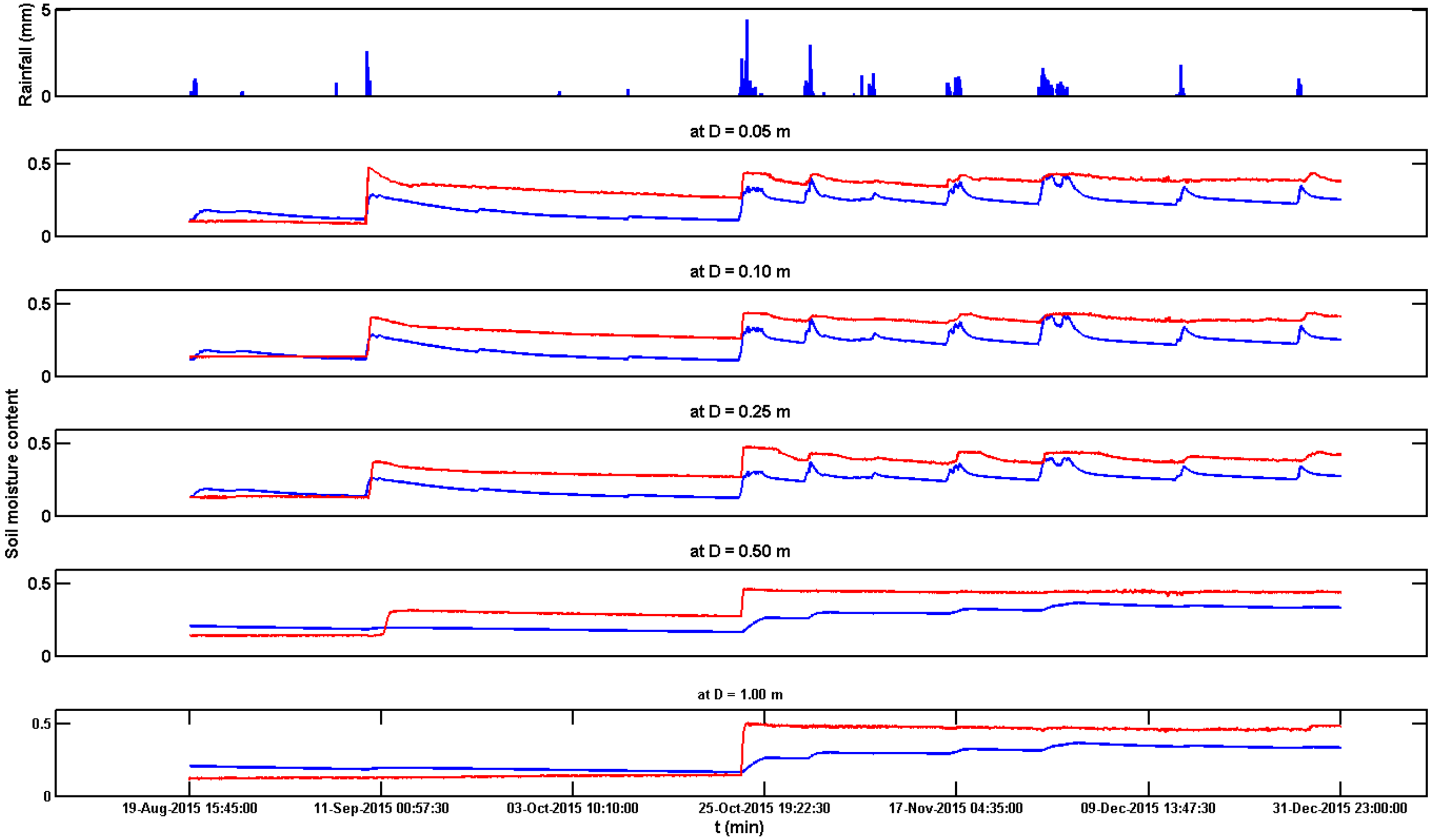

Figure B- 23 Time series of simulated and observed soil moisture content at CELB location using CASA QPE at 1/2HRAP resolution and a priori SAC parameters at 1/4 HRAP resolution. Simulated soil moisture depicted in blue and observed soil moisture in red.

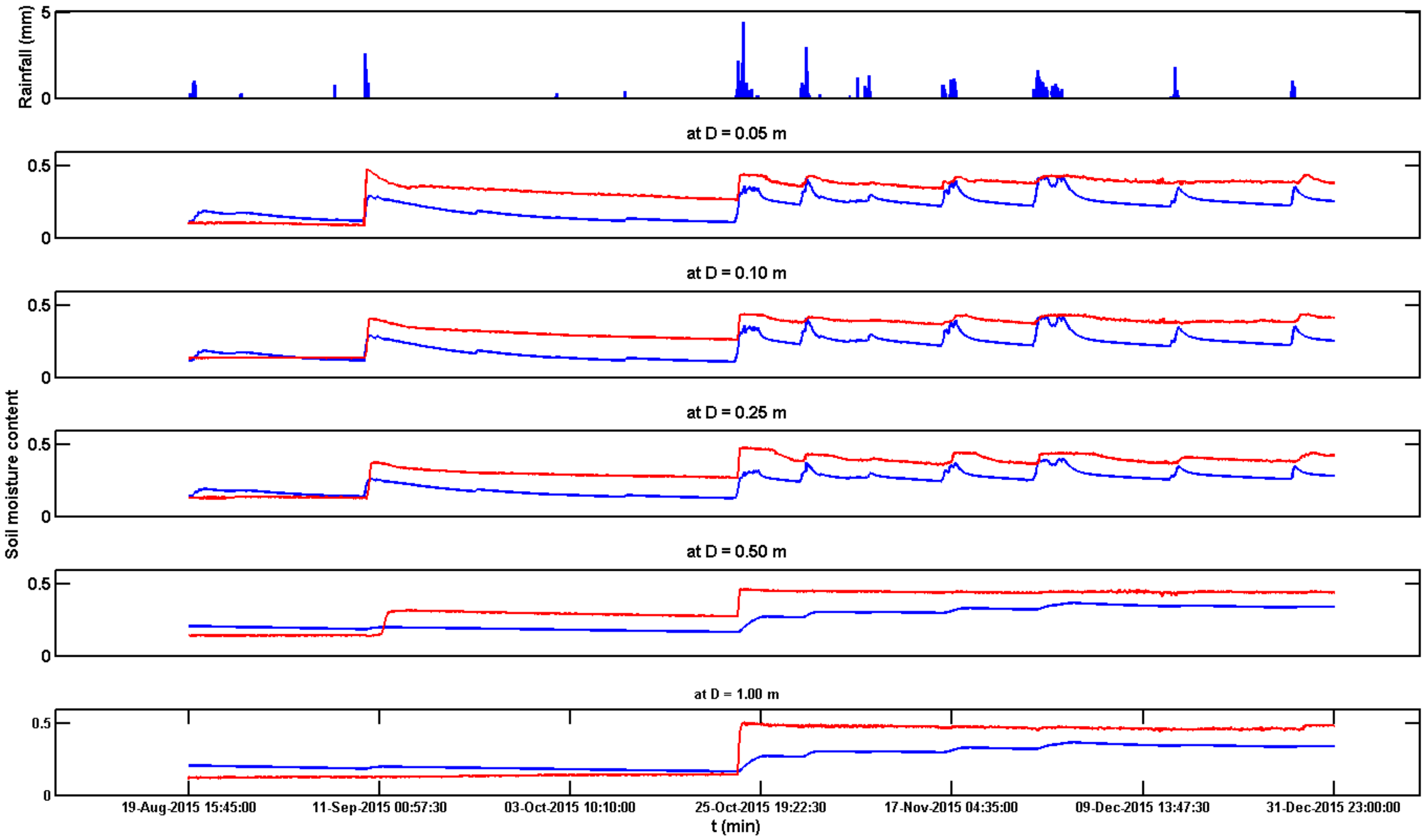

Figure B- 24 Time series of simulated and observed soil moisture content at CELB location using CASA QPE at 1/2HRAP resolution and a priori SAC parameters at 1/8 HRAP resolution. Simulated soil moisture depicted in blue and observed soil moisture in red.

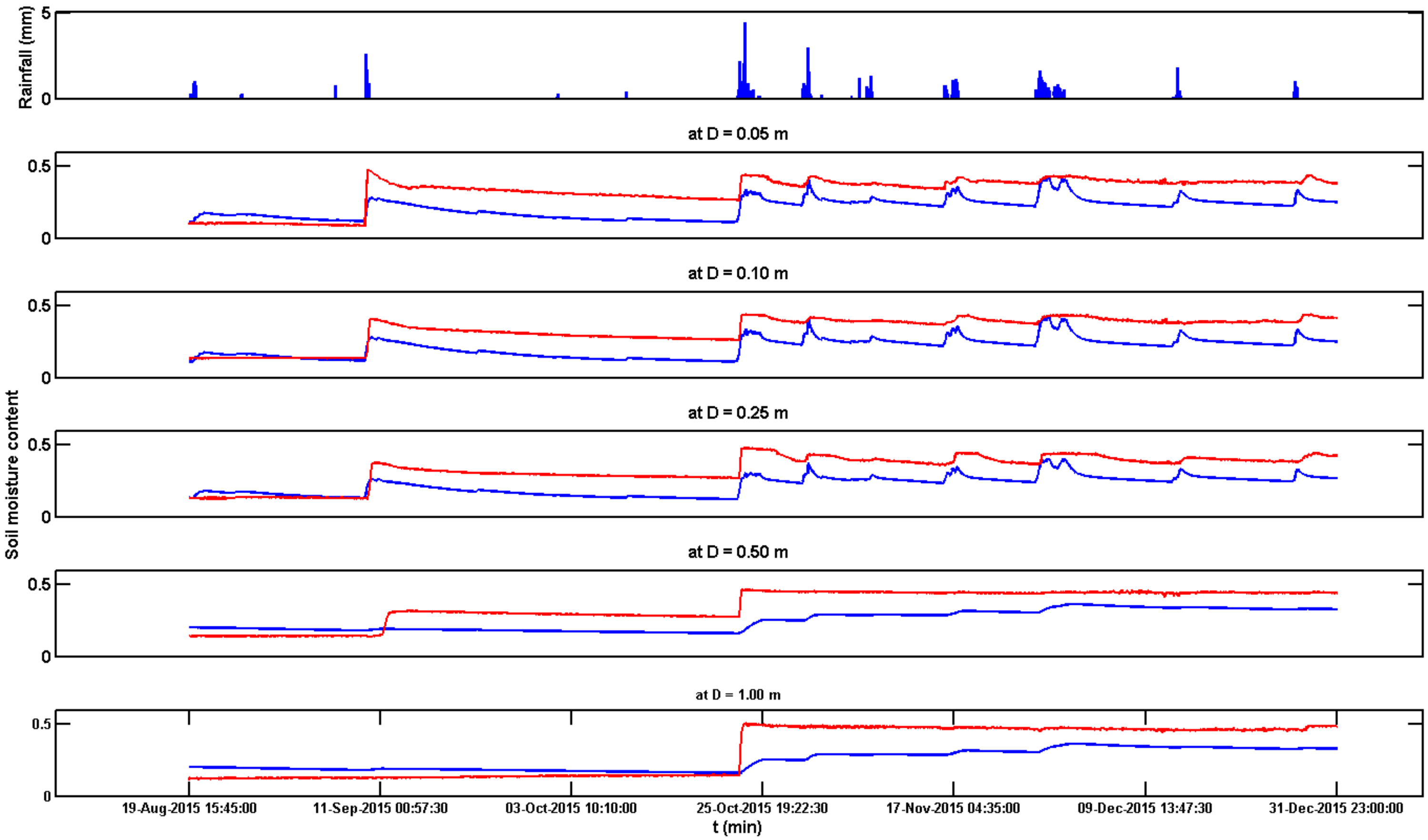

Figure B- 25 Time series of simulated and observed soil moisture content at CELB location using CASA QPE at 1/2HRAP resolution and a priori SAC parameters at 1/16 HRAP resolution. Simulated soil moisture depicted in blue and observed soil moisture in red.

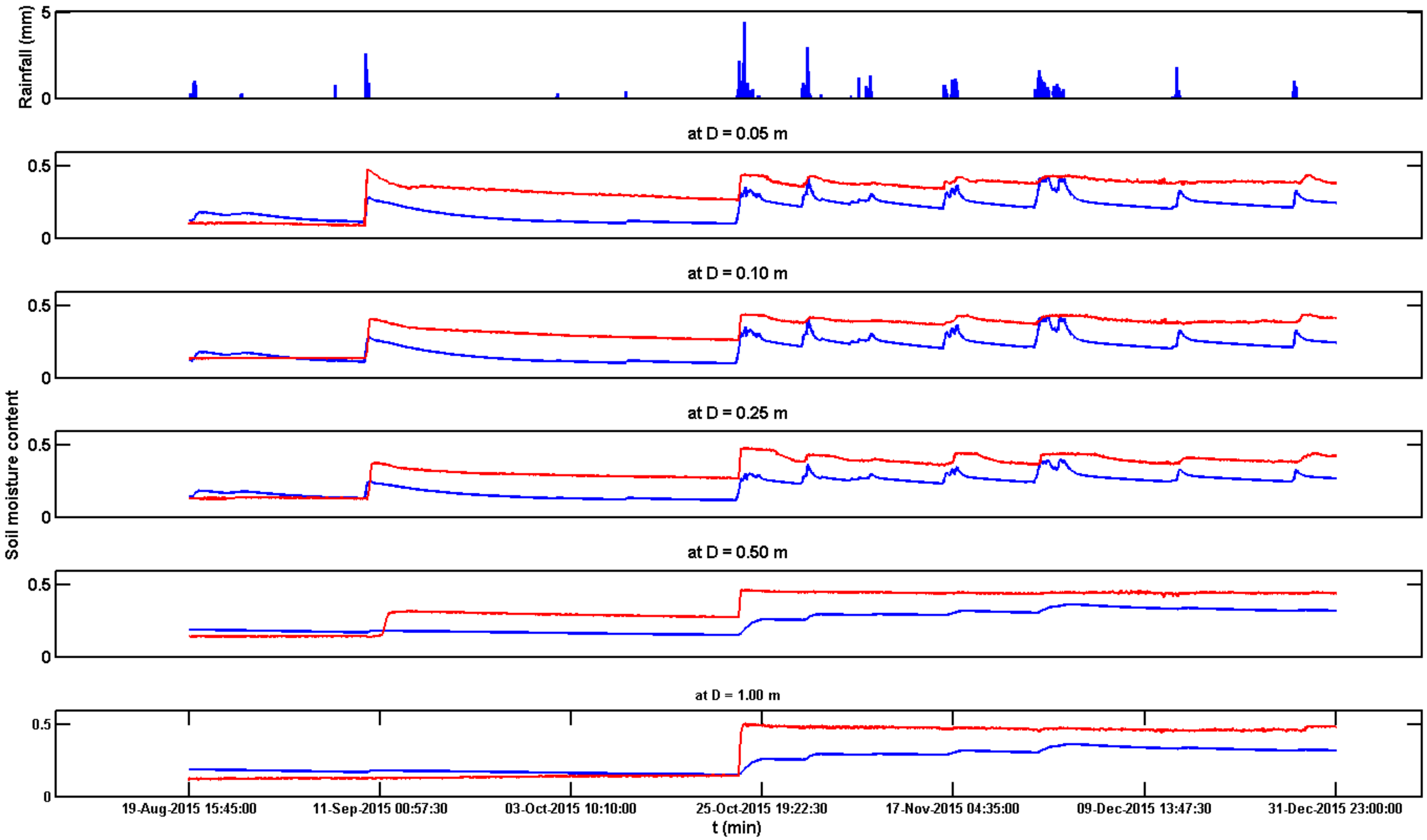

Figure B- 26 Time series of simulated and observed soil moisture content at CELB location using CASA QPE at 1/4 HRAP resolution and a priori SAC parameters at 1 HRAP resolution. Simulated soil moisture depicted in blue and observed soil moisture in red.

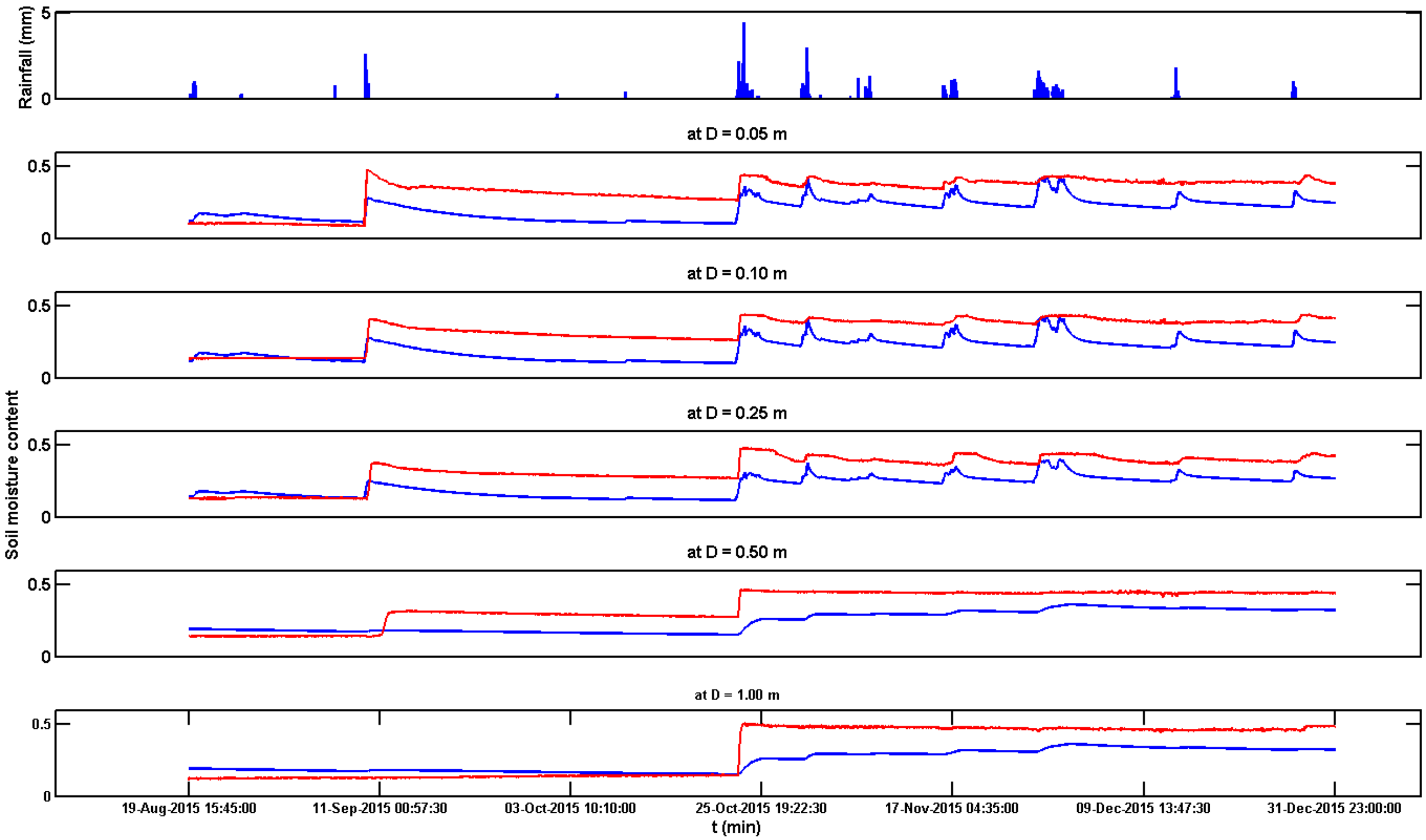

Figure B- 27 Time series of simulated and observed soil moisture content at CELB location using CASA QPE at 1/4 HRAP resolution and a priori SAC parameters at 1/2 HRAP resolution. Simulated soil moisture depicted in blue and observed soil moisture in red.

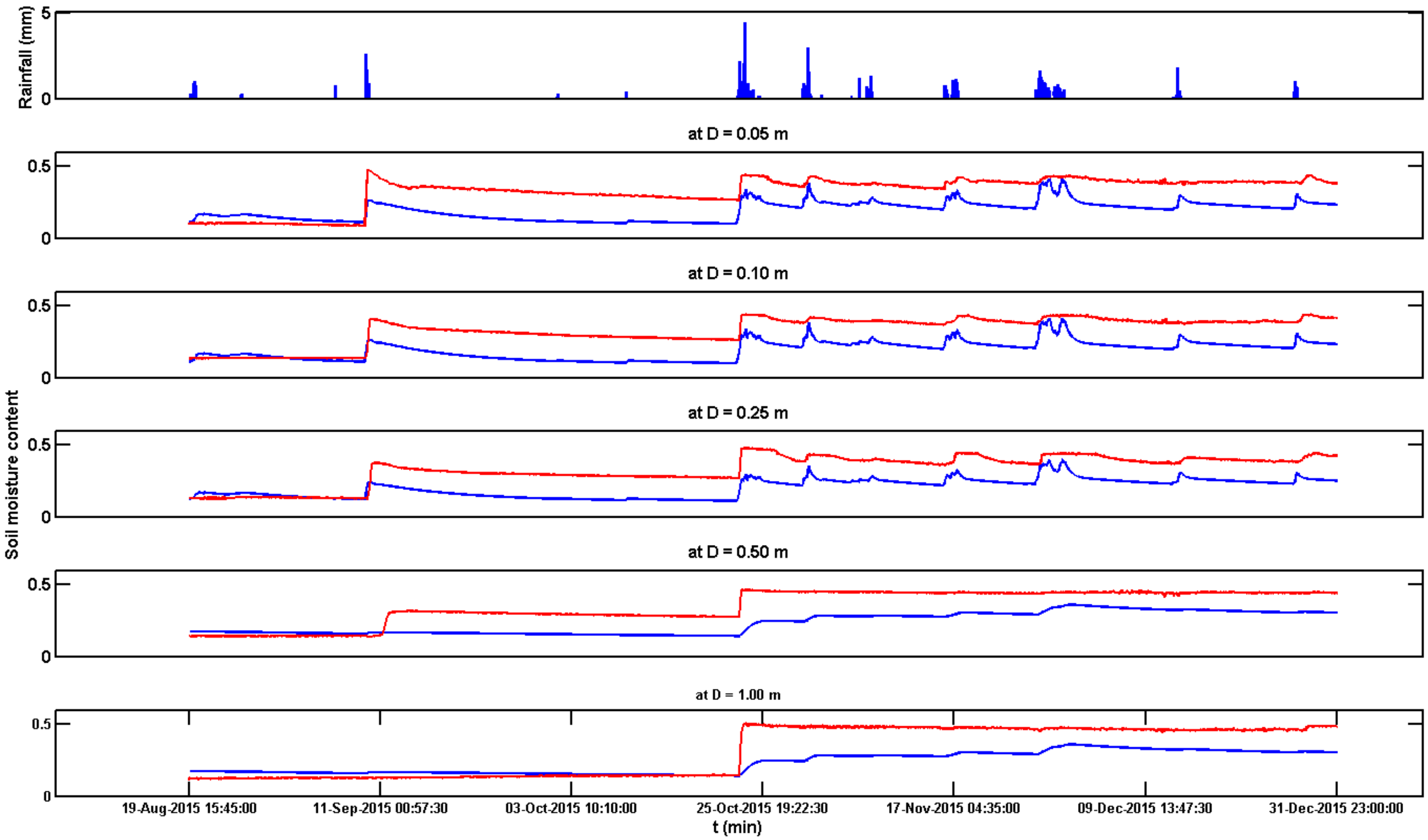

Figure B- 28 Time series of simulated and observed soil moisture content at CELB location using CASA QPE at 1/4 HRAP resolution and a priori SAC parameters at 1/4 HRAP resolution. Simulated soil moisture depicted in blue and observed soil moisture in red.

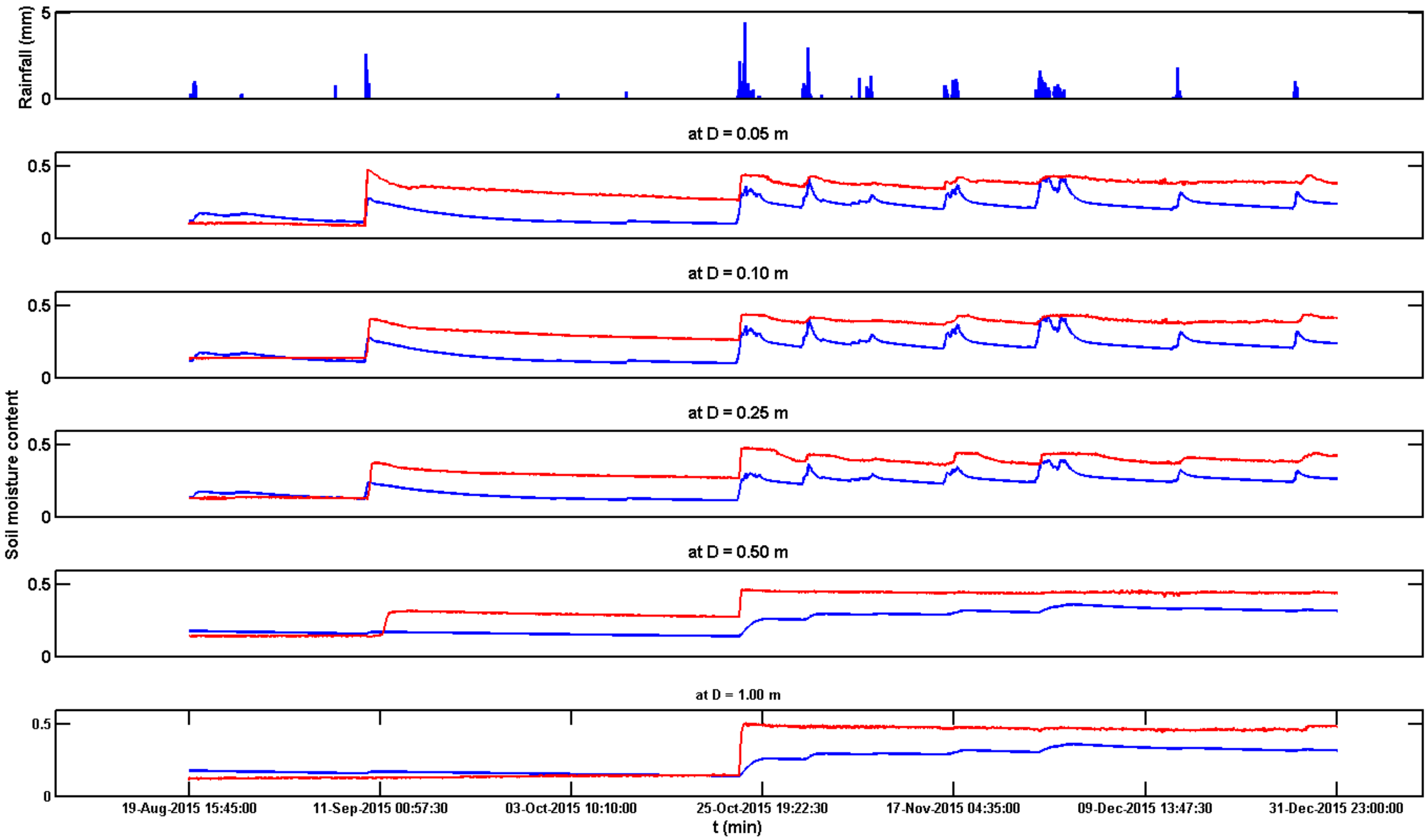

Figure B- 29 Time series of simulated and observed soil moisture content at CELB location using CASA QPE at 1/4 HRAP resolution and a priori SAC parameters at 1/8 HRAP resolution. Simulated soil moisture depicted in blue and observed soil moisture in red.

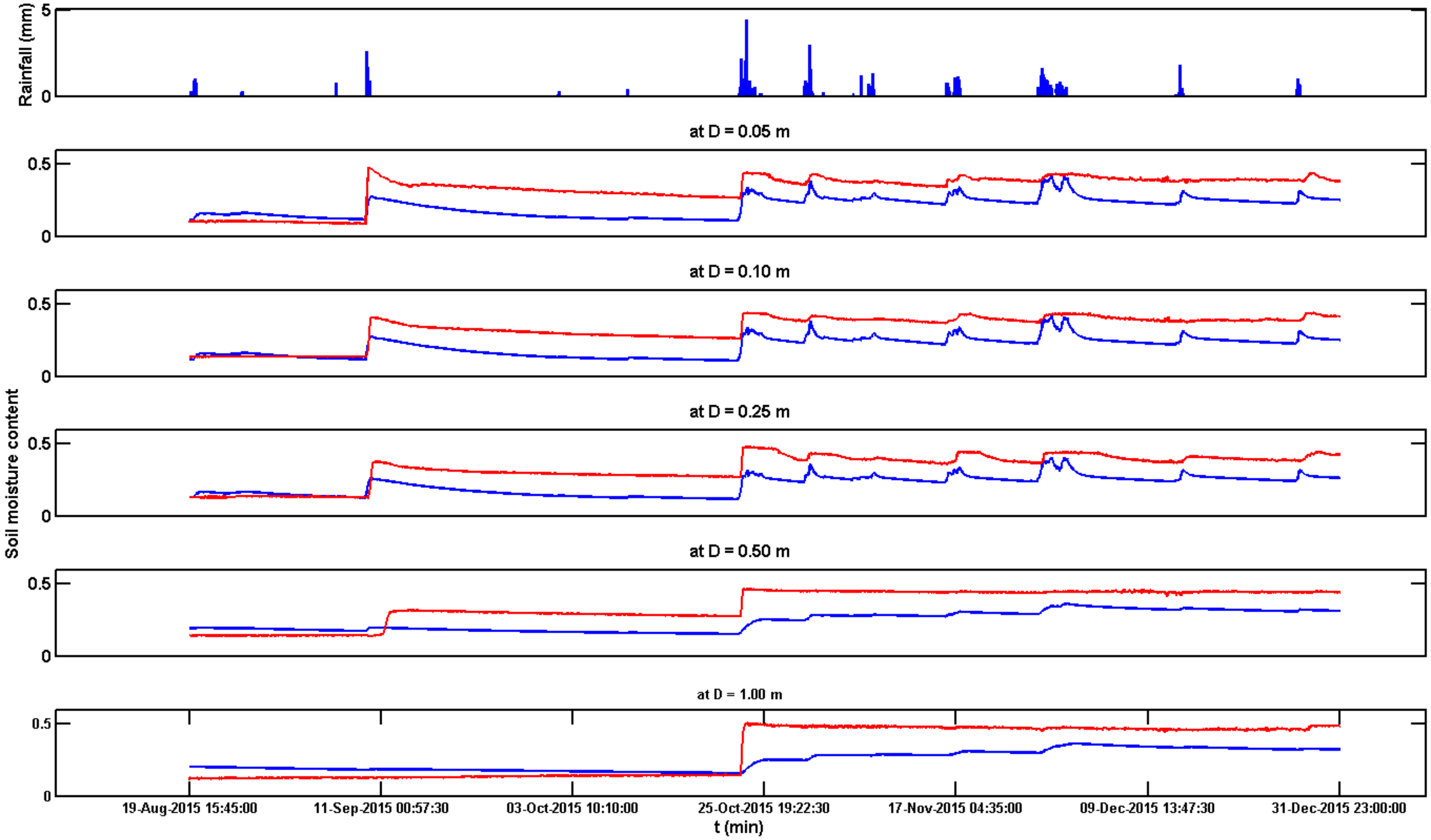

Figure B- 30 Time series of simulated and observed soil moisture content at CELB location using CASA QPE at 1/4 HRAP resolution and a priori SAC parameters at 1/16 HRAP resolution. Simulated soil moisture depicted in blue and observed soil moisture in red.

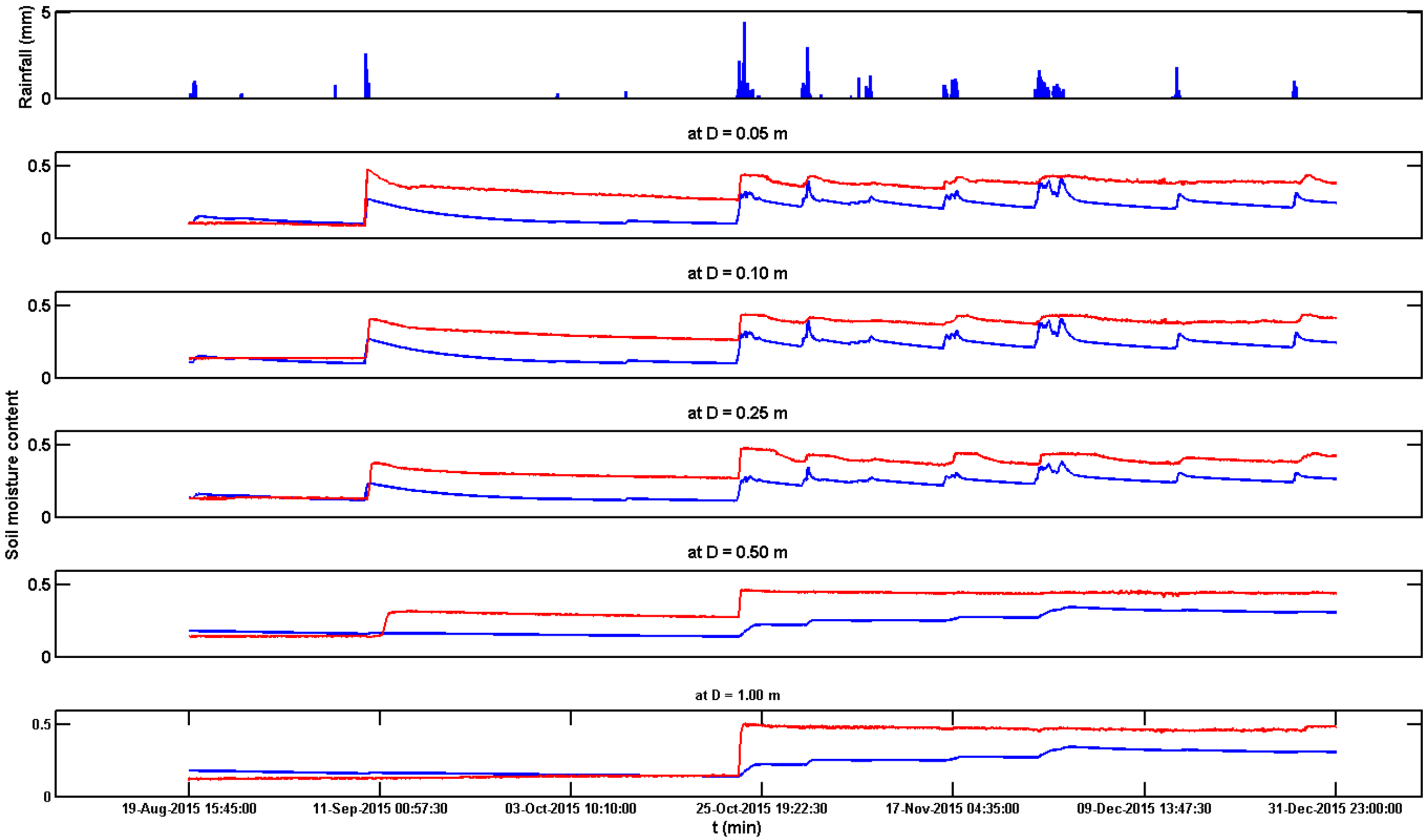

Figure B- 31 Time series of simulated and observed soil moisture content at CELB location using CASA QPE at 1/8 HRAP resolution and a priori SAC parameters at 1 HRAP resolution. Simulated soil moisture depicted in blue and observed soil moisture in red.

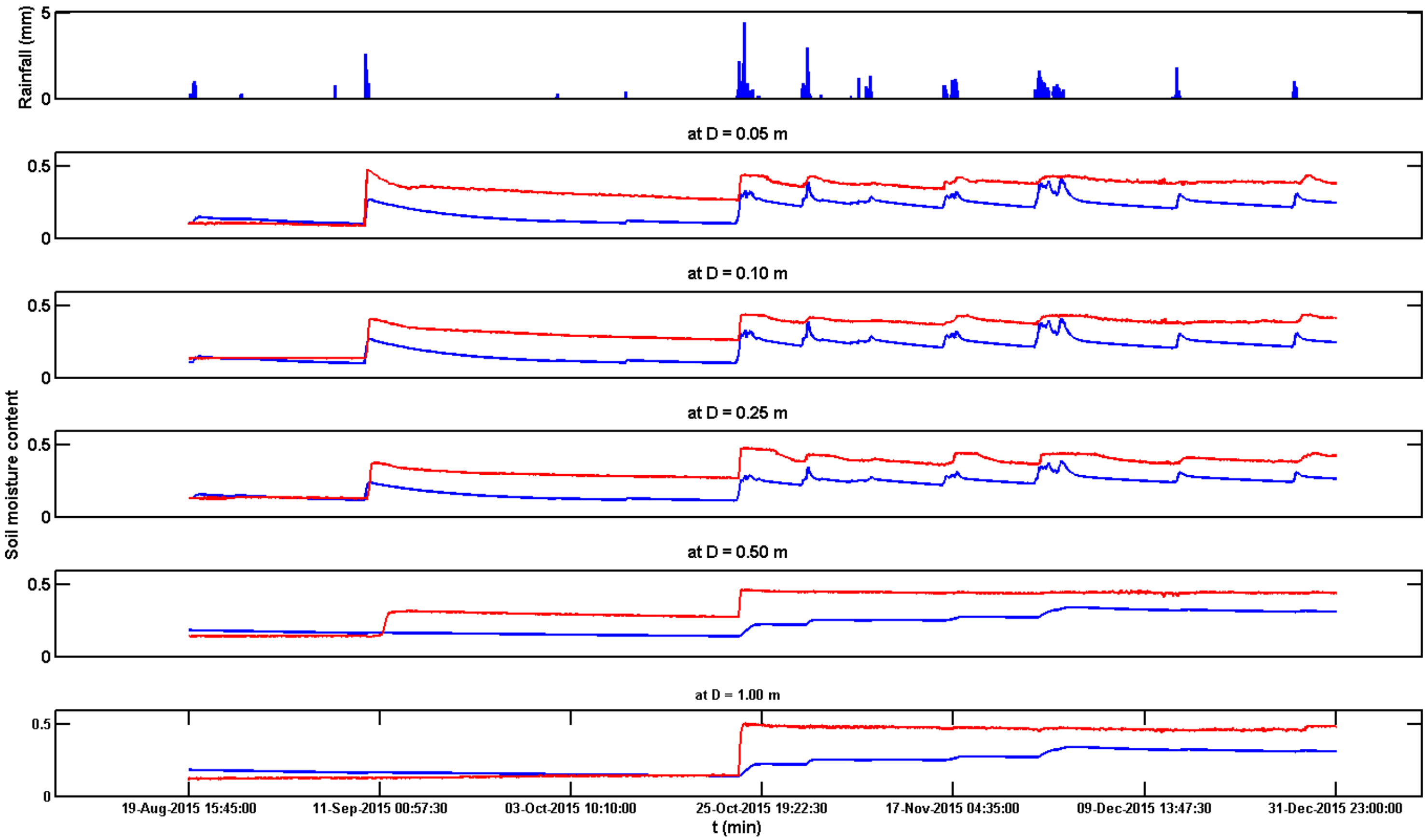

Figure B- 32 Time series of simulated and observed soil moisture content at CELB location using CASA QPE at 1/8 HRAP resolution and a priori SAC parameters at 1/2 HRAP resolution. Simulated soil moisture depicted in blue and observed soil moisture in red.

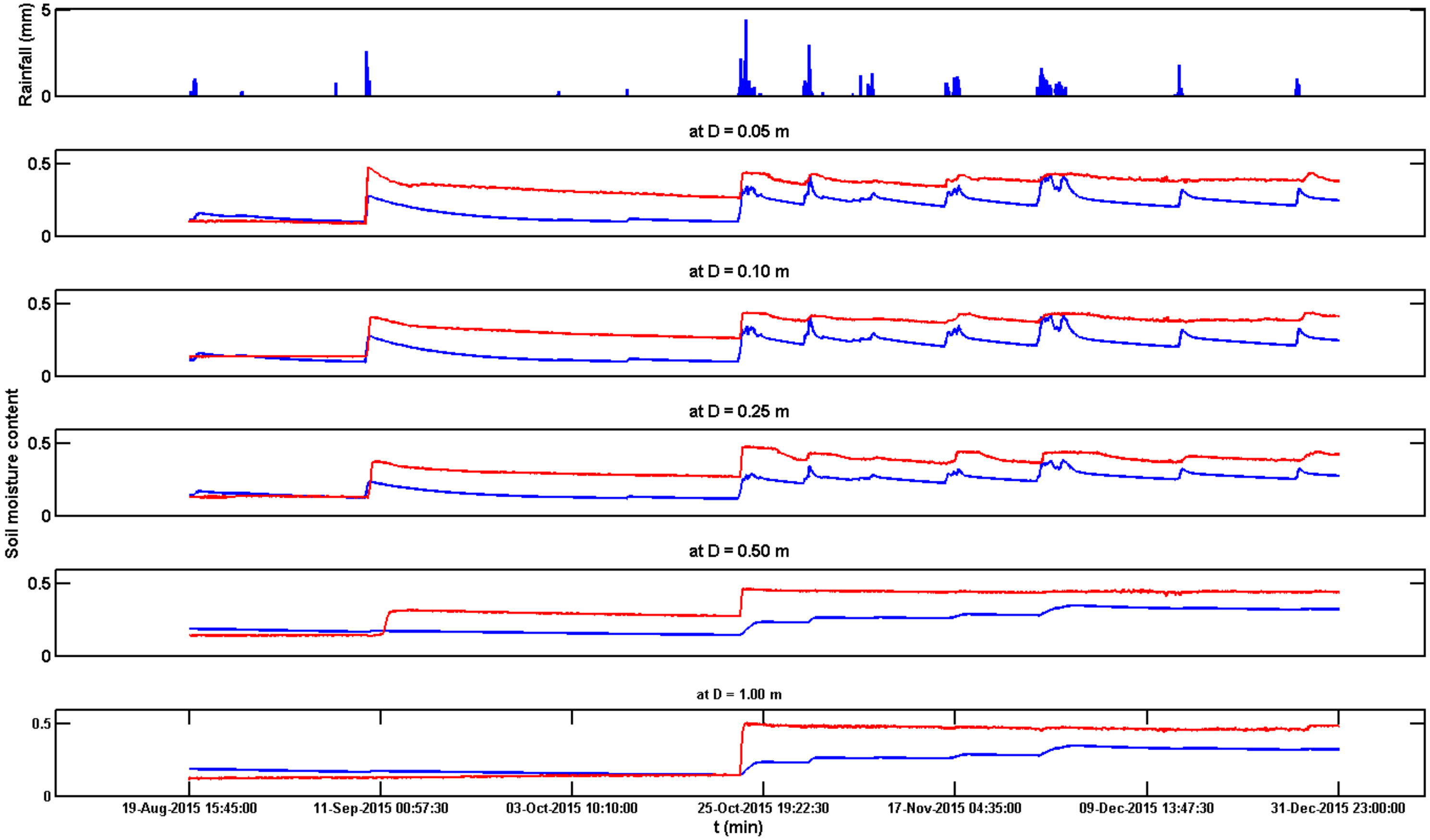

Figure B- 33 Time series of simulated and observed soil moisture content at CELB location using CASA QPE at 1/8 HRAP resolution and a priori SAC parameters at 1/4 HRAP resolution. Simulated soil moisture depicted in blue and observed soil moisture in red.

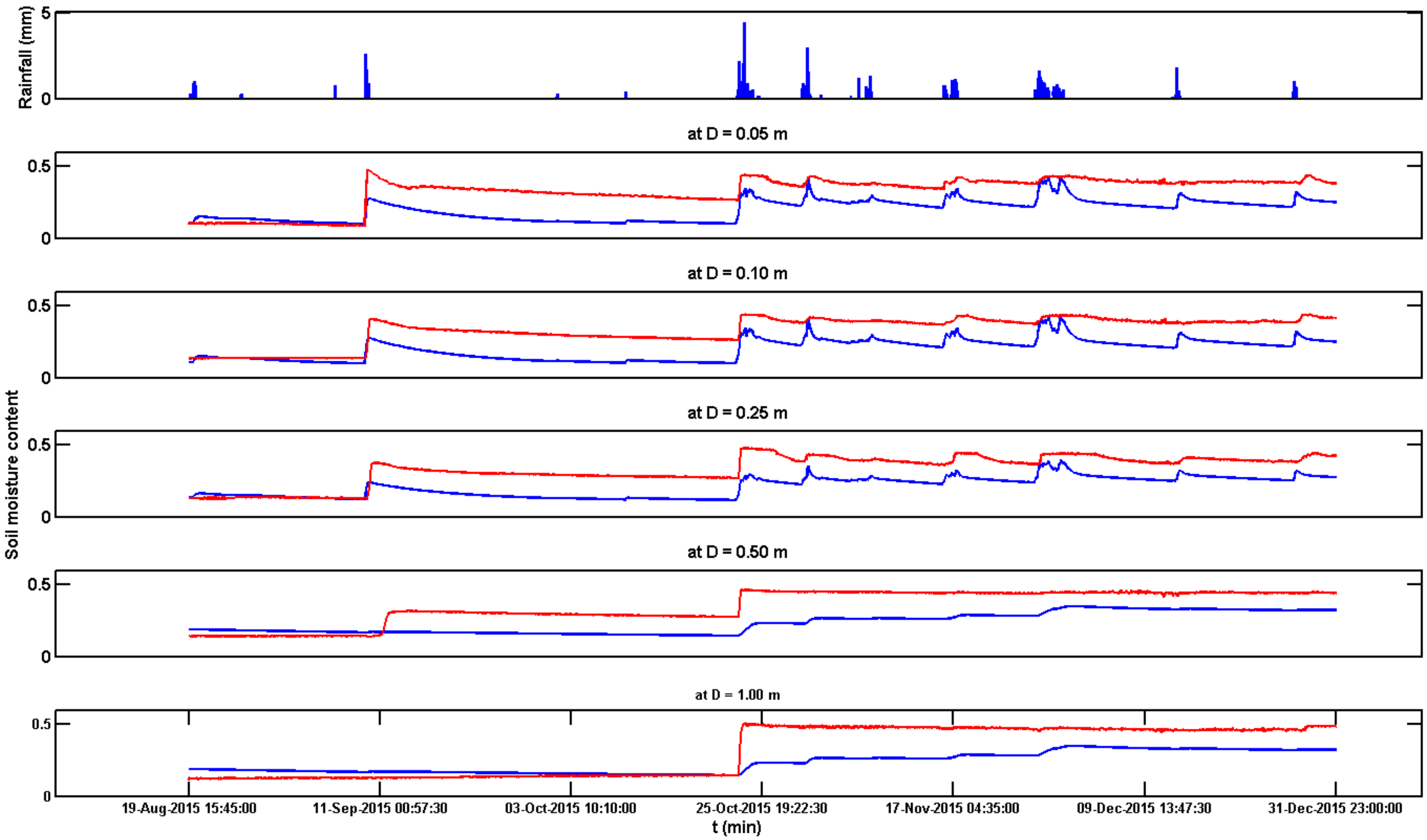

Figure B- 34 Time series of simulated and observed soil moisture content at CELB location using CASA QPE at 1/8 HRAP resolution and a priori SAC parameters at 1/8 HRAP resolution. Simulated soil moisture depicted in blue and observed soil moisture in red.

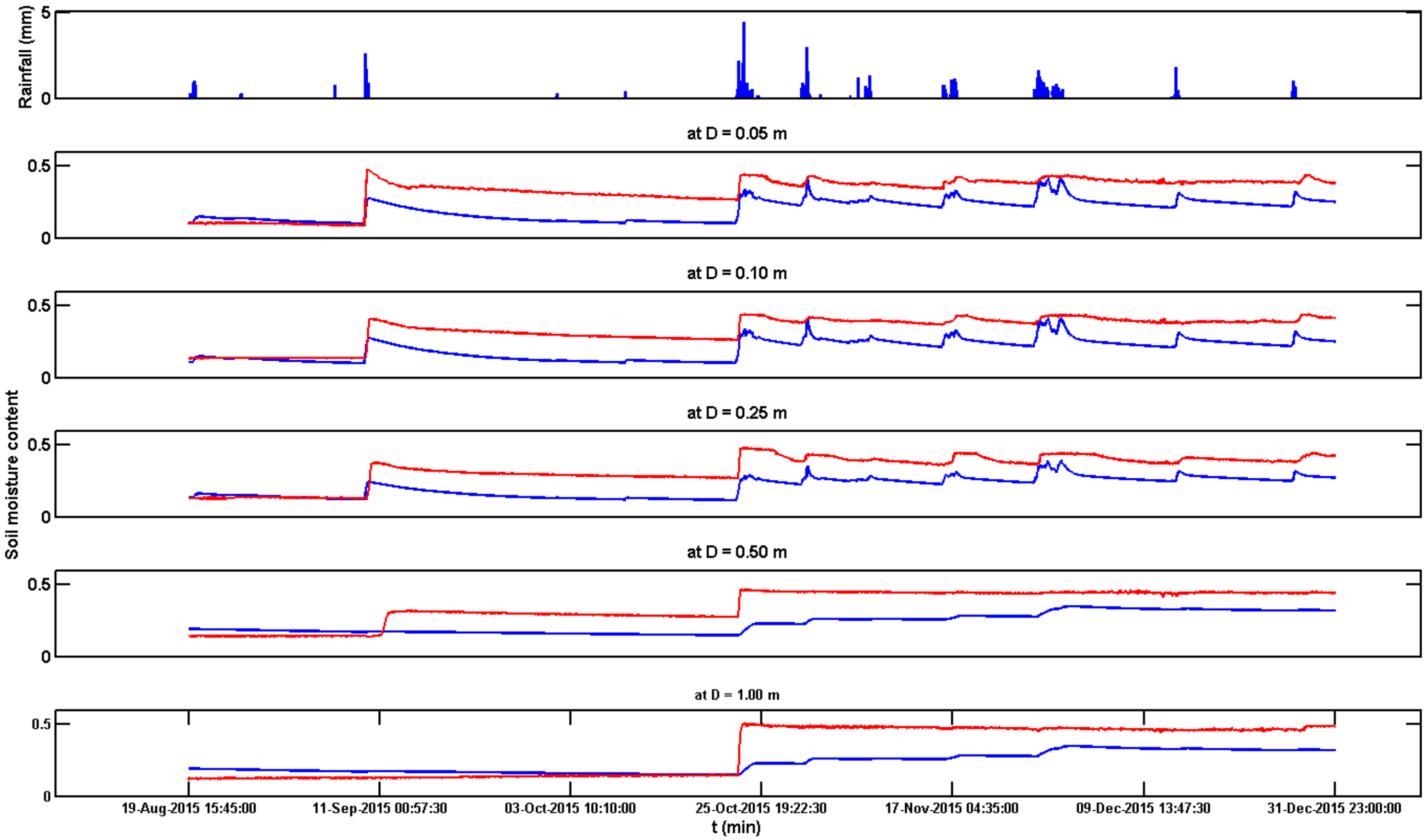

Figure B- 35 Time series of simulated and observed soil moisture content at CELB location using CASA QPE at 1/8 HRAP resolution and a priori SAC parameters at 1/16 HRAP resolution. Simulated soil moisture depicted in blue and observed soil moisture in red.

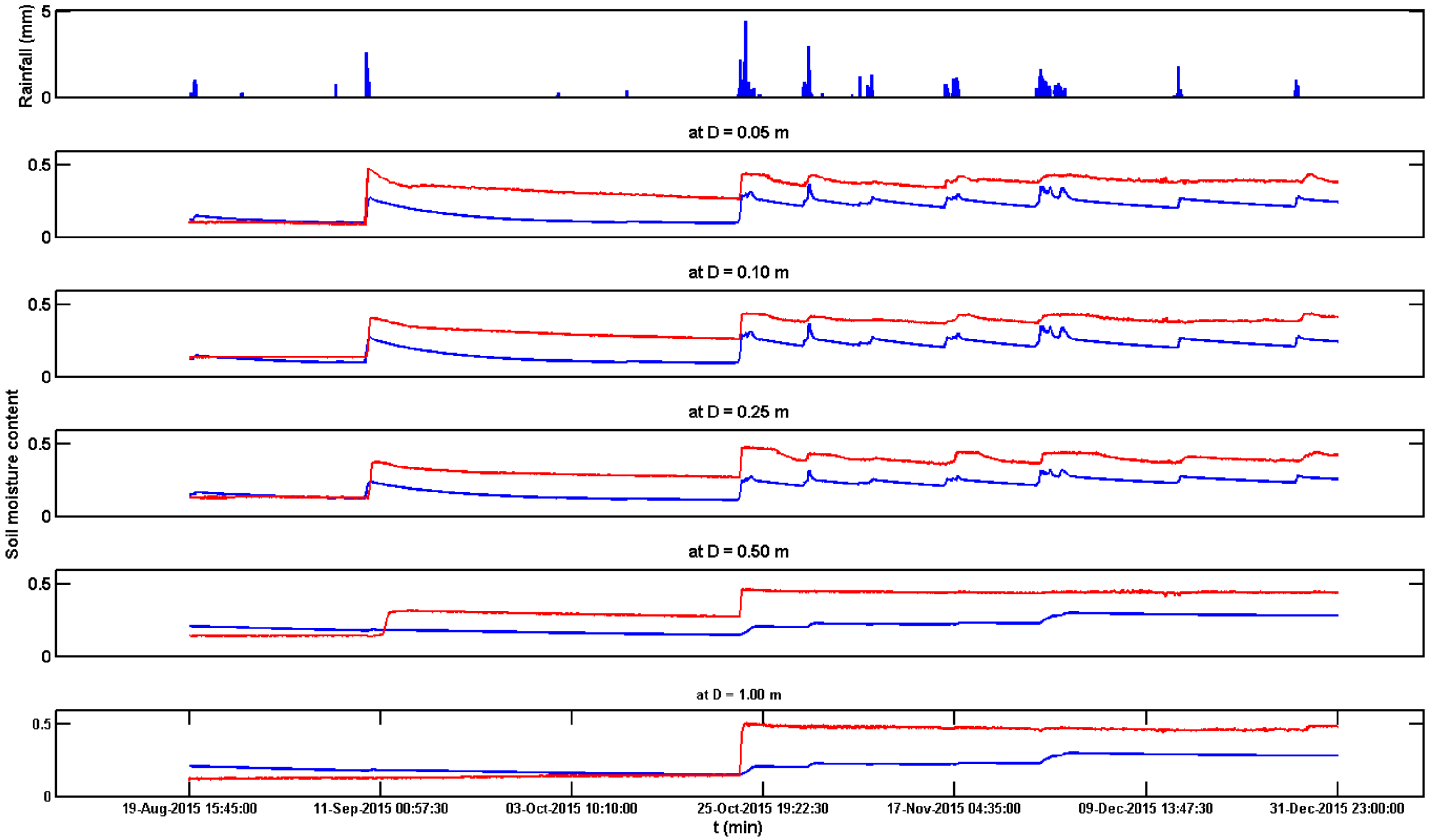

Figure B- 36 Time series of simulated and observed soil moisture content at CELB location using CASA QPE at 1/16 HRAP resolution and a priori SAC parameters at 1 HRAP resolution. Simulated soil moisture depicted in blue and observed soil moisture in red.

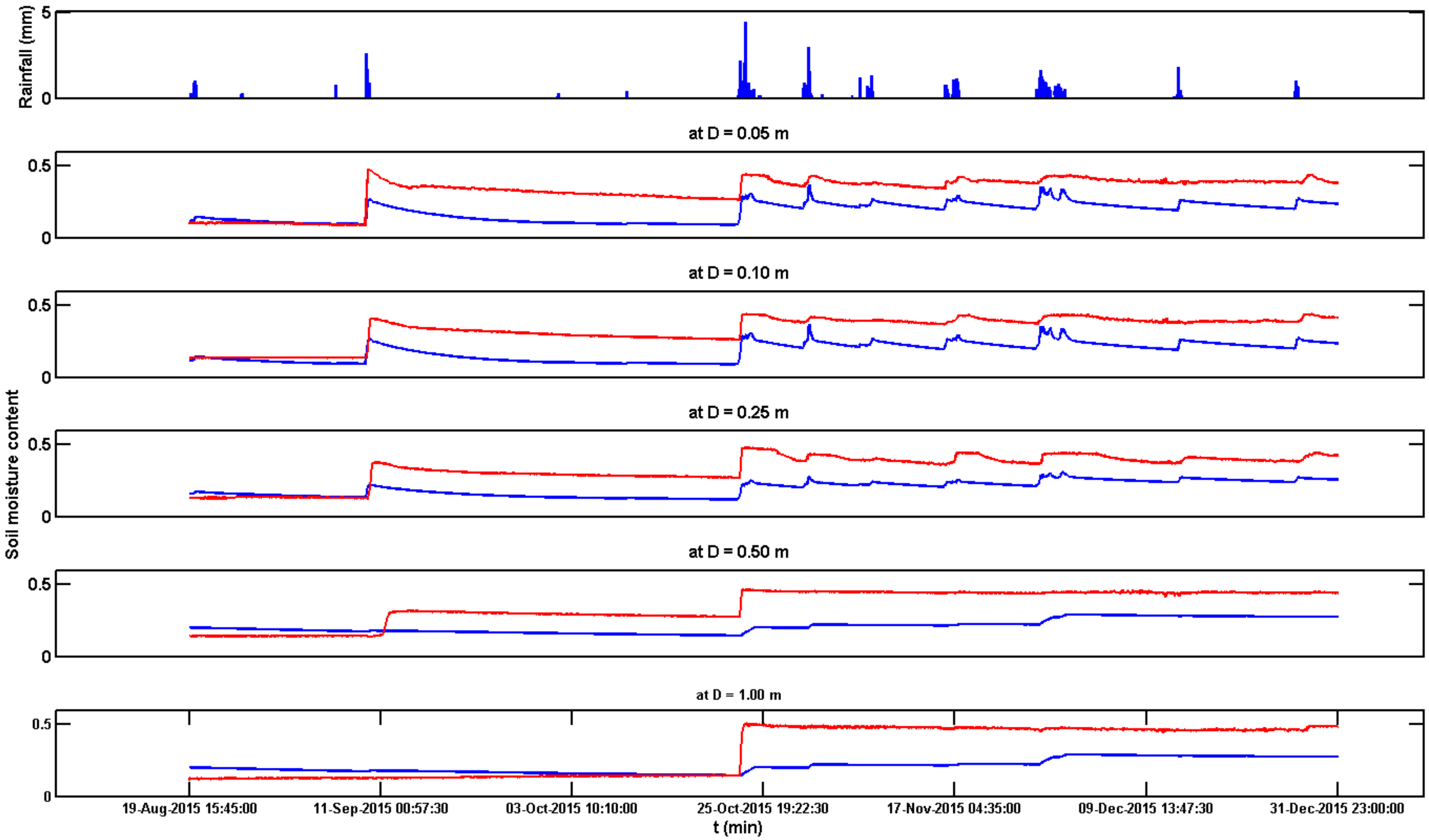

Figure B- 37 Time series of simulated and observed soil moisture content at CELB location using CASA QPE at 1/16 HRAP resolution and a priori SAC parameters at 1/2 HRAP resolution. Simulated soil moisture depicted in blue and observed soil moisture in red.

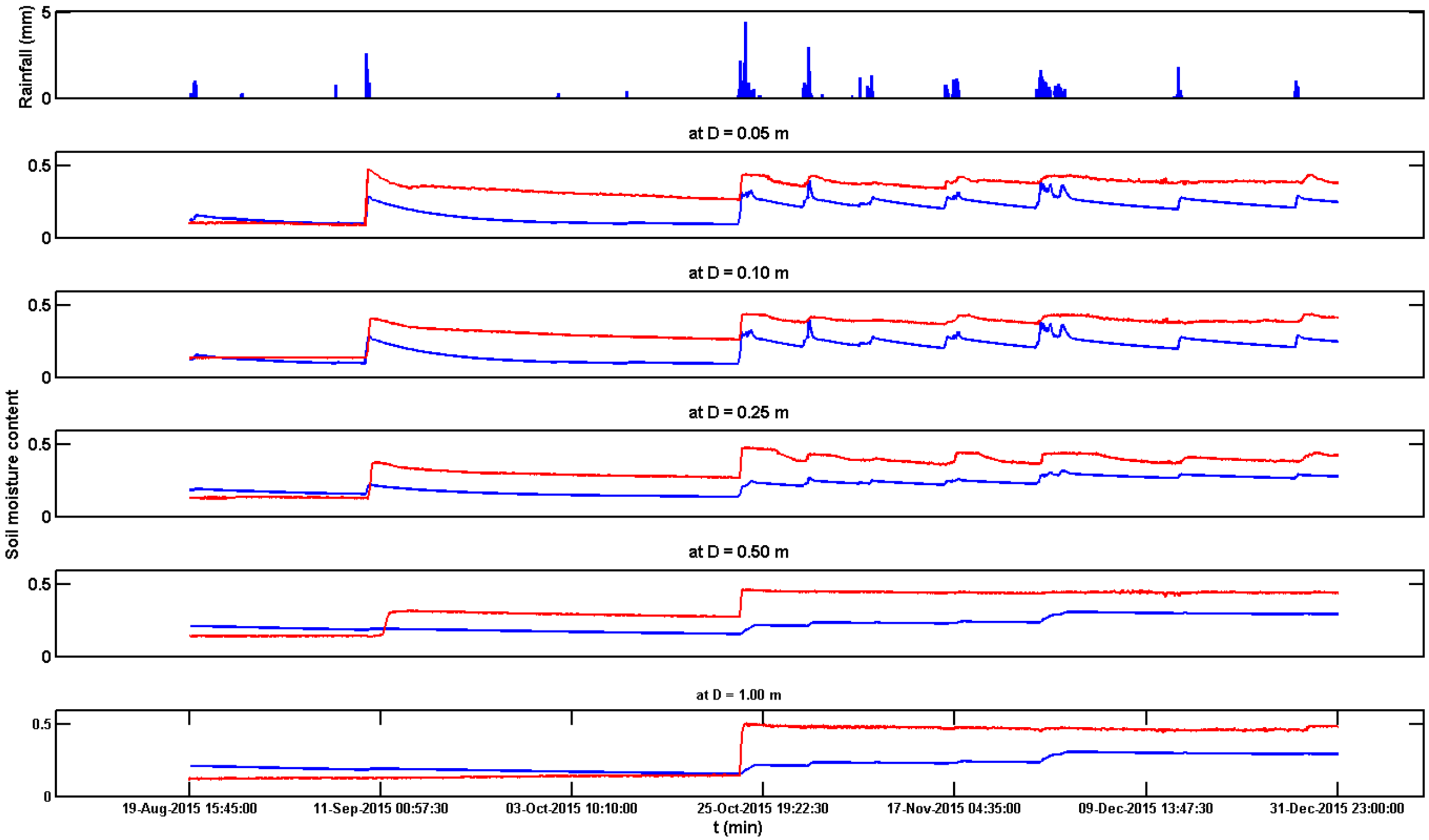

Figure B- 38 Time series of simulated and observed soil moisture content at CELB location using CASA QPE at 1/16 HRAP resolution and a priori SAC parameters at 1/4 HRAP resolution. Simulated soil moisture depicted in blue and observed soil moisture in red.

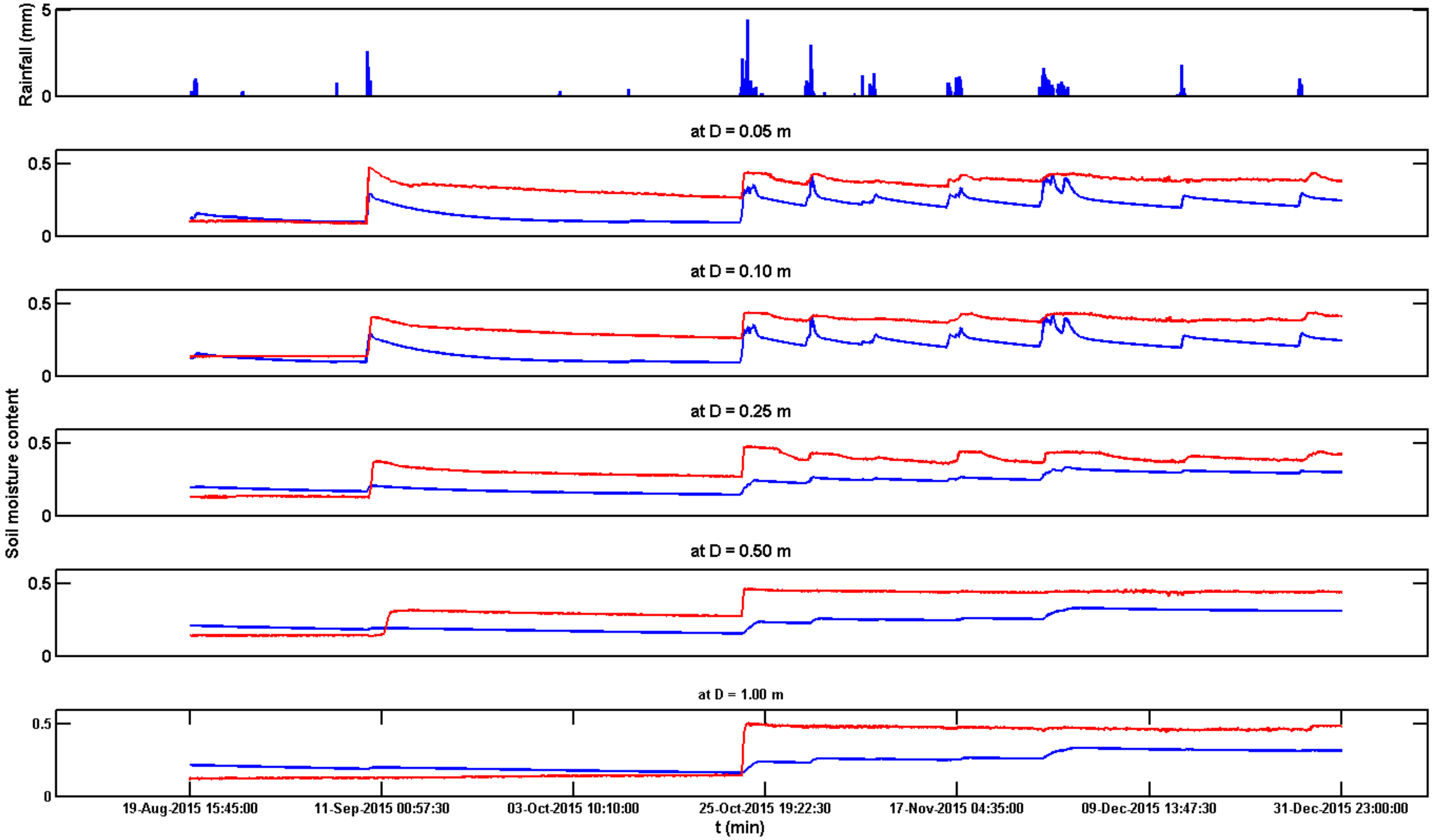

Figure B- 39 Time series of simulated and observed soil moisture content at CELB location using CASA QPE at 1/16 HRAP resolution and a priori SAC parameters at 1/8 HRAP resolution. Simulated soil moisture depicted in blue and observed soil moisture in red.

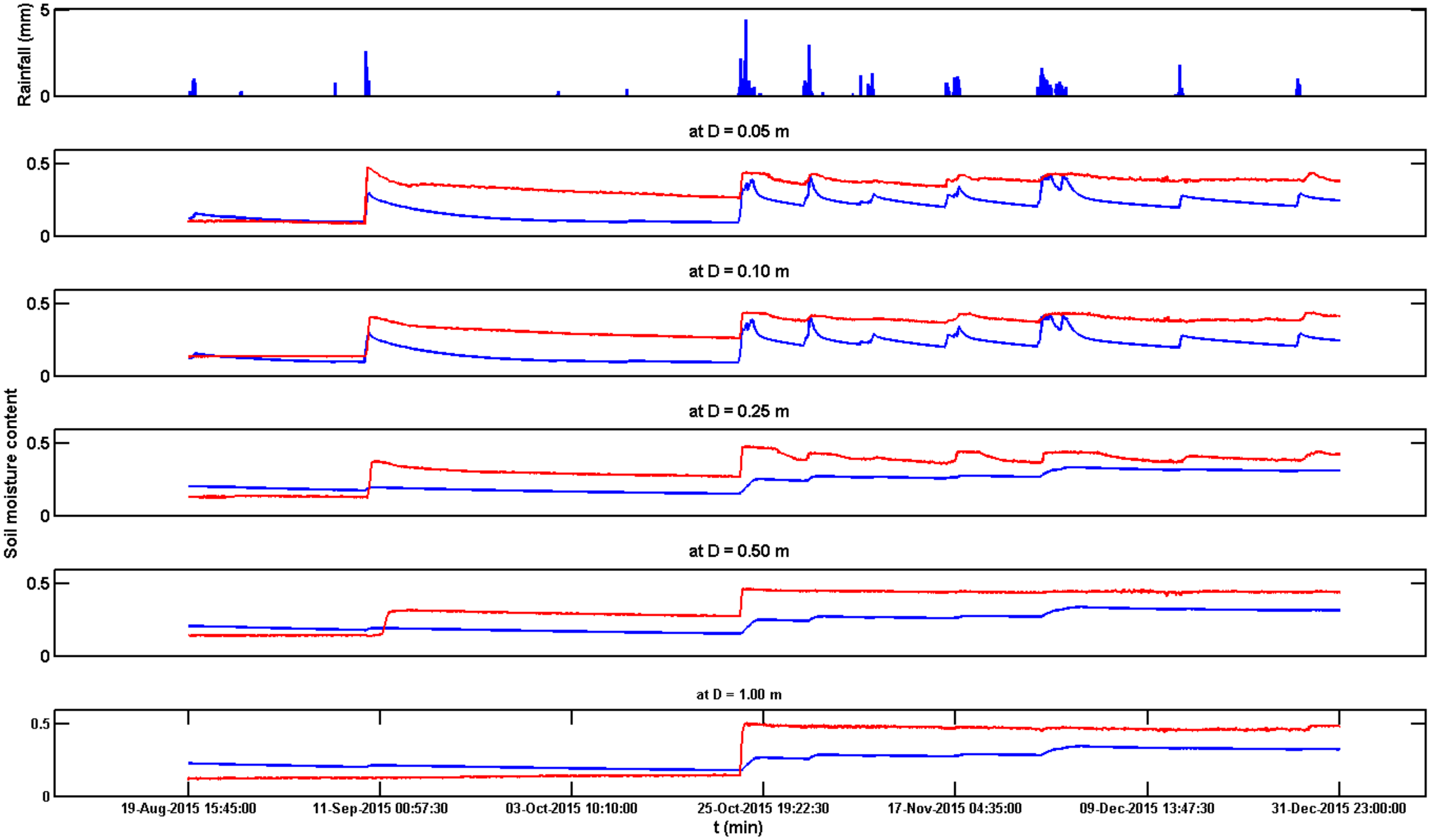

Figure B- 40 Time series of simulated and observed soil moisture content at CELB location using CASA QPE at 1/16 HRAP resolution and a priori SAC parameters at 1 HRAP resolution. Simulated soil moisture depicted in blue and observed soil moisture in red.

Appendix C

Bivariate Lognormal Distribution

The bivariate lognormal probability distribution function (PDF) is given by:

$$f(x_1, x_2) = \frac{1}{2\pi x_1 x_2 \sigma_{y_1} \sigma_{y_2} \sqrt{1-\rho^2}}$$
$$\exp\left(-\frac{1}{2(1-\rho^2)} \left[\left(\frac{\ln x_1 - \mu_{y_1}}{\sigma_{y_1}} \right)^2 - 2\rho \left(\frac{\ln x_1 - \mu_{y_1}}{\sigma_{y_1}} \right) \left(\frac{\ln x_2 - \mu_{y_2}}{\sigma_{y_2}} \right) + \left(\frac{\ln x_2 - \mu_{y_2}}{\sigma_{y_2}} \right)^2 \right] \right) \quad \text{(C1)}$$

where x_1 and x_2 are the two correlated lognormal random variables, y_1 and y_2 denote ln x_1 and ln x_2, respectively, ρ denotes correlation between y_1 and y_2, μ_{y_1} and μ_{y2} denote $E[y_1]$ and $E[y_2]$, respectively, and σ_{y_1} and σ_{y2} denote standard deviation of y_1 and y_2, respectively. The standard deviation and mean of y are related to those of x via:

$$\sigma_y = \left[\ln\left(1 + \frac{\sigma_x^2}{\mu_x^2} \right) \right]^{1/2} \quad \text{(C2)}$$

$$\mu_y = \ln(\mu_x) - \frac{\sigma_y^2}{2} \quad \text{(C3)}$$

$$\mu_x = 2\ln(\mu_y) - \frac{1}{2}\ln(\sigma_y^2 + \mu_y^2) \quad \text{(C4)}$$

$$\sigma_x^2 = -2\ln(\mu_y) + \ln(\sigma_y^2 + \mu_y^2) \quad \text{(C5)}$$

where μ_x denote E[x] and σ_x denote the mean and standard deviation of x, respectively.

We assume $P(u) \sim LN(\mu_u, \sigma_u^2)$ for P(u)>0. Then, mean and variance of ln(P(u)), P(u)>0, are given by (E4) and (E5), respectively, as:

$$\mu_u = 2\ln(E[P(u) \mid P(u) > 0] - 0.5\ln(Var[P(u) \mid P(u) > 0] + E^2[P(u) \mid P(u) > 0]) \quad \text{(C6)}$$

$$\sigma_u^2 = -2\ln(E[P(u) \mid P(u) > 0]) + \ln(Var[P(u) \mid P(u) > 0] + E^2[P(u) \mid P(u) > 0]) \quad \text{(C7)}$$

Once $E[P(u), P(v) \,|\, i_{I\,\mathrm{int}}(u) = 1, i_{I\,\mathrm{int}}(v) = 1, \int_A I_{\mathrm{int}}(u)du > 0]$ is evaluated by Eq.(7-16), the correlation coefficient between ln(P(u)) and ln(P(v)), ρ_{uv}, may be solved for from the following relationship:

$$\begin{aligned} &E[P(u), P(v) \,|\, i_{I\,\mathrm{int}}(u) = 1, i_{I\,\mathrm{int}}(v) = 1, \int_A I_{\mathrm{int}}(u)du > 0] \\ &= \exp(\tfrac{1}{2}\sigma_u^2 + \tfrac{1}{2}\sigma_v^2 + \mu_u + \mu_v)\exp(\rho_{uv}\sigma_u\sigma_v) \end{aligned} \tag{C8}$$

Appendix D

Bivariate Weibull Distribution

We use the following mixture type whose CDF is given by (Johnson et al., 1999):

$$P[X > x, Y > y] = \exp\left[-\left\{\left(\frac{x}{\theta_1}\right)^{\beta_1/\delta} + \left(\frac{y}{\theta_2}\right)^{\beta_2/\delta}\right\}^{\delta}\right], \quad 0 < \delta \le 1 \qquad \text{(D1)}$$

where X and Y are the correlation Weibull-distributed random variables, and y are the experimental values that X and Y take on, respectively, β_1 and β_2 are the shape parameters, and θ_1 and θ_2 are the scale parameters. Correlation is almost inversely linear in δ for $\beta_1=\beta_2$. The PDF of the above CDF is given by (Johnson et al., 1999):

$$f(x,y) = \frac{\beta_1}{\theta_1}\left(\frac{x}{\theta_1}\right)^{(\beta_1/\delta)-1} \frac{\beta_2}{\theta_2}\left(\frac{y}{\theta_2}\right)^{(\beta 2/\delta)-1} \left\{\left(\frac{x}{\theta_1}\right)^{\beta_1/\delta} + \left(\frac{y}{\theta_2}\right)^{\beta_2/\delta}\right\}^{\delta-2}$$

$$\left[\left\{\left(\frac{x}{\theta_1}\right)^{\beta_1/\delta} + \left(\frac{y}{\theta_2}\right)^{\beta_2/\delta}\right\}^{\delta} + \frac{1}{\delta} - 1\right] \exp\left[-\left\{\left(\frac{x}{\theta_1}\right)^{\beta_1/\delta} + \left(\frac{y}{\theta_2}\right)^{\beta_2/\delta}\right\}^{\delta}\right] \qquad \text{(D2)}$$

Lu and Bhattacharyya (1990) provides the moments as follows:

$$E[X] = \theta_1 \Gamma(1/\beta_1 + 1) \qquad \text{(D3)}$$

$$Var[X] = \theta_1^2\{\Gamma(2/\beta_1 + 1) - \Gamma^2(1/\beta_1 + 1)\} \qquad \text{(D4)}$$

$$Cov[X,Y] = \frac{\theta_1\theta_2\left[\Gamma\left(\frac{\delta}{\beta_1}+1\right)\Gamma\left(\frac{\delta}{\beta_2}+1\right)\Gamma\left(\frac{1}{\beta_1}+\frac{1}{\beta_2}+1\right) - \Gamma\left(\frac{1}{\beta_1}+1\right)\Gamma\left(\frac{1}{\beta_2}+1\right)\Gamma\left(\frac{\delta}{\beta_1}+\frac{\delta}{\beta_2}+1\right)\right]}{\Gamma\left(\frac{\delta}{\beta_1}+\frac{\delta}{\beta_2}+1\right)} \qquad \text{(D5)}$$

As in (E3), once Cov[X,Y], E[X], Var[X], E[Y] and Var[Y] are specified δ may be solved for using (F5), which then completely prescribes the PDF.

Appendix E

Bivariate Gamma Distribution

The bivariate gamma distribution used in this work is the Nagao and Kadoya Model 1 (Nagao and Kadoya, 1970; Iliopoulos et al., 2005) which is based on the 5-parameter model of *Izawa*, 1953:

$$f(x,y)=\frac{(\lambda_1\lambda_2)^{\upsilon}}{(1-\rho)\Gamma(\upsilon)}\left(\frac{xy}{\rho\lambda_1\lambda_2}\right)^{\frac{\upsilon-1}{2}}\exp\left(-\frac{\lambda_1 x+\lambda_2 y}{1-\rho}\right)I_{\upsilon-1}\left(\frac{2\sqrt{\rho\lambda_1\lambda_2 xy}}{1-\rho}\right) \qquad \text{(E1)}$$

In the above, λ_1 and λ_2 denote the rate parameters for x and y, respectively, v denotes the shape parameter, ρ denotes the correlation coefficient, and $I_v(\cdot)$ denotes the modified Bessel function of the first kind of order v defined as:

$$I_{\upsilon}(\alpha)=\sum_{\kappa=0}^{\infty}\frac{(\alpha/2)^{2\kappa+\upsilon}}{\Gamma(\kappa+\nu+1)\kappa!},\quad \alpha>0 \qquad \text{(E2)}$$

where Γ(·) denotes the gamma function. The marginal PDFs of x is given by:

$$f(x)=\frac{\lambda^{\upsilon}}{\Gamma(\nu)}x^{\upsilon-1}\exp(-\lambda x) \qquad \text{(E3)}$$

If v=1, Eq.(F1) reduces to the bivariate exponential function of Downton (1970).

References

Ali, M., Khan, Z., Khan, S. J., and Aslam, I., 2011. Simulation of the impacts of land-use change on surface runoff of lai nullah basin in islamabad, pakistan. Landscape and Urban Planning, 102(4), 271-279. doi:10.1016/j.landurbplan.2011.05.006

Anderson, R.M., Koren, V., and Reed, S.M., 2006. Using SSURGO Data to Improve Sacramento Model a-priori Parameter Estimates. J. of Hydrol., 320(1): 103-116.

Alouini, M. S., Abdi A., and Kaveh M., 2001. Sum of gamma variates and performance of wireless communication systems over Nakagami-fading channels, IEEE Trans. Veh. Technol., 50(6), 1471–1480, doi:10.1109/25.966578.

Aucoin, F., 2015. FAmle: Maximum Likelihood and Bayesian Estimation of Univariate Probability Distributions.

Berne, A., Delrieu, G., Creutin, J.-D., Obled, C., 2004. Temporal and spatial resolution of rainfall measurements required for urban hydrology, J. Hydrol., 299 (2004), pp. 166–179.

Berne, A., and Krajewski, W. F., 2013. Radar for hydrology: Unfulfilled promise or unrecognized potential?, Adv. Water Resour., 51, 357–366.

Blonquist Jr., J. M., Jones, S. B., and Robinson, D. A., 2006. Precise irrigation scheduling for turfgrass using a subsurface electromagnetic soil moisture sensor, Agricultural Water Management, Vol. 84, 153-165.

Blyth, E., 2001. Modelling soil moisture for a grassland and a woodland site in south-east England. Hydrol. Earth Syst. Sci. 6, 39–48. doi:10.5194/hess-6-39-2002.

Bradley, A. A., and Potter K. W., 1992. Flood frequency analysis of simulated flows, Water Resour. Res., 28(9), 2375–2385, doi:10.1029/92WR01207.

Brimelow, J. C., Hanesiak, J. M., and Raddatz, R., 2010. Validation of soil moisture simulations from the PAMII model, and an assessment of their sensitivity to uncertainties in soil hydraulic parameters. Agricultural and Forest Meteorology, 150(1), 100-114. doi: 10.1016/j.agrformet.2009.09.006

Bringi, V. N. and Chandrasekar, V., 2001. Polarimetric Doppler Weather Radar: principles and Applications, Cambridge University Press, 648 pp.

Brock, F.V., Crawford, K.C., Elliott, R.L., Cuperus, G.W., Stadler, S.J., Johnson, H.L., and Eilts, M.D., 1995. The Oklahoma Mesonet: A technical overview., J Atmos Ocean Tech, 12, 5–19.

Bruni, G., Reinoso, R., van de Giesen, N. C., Clemens, F. H. L. R., and ten Veldhuis, J. A. E., 2015. On the sensitivity of urban hydrodynamic modeling to rainfall spatial and temporal resolution, Hydrol. Earth Syst. Sci., 19, 691–709, doi:10.5194/hess-19-691-2015.

Brunner, G., 2010. HEC-RAS river analysis system user's manual, Version 4.1, U.S. Army Corps of Engineers Hydrologic Engineering Center CPD-68, 766, Davis, CA.

Burnash, R.J., Ferral, R.L., and McGuire, R.A., 1973. A Generalized Streamflow Simulation System: Conceptual Modeling for Digital Computers, U.S. Department of Commerce National Weather Service and State of California Department of Water Resources.

Burns, D., Vitvar, T., McDonnell, J., Hassett, J., Duncan, J., and Kendall, C., 2005. Effects of suburban development on runoff generation in the Croton River basin, New York, USA. Journal of Hydrology, 311(1-4), 266–281. http://doi.org/10.1016/j.jhydrol.2005.01.022

Chandasekar, V. and Lim, S., 2008. Retrieval of reflectivity in a networked radar environment. J. Atmos. Oceanic Technol., 25, 1755-1767.

Chandrasekar, V. and Cifelli, R., 2012. Concept and principles of rainfall estimation from radar: multi sensor environment and data fusion. Indian Journal of Radio & Space Physics, 41, 389-402.

Chen, S., Gourley, J.J., Hong, Y., Kirtrtter, P.E., Zhang, J., Howard, K., Flamig, Z.L., Hu, J.J. and Qi, Y.C., 2013. Evaluation and Uncertainty Estimation of NOAA/NSSL Next-Generation National Mosaic Quantitative Precipitation Estimation Product (Q2) over the Continental United States. Journal of Hydrometeorology, 14(4), 1308-1322.

Chormanski, J., Van de Voorde, T., De Roeck, T., Batelaan, O., and Canters, F., 2008. Improving distributed runoff prediction in urbanized catchments with remote sensing based estimates of impervious surface cover. Sensors, 8(2), 910-932. doi:10.3390/s8020910

Chow, V.T., Maidment, D.R., and Mays, L.W., 1988. Applied Hydrology, McGraw-Hill, New York.

Chu, M. L., Knouft, J. H., Ghulam, A., Guzman, J. A., and Pan, Z., 2013. Impacts of urbanization on river flow frequency: A controlled experimental modeling-based evaluation approach. Journal of Hydrology, 495, 1-12. doi:10.1016/j.jhydrol.2013.04.051

Crawford, T.M., Stensrud, D.J., Carlson, T.N., Capehart, W.J., 2000. Using a soil hydrology model to obtain regionally averaged soil moisture values., J Hydrometeorol, 1, 353–363.

Dams, J., Dujardin, J., Reggers, R., Bashir, I., Canters, F., and Batelaan, O., 2013. Mapping impervious surface change from remote sensing for hydrological modeling. Journal of Hydrology, 485, 84–95. http://doi.org/10.1016/j.jhydrol.2012.09.045

David, C.H., Maidment, D.R., Niu, G.-Y., Yang, Z.-L., Habets, F., and Eijkhout, V., 2011. River network routing on the NHDPlusdataset. J. Hydrometeor, 12, 913–934.

Downton, F. 1970. Bivariate Exponential Distributions in Reliability Theory, J. R. Stat. Soc. Ser. B Methodol., 32(3), 408–417.

Du, J. K., Qian, L., Rui, H. Y., Zuo, T. H., Zheng, D. P., Xu, Y. P., and Xu, C. Y., 2012. Assessing the effects of urbanization on annual runoff and flood events using an integrated hydrological modeling system for qinhuai river basin, china. Journal of Hydrology, 464, 127-139. doi:10.1016/j.jhydrol.2012.06.057

Fares, A., Awal, R., Michaud, J., Chu, P.S., Fares, S., Kodama, K. and Rosener, M., 2014. Rainfall-runoff modeling in a flashy tropical watershed using the distributed HL-RDHM model. Journal of Hydrology, 519, 3436-3447.

Frankenberger, J.R., Brooks, E.S., Walter, M.T., Walter, M.F., and Steenhuis, T.S., 1999. A GIS-based variable source area hydrology model. Hydrol. Process. 13, 805–822. doi:10.1002/(SICI)1099-1085(19990430)13:6<805::AID-HYP754>3.0.CO;2-M

Lindner, G. and Miller, A., 2012. Numerical Modeling of Stage-Discharge Relationships in Urban Streams, J. Hydrol. Eng., 10.1061/(ASCE)HE.1943-5584.0000459, 590-596.

Gires, A., Schertzer, D., Tchiguirinskaia, I., Lovejoy, S., Onof, C., Maksimovic, C., and Simoes, N., 2011. Impact of small scale rainfall uncertainty on urban discharge forecasts. Weather Radar and Hydrology 400 : 400–406.

Gires, A., Giangola-Murzyn, A., Abbes, J., Tchiguirinskaia, I., Schertzer, D. and Lovejoy, S., 2014. Impacts of small scale rainfall variability in urban areas: a case study with 1D and 1D/2D hydrological models in a multifractal framework. Urban Water Journal, pp. 1-11.

Georgakakos, K., Graham, N.E., Georgakakos, A.P., and Yao, H., 2011. Demonstrating Integrated Forecast and Reservoir Management (INFORM) for Northern California in an Operational Environment. American Geophysical Union, Fall Meeting 2011, abstract #H31J-08.

Greene, D.R., and Hudlow, M.D., 1982. Hydrolometeorologic grid mapping procedure. Proc. 488 International Symposium on Hydrometeorology Conf. Denver, CO.

Gumindoga, W., Rientjes, T., Shekede, M. D., Rwasoka, D. T., Nhapi, I., and Haile, A. T., 2014. Hydrological impacts of urbanization of two catchments in harare, zimbabwe. Remote Sensing, 6(12), 12544-12574. doi:10.3390/rs61212544

Habibi, H., Rafieeinasab, A., Norouzi, A., Nazari, B., Seo, D.-J., Muttiah, R., and Davis, C., 2016. High-resolution flash flood forecasting for the Dallas-Fort Worth Metroplex (DFW), Journal of Water Management Modeling. DOI: 10.14796/JWMM.C401.

Hahn, T., 2007, Cuba—A library for multidimensional numerical integration, Comput. Phys. Commun., 176(11–12), 712–713, doi:10.1016/j.cpc.2007.03.006.

HL-RDHM user manual v. 3.0.0, 2009. (http://www.cbrfc.noaa.gov/present/rdhm/RDHM_3_0_0_User_Manual.pdf).

Homer, C. H., Fry, J. A., and Barnes, C. A., 2012. USGS Fact Sheet 2012–3020: The National Land Cover Database, U.S. Geological Survey Fact Sheet 2012-3020.

Homer, C.G., Dewitz, J.A., Yang, L., Jin, S., Danielson, P., Xian, G., Coulston, J., Herold, N.D., Wickham, J.D., and Megown, K., 2015. Completion of the 2011 National Land Cover Database for the conterminous United States-Representing a decade of land cover change information. Photogrammetric Engineering and Remote Sensing, Vol. 81(5), 345-354.

Iliopoulos, G., Karlis, D., and Ntzoufras, I., 2005. Bayesian estimation in Kibble's bivariate gamma distribution, Can. J. Stat., 33(4), 571–589, doi:10.1002/cjs.5550330408.

Izawa, T., 1953. The bivariate gamma distribution, Clim. Stat., 4(1), 9–15.

Javier, J. R. N., Smith, J. A., Meierdiercks, K. L., Baeck, M. L., and Miller, A. J., 2007. Flash Flood Forecasting for Small Urban Watersheds in the Baltimore Metropolitan Region. Weather and Forecasting, 22(6), 1331–1344. http://doi.org/10.1175/2007WAF2006036.1

Jobson, H.E., 1996. Prediction of traveltime and longitudinal dispersion in rivers and streams. U.S. Geological Survey. <http://pubs.usgs.gov/wri/1996/4013/documents/dispersion.pdf>

Jones, S. B., Wraith, J. M., and Or, D., 2002. Time domain reflectometry measurement principles and applications. Hydrological Processes, 16(1), 141-153. doi:10.1002/hyp.513

Jones, E.T., Slidell, L., Roth, K., and Costanza, K., 2009. A Comparison of the NWS Distributed Versus Lumped Hydrologic Model. Presented at the 23rd Conference on Hydrology.

Johnson, R. A., Evans, J. W., and Green, D. W., 1999. Some bivariate distributions for modeling the strength properties of lumber, U.S. Dept. of Agriculture, Forest Service, Forest Products Laboratory, Madison, WI.

Journel, A. G., and Huijbregts C. J., 1978. Mining Geostatistics, Academic Press.

Junyent, F., Chandrasekar, V., McLaughlin, Insanic, D., and Bharadwaj, N., 2010: The CASA Integrated Project 1 Networked Radar System. J. Atmos. Oceanic Technol., 27, 61–78. doi: http://dx.doi.org/10.1175/2009JTECHA1296.1

Kean, J. W., and Smith, J. D., 2004. Flow and boundary shear stress in channels with woody bank vegetation, in Riparian Vegetation and Fluvial Geomorphology, Water Sci. Appl. Ser., Vol. 8, edited by S. J. Bennett and A. Simon, pp. 237– 252, AGU, Washington, D. C.

Kean, J.W., and Smith, J.D., 2005. Generation and verification of theoretical rating curves in the Whitewater River Basin, Kansas. J. Geophys. Res., 110.

Kean, J.W., and Smith, J.D., 2010. Calculation of stage-discharge relations for gravel belled channels. Journal of Geophysical Research-Earth Surface, 115.

Kim, Y., Tachikawa, Y., Shiiba, M., Kim, S., Yorozu, K., and Noh, S. j., 2013. Simultaneous estimation of inflow and channel roughness using 2D hydraulic model and particle filters. J. Flood Risk Manage 6, 112–123. doi:10.1111/j.1753-318X.2012.01164.x

Kitzmiller, D., Cooten, S.V., Ding, F., Howard, K., Langston, C., Zhang, J., Moser, H., Zhang, Y., Gourley, J.J., Kim, D., and Riley, D., 2011. Evolving multisensor precipitation estimation methods: Their impacts on flow prediction using a distributed hydrologic model. J. Hydrometeorology, 12 (6), 1414-1431.

Kollet, S. J. and Maxwell, R. M., 2006. Integrated surface–groundwater flow modeling: A free-surface overland flow boundary condition in a parallel groundwater flow model. Advances in Water Resources, 29 (7), 945-958.

Koren, V., Schaake, J., Mitchell, K., Duan, Q. Y., Chen, F., and Baker, J. M.,1999. A parameterization of snowpack and frozen ground intended for NCEP weather and climate models. Journal of Geophysical Research-Atmospheres, 104(D16), 19569-19585.

Koren, V.I., Smith, M., Wang, D., and Zhang, Z., 2000. Use of soil property data in the derivation of conceptual rainfall-runoff model parameters, American Meteorological Society 15th Conference on Hydrology, Long Beach, CA, pp. 103-106.

Koren, V., Smith, M., and Duan, Q., 2003. Use of a priori parameter estimates in the derivation of spatially consistent parameter sets of rainfall-runoff models. In: Calibration of Watershed Models: Water Science and Applications 6, AGU Press, Duan et al., Editors, 239-254.

Koren, V., S. Reed, M. Smith, Z. Zhang and D.J. Seo., 2004. Hydrologic Laboratory Modeling System (HL-RMS) of the US National Weather Service. Journal of Hydrology (291), 297-318.

Koren, V., Moreda, F., Reed, S., Smith, M., and Zhang, Z., 2006. Evaluation of a grid-based distributed hydrological model over a large area, in: Predictions in Ungauged Basins: Promise and Progress. Presented at the Symposium S7 held during the Seventh IAHS Scientific Assembly, Foz do Iguaçu, Brazil.

Koren, V., Moreda, F., and Smith, M., 2008. Use of soil moisture observations to improve parameter consistency in watershed calibration. Physics and Chemistry of the Earth, 33(17), 1068-1080. doi:10.1016/j.pce.2008.01.003.

Koren, V., Smith, M., and Cui, Z., 2014. Physically-based modifications to the Sacramento Soil Moisture Accounting model. Part A: Modeling the effects of frozen ground on the runoff generation process. Journal of Hydrology, 519, 3475-3491.

Lamond, J., Stanton-Geddes, Z., Bloch, R., and Proverbs, D., 2013. Cities and flooding: Lessons in resilience from case studies of integrated urban flood risk management. Presented at the CIB 2013 World Congress, Special Conference Session: Making Cities More Resilient, CIB, Brisbane.

Lee, H., Seo, D. J., & Koren, V., 2011. Assimilation of streamflow and in situ soil moisture data into operational distributed hydrologic models: Effects of uncertainties in the data and initial model soil moisture states. Advances in Water Resources,34(12), 1597-1615. doi:10.1016/j.advwatres.2011.08.012

Lee, J. G., and Heaney, J. P., 2003. Estimation of Urban Imperviousness and its Impacts on Storm Water Systems, J. Water Resour. Plan. Manag., 129(5), 419–426, doi:10.1061/(ASCE)0733-9496(2003)129:5(419).

Lim, S., Chandrasekar, V., Lee, P., and Jayasumana, A.P., 2011. Real-time implementation of a network-based attenuation correction in the CASA IP1 testbed. J. Atmos. Oceanic Technol., 28, 197–209. doi: http://dx.doi.org/10.1175/2010JTECHA1441.1.

López, R., Barragán, J., and Colomer, M. À., 2007. Flow resistance equations without explicit estimation of the resistance coefficient for coarse-grained rivers. Journal of Hydrology, 338(1), 113-121. doi:10.1016/j.jhydrol.2007.02.027

Lu, J.-C. and Bhattacharyya, G. K., 1990. Some new constructions of bivariate Weibull models, Ann. Inst. Stat. Math., 42(3), 543–559, doi:10.1007/BF00049307.

Ma, Y., Feng, S., Su, D., Gao, G. and Huo, Z., 2010, Modeling water infiltration in a large layered soil column with a modified Green-Ampt model and HYDRUS-1D. Computers and Electronics in Agriculture., 71, S40-S47.

Mantoglou, A. and Wilson, J. L., 1982. The Turning Bands Method for simulation of random fields using line generation by a spectral method, Water Resour. Res., 18(5), 1379–1394, doi:10.1029/WR018i005p01379.

McLaughlin, D.J., Chandrasekar, V., Droegemeier, K., Frasier, S., Kurose, K., Junyent, F., Philips, B., Cruz-Pol, S., and Colom, J., 2005. Distributed collaborative adaptive sensing (DCAS) for improved detection, understanding, and prediction of atmospheric hazards. Ninth Symposium on Integrated Observing and

Assimilation Systems for the Atmosphere, Oceans, and Land Surface (IOAS-AOLS), Amer. Meteor. Soc.

McLendon, D., 2002. Hydrologic Investigation Of The NRCS Curve Number For Texas Watersheds Using Historical Records Of Rainfall And Runoff, MS Thesis, Dept. of Civil Eng., Texas Tech. University, Lubbock, TX.

Mejía, A. I., and Moglen, G. E., 2010. Impact of the spatial distribution of imperviousness on the hydrologic response of an urbanizing basin, Hydrol. Process., 24(23), 3359–3373, doi:10.1002/hyp.7755.

Mehta, V.K., Walter, M.T., Brooks, E.S., Steenhuis, T.S., Walter, M.F., Johnson, M., Boll, J., and Thongs, D., 2004. Application of SMR to Modeling Watersheds in the Catskill Mountains. Environmental Modeling & Assessment 9, 77–89. doi:10.1023/B:ENMO.0000032096.13649.92.

Miller, A.J. and Linder, G.A., 2012. Numerical Modeling of Stage-Discharge Relationships in Urban Streams. Journal of Hydrologic Engineering, 17(4), 590-596.

Miller, D.A., White, R.A., 1998. A Conterminous United States Multilayer Soil Characteristics Dataset for Regional Climate and Hydrology Modeling. Earth Interact. 2, 1–26. doi:10.1175/1087-3562(1998)002<0001:ACUSMS>2.3.CO;2

Moradkhani, H., and Sorooshian, S., 2008. General review of rainfall-runoff modeling: Model calibration, data assimilation, and uncertainty analysis. In Hydrological Modelling and the Water Cycle (pp. 1–24).

Moschopoulos, P. G., 1985. The distribution of the sum of independent gamma random variables, Ann. Inst. Stat. Math., 37(1), 541–544, doi:10.1007/BF02481123.

Murphy, A. H., and Winkler, R. L. (1987). A general framework for forecast verification. Monthly Weather Review, 115(7), 1330-1338.

Nadarajah, S., 2008. A Review of Results on Sums of Random Variables, Acta Appl. Math., 103(2), 131–140, doi:10.1007/s10440-008-9224-4.

Nagao, M., and Kadoya, M., 1970. The study on bivariate gamma distribution and its applicability, Ann. Disaster Prev. Res. Inst. Kyoto Univ., 13B, 105–115.

Nathanson, M., Kean, J. W., Grabs, T. J., Seibert, J., Laudon, H., and Lyon, S. W., 2012. Modeling rating curves using remotely sensed LiDAR data, Hydrological Processes, Vol. 26, Issue 9, 1427-1434.

National Weather Service, 2015. http://www.erh.noaa.gov/cle/safety/svrwx_flood.html, accessed 2015.

National Weather Service. 2015. http://www.srh.noaa.gov/fwd/?n=dnarrative (accessed 2015).

Nelson, J.M., and McDonald, R.R., 1996. Mechanics and modeling of flow and bed evolution in lateral separation eddies, USGS Director's approved report submitted to the USGS Grand Canyon Monitoring and Research Center and available at: http://www.gcmrc.gov/library/reports/GCES/Physical/hydrology/Nelson1996.pdf

Nelson, J.M., Bennett, J.P., and Wiele, S.M., 2003. Flow and sediment-transport modeling, in Kondolf, G.M., and Piegay, H., (eds.), Tools in fluvial geomorphology, England, Wiley, p. 539-576.

Nelson, B. R., Seo, D. J., and Kim, D. (2010). Multisensor precipitation reanalysis. Journal of Hydrometeorology, 11(3), 666-682.

Norouzi, A., Rafieeinasab, A., Seo, D.J., and Lee, J., 2015.Estimation of stage-discharge relationships in urban streams using a fluid-mechanically-based model, World Environmental Congress, 17-21 May, Austin, TX.

Ochoa-Rodriguez, S., Wang, L. P., Gires, A., Pina, R. D., Reinoso-Rondinel, R., Bruni, G., and ten Veldhuis, M. C., 2015. Impact of spatial and temporal resolution of rainfall inputs on urban hydrodynamic modelling outputs: A multi-catchment investigation. Journal of Hydrology. http://doi.org/10.1016/j.jhydrol.2015.05.035

Pandey, V. and Pandey, P.K., 2010. Spatial and Temporal Variability of Soil Moisture. International Journal of Geosciences, 1(2), pp. 87.

Pratesi, M., Santucci, F., and Graziosi, F., 2006. Generalized moment matching for the linear combination of lognormal RVs: application to outage analysis in wireless systems, IEEE Trans. Wirel. Commun., 5(5), 1122–1132, doi:10.1109/TWC.2006.1633365.

Rafieeinasab, A., Norouzi, A., Kim, S., Habibi, H., Nazari, B., Seo, D.-J., Lee, H., Cosgrove, B., and Cui, Z., 2015a. Toward high-resolution flash flood prediction in large urban areas – Analysis of sensitivity to spatiotemporal resolution of rainfall input and hydrologic modeling, Hydrologic Applications of Weather Radar Special Issue of Journal of Hydrology, Vol. 531, Part 2, 370-388.

Rafieeinasab, A., Norouzi, A., Seo, D.-J., and Nelson, B., 2015b. Improving High-Resolution Quantitative Precipitation Esti-mation via Fusion of Multiple Radar-Based Precipitation Products, Hydrologic Applications of Weather Radar Special Issue of Journal of Hydrology, Vol. 531, Part 2, 320-336.

Rafieeinasab, A., A. Norouzi, T. Mathew, D.J. Seo, H. Chen, V. Chandrasekar, P. Rees, and B. Nelson, 2015. Comparative evaluation of multiple radar-based QPEs for North Texas, International Symposium Weather Radar and Hydrology, Apr 7-10, Reston, VA.

Rahardjo, H., Ong, T. H., Rezaur, R. B., Leong, E. C. and Fredlund, D. G., 2010. Response parameters for characterization of infiltration. Environmental Earth Science. 60(7), 1369-80.

Rantz, S. E.,1982a. Measurement and computation of streamflow: Volume 1, Measurement of Stage and Discharge, Water-Supply Paper 2175 , U.S. Geological Survey, 284, Menlo Park, CA.

Rantz, S. E.,1982b. Measurement and computation of streamflow: Volume 2, computation of discharge, Water-Supply Paper 2175 , U.S. Geological Survey, 346, Menlo Park, CA.

Reed, S.M., 2003. Deriving flow directions for coarse-resolution (1-4 km) gridded hydrologic modeling. Water Resources Research, 39 (9), 1238, doi:10.1029/2003WR001989,2003

Reed, S., Koren, V., Smith, M., Zhang, Z., Moreda, F., Seo, D.J., and DMIP Participants, 2004. Overall distributed model intercomparison project results. Journal of Hydrology, Vol. 298, Nos. 1-4, 27-60.

Robinson, D.A., Campbell, C.S., Hopmans, J.W., Hornbuckle, B.K., Jones, S.B., Knight, R., Ogdent, F., Selker, J. and Wendroth, O., 2008. Soil moisture measurement for ecological and hydrological watershed-scale observatories: A review. Vadose Zone Journal, 7(1), 358-389.

Romano, N., 2014. Soil moisture at local scale: Measurements and simulations. Journal of Hydrology, 516, 5-20.

Rose, S. and Peters, N.E., 2001. Effects of urbanization on streamflow in the Atlanta area (Georgia, USA): a comparative hydrological approach. Hydrol. Process. 15, 1441–1457. doi:10.1002/hyp.218

Seiler, K. P., and Gat, J. R., 2007. Groundwater recharge from run-off, infiltration and percolation Springer. doi:10.1007/978-1-4020-5306-1

Seo, D.J., and Smith, J. A., 1991. Rainfall estimation using raingages and radar — A Bayesian approach: 1. Derivation of estimators, Stoch. Hydrol. Hydraul., 5(1), 17–29, doi:10.1007/BF01544175.

Seo, D.J., 1996. Nonlinear estimation of spatial distribution of rainfall — An indicator cokriging approach, Stoch. Hydrol. Hydraul., 10(2), 127–150, doi:10.1007/BF01581763.

Seo, D.J., and Smith, J. A., 1996a. Characterization of the Climatological Variability of Mean Areal Rainfall Through Fractional Coverage, Water Resour. Res., 32(7), 2087–2095, doi:10.1029/96WR00486.

Seo, D.J., and Smith, J. A., 1996b. On the Relationship Between Catchment Scale and Climatological Variability of Surface-Runoff Volume, Water Resour. Res., 32(3), 633–643, doi:10.1029/95WR03641.

Seo, D.J., 1998. Real-time estimation of rainfall fields using rain gage data under fractional coverage conditions, J. Hydrol., 208(1–2), 25–36, doi:10.1016/S0022-1694(98)00140-1.

Seo, D.J., Breidenbach, J., Fulton, R., Miller, D., and O'Bannon, T., 2000. Real-Time Adjustment of Range-Dependent Biases in WSR-88D Rainfall Estimates due to Nonuniform Vertical Profile of Reflectivity, J. Hydrometeorol., 1(3), 222–240, doi:10.1175/1525-7541(2000)001<0222:RTAORD>2.0.CO;2.

Seo, D.J., Seed, A., and Delrieu, G., 2010. Radar-based rainfall estimation, chapter in AGU Book Volume on Rainfall: State of the Science, F. Testik and M. Gebremichael, Editors. Geophys. Monogr. Ser. 191. doi:10.1029/GM191.

Seo, Y., Choi, N.J., and Schmidt, A. R., 2013. Contribution of directly connected and isolated impervious areas to urban drainage network hydrographs, Hydrol Earth Syst Sci, 17(9), 3473–3483, doi:10.5194/hess-17-3473-2013.

Seo D., Lakhankar T., Mejia J., Cosgrove B., and Khanbilvardi R., 2013, Evaluation of Operational National Weather Service Gridded Flash Flood Guidance over the Arkansas Red River Basin. JAWRA Journal of the American Water Resources Association.;49(6):1296-307.

Slack, J.R., and Landwehr J.M., 1992. Hydro-Climatic Data Network (HCDN): A U.S. Geological Survey streamflow data set for the United States for the study of climate variations, 1874-1988, U.S. Geological Survey, Open-File Report 92-129, available at http://pubs.usgs.gov/of/1992/0129/report.pdf

Sharif, H.O., Yates, D., Roberts, R., and Mueller, C., 2006. The Use of an Automated Nowcasting System to Forecast Flash Floods in an Urban Watershed. J. Hydrometeor 7, 190–202. doi:10.1175/JHM482.1.

Sheikh, V., Visser, S., and Stroosnijder, L., 2009. A Simple Model to Predict Soil Moisture: Bridging Event and Continuous Hydrological (BEACH) Modelling. Environ. Model. Softw. 24, 542–556. doi:10.1016/j.envsoft.2008.10.005

Shi, Y., Davis, K. J., Zhang, F., Duffy, C. J., and Yu, X., 2014. Parameter estimation of a physically based land surface hydrologic model using the ensemble Kalman filter: A synthetic experiment. Water Resources Research, 50(1), 706–724. http://doi.org/10.1002/2013WR014070

Smith, C.B., Lakhtakia, M., Capehart, W.J., and Carlson, T.N., 1994. Initialization of soil water content in regional-scale atmospheric prediction models. Bull. Am. Meteor. Soc., 75, 585-593.

Smith, M.B., Seo, D. J., Koren, V. I., Reed, S., Zhang, Z., Duan, Q.Y., Moreda, F., and Cong, S., 2004. The distributed model intercomparison project (DMIP): motivation and experiment design. Journal of Hydrology, Vol. 298, Nos. 1-4, 4-26.

Smith, M., Koren, V., Zhang, Z., Zhang, Y., Reed, S.M., Cui, Z., Moreda, F., Cosgrove, B.N. Mizukami, N., Anderson, N., and DMIP2 Participants., 2012. Results of the DMIP 2 Oklahoma Experiments. J. of Hydrol. 418-419, 17-48.

Solow, A. R., 1986. Mapping by simple indicator kriging, Math. Geol., 18(3), 335–352, doi:10.1007/BF00898037.

Stedinger, J. R., Vogel, R. M., and Foufoula-Georgiou, E., 1993. Frequency analysis of extreme events, in Handbook of Hydrology, edited by D. Maidment, McGraw-Hill Education, New York.

Tavakoli, M. and De Smedt, F., 2012. Impact of Climate Change on Streamflow and Soil Moisture in the Vermilion Basin, Illinois, 2012. Journal of Hydrologic Engineering 17, 1059–1070. doi:10.1061/(ASCE)HE.1943-5584.0000546

Tang, Y., Reed, P., van Werkhoven, K., and Wagener, T., 2007. Advancing the identification and evaluation of distributed rainfall-runoff models using global sensitivity analysis. Water Resources Research, 43(6), W06415. doi:10.1029/2006WR005813

Tavakoli, M., and Smedt, F.D., 2012. Validation of soil moisture simulation with a distributed hydrologic model (WetSpa). Environ Earth Sci 69, 739–747. doi:10.1007/s12665-012-1957-8

Tenenbaum, D. E., Band, L. E., Kenworthy, S. T. and Tague, C. L., 2006. Analysis of soil moisture patterns in forested and suburban catchments in Baltimore, Maryland, using high-resolution photogrammetric and LIDAR digital elevation datasets. Hydrol. Process. 20, 219–240.

Ten Veldhuis, J. A. E., Ochoa-Rodriguez, S., Bruni, G., Gires, A., Van Assel, J., Ichaba, A., and Willems, P., 2014. High resolution radar rainfall for urban pluvial flood management: Lessons learnt from 10 pilots in North-West Europe within the RainGain project. In 13th IWA/IAHR International Conference on Urban Drainage, Sarawak, Malaysia, 7-12 September 2014. Retrieved from http://repository.tudelft.nl/view/ir/uuid:7194c54c-a74f-4f90-ae30-215c6a06dae5/.

USDA, 1986. Urban hydrology for small watersheds. Technical Release 55 (TR-55) (Second ed.)., Natural Resources Conservation Service, Conservation Engineering Division.

van Werkhoven, K., Wagener, Th., Reed, P. and Tang, Y., 2008. Rainfall characteristics define the value of streamflow observations for distributed watershed model identification. Geophysical Research Letters, 35(11), np. doi:10.1029/2008GL034162

Vasiloff, S.V., Seo, D.J., Howard, K.W., Zhang, J., Kitzmiller, D.H., Mullusky, M.G., Krajewski, W.F., Brandes, E.A., Rabin, R.M., Berkowitz, D.S., Brooks, H.E, McGinley, J.A., Kuligowski, R.J., and Brown, B.G., 2007. Improving QPE and very short-term QPF: An initiative for a community-wide integrated approach, Bull. Amer. Meteor. Soc., 88, 1899-1911.

Verbeiren, B., Van de Voorde, T., Canters, F., Binard, M., Cornet, Y., and Batelaan, O., 2013. Assessing urbanisation effects on rainfall-runoff using a remote sensing supported modelling strategy. International Journal of Applied Earth Observation and Geoinformation, 21, 92-102. doi:10.1016/j.jag.2012.08.011

Vereecken, H., Huisman, J.A., Pachepsky Y., Montzka, C., van der Kruk, J., Bogena, H., Wwihermuller, L., Herbst, M., Martinez, G. and Vanderborght, J., 2014. On the spatio-temporal dynamics of soil moisture at the field scale. Journal of Hydrology, 516, 76-96.

Vieux, B., Park, J., and Kang, B. 2009. Distributed hydrologic prediction: Sensitivity to accuracy of initial soil moisture conditions and radar rainfall input. J. Hydrol. Eng., 14(7), 671–689.

Villarini, G., Smith, J. A., Serinaldi, F., Bales, J., Bates, P. D., and Krajewski, W. F., 2009. Flood frequency analysis for nonstationary annual peak records in an urban drainage basin, Adv. Water Resour., 32(8), 1255–1266, doi:10.1016/j.advwatres.2009.05.003.

Warrick, A. W., Lomen, D. O. and Yates, S. R., 1985, Generalized Solution to Infiltration. Soil Science Society of America Journal Vol. 49, No. 1, 34-38.

Western, A.W., Zhou, S.L., Grayson, R.B., McMahon, T.A., Blöschl, G., and Wilson, D.J., 2004. Spatial correlation of soil moisture in small catchments and its relationship to dominant spatial hydrological processes. Journal of Hydrology 286, 113–134. doi:10.1016/j.jhydrol.2003.09.014.

World Meteorological Organization (WMO), 2008. Guide to meteorological instruments and methods of observation, WMO-No.8, 7th Ed. https://www.wmo.int/pages/prog/gcos/documents/gruanmanuals/CIMO/CIMO_Guide-7th_Edition-2008.pdf.

Yang, C., Sheng, D. and Carter, J. P., 2012. Effect of hydraulic hysteresis on seepage analysis for unsaturated soils. Computers and Geotechnics, 41, 36-56.

Yilmaz, K. K., Gupta, H. V. and Wagener, Th., 2008. A process-based diagnostic approach to model evaluation: Application to the NWS distributed hydrologic model. Water Resources Research, 44(9), W09417. doi:10.1029/2007WR006716

Yu, X., and Pradhan, A., 2012. Real-Time monitoring of Bridge scour in clayey sediments, ICSE6 Paris, August 27-31, 2012.

Yu, X. and Drnevich, V. P., 2004. Soil water content and dry density by time domain reflectometery, Journal of Geotechnical and Geoenvironmental Engineering, Vol. 130, No., 9, 922-934.

Zahran, S., Brody, S. D., Peacock, Vedlitz, W. G., A., and Grover, H., 2008. Social vulnerability and the natural and built environment: a model of flood casualties in Texas, Disasters, 32(4), 537–560, doi:10.1111/j.1467-7717.2008.01054.x.

Zhang, X., Friedl, M. A., and Schaaf, C. B., 2006. Global vegetation phenology from Moderate Resolution Imaging Spectroradiometer (MODIS): Evaluation of global patterns and comparison with in situ measurements, J. Geophys. Res., 111, *G04017, doi:*10.1029/2006JG000217.

Zhang, J., Howard, K., Langston, C., Vasiloff, S., Kaney, B., Arthur, A., Cooten, S.V., Kelleher, K., Kitzmiller, D., Ding, F., Seo, D.J., Wells, E., and Dempsey, C., 2011. National mosaic and multi-sensor QPE (NMQ) system description, results and future plans. Bull. Amer. Meteor. Soc., 92, 1321–1338. doi: http://dx.doi.org/10.1175/2011BAMS-D-11-00047.1

Zhang, Y., Zhang, Z., Reed, S. and Koren, V., 2011. An enhanced and automated approach for deriving a priori SAC-SMA parameters from the soil survey geographic database. Computers and Geosciences, 37(2), 219-231.

Zhang, Y., and Shuster, W., 2015. Detectability and Interpretational Uncertainties: Considerations in Gauging the Impacts of Land Disturbance on Streamflow, J. Hydrol. Eng., 20(8), 04014088, doi:10.1061/(ASCE)HE.1943-5584.0001115.

Zhang, Y., Seo, D.-J., Habib, E., and McCollum, J., 2015. Differences in scale-dependent, climatological variation of mean areal precipitation based on satellite and radar-gauge observations, J. Hydrol., 522, 35–48, doi:10.1016/j.jhydrol.2014.11.077.

Zhang, Z. Y., Koren, V., Reed, S., Smith, M., Zhang, Y., Moreda, F., and Cosgrove, B., 2012. SAC-SMA a priori parameter differences and their impact on distributed hydrologic model simulations. Journal of Hydrology, 420, 216-227. doi:10.1016/j.jhydrol.2011.12.004

Biographical Information

Amir Norouzi received a Bachelor of Science degree in Civil Engineering from Isfahan University of Technology in 2003 and a Master of Science degree in Civil Engineering from Southern Methodist University in 2011. He began doctoral studies in water recourses engineering at the University of Texas at Arlington in 2012. He has served as a Graduate Research assistant and Graduate Teaching assistant in the Department of Civil Engineering at the University of Texas at Arlington.